2010

Experimental injector element stability characterization and combustion imaging

Robert LaShawn Ikard

EXPERIMENTAL INJECTOR ELEMENT STABILITY CHARACTERIZATION AND COMBUSTION IMAGING

by

ROBERT LASHAWN IKARD

A THESIS

Submitted in partial fulfillment of the requirements
for the degree of Master of Science in Engineering
in
The Department of Mechanical and Aerospace Engineering
to
The School of Graduate Studies
of
The University of Alabama in Huntsville

HUNTSVILLE, ALABAMA

2010

In presenting this thesis in partial fulfillment of the requirements for a master's degree from The University of Alabama in Huntsville, I agree that the Library of this University shall make it freely available for inspection. I further agree that permission for extensive copying for scholarly purposes may be granted by my advisor or, in his/her absence, by the Chair of the Department or the Dean of the School of Graduate Studies. It is also understood that due recognition shall be given to me and to The University of Alabama in Huntsville in any scholarly use which may be made of any material in this thesis.

Robert L. Ikard

Robert LaShawn Ikard

11/19/09

(date)

THESIS APPROVAL FORM

Submitted by Robert LaShawn Ikard in partial fulfillment of the requirements for the degree of Master of Science in Engineering in Mechanical and Aerospace Engineering and accepted on behalf of the Faculty of the School of Graduate Studies by the thesis committee.

We, the undersigned members of the Graduate Faculty of The University of Alabama in Huntsville, certify that we have advised and/or supervised the candidate of the work described in this thesis. We further certify that we have reviewed the thesis manuscript and approve it in partial fulfillment of the requirements for the degree of Master of Science in Engineering in Mechanical and Aerospace Engineering.

Robert Frederick Jr. 11/19/09
Dr. Robert A. Frederick, Jr. (Date) Committee Chair

Marlow D Moser 11/19/09
Dr. Marlow D. Moser (Date)

11/19/09
Dr. D. Brian Landrum (Date)

11/24/09
Dr. Kader Frendi (Date) Department Chair

11/24/09
Dr. Phillip A. Farrington (Date) College Dean

Debra M. Moriarity 3/30/10
Dr. Debra M. Moriarity (Date) Graduate Dean

ABSTRACT

School of Graduate Studies
The University of Alabama in Huntsville

Degree Master of Science in Engineering College/Dept. Engineering/Mechanical and Aerospace Engineering

Name of Candidate Robert LaShawn Ikard

Title Experimental Injector Element Stability Characterization and Combustion Imaging

This research evaluated the stability characteristics of a swirl-coaxial injector in an atmospheric combustion chamber using gaseous oxygen and gaseous methane as the propellants. The experiment studies the mixing processes in a laboratory-scale analogue to full-scale engine operating conditions. The injector was tested over a range of mass flow conditions that matched specified scaling parameters for a notional space engine. The scaling parameters used were mixture ratio, velocity ratio, momentum ratio, and momentum flux ratio. A maximum amplitude of 3.52% of chamber pressure was measured when the injector was placed 19 mm from the chamber wall. The associated instability mode—determined by phase and amplitude analysis from high-frequency pressure measurements—corresponded to a second tangential mode. The scaling parameters that most closely correlated to combustion instability were the design exit velocities and mixture ratio. CH^* chemiluminescence emissions were shown to occur in phase with pressure oscillations, and during unstable combustion, the combustion zone appeared to lift off the injector. Fuel annulus resonant frequencies possibly caused repeated flame blowout at lower fuel flow rates.

Abstract Approval: Committee Chair Robert A Frederick Jr 11/19/09

Dr. Robert A. Frederick, Jr.

Department Chair 11/24/09

Dr. Kader Frendi

Graduate Dean Debra M. Moriarity 3/30/10

Dr. Debra M. Moriarity

ACKNOWLEDGMENTS

This research was possible by funding through NASA Marshall Space Flight Center under the direction of David D. Stevenson and Huu P. Trinh. I would like to thank my advisor, Dr. Robert Frederick, for guiding me through the project and teaching me so much in the field of engineering. I express my sincere gratitude to the late Dr. Clark Hawk for having faith in me and hiring me as a graduate research assistant at the Propulsion Research Center, even without previous research experience.

To my committee, I want to thank Dr. Marlow Moser for his detailed explanations of anything I asked him and Dr. Brian Landrum for serving as a model to effectively communicate through spoken and written word. Dr. Vladimir Bazarov also deserves recognition for teaching me about injector design. Jim Hulka warrants mentioning for his monthly lessons on critical thinking.

I must acknowledge Dr. David Lineberry with his help in understanding data analysis and Tony Hall for fixing any problems that occurred. I would like to recognize the aid of Jason Bush, John Brooks, and Brian Sweeney with the experiment design, setting up the facility, and running the tests. Mr. Royal Ritchey, Mr. Ted Rogers, and Mr. Chris Underwood deserve recognition for their outstanding craftsmanship in the fabrication of various experimental components.

TABLE OF CONTENTS

LIST OF FIGURES

LIST OF TABLES

LIST OF SYMBOLS

SYMBOL	DEFINITION
a	Speed of Sound, Non-Dimensional Swirl Parameter
A	Cross-Sectional Area, Nominal Operating Point, Amplitude, Characteristic Swirl Geometry Parameter
CFD	Computational Fluid Dynamics
CH	Methylidyne Radical
d	Diameter
DAQ	Data Acquisition
e	Error
E	Energy
f	Frequency
FFT	Fast Fourier Transform
g	Gravitational Constant
GCH_4	Gaseous Methane
GOX	Gaseous Oxygen
h	Planck's Constant, Film Thickness
$\bar{h}$	Normalized Film Thickness

I	Intensity
I_{sp}	Specific Impulse
ICCD	Intensified Charge-Coupled Device
J	Momentum Flux Ratio
L	Length
LCH_4	Liquid Methane
LOX	Liquid Oxygen
LPRE	Liquid Propellant Rocket Engine
m	Radial Mode Order
$\dot{m}$	Mass Flow Rate
MR	Momentum Ratio
MW	Molecular Weight
n	Number, Tangential Mode Order
OF	Mixture Ratio
OH	Hydroxyl Radical
P	Pressure
PLC	Programmable Logic Controller
q	Longitudinal Mode Order
$\dot{Q}$	Volumetric Flow Rate

r	Variable Radius
R	Radius
$\bar{R}$	Universal Gas Constant, Stability Margin
Re	Reynolds Number
RFP	Request for Proposals
S	Swirl Number
SP	Setpoint
t	Transverse Mode Order
T	Temperature
Th	Thrust
UV	Ultraviolet
v	Emitted Photon Frequency
V	Velocity
VR	Velocity Ratio
X	X-coordinate of Scaling Parameter
Y	Y-coordinate of Scaling Parameter
α	Liquid Spray Angle
γ	Specific Heat Ratio
ΔP	Pressure Drop

$\Delta\phi$	Phase Difference
ζ	Fuel Mass Fraction
μ	Viscosity, Discharge Coefficient
ρ	Density
τ	Time Delay
ϕ	Fullness Factor
Φ	Equivalence Ratio
Ω	Phase, Process Homochronocity

SUPERSCRIPT

$'$	Dynamic
*	Excited-State Radical

SUBSCRIPT

$actual$	Actual
air	Air
avg	Average
c	Chamber
$calc$	Calculated
cr	Critical

est	Estimated
f	Fuel
fs	Full Scale
i	Inner
in	Inlet
inj	Injector
j	Jet
LCH_4	Liquid Methane
LOX	Liquid Oxygen
m	Model
mix	Mixing
n	Nozzle
o	Outer
ox	Oxidizer
$p-p$	Peak-to-Peak
rel	Relative
$stoic$	Stoichiometric
vc	Vortex Chamber
z	Axial

θ	Circumferential
Σ	Total

To my family

Do not go where the path may lead, go instead where there is no path and leave a trail.

—Ralph Waldo Emerson

CHAPTER 1

INTRODUCTION

Scientific research consists in seeing what everyone else has seen, but thinking what no one else has thought.

—Anonymous

1.1 Historical Background

The development of propulsion systems, particularly Liquid Propellant Rocket Engines (LPREs), includes many difficult problems, but perhaps the most prevalent and hazardous one is combustion instability. In fact, almost all rocket engine development programs experience some form of combustion instability [1], and it is the cause of the greatest number of engine failures during the developmental stage [2]. Originally discovered in the late 1930s [3], progress in eliminating combustion instability was not really achieved, considered, much less approached until larger propulsion systems were required for intercontinental ballistic missiles and launch vehicles for human space exploration [3]. Instabilities within combustion chambers have caused catastrophic failure of many engines. Most notably, the Saturn F-1 engine experienced instabilities with pressure oscillations comparable to the mean chamber pressure in 20 of its first 44 full-scale tests that had to be controlled [3]. Despite the progress that

has been made over the past few decades, this problem unfortunately still persists. Current computer models predict that the first stage solid rocket booster of the Ares I launch vehicle will generate violent vibrations capable of destroying the rocket [4].

Although the main problems with combustion instability are the destruction it can cause to the vehicle and the danger it poses to humans, a complementary problem is the massive cost and time associated with resolving the problem. Oftentimes, the injector design and layout and the baffle arrangement are the focus of providing stability to an engine, which was the case with the F-1 engine. The instabilities were eliminated after many redesigns and more than 2,700 full-scale tests over several years [3, 5]. Currently, limitations in funding do not allow prolific spending on full-scale tests. Laboratory-scale testing, however, provides a more affordable option for studying basic combustion processes.

Recently, increased interest in liquid oxygen (LOX) and liquid methane (LCH_4) for future space exploration—due to potential increased performance, in-situ resources for lunar and Mars missions, and lower environmental impact—has led to experimentation with the propellant combination. Recent full-scale tests [6,7] using LOX/LCH_4 have been performed with a modified RS-18 engine, the lunar ascent engine from the Apollo program, to study its relatively unknown combustion and ignition characteristics. However, laboratory-scale testing, being less expensive and time-consuming, is a useful tool for avoiding any similar problems seen with the Saturn F-1 engine without expending already limited resources.

1.2 Combustion Instability

Although combustion instability is represented physically by many characteristics, the physical manifestation most commonly associated with combustion instability is chamber pressure oscillations, which have reached amplitudes on the order of 10-1,000 percent of the mean chamber pressure. System vibration is also a common characteristic of combustion instability, with accelerations greater than 1,000 times that of gravity having been measured previously. One concern caused by chamber pressure oscillations and vehicle vibration is the effect they have on the rest of the engine. Large magnitude vibrations can harm guidance, navigation, and control systems or the payload onboard the rocket. Large pressure oscillations can cause damage to the structure of the vehicle, which can cause even greater damage when combined with increased heat transfer, another characteristic of an unstable engine. Fluctuation in propellant mass flow rate is another symptom of combustion instability. Observation of rocket exhaust plumes can reveal signs of combustion instability. Oscillations of Mach diamonds and variations of luminosity in the plume are optical methods for determining the existence of combustion instability [1].

Combustion instability emerges in various forms, usually divided into three categories: low-, intermediate-, or high-frequency instability. Low- and intermediate-frequency instabilities are usually associated with wave motions in the feed system. Although they typically begin low in amplitude, they can eventually increase in amplitude. High-frequency combustion instability occurs when the combustion couples with the fluid dynamics of the system [1]. Depending on injector pattern, baffle

arrangement, or acoustic cavities, these instabilities will either dampen or escalate. Oscillatory energy provided to the system as a result of this coupling can sustain the instability and lead to chamber pressure fluctuations up to and beyond the mean chamber pressure, as well as large temperature and heat flux variations [1]. Large LPREs with extremely high chamber pressures cannot withstand pressure oscillations of such a magnitude due to the increased structural and thermal loads.

When high-frequency combustion instability is present in an LPRE, the chamber pressure oscillates in a wave-like pattern that is dependent on the order of the instability. This order is known as an instability mode. Instability modes are physically represented in two categories: longitudinal and transverse modes. In a longitudinal mode the pressure oscillates along the chamber axis. Transverse modes are subdivided into two categories for cylindrical combustion chambers: radial and tangential modes. Schematics of a first radial mode and a second radial mode are shown in Figure 1.1 [8], where "P" and "V" refer to the pressure and velocity fields, respectively. Areas of maximum pressure are indicated by "+" and solid contour lines, and areas of minimum pressure are indicated by "-" and dashed contour lines. For a radial mode, the minimum and maximum pressure alternate between the center of the chamber and the chamber wall in half-cycle increments, as shown in Figure 1.2 [9]. A circular node line is created where the pressure oscillations remain zero. The order of the radial mode is determined by the number of pressure peaks and node lines. For example, the second radial mode in Figure 1.1 has two pressure peaks and two node lines. The arrows in the velocity field indicate the direction of the mean flow from the high-pressure region to the low-pressure region.

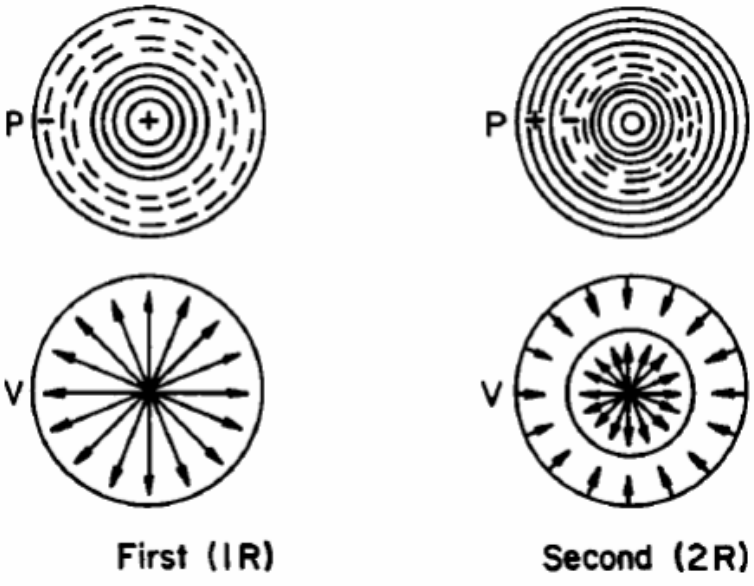

Figure 1.1: First and Second Order Radial Modes

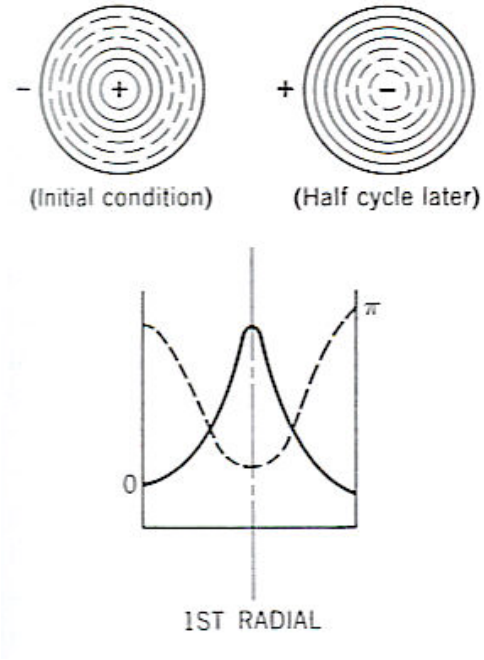

Figure 1.2: Pressure Profile of a First Radial Mode

Figure 1.3 shows the pressure and velocity distributions of a first and second order tangential mode [8]. A tangential mode has a maximum pressure at one side of the chamber wall and a minimum pressure on the other side. The minimum and maximum pressures are separated by a node line that crosses the chamber diameter. For one case, the peak pressure travels circumferentially around the chamber. This type of tangential mode is known as a spinning mode. Sometimes two counter-rotating spinning modes can be present and cause a standing mode, where the peak pressure oscillation occurs at the wall but does not travel along the chamber circumference. The pressure distribution for a spinning and standing mode is shown in Figure 1.4 [9]. Similar to the radial mode, the order of a tangential mode is determined by the number of pressure peaks and node lines. Comparing the first tangential and second tangential modes in Figure 1.3, the node lines for higher-order tangential modes are equidistant. The pressure across each node lines alternates between a maximum and a minimum. The velocity again shows a mean flow movement from the high-pressure area to the low-pressure area.

Modes that have characteristics of multiple longitudinal or transverse modes are known as combined modes. Examples of combined modes are shown in Figure 1.5. The first mode shown is a first tangential-first radial combined mode. The physical manifestation of the combined mode is like a superposition of a first tangential mode and a first radial mode. A single tangential node line crosses the diameter, and a single radial node line is present. The pressure changes from a maximum to a minimum across each node line. Any combination of longitudinal and transverse modes is possible. However, it must be noted that a combined mode is a mode by itself and

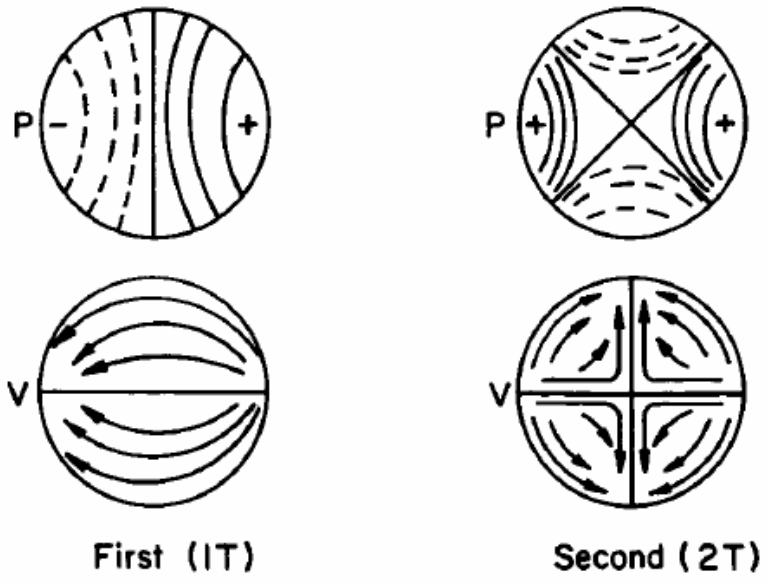

Figure 1.3: First and Second Order Tangential Modes

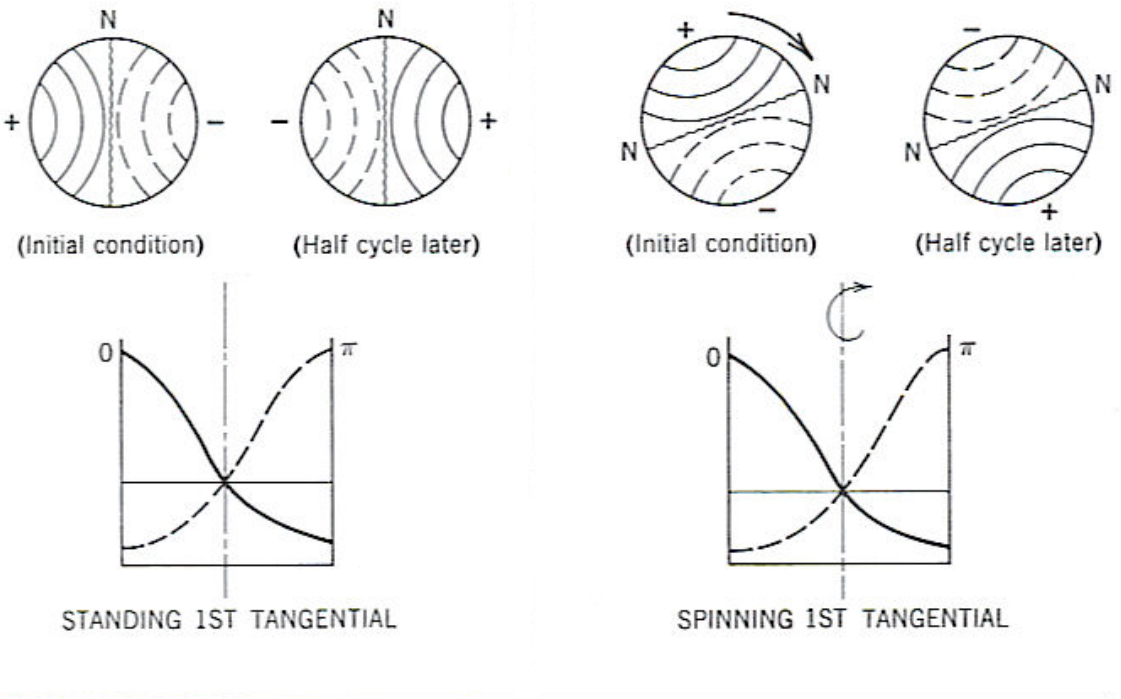

Figure 1.4: Pressure Profile of Spinning and Standing Tangential Modes

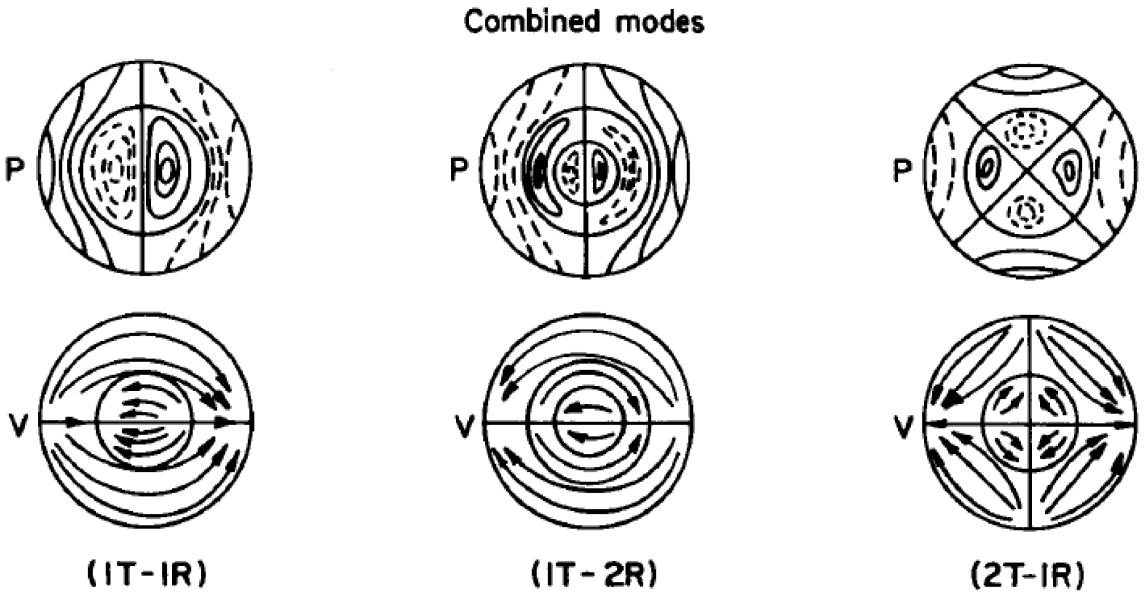

Figure 1.5: Examples of Combined Radial and Tangential Modes

not an actual combination of multiple modes. A first tangential-first radial mode, for example, will occur at a frequency that is different from a first tangential mode or a first radial mode. A simplified naming convention is used to identify instability modes. The order of the mode is listed first, and the first letter of the type of mode is listed second. For example a second tangential mode is shown as a "2T" mode. This convention is also used for combined modes. A second tangential-first radial-third longitudinal mode is denoted as a "2T1R3L" mode.

1.3 Flame Visualization and Chemiluminescence

One of the advantages of combustion compared to other chemical reactions is the presence of a visible flame. Historical observations noted by Gaydon [10] describe the effects pressure perturbations have on the flame. He showed that noisy flames are

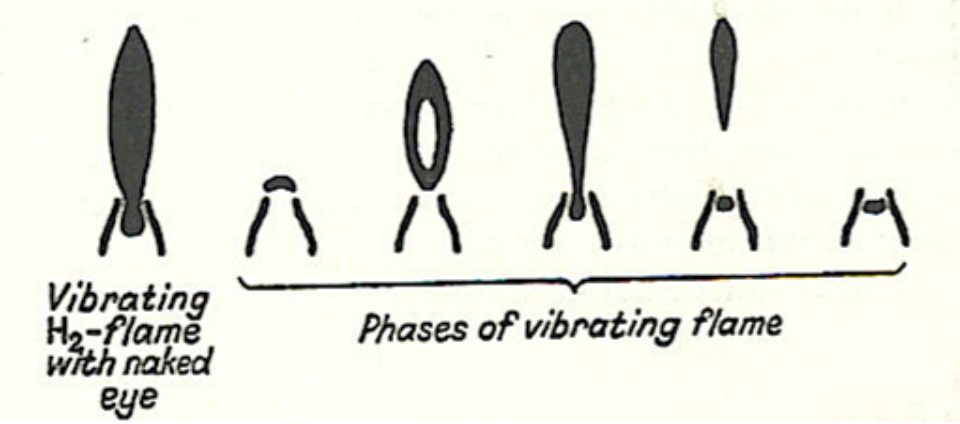

Figure 1.6: Flame Structure Effects from Vibration

associated with the pressure pulses produced by the change in speed and direction of the flame front, which is a result of turbulence. When placed in an enclosure, the flame can resonate with the acoustics of the outer tube, creating a distinct frequency—determined by the mass flow rates and the position within the enclosure—that is known as combustion instability. In this configuration, the pressure effects cause the flame to "vibrate," resulting in a change of the flame structure. The flame grows until it separates into two. The upper portion lifts and burns out, while the lower portion remains at the exit of the injector to begin the process again. He also notes that the vibrations can become so strong that flame blowout can occur. Figure 1.6 shows the changes of the vibrating flame's structure.

The vibration of the flame is initiated by the periodic release of the heat energy provided by the flame [10]. Lord Rayleigh first hypothesized how periodic heat release causes the flame to vibrate, which is now referred to as the Rayleigh criterion [11].

> "If heat be periodically communicated to, and abstracted from, a mass of air vibrating (for example) in a cylinder bounded by a piston, the effect produced will depend upon the phase of the vibration at which the transfer of heat takes place. If heat be given to the air at the moment of greatest condensation, or be taken from it at the moment of greatest rarefaction, the vibration is encouraged. On the other hand, if heat be given at the moment of greatest rarefaction, or abstracted at the moment of greatest condensation, the vibration is discouraged."

The vibrations first initiated by heat release cause vibrations in the supply tube, resulting in mass flow fluctuations. If the mass flow is at a maximum when the pressure in the chamber is at a maximum, the pressure is raised even further, sustaining the vibrations [10].

The variation in heat release can be caused by several factors as described by Gaydon [10]:

1. Pressure: Heat release is usually proportional to pressure and, therefore, not limited by the combustion process, but rather the mixing process.

2. Flame Area: Changes in flame area are caused by variations in mass flow rates and flame movement due to pressure fluctuations.

3. OF ratio: Chamber pressure may affect the flow rates of the fuel and oxidizer differently.

4. Mixing Rate: Unstable combustion increases turbulence and, thus, the mixing rate of the propellants.

The amount of light emitted from a flame can help to understand the fundamental processes that occur during combustion. Studying the spectra of a flame helps to identify intermediate species that are present during combustion. Understanding which chemical species are present, where they are most abundant, and the quantity of the species gives insight into the combustion properties and reaction mechanisms that describe the process [12]. Chemiluminescence is one method of studying the intermediate species that occur during combustion.

During a chemical reaction, such as between an oxidizer and a fuel, energy is added to the molecules, which allows the chemical bonds between different atoms to break apart. The chemical specie that is left is usually not at the ground state, but rather at a higher, excited energy state. Since the specie cannot stay at this higher energy state, it begins to lose energy from vibrations or heat loss until it reaches the lowest energy level above the ground state. The specie then falls to the ground state and emits a photon, a process known as chemiluminescence. This process can occur for many different species that are created from chemical reactions. A generic chemical equation of a typical reaction that creates a radical in an excited state (D^*) can be written as

$$A + B \rightarrow C + D^*, \tag{1.1}$$

where A and B are the reactants and C is a product. The relaxation of the excited radical to its ground state (D) and the emitted energy in the form of a photon can be written as

$$D^* \rightarrow D + hv, \tag{1.2}$$

where h is Planck's constant and v is the frequency of the emitted light. The specific wavelength emitted is based on the energy level from which the molecule relaxes, represented as

$$E_2 - E_1 = hv, \tag{1.3}$$

where E_1 and E_2 are the energies associated with the ground state and excited state, respectively. Figure 1.7 illustrates the process that produces chemiluminescence.

Three radicals that form in the reaction zone—CH, OH, and C_2—are much stronger than normal equilibrium reactions [12]. The radical C_2 has a broadband emission range and was not considered for this research. The particular specie that was imaged during the research for this report was the CH^* radical, which emits at a peak wavelength of 431 nm. This radical is common in hydrocarbon combustion. Initially, the reaction believed to create this radical was

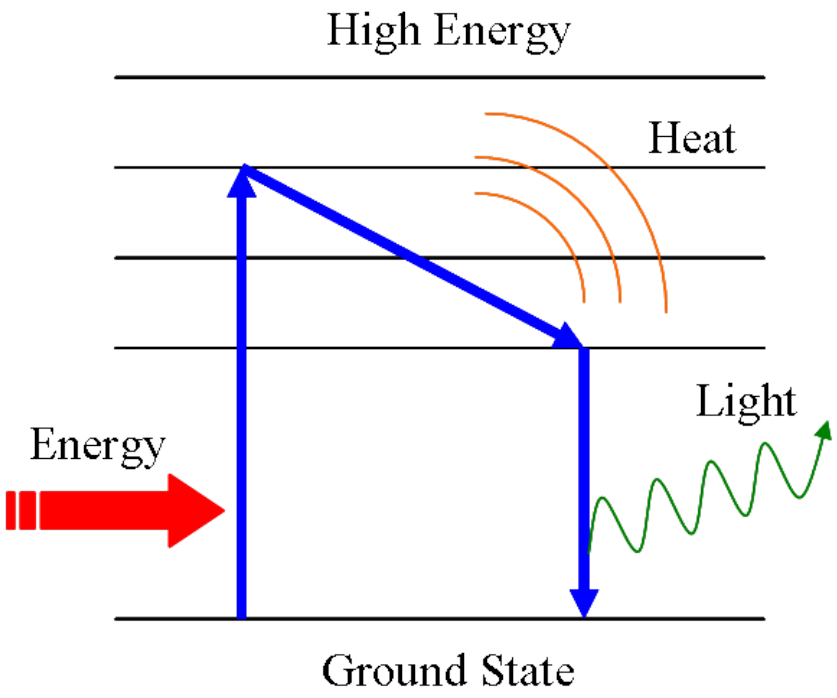

Figure 1.7: Illustration of Chemiluminescence Emission

$$C_2 + OH \rightarrow CO + CH^* \tag{1.4}$$

although a recent study [13] argues the reactions shown in Equation 1.5 and Equation 1.6 are the dominant causes of CH^* formation.

$$C_2H + O \rightarrow CO + CH^* \tag{1.5}$$

$$C_2H + O_2 \rightarrow CO_2 + CH^*. \tag{1.6}$$

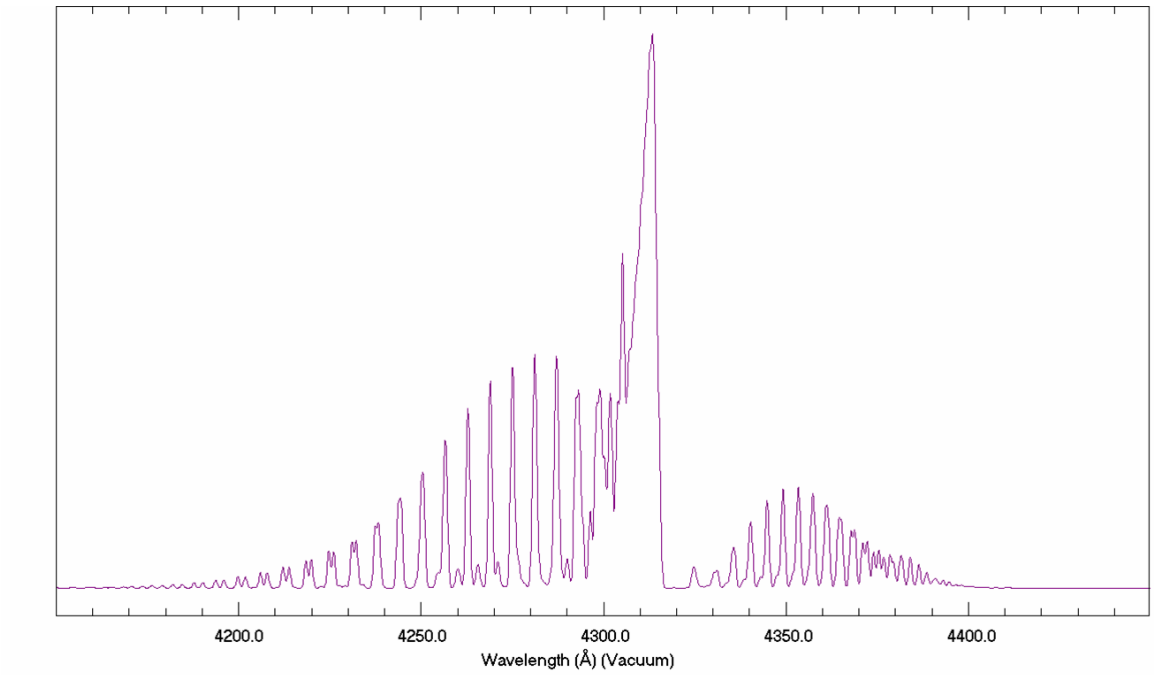

Figure 1.8: Emission Spectra of the CH^* Radical

Each of the previous reactions indicate that the production of CH^* radicals is the result of a chemical excitation and not a thermal excitation. Therefore, it is a purely chemiluminescent process. CH^* emissions are expected to occur at the base of hydrocarbon diffusion flames and become weaker higher in the flame [12]. The spectra for CH^* emission, which were created using LIFBASE software [14], are shown in Figure 1.8.

Another specie that has been studied extensively is OH^*, which emits at a peak wavelength of 309 nm. OH^* radicals are expected to form due to strong excitation in the reaction zone at the base of hydrocarbon flames. The reaction attributed to OH^* creation is

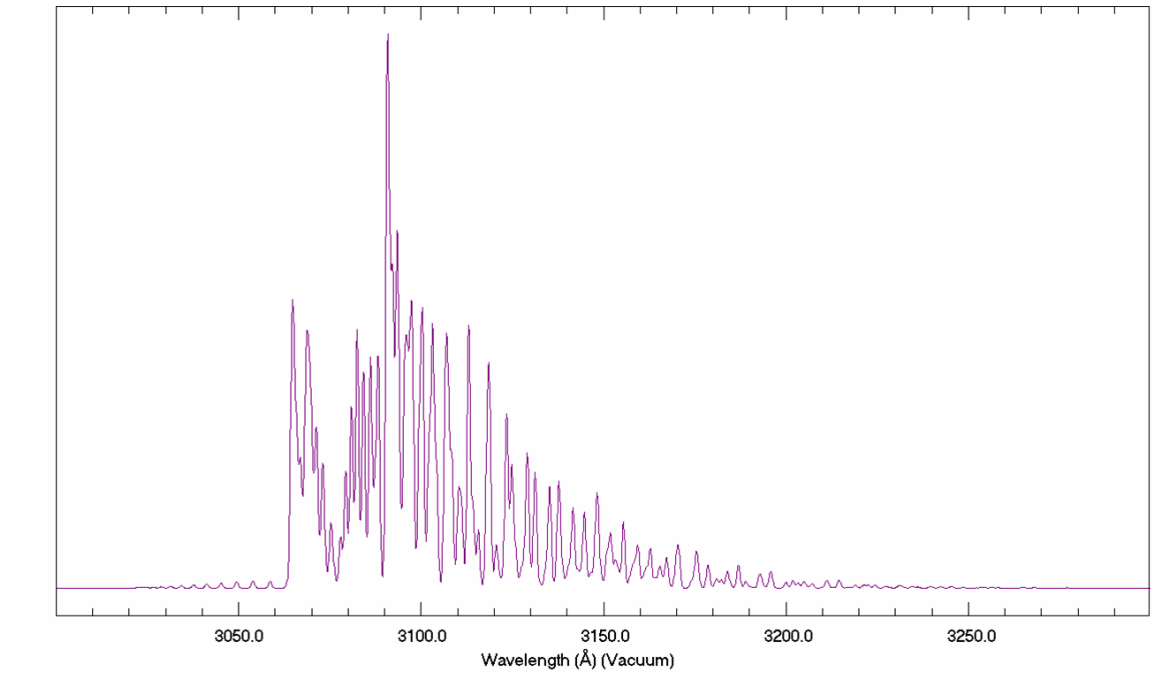

Figure 1.9: Emission Spectra of the OH* Radical

$$CH + O_2 \rightarrow CO + OH^*. \tag{1.7}$$

Due to the similarity between CH* and OH* chemiluminescence and the fact that CH* is easier to image since it emits in the visible range, only the former was the focus for this study. Although OH* chemiluminescence imaging was not done to a large extent, check-out imaging of this molecule was performed during this research to prove that the equipment available was capable of imaging in the UV wavelength range. The OH spectra were created using LIFBASE software and are shown in Figure 1.9.

1.4 Research Objective

The objective of this research was to design and fabricate a swirl-coaxial injector to be tested in a laboratory-scale experiment to study the stability characteristics of the injector. The injector was designed to apply to the current goals of the Constellation space exploration program and utilize a LOX/LCH_4 propellant combination that is in consideration for future lunar and Mars mission architectures—the latter being especially important due to in-situ resources. The experiment, conducted at atmospheric pressure, used gaseous oxygen and gaseous methane as the propellants to simulate full-scale conditions. A map of the injector was created by varying the fuel and oxidizer flow rates and measuring the pressure response in the combustion chamber. The flow rates where high-amplitude oscillations occurred were analyzed to determine the instability mode present. The thermal environment was also thoroughly investigated to determine the average speed of sound in the chamber. The map of flow rates was run with the injector at three different locations within the chamber to excite different instability modes: centered, halfway between the center and the chamber wall, and three-fourths the distance between the center and the wall. The effect of combustion instability on the flame's structure and intensity was studied through high-speed imaging of CH^* chemiluminescence. New measurement diagnostics were implemented and investigated for feasibility in providing additional information on the stability characteristics of an injector for future studies. The new diagnostics were high-frequency pressure transducers in the propellant feed lines and

OH^* chemiluminescence emissions. Five flow rate conditions of interest were repeated to test for variability and to use these new diagnostics.

CHAPTER 2

LITERATURE REVIEW

Research is what I'm doing
when I don't know what I'm doing.

—Wernher von Braun

This experiment is based on an experimental approach used by Russian engineers for studying injector-coupled responses that has only relatively recently been described in the open literature [15]. It was used as a way to quickly and efficiently evaluate the instability characteristics of an injector element to be used in an LPRE. The primary benefit of this method is that it is less expensive to operate than full-scale testing. If combustion instability occurs during full-scale testing, the large pressures can damage the engine, which would require large time and financial efforts to try an alternate configuration. For a laboratory-scale experiment, the less design-intensive hardware and low pressures make testing different injectors or injector geometries quicker, and it is less likely to cause severe damage to the injector or experiment. The low-pressure operation also makes the experiment safer to run, especially for longer durations, a benefit to experimentalists who want to study the complex and destructive phenomena of combustion instability.

2.1 Russian Literature

The hypothetical validity of the experiment relies on a few important physical assumptions of the creation of high-frequency combustion instability in LPREs as well as following specific approaches outlined in the literature. These assumptions and approaches are summarized from References [2] and [15]:

1. This approach is based on partial simulation of a complex process. The most important physical representations of the full-scale processes must be selected and reproduced in the modeled conditions. Matching all similarity parameters is not required—in fact it is practically impossible—but the governing parameters must be selected and modeled correctly to ensure success. The best way to verify the assumptions made is to compare the results of both the model and full-scale tests.

2. A single, full-scale injector element is used to provide the best comparison between the model and full-scale.

3. Bipropellant injectors are assumed to operate independently. Therefore, the interaction of adjacent injector elements at the initial section, the most sensitive to disturbances, is negligible.

4. The boundary conditions and governing criteria should be selected based on the physical concepts being studied.

5. The variation of propellant mass flow rates determines the boundaries of regions of spontaneous excitation and damping.

6. The mean chamber pressure has no effect on the acoustic field within the chamber. The normalized chamber pressure oscillations, $\frac{p'}{p_c}$, are the actual parameters indicative of the acoustic field.

7. It is important to match the phases of the combustion chamber acoustics and the combustion processes of the model to the full-scale conditions. Equation 2.1 shows the relation of the phase characteristics to match.

$$\Omega = (\tau f)_m^{-1} = (\tau f)_{fs}^{-1}. \tag{2.1}$$

Here, τ is the characteristic time delay that represents the time needed for the propellant to convert to combustion gases, and f is the frequency of the acoustic oscillation, or the inverse of the oscillation period.

8. The manifold acoustics and injection processes must also be taken into account by matching the phases between the full scale and the model. Equation 2.2 shows the relation of the phase characteristics to match.

$$\Omega_{inj} = (\tau_{inj} f)_m^{-1} = (\tau_{inj} f)_{fs}^{-1}. \tag{2.2}$$

In this case τ_{inj} is the time delay of acoustic disturbances in the injector passage. The relation of the time delay to the injector length L_{inj} and the speed of sound a_{inj} of the medium within it is $\tau_{inj} \sim L_{inj}/a_{inj} \sim L_{inj}/f_{inj}$, where f_{inj} is the natural frequency of the injector. This parameter can be achieved by properly selecting the model feed line geometry and setting the propellant temperatures

so that the speeds of sound of the model and full-scale tests are equal, $a_{inj,m} = a_{inj,fs}$.

9. It is important to match the frequencies of transverse oscillation modes from the full-scale chamber to the model by Equation 2.3.

$$f_{c,m} = f_{c,fs}. \tag{2.3}$$

Matching the expected frequency can be done through a relation, shown in Equation 2.4, between the full-scale and model diameters and speeds of sound.

$$d_m = \frac{d_{fs} a_m}{a_{fs}}. \tag{2.4}$$

10. Placing the injector close to the model chamber wall excites transverse instabilities, specifically the tangential mode. Tangential instabilities are the most likely to occur during the development of large combustion chambers and gas generators, and they are the most destructive. Therefore, it is best to try to model these instabilities.

11. For LPREs with high chamber pressures and temperatures, the chemical kinetic processes, atomization, and vaporization occur quickly, if at all, and are not the rate-limiting factors in the combustion process. Rather, mixing is considered

to be the governing factor. Thus, the mixing time τ_{mix} is the defining response time of the combustion process.

12. Whether using the actual propellants or simulated propellants, they must be in gas form. The chamber pressure is usually above the critical pressure of the propellants, and the temperatures of the propellants at the injector inlet are close to the critical temperatures. At these conditions, the propellants act more like a dense gas than a liquid. Therefore, using gaseous propellants at low pressures more accurately simulates the physical properties of the liquid propellants at high pressures and temperatures. If the LPRE uses a regenerative cycle and one or both of the propellants enter the combustion chamber in the gas phase, this approach is even more justified.

13. The addition of diluents, inert gases such as nitrogen or helium, helps to provide similar volumetric flow rates and exit velocities while maintaining combustion similarity by keeping the reactive propellant flow rate components intact.

14. Switching the passages the fuel and oxidizer go through is allowed and is sometimes a more accurate representation of the full-scale conditions.

A basic experiment setup provided by the Russian literature is shown in Figure 2.1 [15]. The combustion chamber is a simple cylinder that is open to the atmosphere at the top. It is placed on a flat steel plate over the injector to be tested. The chamber can be water cooled to allow for testing close to the wall. The piping for the gaseous propellants contains a heater coil for heating the propellants, a metering orifice for measuring the flow rates, and a throttling valve for controlling the flow rates.

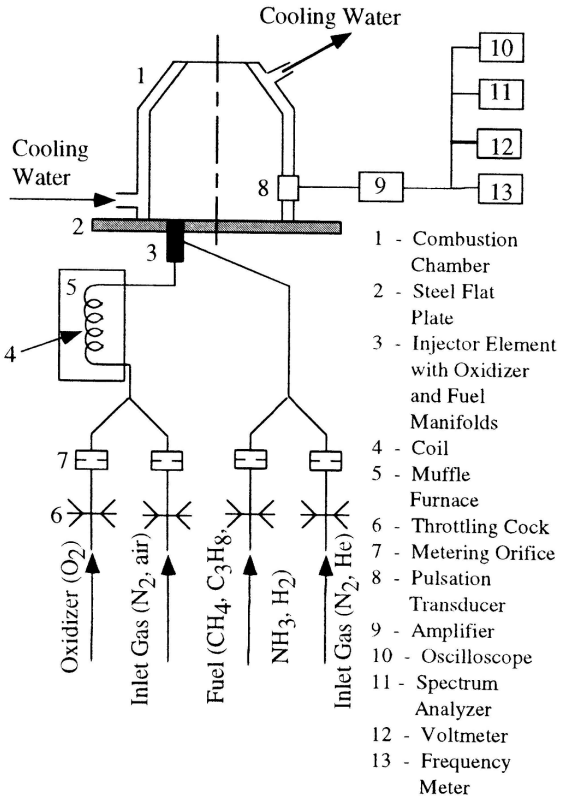

Figure 2.1: Experimental Setup from Russian Literature

O_2 (oxygen) or air is used as the oxidizer, and CH_4 (methane), C_3H_8 (propane), NH_3 (ammonia), and H_2 (hydrogen) are suggested for the fuels. In addition to oxygen and the fuel, inert gases such as N_2 (nitrogen) and He (helium) are supplied to change the velocities and densities of the gases for scaling purposes. A pressure transducer is used to measure the pressure oscillations in the chamber, and multiple instruments are used to evaluate the measurement.

The method of determining the stability boundaries given in the Russian literature is to continuously vary the flow rates until oscillations occur or disappear, denoting the stability boundary or hysteresis boundary, respectively. Figure 2.2 shows a typical instability region that occurs while varying the operating conditions. The

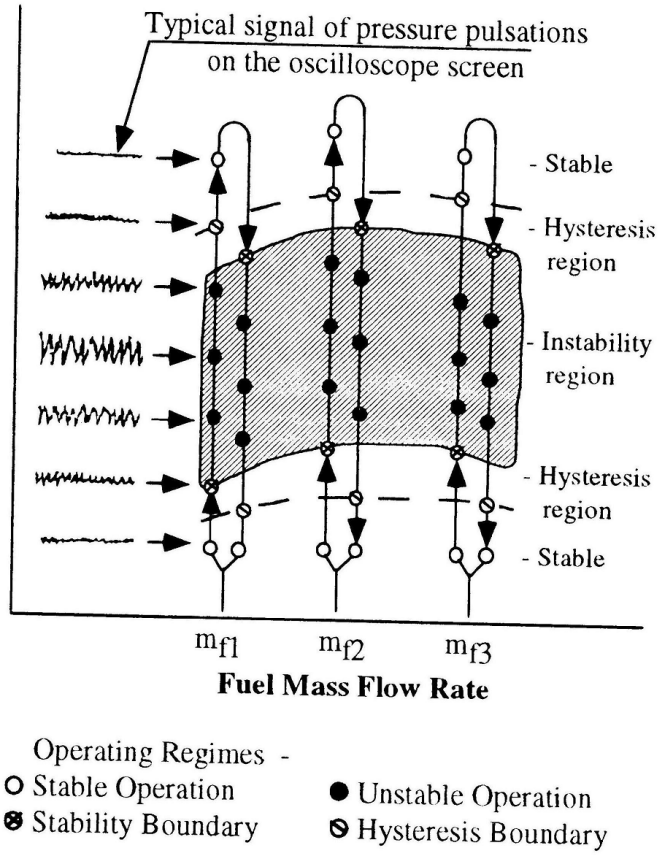

Figure 2.2: Instability Boundaries from Russian Literature

stability margin that indicates the relative stability of the injector compared to other tested injectors can be determined by calculating $\bar{R}$, a non-dimensional parameter indicating how close the operating conditions are to the stability or hysteresis boundaries. Figure 2.3 shows the nominal operating point, A, where X and Y are the desired operating parameters. Using this figure, $\bar{R}$ can then be calculated using Equation 2.5.

$$\bar{R} = \sqrt{\bar{R}_X^2 + \bar{R}_Y^2}, \tag{2.5}$$

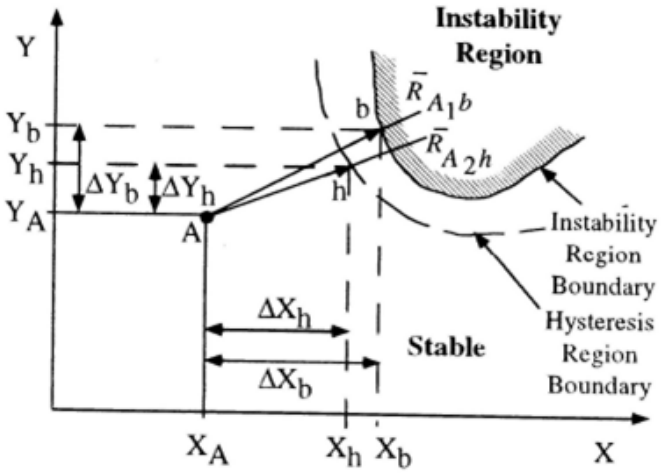

Figure 2.3: Stability Margin Determination from Russian Literature

where $\bar{R}_X$=$\Delta X/X_A$ and $\bar{R}_Y$=$\Delta Y/Y_A$. ΔX and ΔY can be the change in coordinates of either the stability boundary (e.g., ΔX=X_b-X_A) or hysteresis boundary (e.g., ΔY=Y_h-Y_A).

A sample model configuration was provided in the literature that uses the RD-170 injector of the oxidizer-rich preburner stage of the Russian Energia launcher. The LOX-kerosene injector is fuel-swirled in the central post within an oxidizer-swirled post. Gaseous oxygen and gaseous methane are used as the simulant propellants. For volumetric flow rates equal to the full-scale values, the oxidizer will be close to the full-scale Reynolds number, but the fuel is low by an order of magnitude. In order to ensure similarity, the three criteria are determined to govern the simulation:

1. Process homochronicity criterion

$$\Omega = \frac{v_{ox}}{L_{inj}} \tag{2.6}$$

2. Fuel Reynolds number

$$Re_{f,m} = Re_{f,fs} \tag{2.7}$$

3. Fuel mass fraction within the injector

$$\zeta_f = \left(\frac{1}{1+OF_{inj}}\right)_m = \left(\frac{1}{1+OF_{inj}}\right)_{fs} \tag{2.8}$$

Five injector configurations for the preburner were selected and tested for comparison with the full-scale results. The results from two of the injectors are shown in Figure 2.4 where the circles represent model testing and the other symbols represent full-scale testing. The stability boundaries show good consistencies between the model and full-scale testing, proving that the selected parameters were indicative of the onset of combustion instability. Once the model was validated, multiple versions of the injector were tested to determine which has the best stability margin. The influence of faceplate baffles were also tested to determine the effect they have on improving combustion stability.

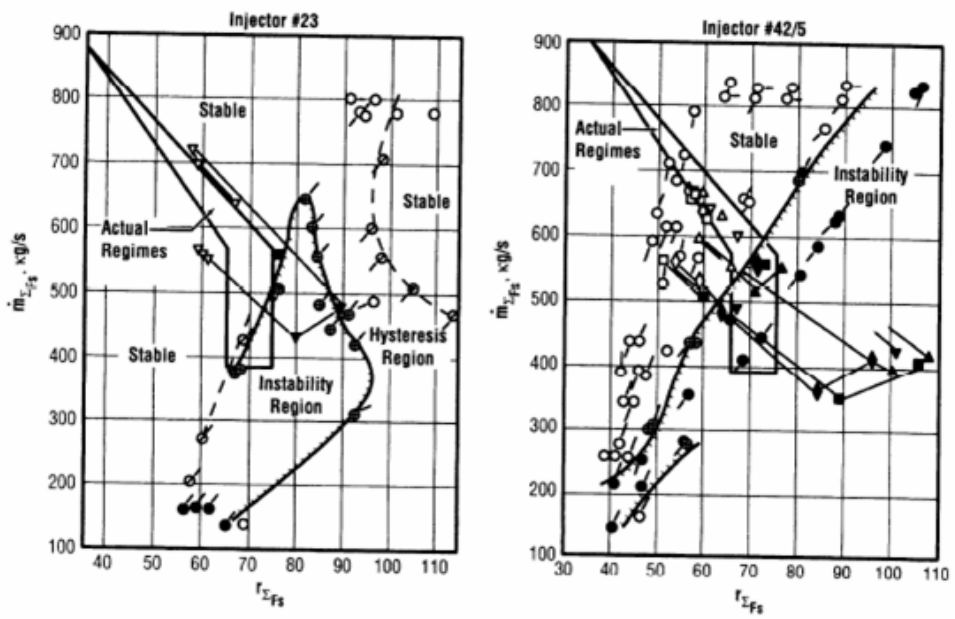

Figure 2.4: Comparison Between Model and Full-Scale Results from Russian Literature

2.2 UAHuntsville Combustion Instability Research

Combustion instability studies using this experimental method first began at UAHuntsville in 2006. The experiment was designed and built by Cavitt to determine whether spontaneous instabilities could be achieved [16, 17]. He tested three pentad impinging injectors with impingement angles of 30°, 45°, and 60°, and found that instabilities could be achieved and that the general regions of instability were repeatable. Maximum pressure amplitudes of up to 17% of chamber pressure were measured. The impingement angle also had an effect on the stability boundaries.

Byrd continued the research by implementing an enhanced diagnostics chamber capable of using up to eight high-frequency pressure transducers to determine instability modes present by comparing the phase shift between transducers [18, 19].

The work by Cavitt was repeated, and Byrd verified the instability modes. The amplitudes of the pressure oscillations were lower than what Cavitt had measured, which Byrd concluded was caused by a change in the fuel feed line geometry. His estimations of the speed of sound were lower than theoretical values for the propellant combination by a factor of three, 380 m/s compared to approximately 1200 m/s. He was also able to show that the position of the injector relative to the chamber wall had an effect on which instability modes occurred.

The most recent work was conducted by Huynh to try to validate the experimental method [20,21]. Using the same diagnostics as Byrd, he tested a shear-coaxial injector that experienced high-frequency combustion instability when tested by Rocketdyne [22]. He used scaled flow conditions to try to recreate the instabilities and frequencies that occurred. The maximum pressure oscillations recorded in his experiments were 4.5% of chamber pressure. The scaling parameters considered were equivalence ratio, volumetric flow rate, velocity ratio, and momentum ratio—all of which are described in Section 3.5.1—but the density ratio of LOX/GCH_4, used in the Rocketdyne experiment, and GOX/GCH_4, used in Huynh's simulation, prevented the momentum ratio from being met. All of the scaled flow conditions could not be matched simultaneously, and he determined that the chamber diameter must be scaled to the frequency of the engine. Huynh suggested heating the propellants to match the full-scale flow rate conditions. Repeated tests at the same flow rates showed an 18% difference between the maximum amplitude and the average, indicating considerable variability. The peak frequency, however, was fairly constant.

2.3 Korean Research

Additional studies using this laboratory-scale method has been performed in Korea. According to the Korean methodology [23], the propellants do not have to be in the supercritical state for the simulation to remain valid. The sample scaling procedure uses LOX/kerosene as the propellants at a chamber pressure of 1.4 MPa, well below the critical pressure of LOX (P_{cr}=5 MPa) and kerosene (P_{cr}=1.71-2.31 MPa) [15]. The Korean method also advises modeling the chamber length to match the longitudinal mode frequency, which depends on whether the model chamber has an open or closed end.

Using the methodology described in [23], a sub-scale model full-scale engine was designed and tested under scaled conditions [24], where kerosene was simulated using a combination of methane and propane. A cluster of five impinging jet injectors, each with two oxygen jets surrounded by two fuel jets with an impingement angle of thirty degrees, was used. The propellant flow rates were scaled so that the density ratio and velocity ratio were matched. Two regions of instability were present during this testing, an upper region and a lower region, and Sohn determined that the lower region was close enough to the operating range of the full-scale engine that any external disturbance in the combustion could initiate combustion instability. Visual observation of the flame at the upper instability region indicated that the large pressure oscillations were caused by flame liftoff.

As a further study, three triplet injectors were tested to determine the effect of the impingement configuration on combustion instability [25]. The three configura-

tions tested were F-O-O-F, F-O-F, and O-F-O, where "F" indicates the fuel jet, "O" indicates the oxidizer jet, and the outer jets had a sixty degree angle between them. An upper and lower instability region was found for each configuration, but the O-F-O configuration had a much broader upper instability region due to localized lean combustion. A cold-flow air-acoustic test indicated the lower instability region was characterized by the hydraulics of the first impingement point, whereas the upper instability region was related to pre-blowout combustion near the flame extinction conditions.

Korean researchers performed a similar study that used various dual-swirl injectors with varying oxidizer post recesses to determine its effect on combustion instability [26]. Gaseous oxygen and a combination of methane and propane were used as the simulant propellants. This experiment used two high-frequency pressure transducers 135° apart. They were able to show that pressure oscillations at the first tangential mode frequency were increased with increasing recess, meaning internal mixing has an effect on the stability characteristics of the injector. They also noted changes in the frequency that were caused by variations of the chamber speed of sound.

2.4 Georgia Tech Research

A small-scale, atmospheric combustion study was performed at the Georgia Institute of Technology that measured OH^*, CH^*, and C_2^* chemiluminescence emissions over a range of fuel and air flow rates [27]. Air and n-heptane were burned inside a 40 mm diameter, optically accessible tube. Two methods were used for mea-

suring chemiluminescence emissions. The first method used a monochromator and photomultiplier tube to measure emissions at selected wavelengths. Multiple wavelength data was recorded by using an imaging spectrometer and an ICCD camera. The authors determined both OH^* and CH^* were good indicators of the overall heat release rate over a range of lean equivalence ratios. They also concluded that optical sensors could be used to gather information to act as an intelligent health monitoring system.

In addition to the single injector combustor, a similar seven injector, optically-accessible combustor with a diameter of 104 mm was developed [28]. Two pressure sensors were placed on the injector face to measure pressure oscillations. Both tangential and longitudinal modes were present at different operating conditions. During stable combustion the equivalence ratio was increased, initiating a tangential instability. Changing the ratio of the primary and secondary swirl streams, while maintaining a constant flow rate, suppressed the instability.

The same setup with seven swirl injectors was used to demonstrate a spinning first tangential mode [29]. The flow rates of air and Jet-A fuel were varied to determine regions of instabilities. The tangential instabilities occurred around the stoichiometric point for higher swirl flows, whereas longitudinal instabilities were present at leaner and richer mixtures. Increasing the inlet air temperature increased the range where tangential modes occurred, decreased the rich longitudinal mode region, and eliminated the lean longitudinal instabilities. Reducing the length of the combustor also had a positive effect on limiting both instabilities. The rotation direction was determined by the overall swirl momentum within the chamber. When the

net swirl momentum was zero, the rotation was shown to be arbitrary. The rotation of the instability was seen by imaging C_2^* on a high-speed camera. CH^* chemiluminescence emissions were measured using three strategically-placed fiber optic probes and photomultiplier tubes around the chamber.

2.5 Additional Studies

Numerous studies have been performed relatively recently that look at chemiluminescence as a diagnostic tool. As mentioned in Section 1.3, heat release helps sustain unstable combustion. One study [30] using air and natural gas showed that CH^* and OH^* chemiluminescence was indicative of the heat release rate. The ratio of the two emissions was also shown to correlate with equivalence ratio from lean to stoichiometric conditions. Another study reports that CH^* and OH^* emissions are indicative of global and local heat release rates [31]. In addition to heat release, chemiluminescence has also been shown to denote the reaction zone of the flame [32].

2.6 Assessment of Literature

The Russian literature provides an explanation for the physical basis of the experiment and a detailed outline for conducting the experiment to achieve proper simulation of combustion instabilities. The example simulation provided indicates the analogy works. It can also be recreated to ensure the experiment works properly. The previous work done at UAHuntsville has shown that combustion instabilities can be created and analyzed effectively. Matching the proper scaling criteria, however, has yet to be done.

The work done in Korea indicates that the full-scale engine does not have to operate in the supercritical regime. However, data was not provided that correlated the model data with the full-scale data. Considering the injector used in this experiment was designed to use subcritical propellants, the Korean work is potentially useful in validating this research. It can also be validated at UAHuntsville by testing the injector in a high-pressure experiment.

Experiments using one or multiple injector elements at Georgia Tech show similar results as those seen at UAHuntsville, where changing flow rates can create or suppress instabilities. Additional optical diagnostics that measured chemiluminescence provide insight into unstable combustion. Various other studies also show that chemiluminescence emissions can be used to indicate the combustion zone and heat release.

CHAPTER 3

EXPERIMENTAL APPROACH

You learn a lot by looking.

—Marlow Moser

3.1 Overview of Experiment

The research presented in this report is one part of a larger scale approach to fully characterize a single injector element through multiple, diverse experiments that provide a database for future injector research. The plan was to design a new injector element to be implemented into three experiments and to be modeled using CFD analysis. The three experiments are a high-pressure, cold-flow spray facility [33], a high-pressure combustion performance experiment [34], and a low-pressure combustion stability study [35], the latter of the three being the one described in this report. The object is to keep the operational conditions among the experiments similar using the proper scaling criteria. References to these experiments will be made throughout the chapter when describing the experiment design conditions.

3.2 Hardware Design

This research involved designing and fabricating a new injector element for experimentation. New optical diagnostics were also to be implemented, which required building an optically-accessible chamber. Additional feed line pressure measurements were added to measure feed system pulsations to determine whether coupling was taking place. The designs are described in the following sections.

3.2.1 Injector Design

In October 2007, a Request for Proposals was submitted by NASA Glenn Research Center for the development of an LPRE that uses liquid oxygen and liquid methane as the oxidizer and fuel, respectively, to be used on the new Lunar Ascent Stage of the Lunar Lander [36]. In order to abide by the design criteria, a notional engine was sized to meet the specifications of this new engine that is currently being developed for the Constellation program. An injector was designed to be implemented into the notional engine. The propellant pressures and temperatures at the injector inlet were given and are summarized in Table 3.1.

Table 3.1: Liquid Propellant Conditions at Injector Inlet

		Oxygen	Methane
Temperature [K]	Maximum	124	124
	Standard	103	103
	Minimum	91	95
Pressure [MPa]	Maximum	2.59	2.59
	Standard	2.24	2.24
	Minimum	1.90	1.90

The "Standard" inlet pressures and temperatures were chosen as the design point for the new injector. Two separate injector elements were considered as the nominal injector for the testing: a dual-swirl injector and a swirl-coaxial injector. It was decided that both injectors were promising for use in the Lunar Ascent Engine, and, therefore, the injector would be designed to be modular to change configurations easily and quickly. The ultimate plan was to test the dual-swirl injector; thus, the injector was designed for this configuration. However, initial testing was to be performed using the swirl-coaxial injector configuration. The following description of the injector design outlines the dual-swirl injector design and shows the modifications made to accompany the swirl-coaxial testing presented in this report.

The dual-swirl injector was designed using an analytical method developed by Bazarov [37]. A cross-sectional schematic of the inner fluid dynamics of the swirling liquid is shown in Figure 3.1, where (1) is the injector material, (2) is the swirling

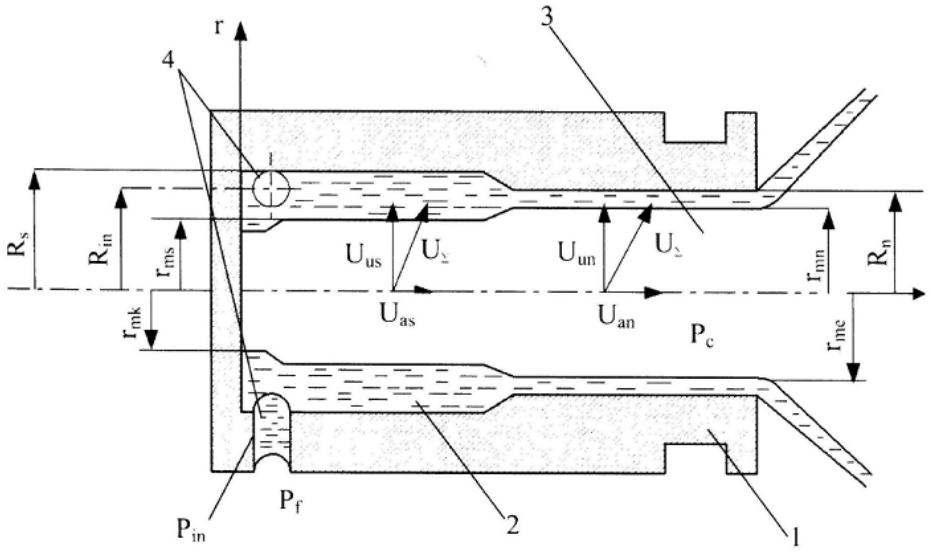

Figure 3.1: Schematic of Swirl Injector

liquid propellant, (3) is the gaseous core caused by the swirling liquid, and (4) is the tangential inlet. The propellant conditions and engine requirements provided by the RFP, as well as other design characteristics required for calculating the injector geometry, were used. These design points are summarized in Table 3.2.

Table 3.2: Criteria for Injector Design

Condition	Unit	Value	Source
Thrust	[kN]	24.5	RFP
Burn Time	[s]	450	RFP
I_{sp}	[s]	355	RFP
α_{LOX}	[°]	90	Assumed
ΔP_{LOX}	[kPa]	345	Assumed
ΔP_{LCH4}	[kPa]	345	Assumed
OF	-	3	Assumed
n_{in}	-	4	Assumed
n_{inj}	-	65	Assumed

While the thrust, burn time, and specific impulse were provided by the RFP, the rest of the parameters were chosen. Reference [37] mentions that most spray angles are between 90° and 120°. Therefore, the LOX spray angle, α_{LOX}, was set to 90° for simplicity. Reference [38] advised a pressure drop, ΔP, between 5% and 20% of the mean chamber pressure. At 18.2% of chamber pressure, the selected value lies within that range. Most engines operate in a fuel-rich regime, and multiple references [39, 40] used $OF = 3$ in their testing, so it was chosen as the nominal condition. The number of tangential inlets, n_{in}, was set to four at equally-spaced intervals to allow for an even propellant distribution within the injector cavity. The number of injectors, n_{inj}, was set as a way to reduce the injector size so that it could

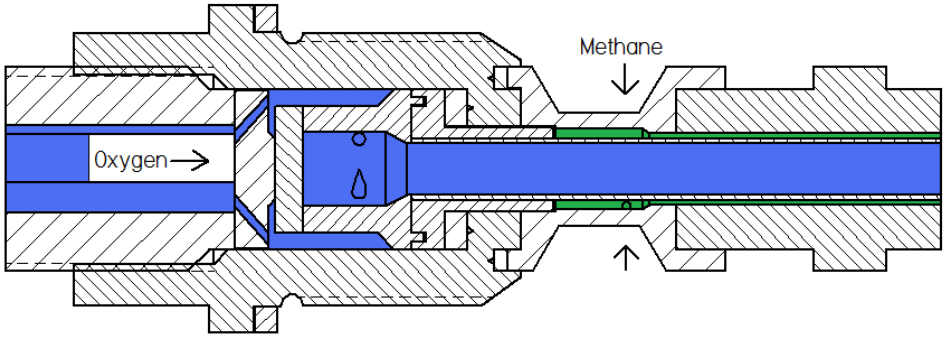

Figure 3.2: Dual-Swirl Injector Cross-Sectional View

fit into the existing experimental facilities. A cross-sectional view of the dual-swirl injector is shown in Figure 3.2.

Since the intention of this LOX/Methane study was to eventually study both the dual-swirl and swirl-coaxial injectors, the injector was designed to be modular as a way to change the injector type as well as allow for parametric studies of different geometries of various injector components. The interior oxidizer swirl nut, LOX post, fuel jacket, and fuel annulus all have the capability of being exchanged for a different geometry. In order to change the dual-swirl injector to the swirl-coaxial injector, the fuel jacket was replaced with one that had straight inlet holes instead of tangentially-drilled holes. The dimensions of the straight fuel jacket were set to keep the same pressure drop as the fuel swirl jacket. A cross-sectional view of the swirl-coaxial injector is shown in Figure B.2. The final injector dimensions are given in Table 3.3.

3.2.2 Chamber Design

A new, fully-instrumented combustion chamber was designed to try to match instability frequencies from the aforementioned spray facility and high-pressure com-

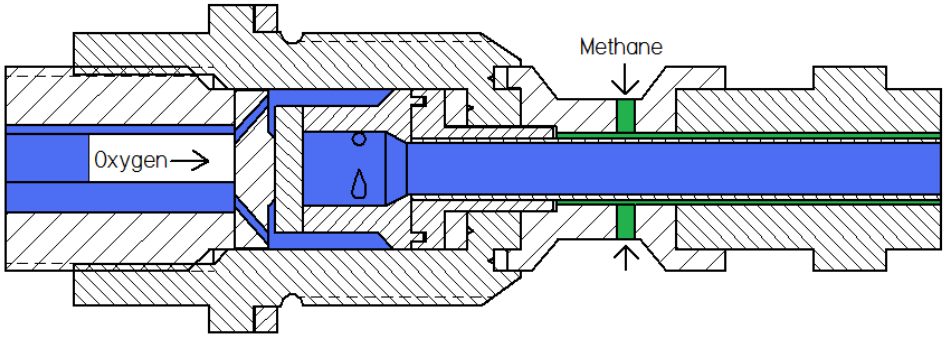

Figure 3.3: Swirl-Coaxial Injector Cross-Sectional View

Table 3.3: Swirl-Coaxial Injector Dimensions

Parameter	Dimension [mm]
Ox. Post Diameter	4.75
Ox. Post Length	49.56
Fuel Annulus Gap	0.50
Ox. Post Recess	0.8
Ox. Tangential Channel Diameter	1.27
Ox. Tangential Channel Length	2.53
Fuel Straight Channel Diameter	1.63
Fuel Straight Channel Length	2.77

bustion experiments. A common frequency of 2.0 kHz was assumed. This frequency corresponds to a first longitudinal mode in the high-pressure combustion engine and a first tangential mode in the atmospheric chamber used for this experiment. The chamber also had to be optically accessible for imaging chemiluminescence emissions. The relation used to find the chamber diameter is

$$\frac{0.586 a_m}{d_m} = \frac{a_{fs}}{2L_{fs}}, \tag{3.1}$$

where a is the chamber speed of sound, d is the chamber diameter, and L is the chamber length. The subscripts "m" and "fs" represent the model and full-scale properties, respectively.

The length of the chamber was calculated by scaling the atmospheric combustion chamber's second longitudinal mode to the first longitudinal mode of the high-pressure engine. These scaling criteria were selected because the high-pressure engine, which is modeled as a closed-closed tube, has one longitudinal node line at the first longitudinal mode, whereas the low-pressure chamber is modeled as a closed-open tube, which has one node line at the second longitudinal mode. Equation 3.2 shows the relation used to calculate the chamber length.

$$\frac{3a_m}{4L_m} = \frac{a_{fs}}{2L_{fs}} \tag{3.2}$$

Obviously, if two separate instability modes are scaled to the same frequency, differentiating between them during analysis would prove difficult; however, the location of the pressure sensors, which will be detailed later in this section, resolves this problem.

Once the scaling method and criteria were developed, an average speed of sound in the chamber had to be estimated. Trying to estimate the speed of sound proved to be a difficult task due to the relatively low speed of sound compared with high-pressure engines. The low speed of sound may be a result of the entrained air coming into the chamber. Since the diameter of the chamber was going to be smaller

to try to match a higher frequency, it was believed that the amount of entrained air would decrease, causing a higher average speed of sound within the chamber. An analytical method was developed to try to alleviate this problem. This model was based on estimated speeds of sound from the testing performed by Byrd [18]. Assuming a percentage of the area within the chamber consisted of the combustion gas properties, and the rest of the area consisted of ambient air, the effective "flame area" was calculated and assumed to be independent of the chamber diameter. This method resulted in an approximate speed of sound of 490 m/s for a chamber diameter of 155 mm and was believed to actually be slightly underestimated. Similar Korean research that tested seven injector elements in a 175 mm chamber found speeds of sound on the order of 520 m/s. This data seemed to indicate the estimated chamber speed of sound was reasonable.

The chamber diameter was selected to be 155 mm, and the length was calculated to be 203 mm. The chamber material was fused silica glass and was chosen because it allows UV-wavelength emissions to pass, which is necessary to image OH^* emissions. A windowed, metal chamber was not chosen because the addition of the window would affect the geometry and possibly the stability properties inside the chamber, and it was important to keep these parameters intact. The disadvantage of using a glass chamber was its delicate nature. Therefore, a separate metal pipe whose inner diameter matched the outer diameter of the glass chamber was cut into small strips that were then attached to the glass using a heat-resistant adhesive. The metal was to provide structural stability to the chamber and give the measurement

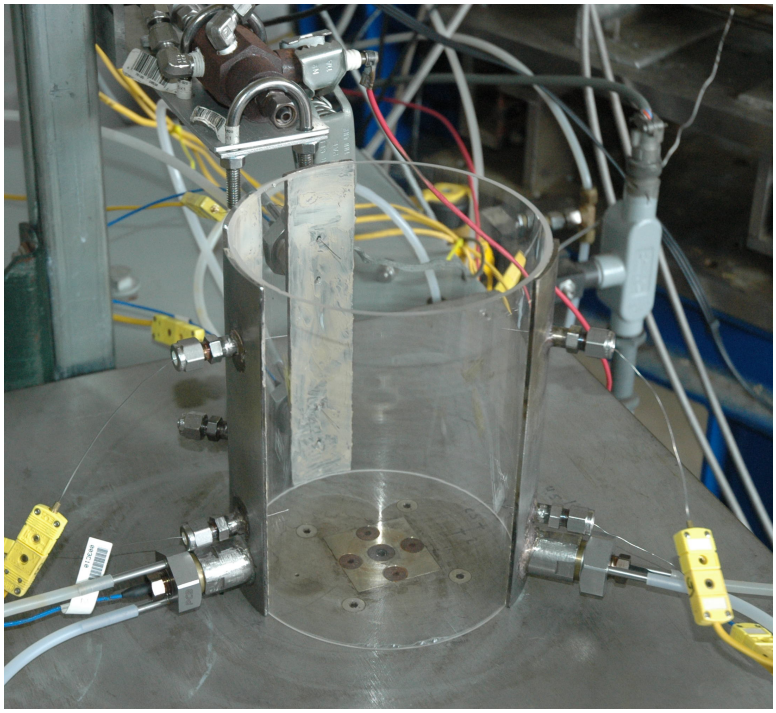

Figure 3.4: Optically Accessible Chamber with Injector

diagnostics a place to be mounted without having to be mounted to the chamber. A picture of the chamber is shown in Figure 3.4.

The chamber was designed to house up to four high-frequency pressure transducers. These locations are the same as previous testing with a different chamber [18, 20]. Although the previous chamber had the capability to use up to six transducers, only four were ever used for the actual testing. The configuration for these transducers was suggested by [41]. An additional two pressure transducers were mounted to the injector face, something that usually cannot be done with experiments that use multiple injector elements. Figure 3.5 shows a top-down view of the atmospheric chamber, and Figure 3.6 shows the camera-side view. In these figures eight areas are designated as measurement locations and are labeled 1-8. Dynamic pressure

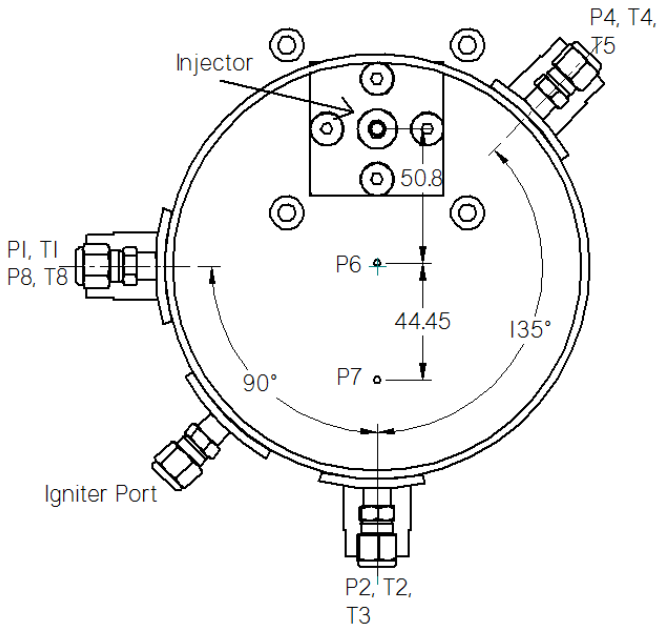

Figure 3.5: Top View of Combustion Chamber, Units in mm

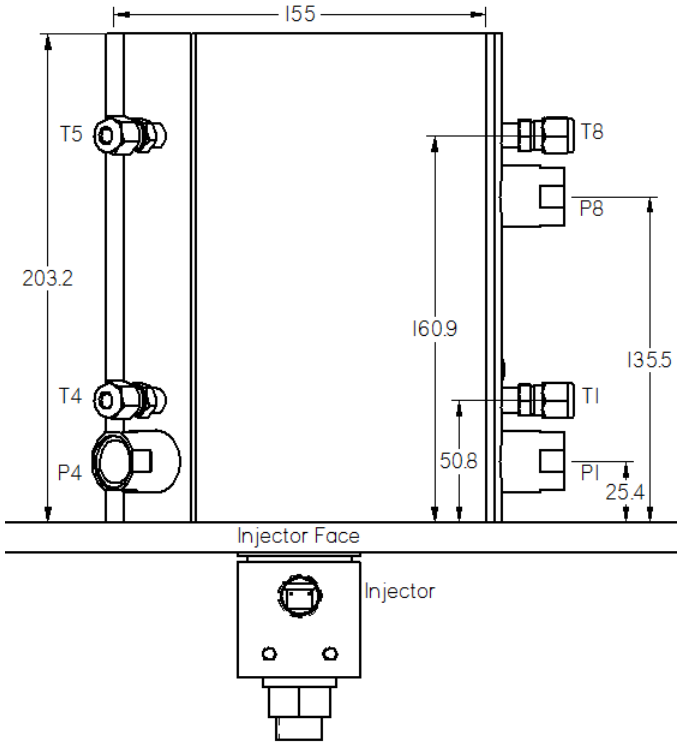

Figure 3.6: Side View of Combustion Chamber, Units in mm

measurements are denoted by "P," and temperature measurements are denoted by "T."

The high-frequency pressure transducers are implemented in separate radial, circumferential, and axial locations within the chamber in order to analyze the instability mode present. Three transducers—P1, P2, and P4—are located on a plane 25.4 mm from the injector face. Another transducer, P8, is located on a higher plane, 135 mm above the injector face, directly above transducer P1. This plane corresponds to the theoretical antinode of the second longitudinal mode. As mentioned previously, analysis of these two transducers allows the first tangential mode and second longitudinal mode to be distinguished, since they were originally estimated to occur at the same frequency. The two transducers P6 and P7 on the injector face are located 50.8 mm and 94.5 mm from the center of the injector, respectively. The location of these two transducers relative to the chamber wall is dependent on the location of the injector within the chamber and cannot be held constant. All six of the temperature measurement locations are divided and placed on two separate planes: one 25.4 mm above pressure transducer P1 and another 25.4 mm above pressure transducer P8. These locations were chosen to try to better approximate the thermal conditions in the chamber rather than on a single plane like the previous research done on this experiment.

3.3 Facility Description

All testing was conducted at the Propulsion Research Center rocket test stand, located at the Johnson Research Center and shown in Figure 3.7. The test stand has

Figure 3.7: UAHuntsville Propulsion Research Center Rocket Test Stand

preexisting capabilities for gaseous propellant testing. Propellant gases are contained in K-bottles that are attached to the test stand plumbing, which is detailed in Figure 3.8. Propellant pressures are controlled by a pressure regulator and dome loaders before reaching the experiment. The atmospheric pressure test apparatus is located on a movable cart that can be easily installed or removed to allow other experiments to utilize the test stand. All experiment control operations are remotely conducted in a separate control room for the safety of the test personnel.

3.3.1 Low-Pressure Test Facility

The test cart was originally designed to encompass all of the hardware and plumbing needed for experimentation to easily implement into the plumbing on the test stand. Oxygen, an oxidizer diluent, methane, a fuel diluent, and propane are all capable of being flowed to the injector for testing. The diluent is currently set up

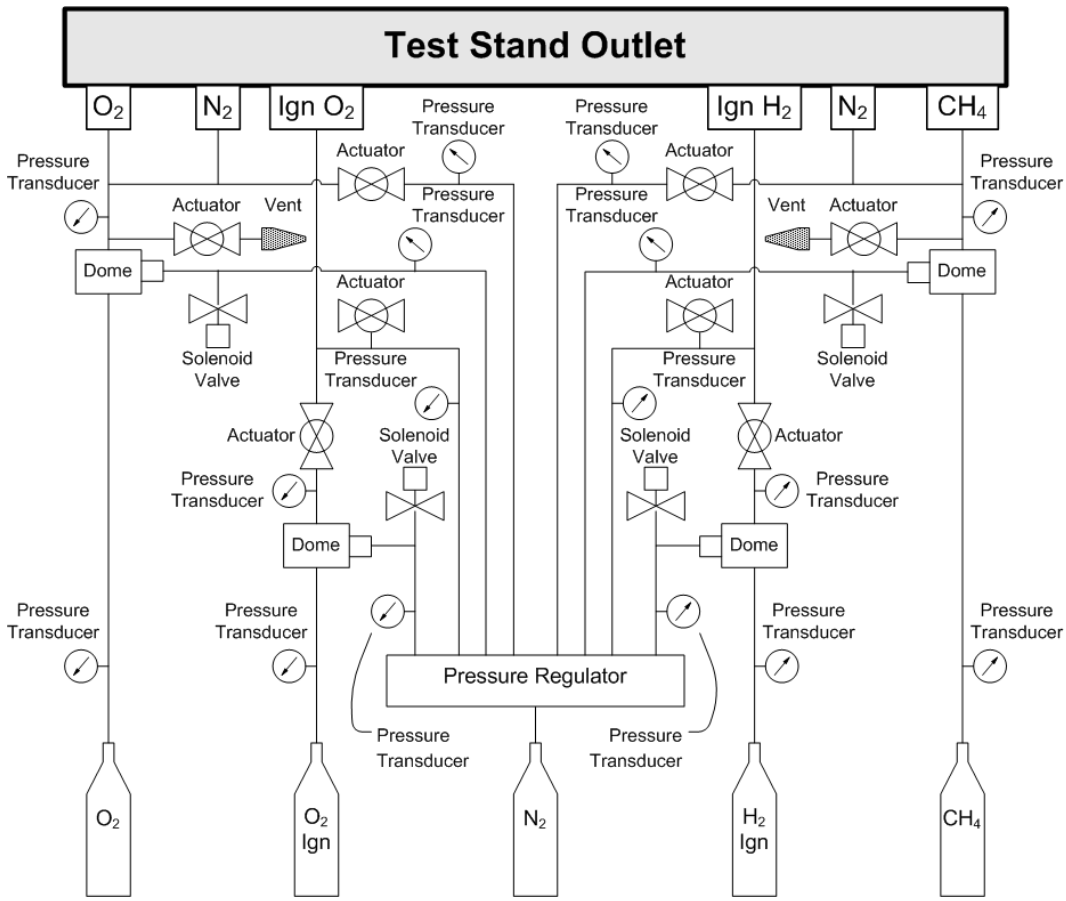

Figure 3.8: Rocket Test Stand Plumbing Diagram

to use nitrogen gas that has been diverted from the purge lines, which are necessary to blow out the flame if needed. No diluent was used in the current study, however. Once the fuel and oxidizer entered the cart, they passed through an actuated fire valve that controls flow to the injector. They are then subjected to another pressure regulator that lowers the pressures to approximately 690 kPa before they enter their respective mass flow controllers. An Omega FMA2613A mass flow controller is used to set the oxygen mass flow rate, and four Omega FMA2609A mass flow controllers are used to set the flow rates for the oxidizer diluent, fuel diluent, methane, and

propane. All mass flow controllers are controlled by serial connection in the control room. The control settings for the mass flow controllers are listed in Table 3.4.

Table 3.4: Mass Flow Controller Settings

Gas	Baud Rate	Unit ID	Data Rate	Proportional	Integral
O_2	2400	A	Slow	200	14,000
O_2 N_2	2400	B	Slow	100	32,000
CH_4	2400	C	Slow	200	15,000
CH_4 N_2	2400	D	Slow	100	5,000
C_3H_8	2400	E	Slow	100	5,000

Downstream of the mass flow controllers are Omega AHP-3741/AHP-5150 inline heaters to allow heating of the propellants to change the properties of the gases for scaling purposes. A separate Watlow circulation heater was installed in the oxygen feed line as a safety measure to prevent sudden overheating of the oxygen and possible auto-ignition [18]. Since the fuel line for propane was not being used, the inline heater was moved further downstream after the fuel collector and immediately before the entrance to the injector. The heaters are powered by Omega CNi853/C24 temperature controllers. The fuel and oxidizer then pass through check valves to prevent reverse flow and are combined in their respective collectors before being ejected through the injector. A detailed piping schematic is shown in Figure 3.9.

3.3.2 Instrumentation

The instrumentation that records various pressures, temperatures, and flow rates are distributed throughout the test facility. Low-frequency pressure measure-

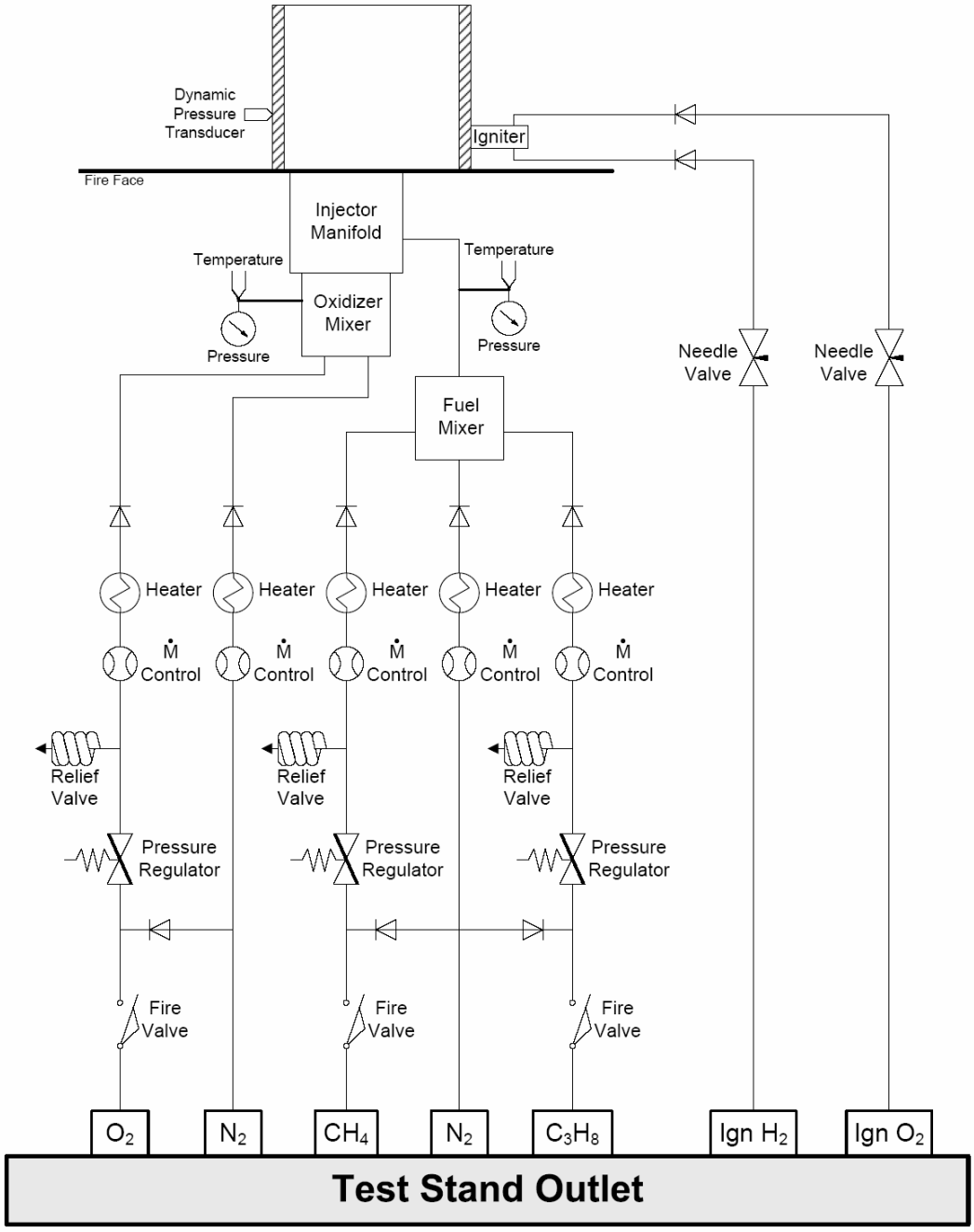

Figure 3.9: Piping Schematic Downstream of Test Stand

ments are displayed and recorded upstream of the propellant inlet to the cart to check for proper system operation. Additional low-frequency static pressure measurements are made immediately before the propellants enter the injector housing to determine the pressure drop across the injector. K-type thermocouples are placed in the propellant feed lines after the inline heaters for the control loop that regulates the heater output. A thermocouple is also placed in each feed line immediately before the fuel and oxidizer enter the injector housing, near where the static pressure transducers are located. High-frequency pressure measurements are made in each feed line immediately before the gases enter the injector housing. A schematic showing the location of the sensors is presented in Figure 3.10. Propellant pressure, temperature, mass flow rate, and volumetric flow rate measurements are also recorded by the mass flow controllers.

In the chamber PCB Model 106B high-frequency pressure transducers are used to measure the dynamic pressure. They are inserted into PCB 064B06 water-cooled adapters to prevent heat sink damage to the transducers. Omega K-type grounded thermocouples are used for thermal measurements inside the chamber. These thermocouples, at approximately 0.5 mm in diameter, are thinner than in previous experiments and have a shorter time constant associated with them. They are placed approximately 25.4 mm into the chamber, rather than closer to the wall, to get a better indication of the thermal environment.

A Miro 4 monochrome high-speed camera is placed to focus directly at the injector straight through the quartz glass chamber to avoid image distortion. A Coastal Optical Systems UV SLR lens (f/4.5 155 mm) is used for imaging emissions

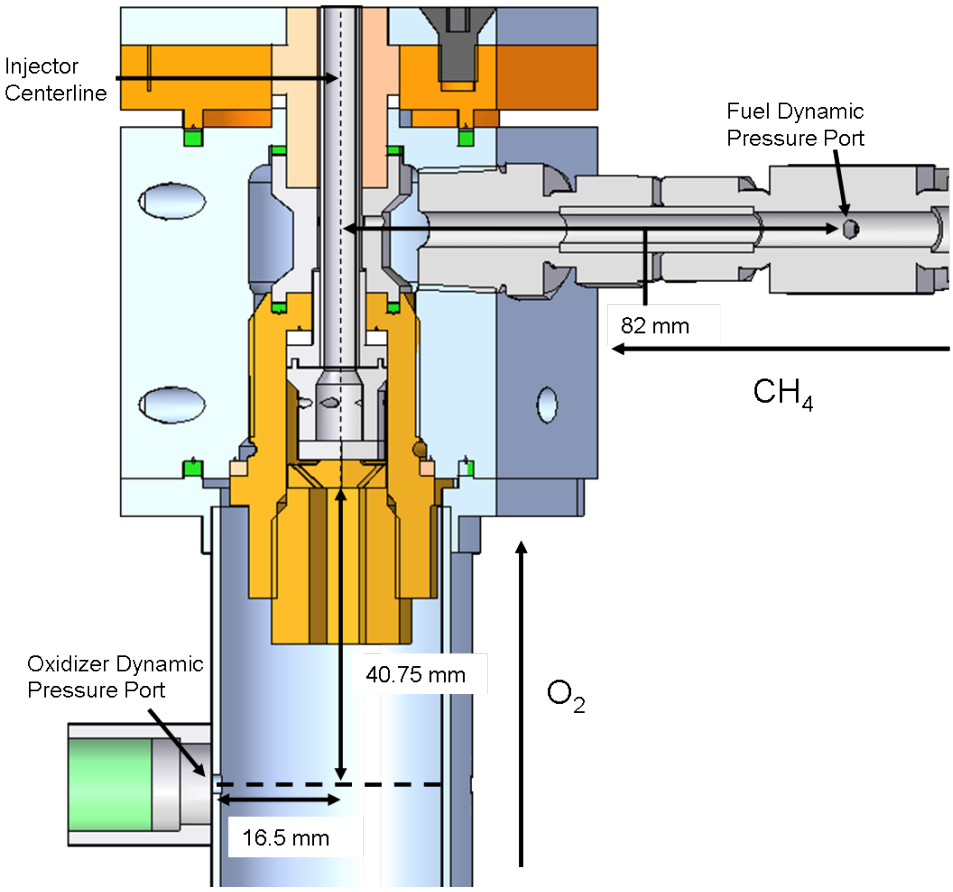

Figure 3.10: Feed Line High-Frequency Pressure Measurement Locations

in the UV wavelength range. Filters are placed in front of the lens to image either CH^* or OH^* emissions. For CH^* emissions an Andover Corporation 450FL07-50 low-pass filter and a 420FG03-50 (GG420) colored glass filter are used. A 011FG09-50 (UG11) filter is used for OH^* chemiluminescence imaging. A test image is acquired, and a "Current Session Reference" is done prior to each day's testing. The test image allows for dimensioning of the acquired images. The Current Session Reference calibrates the images for the specified frame rate and exposure time. For this research the frame rate was set to 5000 fps, and the exposure time was set to 100 μs. A Redlake HS-4

monochrome high-speed camera is also placed to look at the injector, but from a different angle compared to the Miro 4 camera. The frame rate and exposure time is the same as that of the Miro 4 camera, and the cameras are synchronized to take each image at the same time and for the same duration.

3.3.3 Equipment Setup

For preliminary testing setup, one of the pressure signals was sent to a Stanford Research Systems DG645 digital delay generator. An output signal from the delay generator was sent to the high-speed camera's synchronization input. A trigger signal was connected from the data acquisition system to the camera to begin image acquisition. When the computer commenced recording the high-frequency data, a pulse was sent from the data acquisition to the camera. The delay generator would send an output pulse to the camera whenever the pressure signal reached a specified threshold value. The trigger signal, input synchronization signal, the "Ready" signal, and the reference pressure signal were all recorded to assure the correct phase of the signal when the image was acquired. Figure 3.11 shows a schematic of the preliminary setup.

Two cameras were used for the main portion of the testing, and the digital delay generator was not used for phase-locked imaging. Figure 3.12 shows the relative location of the cameras with respect to the injector and high-frequency pressure transducers. Figure 3.13 shows the wiring diagram for synchronizing the two cameras. When the computer begins to record high-frequency data, the trigger signal is sent to both cameras. The synchronization signal of the Miro camera is connected

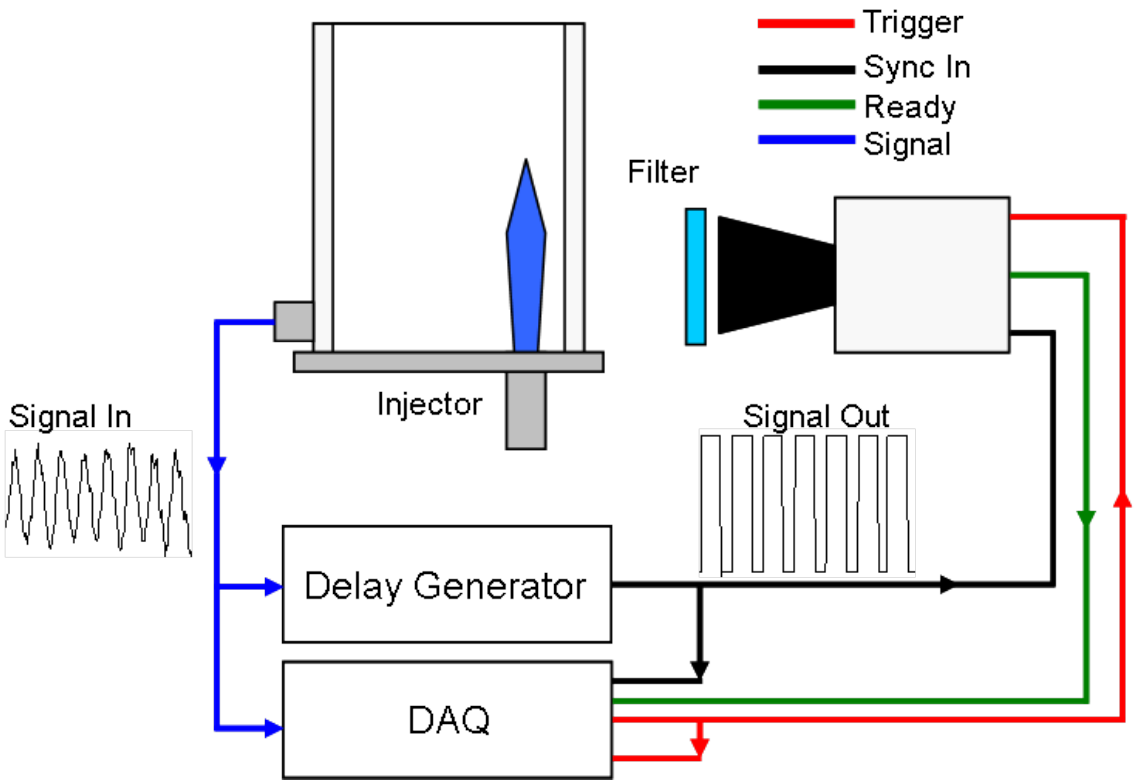

Figure 3.11: Phase-Locked Imaging Setup

to the synchronization input of the Redlake camera. The Miro camera was run in free-run mode—using its internal clock to acquire images—and the Redlake camera was synced to the first camera. The software for each camera was set so that the images were acquired at the exact same moment. The synchronization out signal from the Redlake camera and the "Ready" signal from the Miro camera were recorded to determine the specific phase of the signal related to each image.

3.4 Data Acquisition and Experiment Control

Two data acquisition cards are used to record the data from this experiment. The first is a National Instruments PXI 6052E 16-bit data acquisition card that has

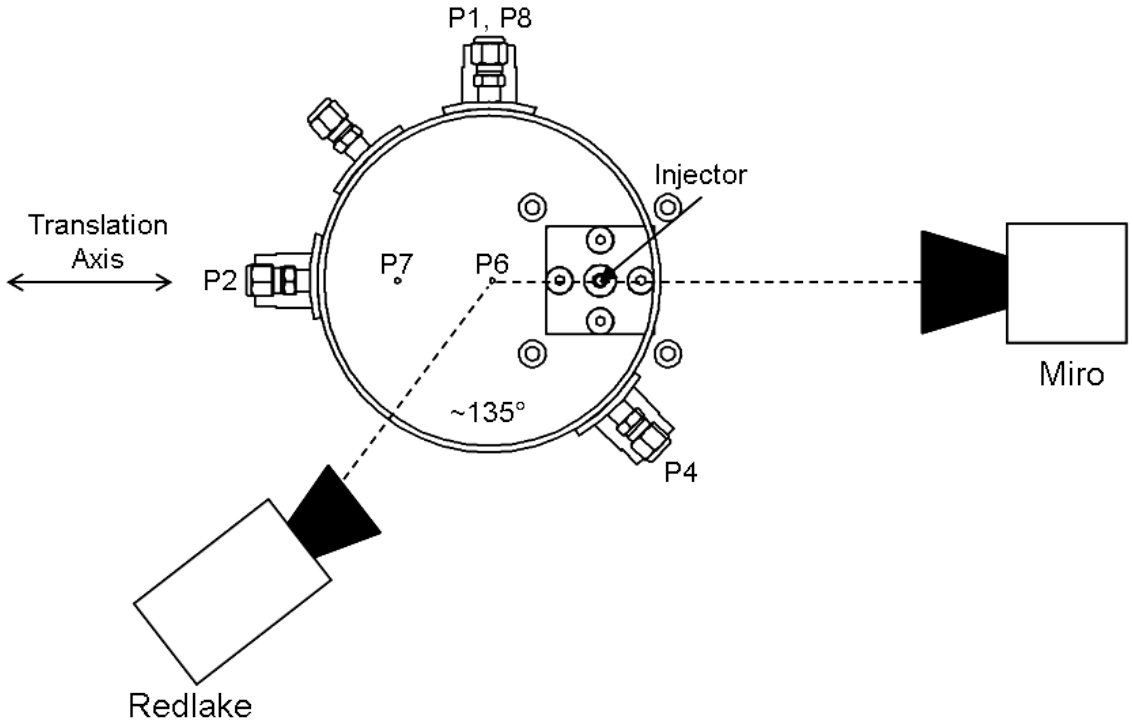

Figure 3.12: Camera Placement

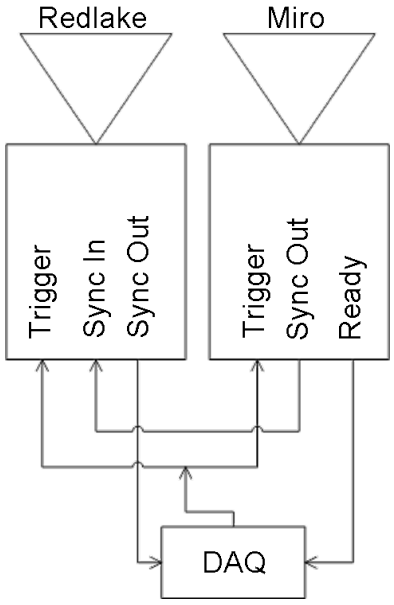

Figure 3.13: Wiring Diagram for Dual Camera Synchronization

a 333 kHz total sampling rate. A National Instruments SCXI-1143 module is used to record the high-frequency pressure measurements from the experiment. It has a total of eight channels available, and the total sampling rate is divided among the active channels. Therefore, the sampling rate is 55.5 kHz when using six high-frequency pressure transducers. The module contains a Butterworth antialiasing filter that has a cutoff frequency of 8.33 kHz at this condition. Beyond this frequency the amplitudes become attenuated.

Low-frequency pressure data are recorded from a National Instruments SCXI 1102B module with a 200 Hz low-pass filter, and low-frequency temperature data are recorded from a National Instruments SCXI 1102 module with a 2 Hz low-pass filter, but both from the same DAQ at a sampling rate of 250 Hz. Unfortunately, since both low- and high-frequency data are recorded using the same DAQ card, it has to alternate collecting data, resulting in gaps in the low-frequency data while the high-frequency data is being recorded.

The high-frequency data are also recorded on a National Instruments PXI 6070E DAQ card along with the "Sync Out" signal from the Redlake high-speed camera and the "Ready" signal from the Miro 4 high-speed camera. This 12-bit DAQ card has a maximum sampling rate of 1.25 MHz. The trigger signal that starts the camera image acquisition is sent from this DAQ card.

The experiment is controlled through a programmable logic controller (PLC) and a LabVIEW 8.0 code. When the "Fire" button on the experiment control panel is pressed, the PLC sends a signal to the code to initiate the data-recording process. At this point the test is run autonomously by the code, only requiring the experimentalist

to shut down the experiment manually after all the data has been recorded. To begin the ignition sequence, the valves are actuated based on timing values uploaded to the PLC beforehand. Hydrogen and oxygen are flowed through the torch igniter located directly above the chamber, and oxygen and methane are flowed through the injector. When the propellants have been ignited, the code sets the flow rates according to a predefined set of flow rate conditions. Once the flow rates have been set for a particular setpoint, the DAQ records the high-frequency data and simultaneously triggers both cameras for image acquisition. The code then proceeds to the next desired flow rate setpoint, and the process is repeated. An abort button is used to end the experiment after all the setpoints have been recorded or in case of an emergency.

3.5 Testing Strategy

Preliminary testing involved running a set of mass flow rate conditions that were scaled from the design conditions that used LOX and LCH_4 as propellants. At each flow rate, high-frequency pressure measurements were taken, and CH^* chemiluminescence emissions were imaged. The images were phase-locked at approximately the zero-phase point on the transducer P2 pressure signal. The pressure signal was sent to the pulse generator, where an output signal was created when the signal reached a threshold value, in this case 0 V. The output signal was then sent to the synchronization input of the Miro 4 high-speed camera to act as a clock for acquiring signals.

For the main portion of the testing, an entire test matrix was devised that contained various scaling parameters. Testing occurred with the injector at three positions relative to the chamber wall: $\frac{r}{r_c}$=0, $\frac{r}{r_c}$=0.50, and $\frac{r}{r_c}$=0.75. The reasoning behind testing at these positions was to try to excite radial, combined, and tangential modes, respectively. Simultaneous high-speed chemiluminescence and non-filtered high-speed images were acquired in free-run mode for each setpoint.

3.5.1 Scaling Parameters

In order to match the conditions of the full-scale model, the proper scaling parameters must be selected. For most scaled combustion experiments, the equivalence ratio, given in Equation 3.3, is selected for maintain combustion similarity. If using different propellants, the equivalence ratio must be used, but the OF ratio can be used if using the same propellants, such as in this experiment.

$$\Phi = \frac{OF_{stoic}}{OF_{actual}} = \frac{\left(\frac{\dot{m}_{ox}}{\dot{m}_f}\right)_{stoic}}{\left(\frac{\dot{m}_{ox}}{\dot{m}_f}\right)_{actual}}, \tag{3.3}$$

where $\dot{m}_{ox}$ and $\dot{m}_f$ are the mass flow rate of the oxygen and fuel, respectively.

In most cases, one would want to match the volumetric flow rate, given in Equation 3.4.

$$\dot{Q} = \frac{\dot{m}}{\rho}, \tag{3.4}$$

where ρ is the density of the ejected propellant.

The result of matching the volumetric flow rate for a full-scale injector element is matching the propellant exit velocity, shown in Equation 3.5.

$$V = \frac{\dot{Q}}{A} \tag{3.5}$$

For this testing the exit velocity was used as a scaling parameter and not the volumetric flow rate. For swirl injectors the liquid propellant is pushed to the outside of the LOX post or fuel annulus, leaving a gaseous core. Using gaseous propellants, the entire area is filled with propellant. Thus, for equal volumetric flow rates, the larger area caused a decrease in exit velocity. Therefore, the exit velocity was matched.

One scaling parameter that is commonly used is the velocity ratio, shown in Equation 3.6. This ratio matches the shear force between the two propellants, which is a common cause of mixing.

$$VR = \frac{V_f}{V_o}, \tag{3.6}$$

where V_f and V_{ox} is the exit velocity of the fuel and oxidizer, respectively.

Another common scaling parameter that was used for this experiment is shown in Equation 3.7 and is the momentum ratio.

$$MR = \frac{(\dot{m}V)_f}{(\dot{m}V)_o} \tag{3.7}$$

The mass flux ratio, shown in Equation 3.8, was also used as a scaling parameter for this testing. It is considered an important indicator of performance in terms of the primary atomization regime for coaxial injectors.

$$J = \frac{(\rho V^2)_f}{(\rho V^2)_o} \tag{3.8}$$

The swirl number is defined as the ratio of the axial flux of the swirl momentum to the axial flux of the axial momentum. This number is a method of quantizing the degree of swirl of the propellant. The swirl number is based solely on the geometry of the injector; thus, only one swirl number was tested in this experiment. The swirl number is given by the following equation:

$$S = \frac{\int_{R_i}^{R_o} \rho V_z V_\theta 2\pi r^2 \, dr}{\int_{R_i}^{R_o} \rho \left(V_z^2 - \frac{V_\theta^2}{2} \right) 2\pi R_o r \, dr}, \tag{3.9}$$

where R_i is the inner radius, R_o is the outer radius, V_z is the axial velocity component, and V_θ is the circumferential component of the velocity. A summary of the design scaling parameters is given in Table 3.5.

Table 3.5: Swirl-Coaxial Injector Scaling Parameters

Scaling Parameter	Value
$\dot{Q}_{ox}$	$74.9\frac{cm^3}{s}$
$\dot{Q}_f$	$61.8\frac{cm^3}{s}$
Φ	1.33
VR	1.545
MR	0.515
J	0.963
S_{ox}	0.904

3.5.2 Test Matrix

For preliminary testing, a set of twelve flow rate conditions was created to match certain scaling parameters. At least one propellant for each setpoint matches either the design total velocity or axial velocity. The other propellant was set to match either the OF ratio or the momentum ratio. Of course, for the points where both propellants match the total or axial velocity, the velocity ratio is matched. Table 3.6 shows the mass flow rates and scaling parameters associated with each setpoint.

A complete test matrix was devised using the scaling parameters detailed in Section 3.5.1. The matrix was divided into eight "tests," with each test containing thirteen "setpoints" for a total of 104 unique mass flow rate combinations. For each test the fuel mass flow rate would remain constant while the oxygen would increase. The tests are labeled Test 1.0 to Test 4.5 in 0.5 increments to stay consistent with previous tests and for convenience in running the LabVIEW code. The two primary fuel flow rates selected match the design axial and total velocities, corresponding with Tests 1.5 and 4.0, respectively. Both of these tests are bounded on the lower

Table 3.6: Preliminary Test Flow Rates

Setpoint	$\dot{m}_f$ $[g/s]$	$\dot{m}_{ox}$ $[g/s]$	Methane Scaling Parameter	Oxygen Scaling Parameter
1	0.122	0.318	Axial Velocity	Momentum Ratio
2	0.122	0.367	Axial Velocity	OF Ratio
3	0.122	0.412	Axial Velocity	Axial Velocity
4	0.122	0.582	Axial Velocity	Total Velocity
5	0.137	0.412	OF Ratio	Axial Velocity
6	0.159	0.412	Momentum Ratio	Axial Velocity
7	0.194	0.582	OF Ratio	Total Velocity
8	0.224	0.582	Momentum Ratio	Total Velocity
9	0.259	0.412	Total Velocity	Axial Velocity
10	0.259	0.582	Total Velocity	Total Velocity
11	0.259	0.673	Total Velocity	Momentum Ratio
12	0.259	0.777	Total Velocity	OF Ratio

and higher ends, respectively, by a test so that the design points were completely encompassed. The fuel flow rates vary from 0.1091 g/s to 0.2910 g/s.

The design oxygen exit velocity is included in each test, occurring at setpoint thirteen in Test 1.0 and setpoint 1 in Test 4.5. The oxygen mass flow rates are associated with a specific equivalence ratio that ranges between ϕ=2 at the first setpoint to ϕ=0.75 at the thirteenth setpoint. Within each test one oxygen flow rate corresponds to each of the design scaling parameters: velocity ratio, momentum ratio, momentum flux ratio, and mixture ratio. A stoichiometric point is also included in each test, as well as several fuel lean setpoints. Although most engines, including the Lunar Ascent Engine, do not operate in the lean regime, multiple sources [31, 32] indicate that combustion instability is more likely to occur under lean conditions. Therefore, these setpoints were added to drive instabilities. A graphical representation of the test matrix is shown in Figure 3.14. In this figure the dots represent the desired flow

rate conditions for testing, and the lines represent a particular scaling parameter that is held constant versus fuel mass flow rate. A tabular version of the test matrix is shown in Table 3.7.

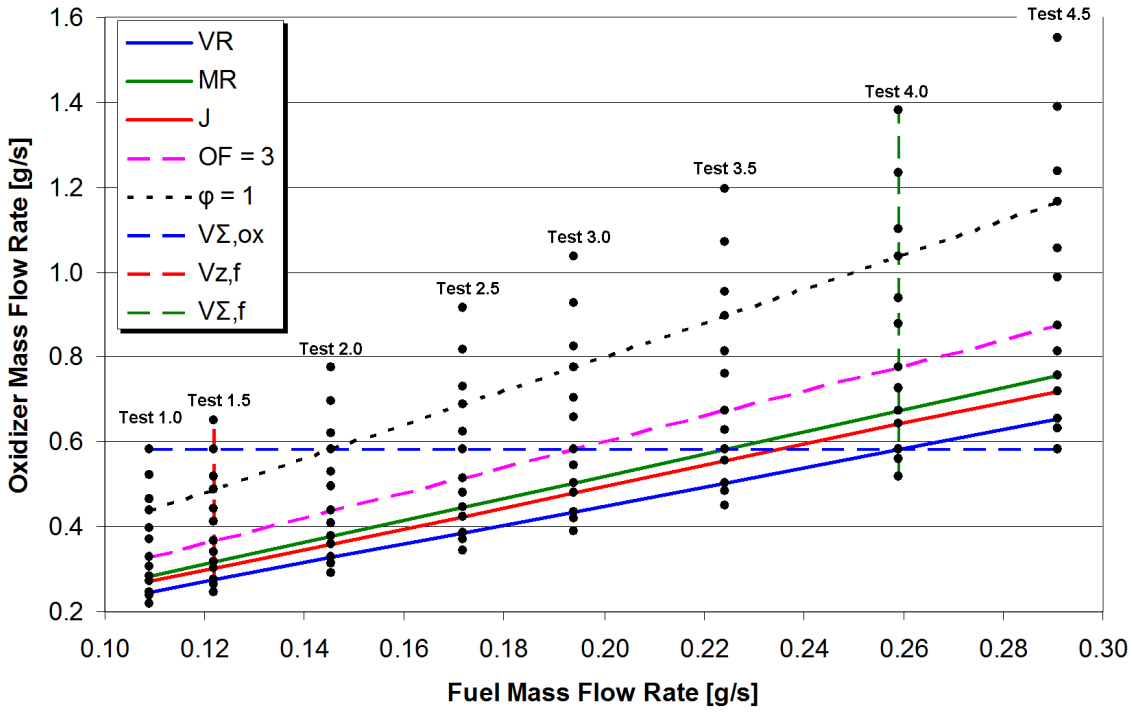

Figure 3.14: Test Matrix

Table 3.7: Test Matrix

Test	$\dot{m}_f$ $[g/s]$	$\dot{m}_{ox}$ $[g/s]$	ϕ	VR	MR	J
1.0	0.1091	0.2183-0.5820	2.00-0.75	1.736-0.651	0.868-0.122	1.507-0.079
1.5	0.1220	0.2441-0.6508	2.00-0.75	1.736-0.651	0.868-0.122	1.507-0.079
2.0	0.1455	0.2911-0.7762	2.00-0.75	1.736-0.651	0.868-0.122	1.507-0.079
2.5	0.1717	0.3433-0.9156	2.00-0.75	1.736-0.651	0.868-0.122	1.507-0.079
3.0	0.1940	0.3880-1.0345	2.00-0.75	1.736-0.651	0.868-0.122	1.507-0.079
3.5	0.2242	0.4483-1.1955	2.00-0.75	1.736-0.651	0.868-0.122	1.507-0.079
4.0	0.2590	0.5180-1.3813	2.00-0.75	1.736-0.651	0.868-0.122	1.507-0.079
4.5	0.2910	0.5819-1.5518	2.00-0.75	1.736-0.651	0.868-0.122	1.507-0.079

CHAPTER 4

EXPERIMENTAL RESULTS

To write it, it took three months;
to conceive it–three minutes;
to collect the data in it–all my life.

—Anonymous

This chapter presents the results from the testing of the swirl-coaxial injector. Some interesting observations were made of the relatively unstable nature of the injector and will be discussed. Higher frequencies than had been seen previously from the experiment were common. Overall, the flame exhibited indications of interaction with the flowfield; however, amplitudes were lower than what is usually considered unstable. A description of the analysis methods are presented first and will be followed by the test results.

4.1 Tests Run

Preliminary testing of the swirl-coaxial injector in the optically-accessible chamber took place on July 6, 2009. The objective of this testing was to determine the capability of the experimental setup, including the effectiveness of the glass chamber and usefulness of phase-locking the high-speed images. The rest of the testing was conducted from September 14 to September 24, 2009, after modifications

to the test setup had been made. Testing of the swirl-coaxial injector was done at three separate injector locations within the chamber. Initially, hot-fire testing was performed for the entire test matrix to characterize the stability characteristics of the injector. Several mass flow rate setpoints were then chosen for more testing with new diagnostics, which included feed line high-frequency pressure measurements and OH^* emission imaging. During these hot-fire tests, consistent problems with flame blowout at specific fuel mass flow rates occurred. An audible noise was produced at these flow rates during leak checks, so cold-flow testing was done to determine if it was the source. Table 4.1 lists all the setpoints of each test which good data was able to be acquired.

Table 4.1: Test Schedule

Date	9/14/2009	9/15/2009	9/18/2009	9/18/2009	9/22/2009	9/24/2009
Test	Hot Fire	Hot Fire	Hot Fire	Hot Fire	Hot Fire	Cold Flow
Feed Line	No	No	No	No	Yes	No
$\frac{r}{r_c}$	0%	75%	75%	50%	75%	75%
Test 1.0	SP 1-13	SP 1-13	-	SP 1-13	SP 12	Fuel
Test 1.5	SP 1-8	-	SP 1-13	SP 1-13	-	Fuel, Ox. SP 8
Test 2.0	SP 1-13	-	SP 1-9	SP 1-13	-	Fuel, Ox. SP 8
Test 2.5	SP 1-13	SP 1-13	-	SP 1-13	-	-
Test 3.0	SP 1-13	SP 1-13	-	SP 1-13	SP 7	-
Test 3.5	SP 1-13	SP 1-13	-	SP 1-13	-	-
Test 4.0	SP 1-13	SP 1-13	-	SP 1-12	SP 3, SP 13	Ox. SP 13
Test 4.5	SP 1-13	SP 1-13	-	SP 1-11	SP 7	-

Each column indicates the injector location, whether feed line pressure transducers were used, and whether the testing was hot fire or cold flow. The setpoints that produced good data from each test are listed. For the column listing the cold-flow tests, "Fuel" means that only methane was flowed through the injector at the

flow rate associated with that test number. "Ox" means only oxygen was flowed at the flow rate associated with the setpoint for that test number.

4.2 Analysis Methods

Large quantities of data are acquired during the course of testing, and a method was previously developed to analyze the data as a whole before looking at an individual set of data in detail. Once the test matrix is completed for a given injector location, the chamber dynamic pressure and temperature data can be analyzed.

4.2.1 Stability Mapping

In order to determine which mass flow rate setpoints had the highest chamber pressure oscillations, a method for analyzing the entire data set from the test matrix was previously established [16]. Since the method was first developed, multiple high-frequency pressure transducers have been implemented into the test facility, and the analysis script was modified to incorporate these changes. This script—written in VBScript and run through National Instruments DIAdem v10.0 software—goes through the data recorded at each setpoint, performs an FFT of the dynamic pressure from each transducer, and stores the maximum amplitude and its corresponding frequency. The FFTs are individually plotted and saved. Figure 4.1 shows an example of what the FFT plot looks like. A waterfall plot is created for each test by plotting the FFT from each setpoint in a three-dimensional graph. It shows the transition of the frequencies and amplitudes as the oxygen mass flow rate is increased. Figure 4.2 shows an example waterfall plot.

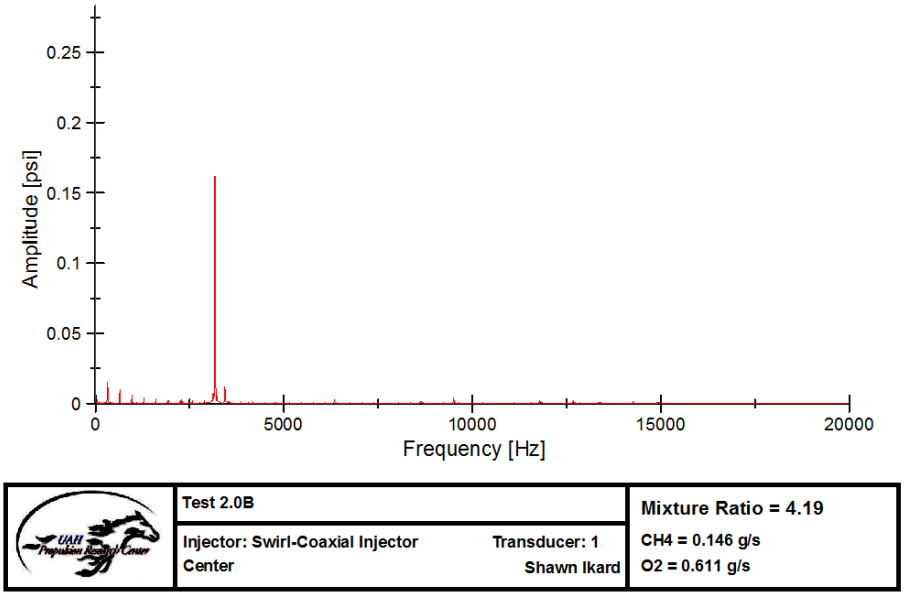

Figure 4.1: Sample FFT Plot

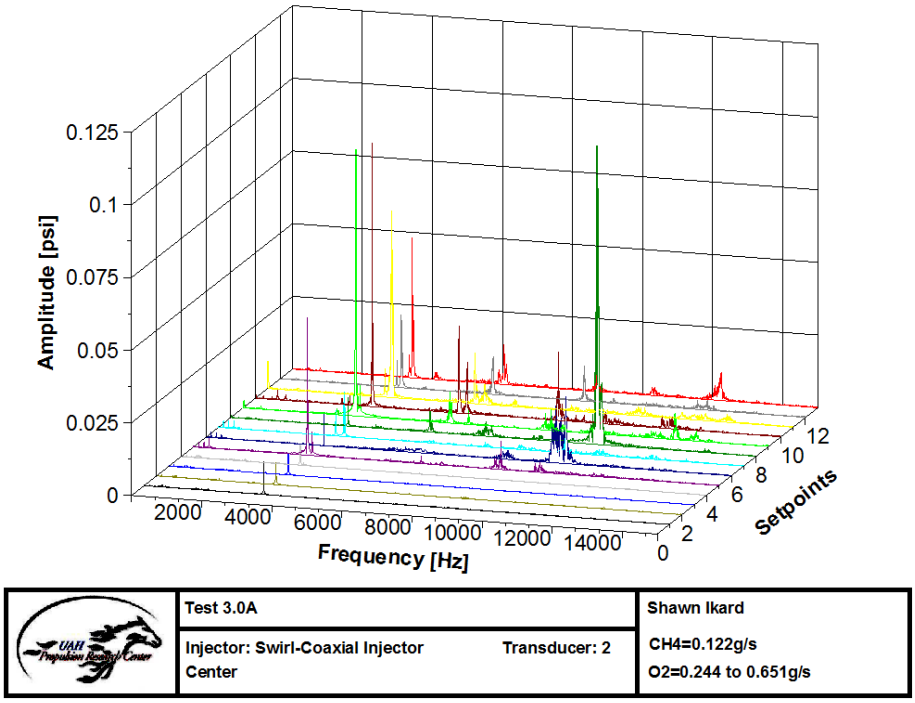

Figure 4.2: Sample Waterfall Plot

The maximum amplitudes and corresponding frequencies are then run through a script written in Matlab that plots all the oxygen mass or volumetric flow rates versus all the fuel mass or volumetric flow rates. The pressure amplitude is indicated by color scale that is linearly interpolated between each value to create a mesh that transitions between flow rate setpoints. Frequency maps are also created that use the frequency of the maximum amplitude as the color scale instead of the amplitude.

4.2.2 Speed of Sound Approximation

As mentioned previously, estimating the average speed of sound within the chamber is difficult, but is necessary when determining the instability modes present. Previous work done by Byrd [18] and Huynh [20] first determined the instability mode, and using Equation 4.1 from Barrere [42] calculated the needed speed of sound for a given frequency and instability mode.

$$f_{m,n,q} = \frac{a}{2}\sqrt{\left(\frac{t_{mn}}{R_c}\right)^2 + \left(\frac{q}{L_c}\right)^2}, \tag{4.1}$$

where a is the average speed of sound within the chamber, t_{mn} is the "effective transverse mode order" [18], r_c is the chamber radius, q is the longitudinal mode order, and L_c is the chamber length. The effective transverse mode order is derived from the roots of the Bessel function and indicates the order of tangential, radial, or any combination of the two modes. The subscript m refers to the tangential mode

order, and the subscript n refers to the radial mode order. For example, a 2T1R mode would have m=2 and n=1, which corresponds to t_{mn}=2.135 from Table 4.2 [42].

Table 4.2: Roots of Bessel Function

$\downarrow m/n\rightarrow$	0	1	2	3
0	0	1.220	2.233	3.238
1	0.586	1.697	2.714	3.726
2	0.972	2.135	3.173	4.192
3	1.337	2.551	3.611	4.693

Analyzing the temperature data taken by Byrd [18] found that they could be used to provide a first-order approximation of the average speed of sound. Since the estimated speeds of sound were relatively low compared to adiabatic conditions, the thermal properties within the combustion chamber were assumed to be that of air, where the temperature was found by calculating the average temperature from each chamber thermocouple for a short amount of time before the high-frequency data were acquired. Equation 4.2 could then be used to find the average speed of sound. This method resulted in values similar to what Byrd estimated.

$$a_{est} = \sqrt{\gamma_{air} \frac{\bar{R}}{MW_{air}} T_{avg}}, \tag{4.2}$$

where γ_{air} is the ratio of specific heats for air, $\bar{R}$ is the universal gas constant, MW_{air} is the molecular weight of air, and T_{avg} is the average temperature calculated from the thermocouple data.

Although the first method was used for the analysis in this report, the second method was implemented to provide further verification of the thermal environment by using actual measured data. To quickly analyze the large amounts of temperature data recorded from the experiments, a script written in VBScript using DIAdem v10.0 software was developed. This script found the point immediately before the high-frequency data were taken and averaged the previous 100 data points from each thermocouple placed in the chamber. The temperatures were not averaged together by the computer code so that the thermal profile around the chamber circumference could be evaluated.

4.2.3 Phase and Amplitude Analysis

Once the setpoints with the highest amplitudes have been found, those points can be analyzed to determine the instability mode present. Determining the instability mode requires knowledge of the physical manifestation of the pressure oscillations within the chamber and the orientation of the pressure transducers. The phase differences between each transducer and a reference transducer, usually transducer P1, are calculated. These differences are usually neither 0° or 180° exactly, but they are close enough to be divided into these groups. If the phase difference is 0°, the pressure signals are in phase. The pressure oscillations occur together in this case. In-phase signals signify an even number of node lines between the two transducers. If the phase difference is ±180°, the signals are in antiphase. The pressure oscillations are opposite one another in this case, meaning the pressure measured at one transducer is at a maximum, and the pressure measured at the other is at a minimum. Antiphase sig-

nals indicate an odd number of node lines between the two transducers. The relative amplitude of the two signals determines the proximity of the node line to the pressure transducer. If the amplitude of one signal is higher, the node line is farther from the pressure transducer; if a signal has a lower amplitude, the transducer is closer to a node line. The coherence between the two signals is also considered when determining instability modes. A higher coherence—above 0.80 is usually considered good for this analysis—indicates the signals correlate closely in terms of relative phase.

4.2.4 Image Processing

The chemiluminescence images acquired from the high-speed camera had a time stamp on them to help determine when they were taken compared to a given dynamic pressure signal. To begin the image processing procedure, the image was converted to an array of intensity values using ImageJ software [43]. The time stamp information was then cropped by running the text image through a Matlab code. The array was converted back to an actual image, and the grayscale range was set from 0 to 500. This constant scale allowed qualitative comparison among all the different images. Converting to a color scale enhanced the higher intensity regions from the lower intensity regions.

A sample graph showing the camera and pressure signals used for phase-locking the images is shown in Figure 4.3. The low state of the "Ready" signal indicates acquisition of the first image. The "Sync Out" pulse high state indicates the beginning of a single image acquisition, and the pulse width indicates the exposure time. The times at the pulse high edge and low edge are averaged to give a specific time value to

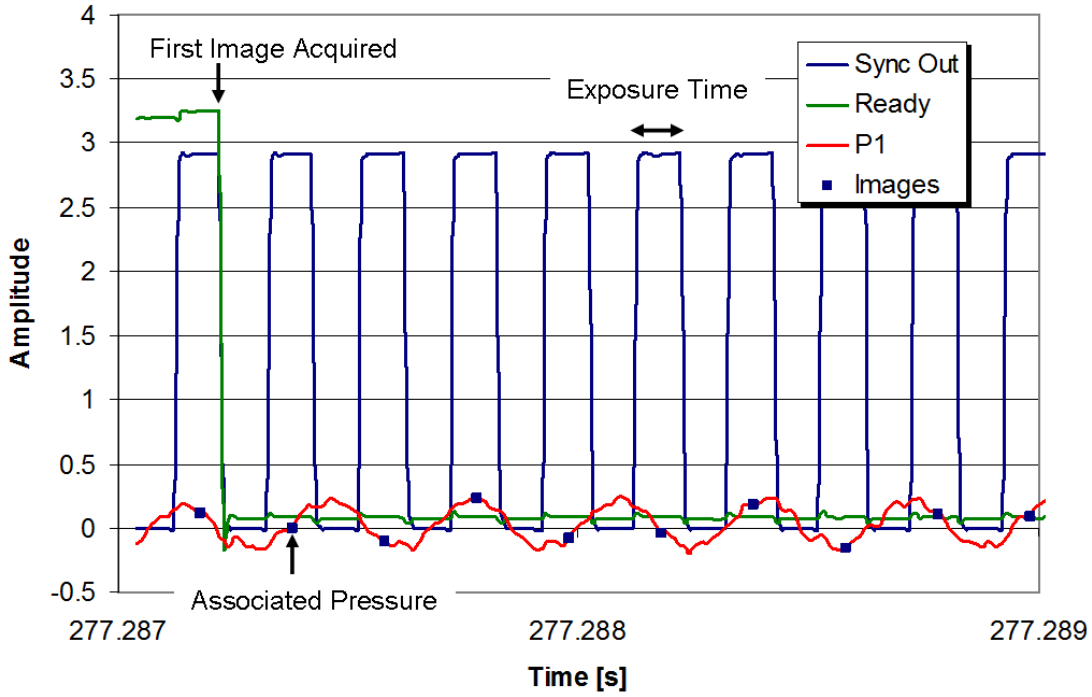

Figure 4.3: Diagram for Phase-Locking CH* Images to a Pressure Signal

the image. The corresponding pressure value for a given transducer is then supplied to the image for reference. The time corresponding to the image is then converted to the phase based on the period of the oscillation. The images are then sorted by phase to determine the emission response with respect to phase.

The imaging done in this experiment is a line-of-sight technique, meaning the image is integrated along the flame volume. This technique does not provide spatially-resolved images of the combustion zone, but rather an overall indication of the high-intensity heat release regions. A deconvolution technique [44] can be applied to the images to see a cross-section of the heat release zone. This procedure, however, assumes an axisymmetric object. Since this research features unstable combustion

with a highly turbulent flame, the flame is not axisymmetric. Therefore, the method was not used. It can be used, however, in future studies of stable combustion at atmospheric pressure.

4.3 Instability Mode Determination

The first goal of this research was to characterize the stability boundaries of the swirl-coaxial injector over a range of mass flow rates by finding the mass flow rate setpoints that produce the largest pressure oscillations. The results are presented for each injector location.

4.3.1 Preliminary Testing Results

The objective of this initial testing was to determine the frequencies and instability modes that were present; therefore, a relatively low threshold value of 345 Pa amplitude, approximately 0.68% P_c, was set as an "unstable" condition. The frequencies that had an amplitude above this threshold were analyzed for mode determination. Table 4.3 shows the frequencies of peak amplitude for a given setpoint. In the

Table 4.3: Preliminary Testing Results

SP	1	2	3	4	5	6	7	8	9	10	11	12
$\dot{m}_{ox}$ [g/s]	0.318	0.367	0.412	0.582	0.412	0.412	0.582	0.582	0.412	0.582	0.673	0.777
$\dot{m}_f$ [g/s]	0.122	0.122	0.122	0.122	0.137	0.159	0.194	0.224	0.259	0.259	0.259	0.259
f [kHz]	0.3	0.3	0.3	5.1	5.1	9.4	10.5	2.6	0.3	2.6	5.3	11.1
A_{p-p} [%P_c]	0.33	0.28	0.26	1.68	0.82	1.52	1.42	1.19	0.59	1.42	2.02	2.05
Stability	S	S	S	US	US	US	US	US	S	US	US	US
Mode	-	-	-	1T1R2L	1T1R2L	UK	UK	2T	-	2T	1T1R	UK
a_{est} [m/s]	395	434	423	425	428	458	446	441	446	437	453	454
a_{calc} [m/s]	-	-	-	442	442	-	-	415	-	415	488	-
e_{rel}	-	-	-	3.9%	3.3%	-	-	6.3%	-	5.3%	7.1%	-

table, the setpoints are listed "S" for stable and "US" for unstable. The instability modes that could not be determined are listed as "UK" for unknown. The injector was located at $\frac{r}{r_c}$=0.67 for this testing.

The setpoints labeled "Stable" had peaks below the given threshold and were not analyzed. The first two unstable setpoints had the same frequency. The phase difference of each transducer with respect to transducer P1 is given in Table 4.4. Note that these and all phase differences listed in this report are not the actual phase differences. They have been rounded to 0° or ±180° to indicate whether two signals are in phase or antiphase. The phase differences between P1 and P4 and P1 and P6 indicate the presence of a tangential node line and a radial node line. Transducers P1 and P8 are in antiphase; therefore, a node line exists between them. Since the chamber is a closed-open tube, this phase difference indicates a second longitudinal component. As noted in the table, the mode was determined to be a 1T1R2L mode. Interestingly, it is the first time a second longitudinal mode has been known to exist in this experiment. A schematic of the mode is shown in Figure 4.4. Since it is difficult to show both longitudinal and transverse mode shapes simultaneously, they have been split to show the transverse part of the mode from a top view and the longitudinal part from a side view.

Similarly, SP 8 and SP 10 have the same frequency and mode. The phase information is given in Table 4.5. The relative phase of P2 and P4 with P1 indicate two tangential node lines. Since transducers P6 and P7 have the same relative phase as P2 and P4, no radial node lines are present. A visual representation of the mode is given in Figure 4.5. The 2T mode present at these setpoints is common when

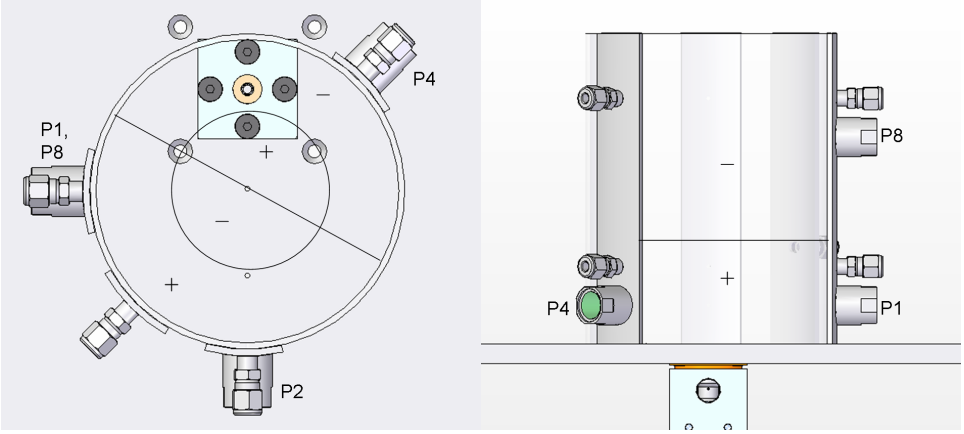

Figure 4.4: Visual Representation of 1T1R2L Mode from SP 4 and SP 5

Table 4.4: SP 4 and SP 5 Phase Relationship at $\frac{r}{r_c}$=0.67

Transducer	P1	P2	P4	P6	P7	P8	Mode
$\Delta\phi$	-	0°	180°	180°	0°	180°	1T1R2L

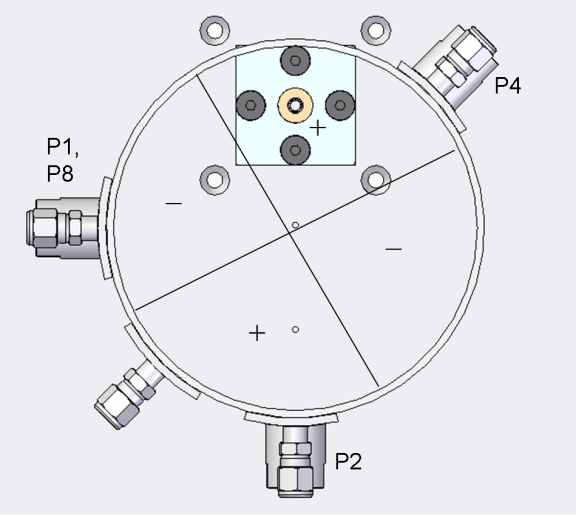

Figure 4.5: Visual Representation of 2T Mode from SP 8 and SP 10

Table 4.5: SP 8 and SP 10 Phase Relationship at $\frac{r}{r_c}$=0.67

Transducer	P1	P2	P4	P6	P7	P8	Mode
$\Delta\phi$	–	180°	180°	180°	180°	0°	2T

compared to previous research with different injectors. The 2T mode has usually been the dominant mode when close to the wall.

The last setpoint whose mode could be determined was SP 11. The phase information, shown in Table 4.6, is similar to the 1T1R2L modes, and the frequency is slightly higher. However, no longitudinal node line exists at this setpoint, and transducer P7 is in phase with P1. The mode is determined to be a 1T1R mode, but the mode has a slightly different shape compared to the previous 1T1R component from SPs 4 and 5. The change is indicative of the complex temperature gradients present in the chamber. The mode shape is shown in Figure 4.6.

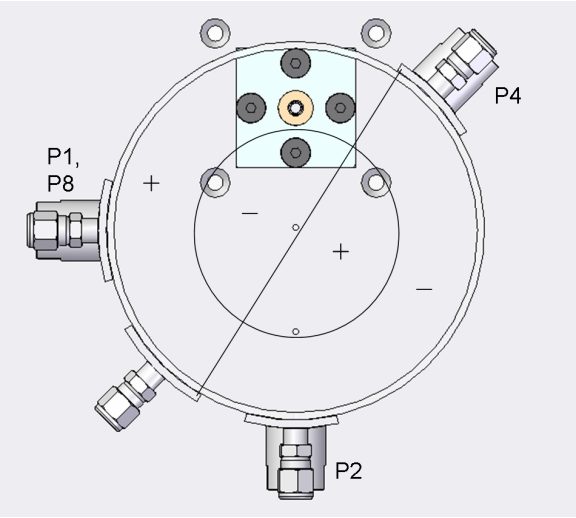

Figure 4.6: Visual Representation of 1T1R Mode from SP 11

Table 4.6: SP 11 Phase Relationship at $\frac{r}{r_c}$=0.67

Transducer	P1	P2	P4	P6	P7	P8	Mode
$\Delta\phi$	−	-180°	-180°	-180°	0°	0°	1T1R

The remaining setpoints had much higher frequencies on the order of 10.0 kHz. The highest frequency previously seen in this experiment was on the order of 4.0 kHz. The problem with higher frequencies, especially in a complicated thermal environment, is that multiple modes can be possible, including higher order modes that cannot be differentiated with the diagnostics used. Therefore, all of these modes are considered undetermined.

The temperature data from each setpoint were used to find the average speed of sound as described in Section 4.2.2. The results are shown in Figure 4.7. The estimated speed of sound for each setpoint stayed in the range between 420 m/s and 460 m/s. Looking at the 2T and 1T1R2L modes, Barrere's equation gives speeds of

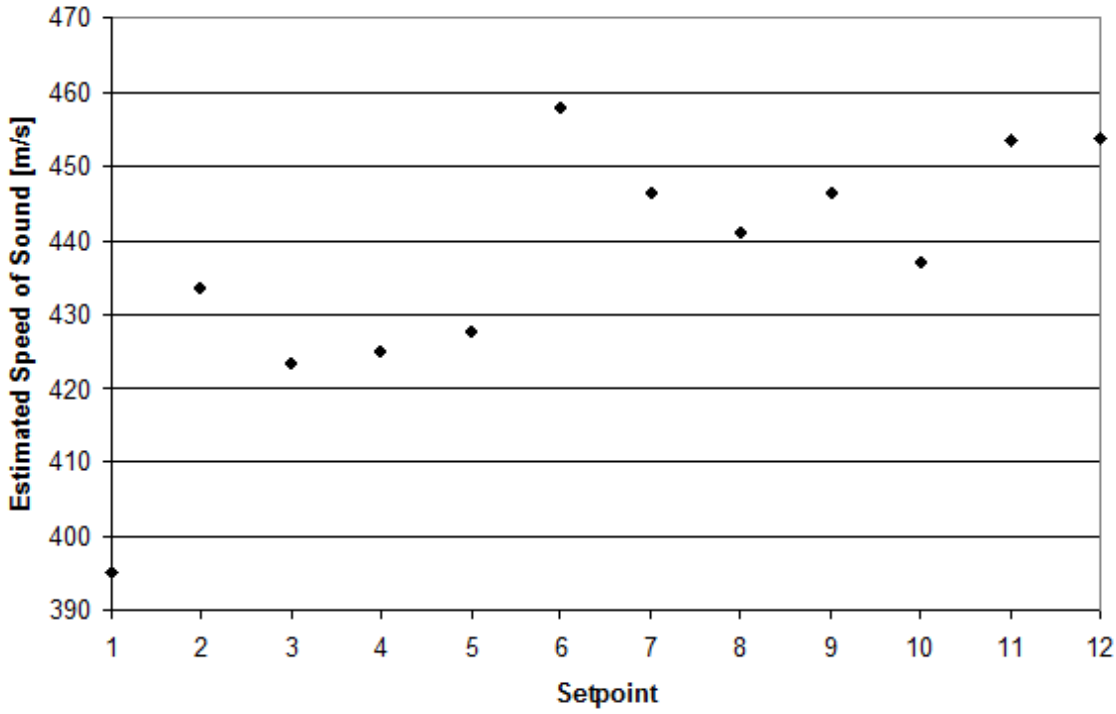

Figure 4.7: Estimated Speed of Sound from Average Temperatures for Each Setpoint

sound of 415 m/s and 440 m/s, respectively. Using Equation 4.3 the relative error—where the estimated value derives from the thermocouple data, and the calculated value comes from Barrere's equation—shows good relation with 6.2% and 3.5% errors, respectively.

$$e_{rel} = |\frac{a_{est} - a_{calc}}{a_{calc}}| \cdot 100\% \tag{4.3}$$

A representative CH^* chemiluminescence image is shown for each setpoint in Figure 4.8. The chemiluminescence imaging shows a relatively constant flame structure among the setpoints, although two are noticeably different. SP 4 is a shorter and wider flame compared with the rest, and SP 9 is thinner and less intense farther from the injector exit. SP 4 is the only flow rate condition that is fuel lean. Since more oxygen is present, it would take less time for all of the fuel to react. Combustion would not occur as far from the injector, which could explain why the flame is short. Another explanation is that combustion instability causes increased mixing, resulting in more efficient combustion. The width could be a result of the higher velocity oxygen overpowering the fuel and pushing the combustion outward. Reaching the flow rates at this setpoint proved problematic because the flame would blow out easily, a result of the lower velocity ratio and low fuel flow rate. SP 9 is the richest setpoint. It seems the opposite happens at this condition compared to SP 4. The higher velocity ratio makes the flame thinner.

One of the most interesting findings from this preliminary testing was the existence of a lifted primary combustion zone for most of the setpoints. Figure 4.9

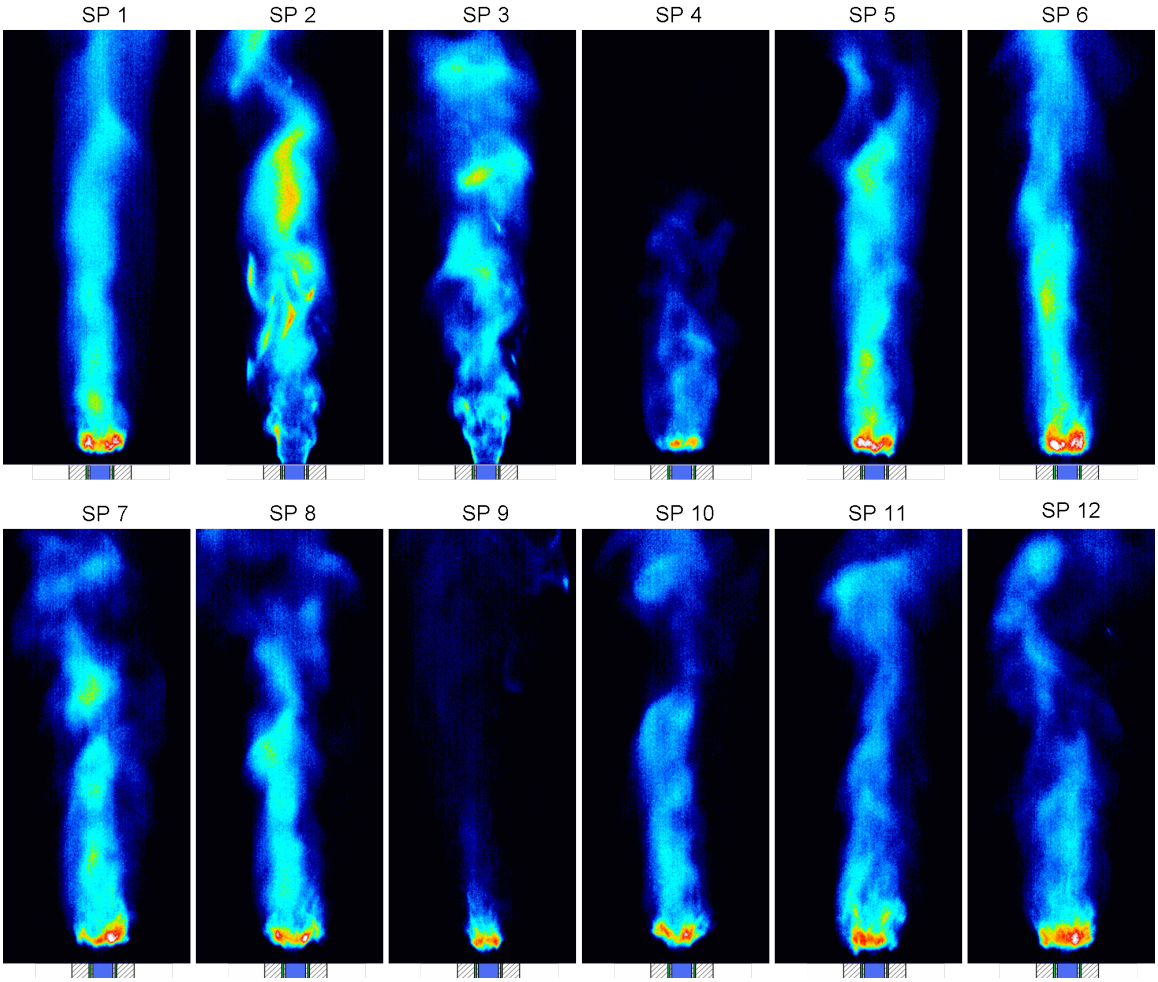

Figure 4.8: Sample CH* Chemiluminescence Images from SPs 1-12

shows a close up CH* image from SP 3 where the flame was attached to the injector lip and at SP 10 where the combustion zone is lifted off the injector. Although it appears to be detached, the flame is indeed still connected to the injector lip. The emission in this region is too low to be detected at the specified exposure time. When the flame is attached, the combustion zone appears smooth and stable. When the combustion zone becomes lifted, it occurs at a point just above the injector exit. This region also appears more intense, indicating a concentration of localized heat release,

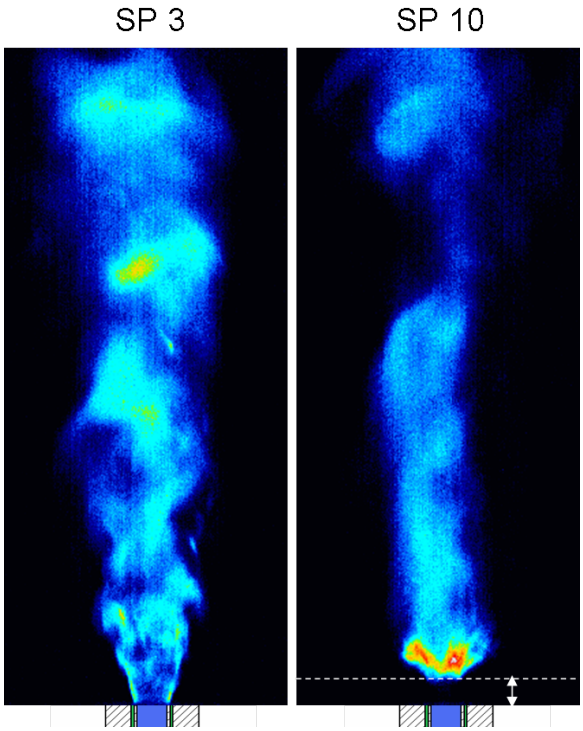

Figure 4.9: Comparison Between Attached and Lifted Combustion Zone

a common sign of combustion instability. The only two setpoints that did not have a lift combustion zone were SP 2 and SP 3.

This phenomenon can also be seen with high-definition video and not just with chemiluminescence emissions. Figure 4.10 and Figure 4.11 show two successive images taken from a high-definition camera that illustrate the transition from a typical flame to a lifted combustion zone. From these two images the flame is clearly seen to be attached to the injector, but the illumination below the lifted combustion zone is considerably less. The flame was not seen to oscillate between the attached and lifted conditions with the naked eye. The high-speed images corroborate that once the combustion zone lifts, it does not return to its initial structure. Even though

Figure 4.10: Stable Flame Attached to Injector

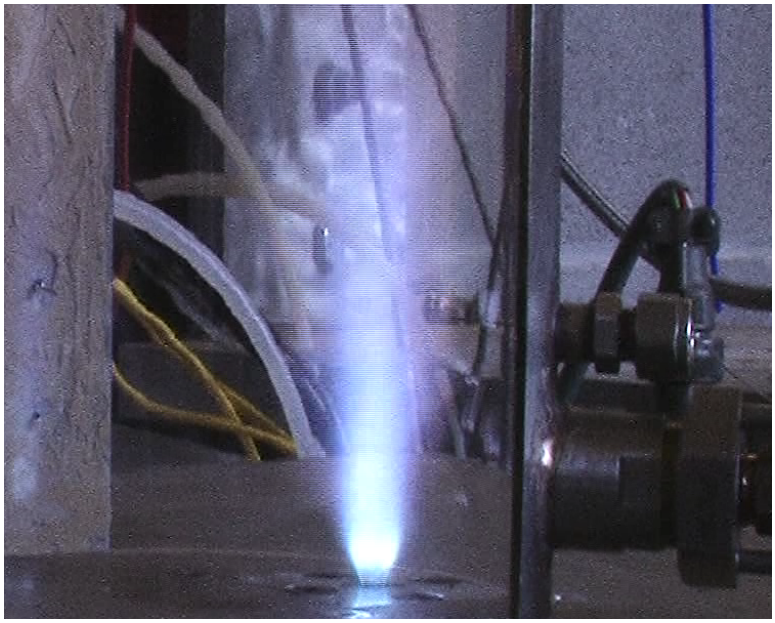

Figure 4.11: Lifted Combustion Zone

previous combustion chambers have had optical access from the top of the chamber, the lifted combustion zone could never be seen from a top-down view.

After this preliminary testing, it was realized that a few problems occurred. First, using the delay generator to try to phase-lock the images to a pressure signal provided erratic imaging because the pressure signal had to be above a threshold before the pulse was sent to the camera to take the image, and the signal did not always reach this threshold. The exposure time seemed to vary based on the time stamp even though it was set to 25 μs. Only images with 25 μs exposure times were used in the preliminary analysis, however. The second problem was the location of the injector within the chamber. The transducer P6 was close to the center of the chamber—and thus a possible tangential mode line—which made mode determination slightly more difficult. For the next set of testing, the camera was run in an internal synchronization mode, and the phase-locked analysis of the images would take place post test. The injector locations chosen put transducer P6 farther from the center of the chamber, which eased mode determination.

4.3.2 Results at Injector Location $\frac{r}{r_c} = 0\%$

Testing at the centered, or $\frac{r}{r_c}$=0, position was done for the entire test matrix, but data were not acquired for a few setpoints in one test. Test 1.5, corresponding to a fuel mass flow rate of 0.1220 g/s, was the only test not to reach completion due to flame blowout just past the halfway point in the test, although this particular test was attempted multiple times. Figure 4.12 is the resulting surface plot from transducer P1. The larger circle indicates where the data could not be acquired. The smaller

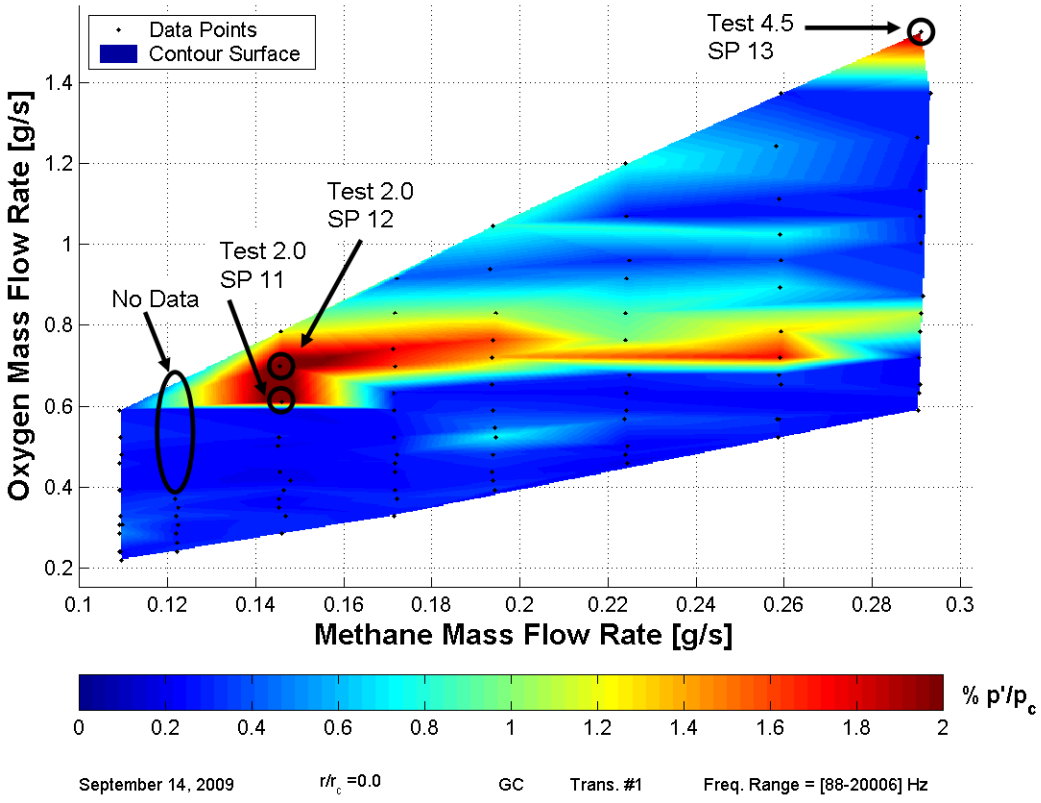

Figure 4.12: $\frac{r}{r_c}$=0.0 Surface Plot Transducer P1

circles, denoted by the test and setpoint number, indicate points that were analyzed and will be described.

The red and green areas in the center and the top-right corner of the graph are the areas of higher amplitudes. Although the highest amplitudes are on the order of 1%-2% of chamber pressure, the flame exhibited noticeable characteristics of high-frequency combustion instability at many setpoints, including louder combustion, flame bending and whipping, and higher flame luminosity. Even during stable combustion the flame would bend slightly and react to pressure oscillations. At some

setpoint during each test the combustion zone would lift off the injector lip and not return to its original state.

Several peaks are noticeably higher in amplitude, with two occurring at lower fuel flow rates and one occurring at the highest total mass flow rate in the top-right corner of the map. The properties of each of the analyzed setpoints are listed in Table 4.7. The phase differences between each transducer with respect to P1 are shown in Table 4.8. Notice that transducer P7 is located outside the chamber for this injector position and is not listed in the phase analysis. The highest peak-to-peak amplitude is about 2.2% of chamber pressure and occurred at Test 2.0 SP 11. The signal from P8 indicates a longitudinal component does not exist. Since the signal from transducer P1 is in phase with P2 and P4 and in antiphase with P6, the first radial mode is present. The 1R, or first radial, mode is shown in Figure 4.13. The 1R mode was expected due to the injector's location within the chamber. Placing

Table 4.7: Setpoint Properties at $\frac{r}{r_c}$=0.0 from P1 Stability Map

Test	SP	A_{p-p} [$\%P_c$]	f [kHz]	$\dot{m}_{ox}$ [g/s]	$\dot{m}_f$ [g/s]
2.0	11	2.21	3.1	0.6108	0.1458
2.0	12	2.17	3.1	0.6980	0.1454
4.5	13	2.06	3.8	1.5269	0.2911

Table 4.8: Phase Relationships at $\frac{r}{r_c}$=0.0 from P1 Stability Map

Test	SP	Transducer	P1	P2	P4	P6	P8	Mode
2.0	11	$\Delta\phi$	–	0°	0°	180°	0°	1R
2.0	12	$\Delta\phi$	–	0°	0°	180°	0°	1R
4.5	13	$\Delta\phi$	–	0°	0°	180°	180°	1R2L

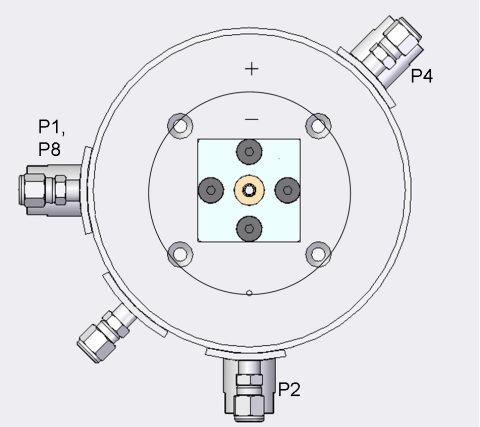

Figure 4.13: Visualization of 1R Mode from Test 2.0 SPs 11 and 12

the injector at the antinode of a specific mode would more likely excite that mode. The setpoint directly above this one, Test 2.0 SP 12, had a similar amplitude and frequency and was determined to have the same mode.

The point in the top-right corner of Figure 4.12 corresponds to Test 4.5 SP 13, the setpoint with the highest total mass flow rate. Referencing Table 4.8, the phase relationships among the transducers are similar to the previous two analyzed setpoints, except P1 and P8 are in antiphase. Therefore, the mode at that this frequency corresponds to a 1R2L mode. A visual representation of the mode is given in Figure 4.14.

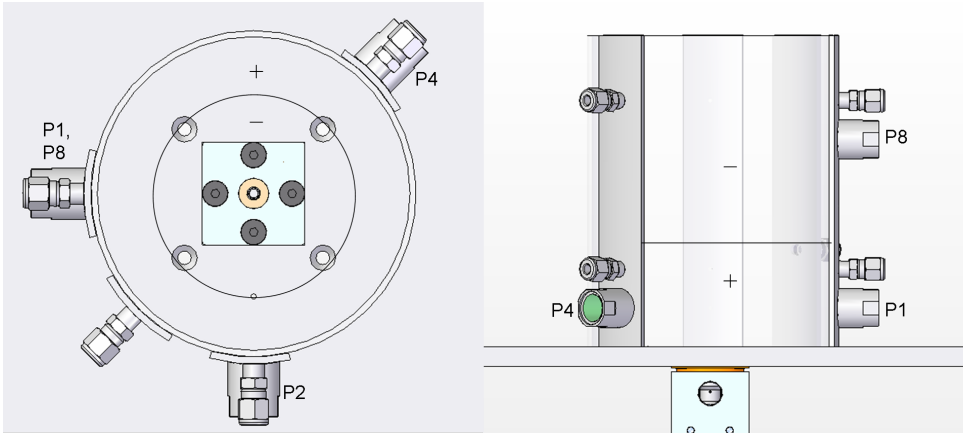

Figure 4.14: Visualization of 1R2L Mode from Test 4.5 SP 13

The higher frequency also indicates a higher-order mode than a 1R mode. This mode has never been previously detected in this experiment. The increased energy supplied by the increased total mass flow rate is the reason for the change in instability.

Looking at stability maps of different transducers shows that other setpoints have areas of relatively high amplitudes. The remaining four stability maps of transducers P2, P4, P6, and P8 are shown in Figures 4.15-4.18. The points of relatively high amplitudes sensed by transducer P2 were the same as transducer P1. Transducer P6 did not see any discrete amplitudes. Transducers P4 and P8 saw relatively high amplitudes at three other setpoints: Test 4.0 SP 8, Test 4.0 SP 13, and Test 4.5 SP 12. The properties at these setpoints are summarized in Table 4.9, and the phase relationships are shown in Table 4.10.

Table 4.9: Various Setpoint Properties at $\frac{r}{r_c}$=0.0

Test	SP#	Transducer	A_{p-p} [%P_c]	f [kHz]	$\dot{m}_{ox}$ [g/s]	$\dot{m}_f$ [g/s]
4.0	8	P8	1.49	9.7	0.8943	0.2591
4.0	13	P4	1.33	6.6	1.3742	0.2594
4.5	12	P4	1.26	6.6	1.3742	0.2933

Table 4.10: Various Phase Relationships at $\frac{r}{r_c}$=0.0

Test	SP#	Transducer	P1	P2	P4	P6	P8	Mode
4.0	8		–	0°	180°	-180°	180°	Unknown
4.0	13	$\Delta\phi$	–	-180°	180°	0°	0°	Unknown
4.5	12		–	-180°	-180°	0°	0°	Unknown

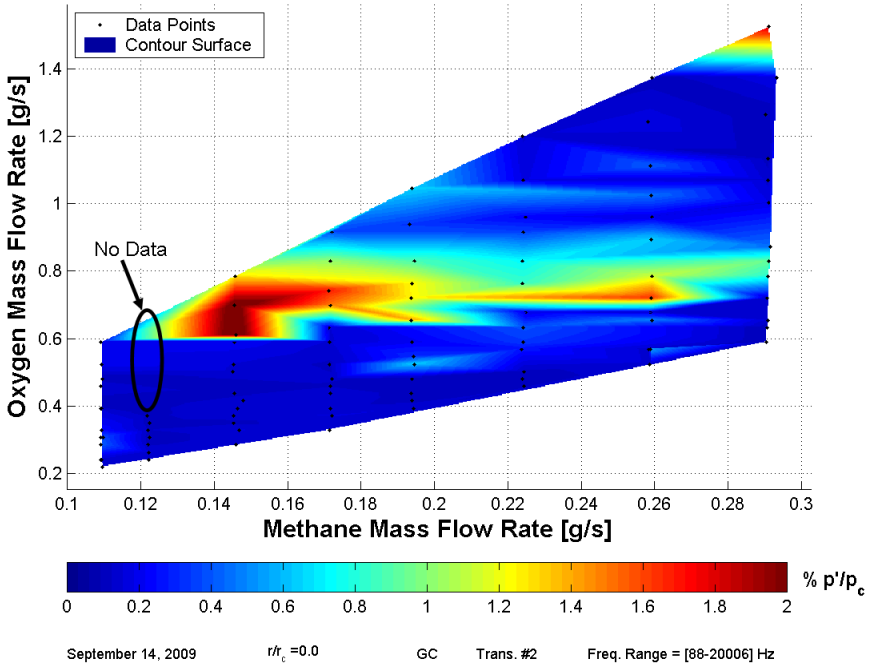

Figure 4.15: $\frac{r}{r_c}$=0.0 Surface Plot Transducer 2

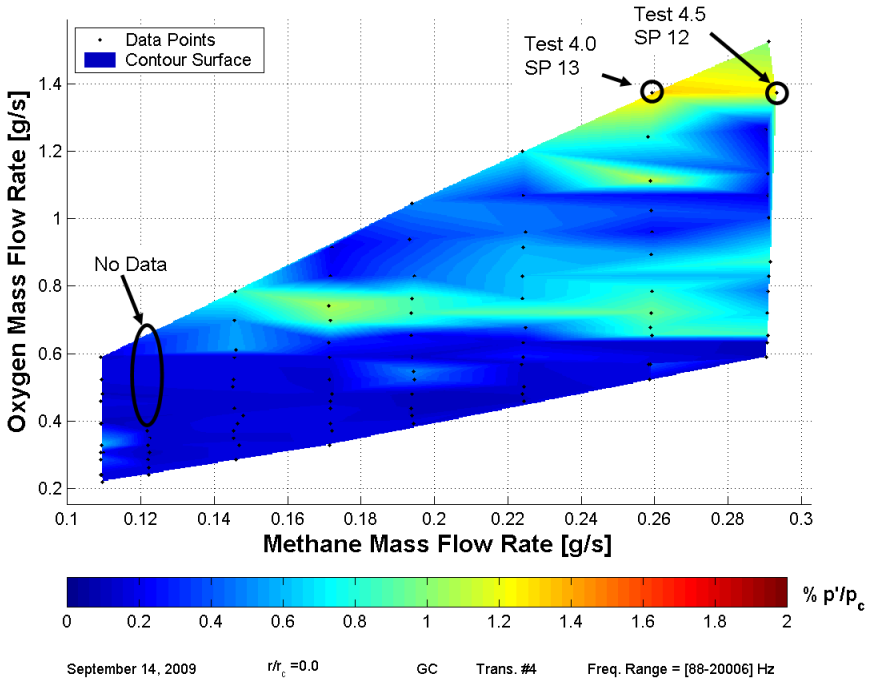

Figure 4.16: $\frac{r}{r_c}$=0.0 Surface Plot Transducer 4

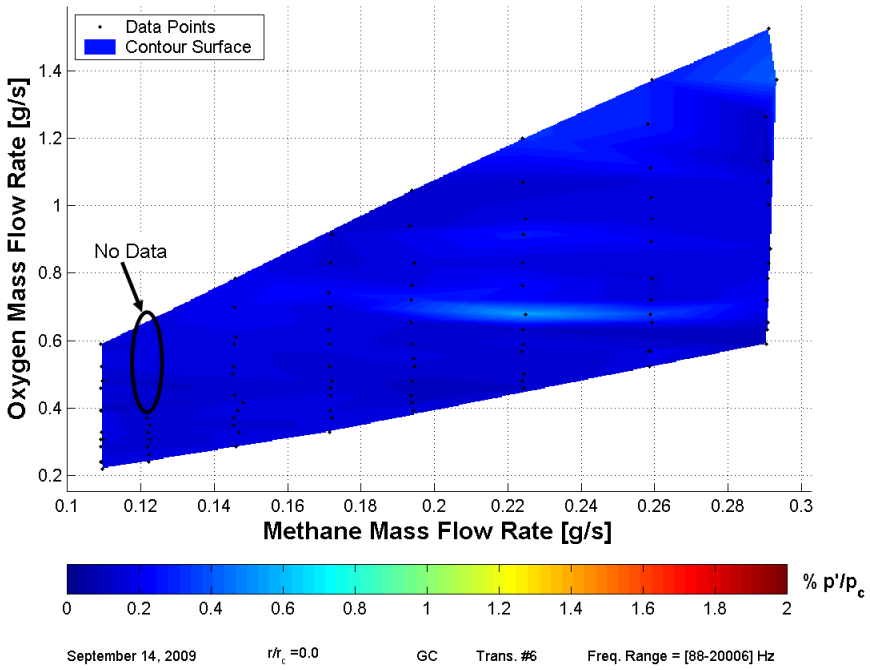

Figure 4.17: $\frac{r}{r_c}$=0.0 Surface Plot Transducer 6

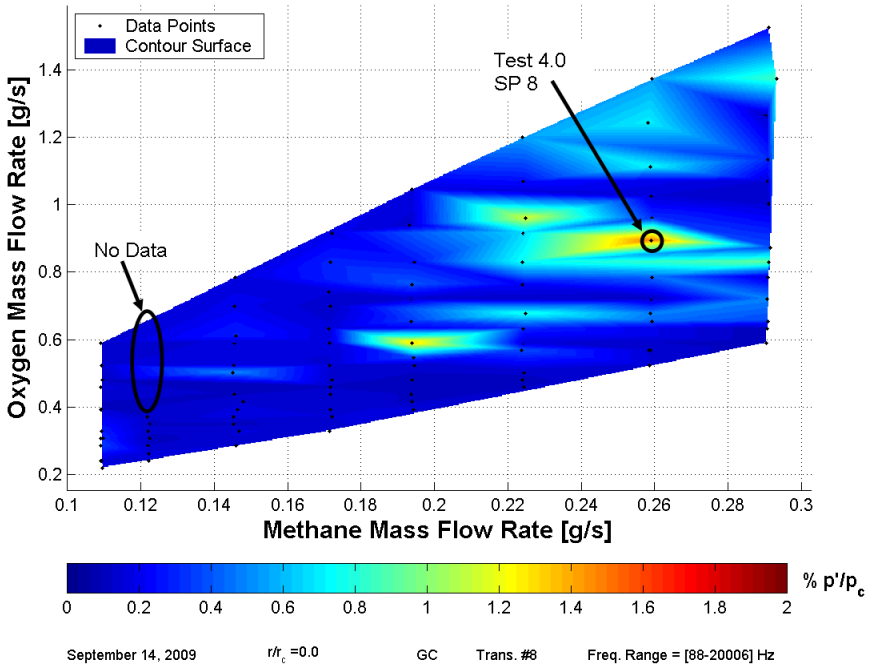

Figure 4.18: $\frac{r}{r_c}$=0.0 Surface Plot Transducer 8

As mentioned in the table, these three modes at frequencies could not be firmly ascertained. Phase analysis of the first setpoint indicates a possible 1T1R2L mode; however, the frequency is much higher than the 5.1 kHz frequency already determined to be that mode. The last two setpoints are possible 2T1R modes, but it seems unlikely to have a tangential mode, even if part of a combined mode, due to the injector's placement at the tangential node line.

The instability modes determined in this analysis can be verified by analyzing the average speed of sound in the chamber. The first three setpoints analyzed and the two possible 2T1R modes were examined. Table 4.11 shows the estimated and calculated speeds of sound and their relative error. All the calculated values are in the same range as calculated in the preliminary testing. The estimated values are consistently high. Other than the last setpoint, they are within a 15% relative error. The relative errors are reasonable considering how complicated the flowfield is. The actual estimated values for the last three setpoints, however, are much higher than expected, which is most likely due to the increased energy released from the higher mass flow rates. The variable pressure and velocity fields may also distribute the hot

Table 4.11: Speed of Sound Relative Error at $\frac{r}{r_c}$=0

Test	SP#	a_{calc} [m/s]	a_{est} [m/s]	% e_{rel}
2.0	11	403	459	13.8
2.0	12	398	403	1.3
4.0	13	464	533	14.8
4.5	12	477	528	10.6
4.5	13	437	566	29.5

combustion products more evenly in the chamber. The temperature data farther from the injector face are much higher than those closer to the injector face. Assuming the instability manifests itself at the lower plane and the temperature at the higher plane is not a primary factor, the estimated speeds of sound can be recalculated using only the three thermocouple data at the lower plane. The recalculated speeds of sound are 491 m/s, 495 m/s, and 520 m/s with relative errors of 5.9%, 3.8%, and 19.1%, respectively. The estimated speeds of sound affirm the instability modes. Although the setpoints that were possible 2T1R modes had frequency, phase, and temperature data that seems to support this mode, it is uncertain how this mode could occur. Therefore, this mode is still listed as undetermined.

4.3.3 Results at Injector Location $\frac{r}{r_c} = 50\%$

This location places the injector approximately 38 mm from the chamber wall. Unlike the other two injector locations tested, each test at the $\frac{r}{r_c} = 50\%$ injector location was able to be run without flame blowout. Three setpoints at the higher total flow rates could not be reached. This problem will be addressed in a later section. A stability map of transducer P1 is shown in Figure 4.19. The peak amplitude at this position is 2% of the chamber pressure. According to the map, the higher amplitudes occurred in the lean regions of the middle of the fuel flow rates tested. The properties of the setpoints analyzed from this map are listed in Table 4.12. This table shows the maximum amplitude occurred at Test 3.0 SP 13. The phase relations for these setpoints are shown in Table 4.13.

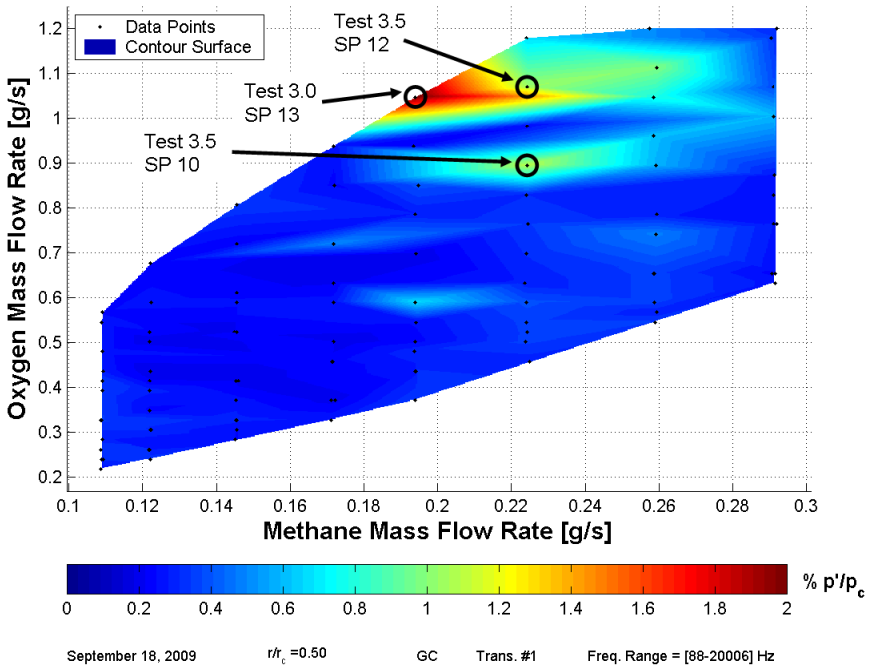

Figure 4.19: $\frac{r}{r_c}$=0.50 Surface Plot Transducer P1

Table 4.12: Setpoint Properties at $\frac{r}{r_c}$=0.50 from P1 Stability Map

Test	SP	A_{p-p} [$\%P_c$]	f [kHz]	$\dot{m}_{ox}$ [g/s]	$\dot{m}_f$ [g/s]
3.0	13	2.02	5.4	1.0470	0.1939
3.5	10	1.09	2.7	0.8943	0.2242
3.5	12	1.04	5.8	1.0689	0.2243

Table 4.13: Phase Relationships at $\frac{r}{r_c}$=0.50 from P1 Stability Map

Test	SP	Transducer	P1	P2	P4	P6	P7	P8	Mode
3.0	13	$\Delta\phi$	–	0°	-180°	-180°	0°	-180°	1T1R2L
3.5	10	$\Delta\phi$	–	180°	-180°	-180°	180°	180°	1T2L
3.5	12	$\Delta\phi$	–	180°	0°	0°	-180°	-180°	2T1R2L

The phase differences at this setpoint indicate a 1T1R2L mode. This particular mode was seen during the preliminary testing, where the injector was also in an off-center position. Off-center injector locations are expected to exacerbate combined transverse instability modes. Although the modes are the same, the frequency changed from 5.1 kHz in the preliminary testing to 5.4 kHz. It is possible that the instability at Test 3.5 SP 12 could be a 1T1R2L mode also, but it is unlikely that the frequency of this mode would change from 5.4 kHz to 5.8 kHz at the same injector location. The aforementioned frequency change from 5.1 kHz to 5.4 kHz can be explained by the change in injector location. For the preliminary testing the injector was placed at $\frac{r}{r_c}$=0.67—slightly farther from the center of the chamber compared to this location. The temperatures are highest when the injector is centered in the chamber and decreases as the injector is placed closer to the wall. Therefore, the speed of sound is higher, increasing the frequency. Hence, it was concluded to be 2T1R2L mode, another combined transverse mode. Visuals of the 1T1R2L mode and 2T1R2L mode are given in Figure 4.20 and Figure 4.21, respectively.

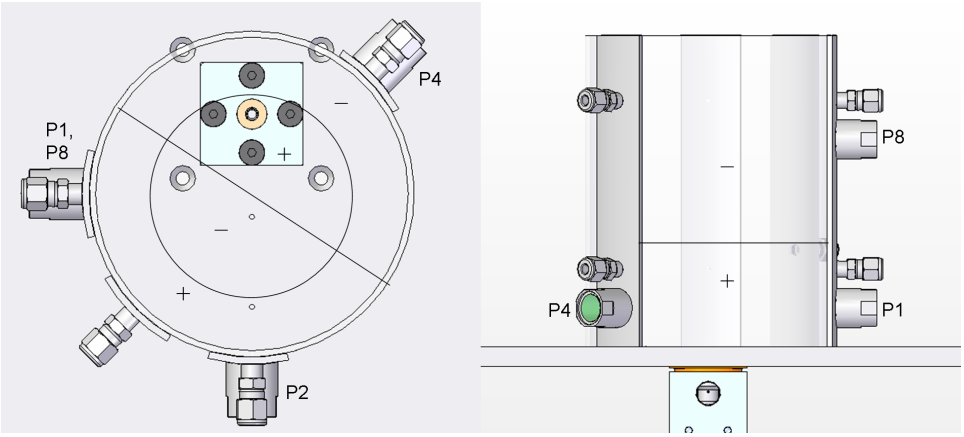

Figure 4.20: Visualization of 1T1R2L Mode from Test 3.0 SP 13

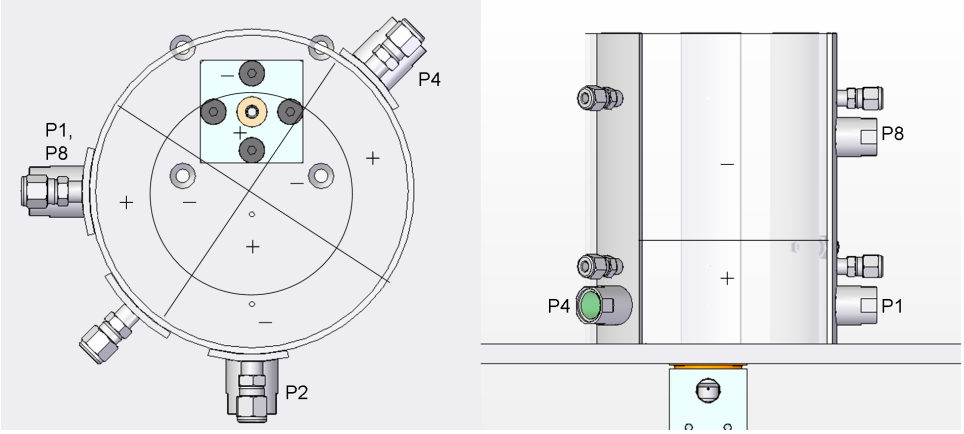

Figure 4.21: Visualization of 2T1R2L Mode from Test 3.5 SP 12

The third setpoint that was analyzed based on the P1 stability map is Test 3.5 SP 10. Referencing Table 4.13, this setpoint was determined to be a 1T2L mode. Phase analysis also showed that a 2T2L mode was possible, but the required average speed of sound to meet the frequency would be much lower than other calculated speeds of sound analyzed in this report. The 1T2L mode is illustrated in Figure 4.22. Although the analysis indicates that this mode is present, 1T modes are expected to

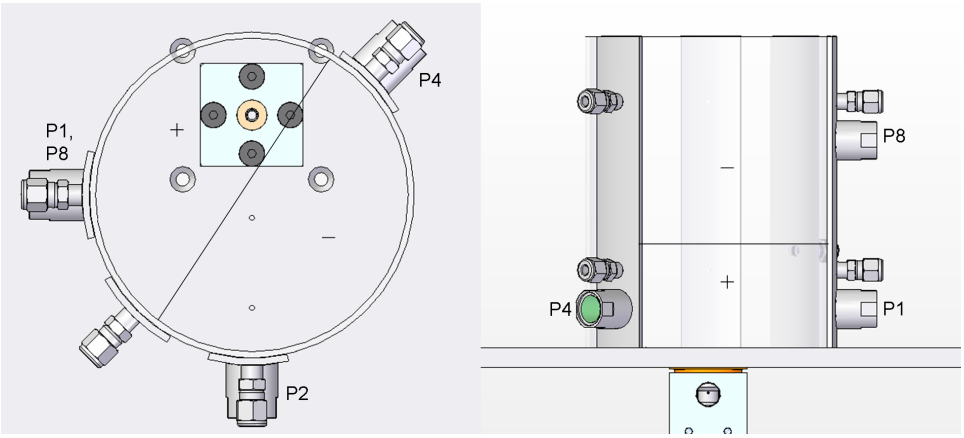

Figure 4.22: Visualization of 1T2L Mode from Test 3.5 SP 10

occur when the injector is closer to the chamber wall. Unlike the 2T1R2L mode from the testing at $\frac{r}{r_c} = 0$, the combustion is not taking place at a node line, so although it is possible the mode could exist, it is improbable.

Additional points of discrete amplitudes can be seen in the stability maps for transducers P2 and P4, shown in Figure 4.23 and Figure 4.24, respectively. The point in the upper right corner of the transducer P2 stability map corresponds to Test 4.0 SP 11. The point from the transducer P4 stability map is Test 4.5 SP 8. The properties for these two setpoints are provided in Table 4.14. Phase and amplitude analysis indicates the points are 1T1R2L modes, similar to Test 3.0 SP 13. Interestingly, the phase data from Test 4.0 SP 11 is exactly the same as the phase data from Test 3.5 SP 12, but different modes were determined for each. The discrepancy is based on reasoning of the frequency and speed of sound. Progressing from SP 4 from the preliminary testing to Test 3.0 SP 13 to Test 4.0 SP 11, the frequency changes from 5.1 kHz to 5.4 kHz to 5.6 kHz. Meanwhile, the estimated speed of sound increases from 425 m/s to 436 m/s to 466 m/s. For Test 3.5 SP 12, the speed of sound increases to 5.8 kHz, but the estimated speed of sound decreases to 447 m/s. Thus, a different instability mode is most likely present.

Table 4.14: Additional Setpoint Properties at $\frac{r}{r_c}$=0.50

Test	SP#	Transducer	A_{p-p} [$\%P_c$]	f [kHz]	$\dot{m}_{ox}$ [g/s]	$\dot{m}_f$ [g/s]
4.0	11	P2	1.62	5.6	1.1125	0.2595
4.5	8	P4	1.01	5.5	1.0034	0.2911

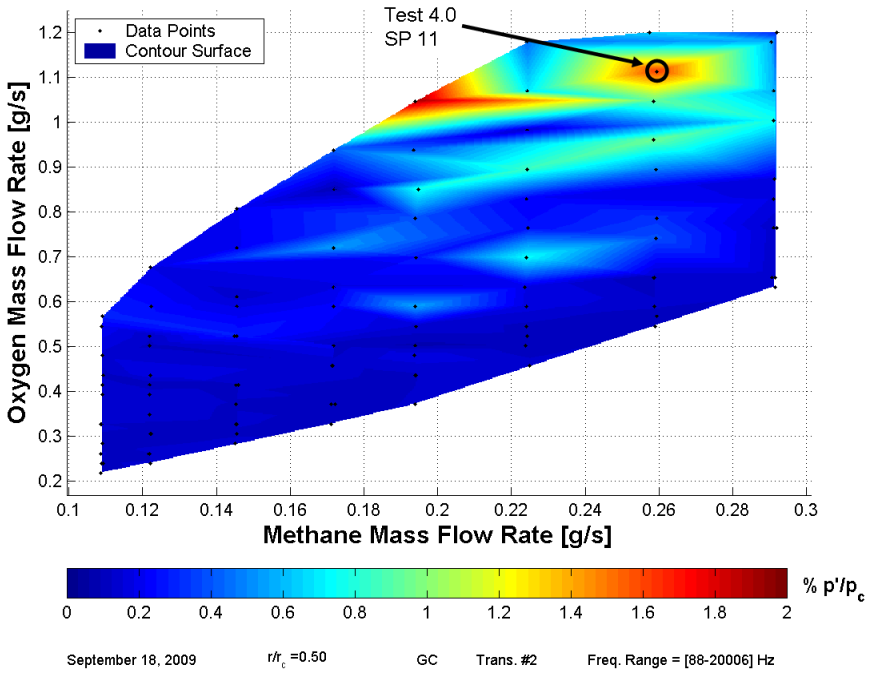

Figure 4.23: $\frac{r}{r_c}$=0.50 Surface Plot Transducer P2

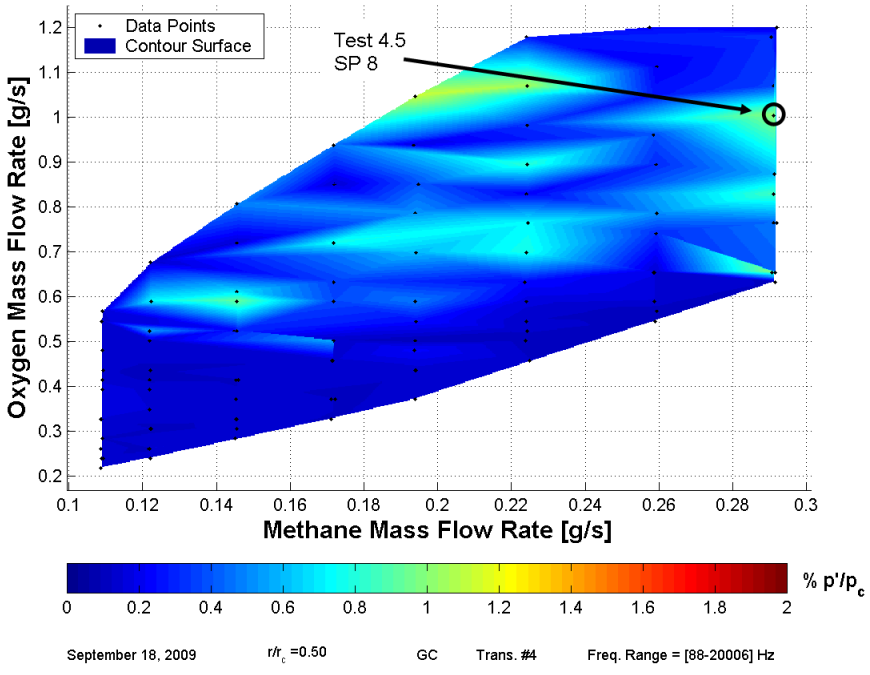

Figure 4.24: $\frac{r}{r_c}$=0.50 Surface Plot Transducer P4

Continuing with the analysis of the speeds of sound, the estimations of the average speed of sounds for these analyzed setpoints are shown in Table 4.15. They correlate well with the calculated values, with less than 11% relative error for each case. The average speed of sound appears to stay in a specific range, from approximately 430 m/s to 470 m/s, similar to the results from Section 4.3.1 and Section 4.3.2. Unlike the centered injector location where the estimated speeds of sound are higher than the calculated values, these estimated speeds of sound are consistently low, a result of lower measured temperatures. Judging from the velocity profiles presented in Section 1.2, the radial modes from the centered testing push the hot gases toward the wall, whereas the combined modes keep the hot gases in the center of the chamber.

Table 4.15: Speed of Sound Relative Error at $\frac{r}{r_c}$=0.50

Test	SP#	a_{calc} [m/s]	a_{est} [m/s]	% e_{rel}
3.0	13	468	435	6.8
3.5	10	508	471	7.3
3.5	12	404	447	10.7
4.0	11	487	466	4.2
4.5	8	479	458	4.4

4.3.4 Results at Injector Location $\frac{r}{r_c} = 75\%$

The next step was to test at the 75 percent of chamber radius location, where the injector is placed approximately 19 mm from the chamber wall. The objective of this injector position was to excite tangential instability modes, specifically the 1T mode. Similar to the $\frac{r}{r_c}$=0.0 position, one test was not able to be completed. Test 2.0

was attempted multiple times, but it consistently had flame blowout about midway through the test. The stability map for transducer P1 is shown in Figure 4.25. The large oval indicates where data was not acquired due to flame blowout. The areas of high amplitudes occur in two distinct locations on the map: in the lean region at the lower fuel flow rates and in the slightly rich region at the higher fuel flow rates. The stability maps from transducers P6, P7, and P8 are similar in this regard, and will not be shown. The properties of the analyzed setpoints are displayed in Table 4.16, and the phase properties are listed in Table 4.17.

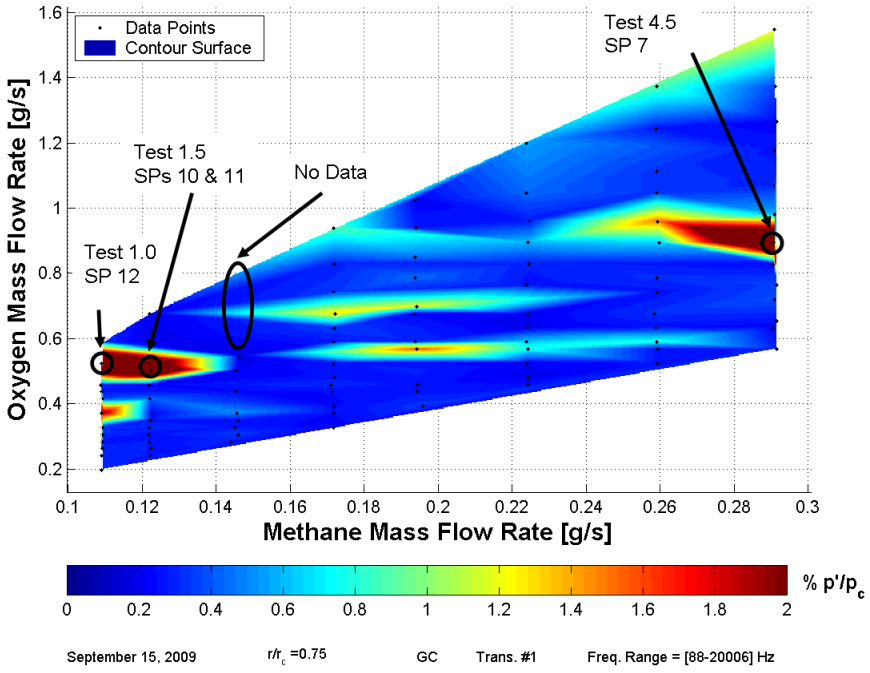

Figure 4.25: $\frac{r}{r_c}$=0.75 Surface Plot Transducer P1

The highest peak-to-peak amplitude was 3.5% of chamber pressure, which occurred at Test 1.0 SP 12. Initially, this mode appears to be a 2T2L mode based on the phase and amplitude analysis. However, at the recorded frequency, a speed of sound less than that of ambient conditions would be required. While a 1T1R2L

Table 4.16: Setpoint Properties at $\frac{r}{r_c}$=0.75 from P1 Stability Map

Test	SP	A_{p-p} [%P_c]	f [kHz]	$\dot{m}_{ox}$ [g/s]	$\dot{m}_f$ [g/s]
1.0	12	3.52	2.4	0.5235	0.1089
1.5	10	2.62	2.4	0.5235	0.1217
1.5	11	3.20	2.4	0.5017	0.1222
4.5	7	3.29	2.4	0.8943	0.2907

Table 4.17: Phase Relationships at $\frac{r}{r_c}$=0.75 from P1 Stability Map

Test	SP	Transducer	P1	P2	P4	P6	P7	P8	Mode
1.0	12	$\Delta\phi$	–	-180°	-180°	-180°	180°	-180°	Undetermined
1.5	10	$\Delta\phi$	–	180°	0°	-180°	180°	0°	2T
1.5	11	$\Delta\phi$	–	-180°	-180°	-180°	180°	0°	2T
4.5	7	$\Delta\phi$	–	-180°	-180°	-180°	-180°	0°	2T

mode is also possible, this mode is of a higher order than the 2T2L mode, which would require an even lower speed of sound. The low frequency limits the number of potential mode shapes, and the only possible ones remaining are either a 2T mode or a 1T2L mode. Both transducers P6 and P8 are 180° out-of-phase with P1, meaning both modes would be eliminated. Truthfully, this mode is undeterminable, but for the speed of sound analysis, it will be treated as a 2T mode.

The second point of relatively high amplitude from the transducer P1 stability map occurred at Test 4.5 SP 7. The phase relationships of this setpoint indicate a 2T mode. This mode is expected when the injector is placed close to the chamber wall. The same mode was present at Test 1.5 SP 10 and SP 11, at mass flow rates of $\dot{m}_{ox}$=0.5235 g/s and $\dot{m}_f$=0.1217 g/s for the former and $\dot{m}_{ox}$=0.5017 g/s and

$\dot{m}_f$=0.1222 g/s for the latter. The signal from transducer P4 is small signifying a close proximity to a node line. Looking at all of the setpoints with a 2T mode, transducers P1 and P4 change from being in phase to antiphase. A minor change in the location of the node lines causes this discrepancy, but the mode remains the same. Comparing these three points with the previous unknown mode, the frequencies are the same, and the amplitudes are on the same order at 2.5%-3.5%. A visualization of the 2T mode from these setpoints is shown in Figure 4.26.

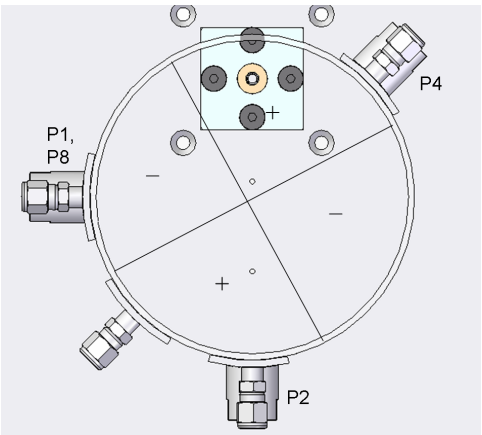

Figure 4.26: Visualization of 2T Mode from Various Setpoints

The stability map from transducer P4, shown in Figure 4.27, has areas of higher amplitudes in the central region of the test matrix. The conditions of the analyzed setpoints are given in Table 4.18. Two of these points, Test 3.5 SP 8 and Test 3.5 SP 11, are similar in amplitude and frequency. The phase differences for the analyzed setpoints are given in Table 4.19. The transducers around the chamber circumference for both of these flow conditions indicate a radial mode. Since transducer P7 is in antiphase with transducers P2 and P6, the radial mode must be second order. A

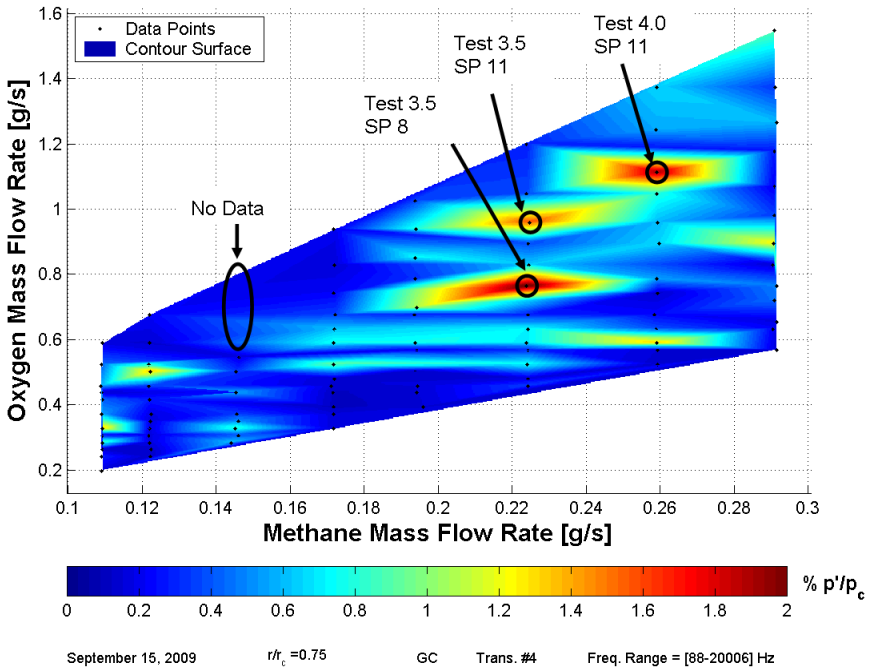

Figure 4.27: $\frac{r}{r_c}$=0.75 Surface Plot Transducer P4

Table 4.18: Setpoint Properties at $\frac{r}{r_c}$=0.75 from P4 Stability Map

Test	SP	A_{p-p} [$\%P_c$]	f [kHz]	$\dot{m}_{ox}$ [g/s]	$\dot{m}_f$ [g/s]
3.5	8	2.04	6.0	0.7635	0.2239
3.5	11	1.58	6.0	0.9598	0.2247
4.0	11	1.90	6.0	1.1125	0.2590

Table 4.19: Phase Relationships at $\frac{r}{r_c}$=0.75 from P4 Stability Map

Test	SP	Transducer	P1	P2	P4	P6	P7	P8	Mode
3.5	8	$\Delta\phi$	–	0°	0°	0°	-180°	180°	2R2L
3.5	11	$\Delta\phi$	–	0°	0°	0°	-180°	180°	2R2L
4.0	11	$\Delta\phi$	–	180°	0°	0°	0°	0°	2T1R

second radial mode has never been detected in this experiment. A first radial mode has been present in previous experimentation at a location close to the wall. Since a radial mode has an alternating antinode at the chamber center and chamber wall, it is possible to have a radial mode at this injector location. The 2R mode is a rather high-order mode, but the higher frequencies dictate that higher-order modes are present. A 2R2L mode is shown in Figure 4.28.

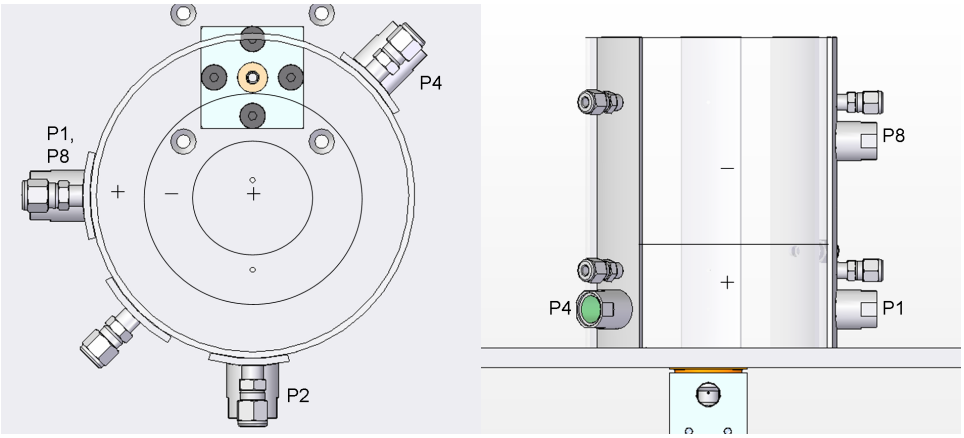

Figure 4.28: Visualization of 2R2L Mode from Test 3.5 SPs 8 and 11

The last setpoint analyzed based on this stability map is at Test 4.0 SP 11. It has a relatively high amplitude of 1.9% of chamber pressure. The phase difference between transducers P1 and P2 denotes a tangential node line between them. The phase difference between P1 and P7 indicates a radial node line. A second tangential node line has to be present to satisfy the phase difference between P1 and P6. The orientation of the two tangential nodes can be placed to correctly match the relative phase of P4 to P1. The 2T1R mode is similar to a previously determined mode. Original work by Cavitt [16] saw a possible 2T1R mode, but Byrd [18] recreated the work

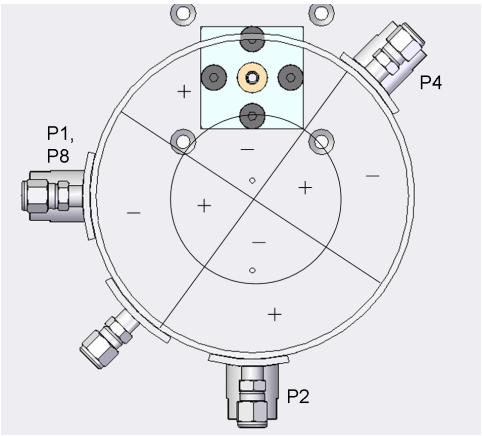

Figure 4.29: Visualization of 2T1R mode from Test 4.0 SP 11

and determined a 1T1R mode was more likely at that condition. A representation of the 2T1R mode is shown in Figure 4.29.

The transducer P2 stability map, shown in Figure 4.30, introduces another point of interest. Test 4.0 SP 3, which corresponds to the scaled fuel and oxidizer velocities, has a 1.7% P_c amplitude at 5.1 kHz. The setpoint properties are given in Table 4.20, and the phase relationships are given in Table 4.21. Analysis implies a 1T1R2L mode at this setpoint. The same mode was seen at the same frequency during preliminary testing, as opposed to the higher frequencies seen at the $\frac{r}{r_c}$=0.50 injector position. The lower frequency is a result of the lower speed of sound in the chamber when the injector is placed closer to the wall. The likeness of this mode is provided in Figure 4.31. As seen by the mode determination of various setpoints with relatively high amplitudes, tangential modes are most likely to occur when the injector is placed closer to the wall. For the current and previous research, the second

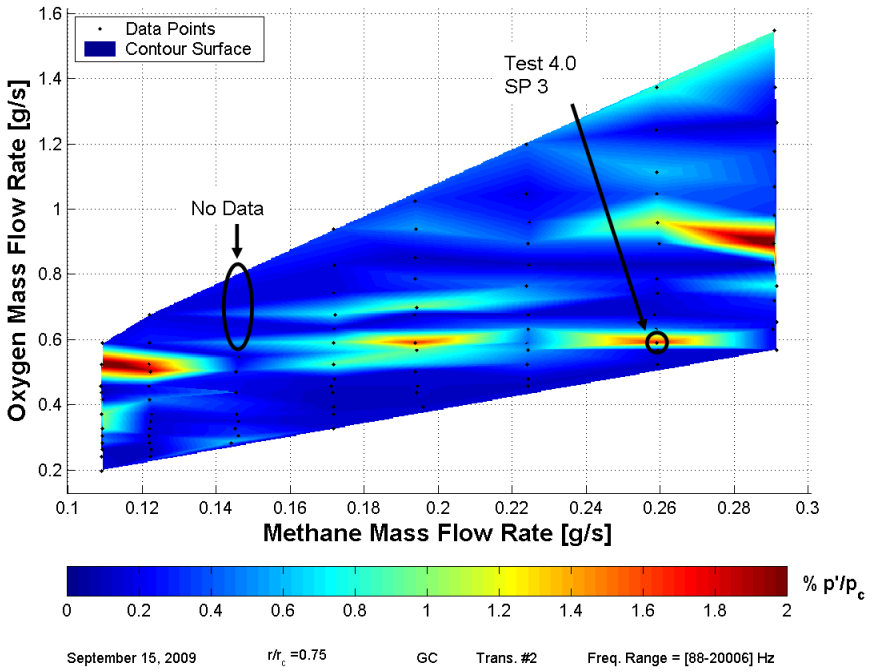

Figure 4.30: Stability Map for Transducer P2 at $\frac{r}{r_c}$=0.75

Table 4.20: Setpoint Properties at $\frac{r}{r_c}$=0.75 from P2 Stability Map

Test	SP	A_{p-p} [$\%P_c$]	f [kHz]	$\dot{m}_{ox}$ [g/s]	$\dot{m}_f$ [g/s]
4.0	3	1.72	5.1	0.5890	0.2591

Table 4.21: Phase Relationship at $\frac{r}{r_c}$=0.75 from P2 Stability Map

Test	SP	Transducer	P1	P2	P4	P6	P7	P8	Mode
4.0	3	$\Delta\phi$	–	180°	180°	-180°	0°	180°	1T1R2L

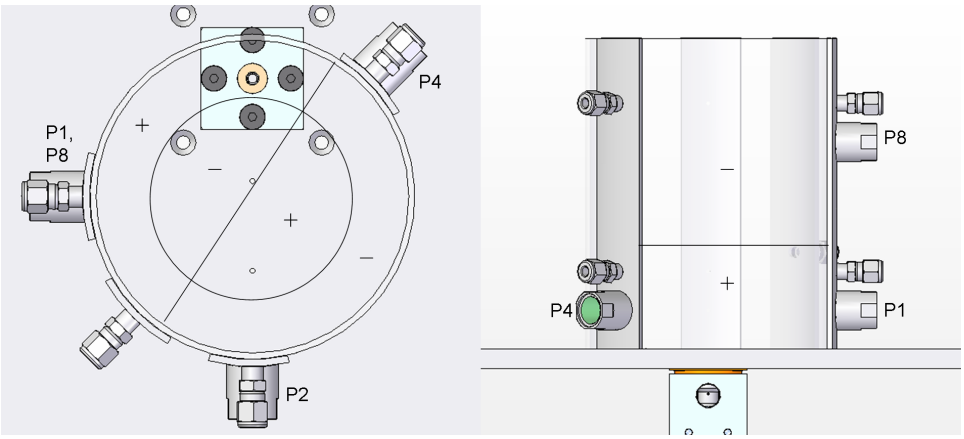

Figure 4.31: Visualization of 1T1R2L Mode from Test 4.0 SP 3

tangential mode was the most common. Radial and combined transverse modes were also present, but they were not as common.

The speed of sound approximations for the $\frac{r}{r_c}$=0.75 injector location are provided in Table 4.22. The calculated and estimated speeds of sound are lower for this injector location than the previous two locations. The placement of the injector close to the chamber wall allows a larger portion of the chamber to be filled with entrained air, lowering the effective speed of sound. Similar to the $\frac{r}{r_c}$=0.0 testing, the estimated speeds of sound are overestimated compared to the calculated values. Although they are consistently high, they are still within 11%, except for one outlier that is approximately 18%. A few of the higher values are probably a result of one particular thermocouple, T5, that measures a considerably higher temperature than the rest. This thermocouple is located almost directly above the flame at this position. It can be argued that this temperature does not represent the temperature of the chamber—or at least the temperature of the plane where the instability takes place—and can be

Table 4.22: Speed of Sound Relative Error at $\frac{r}{r_c}$=0.75

Test	SP#	a_{calc} [m/s]	a_{est} [m/s]	% e_{rel}
1.0	12	386	405	5.0
1.5	10	381	385	1.1
1.5	11	382	388	1.5
3.5	8	403	446	10.6
3.5	11	402	435	8.3
4.0	3	441	481	9.1
4.0	11	439	452	2.9
4.5	7	393	465	18.3

excluded. Recalculating the four estimates with relative errors above 8% results in an adjusted speed of sound of 383 m/s, 395 m/s, 406 m/s, and 421 m/s for Test 3.5 SP 8, Test 3.5 SP 11, Test 4.0 SP 3, and Test 4.5 SP 7, respectively. The adjusted relative errors are 4.8%, 1.8%, 8.0%, and 7.2%, respectively. The adjustment improved the relative error for each of the setpoints.

4.3.5 Scaling Parameter Correlation to Instability

Since scaling is an important part of this experiment, the instabilities must be analyzed in terms of those scaling parameters. Figure 4.32 shows a stability map from the $\frac{r}{r_c}$=0.75 testing. The map combines the highest amplitudes from each transducer. Since the scaling parameters remain constant versus the OF ratio, the map plots the OF ratio against the total mass flow rate. The different scaling parameters tested in this experiment are shown on the map. Each line represents the design scaling parameter versus the total mass flow rate. As observed from the map, instabilities did not occur consistently with any particular scaling parameter. However, unstable

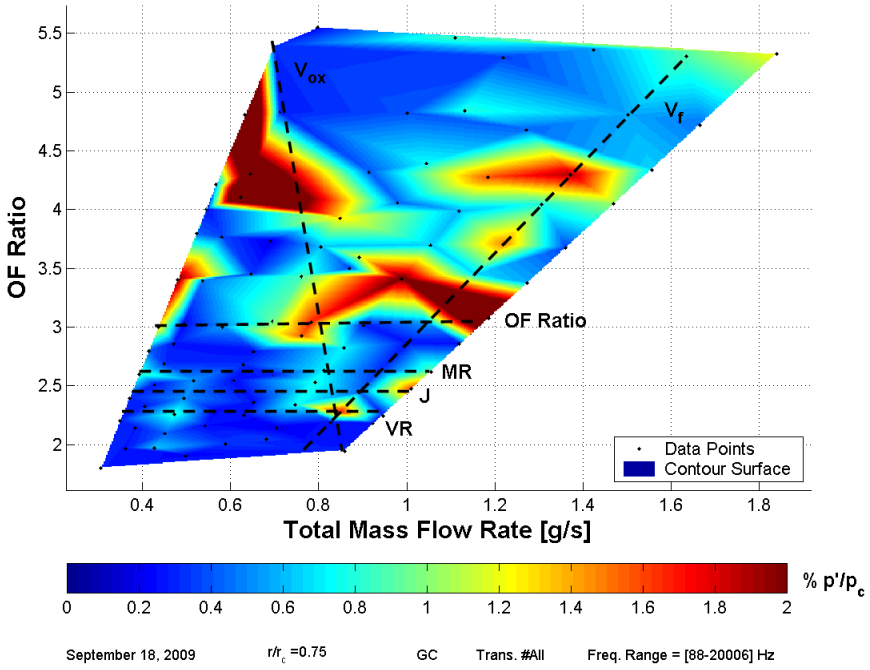

Figure 4.32: Stability Map Showing Scaling Parameters

regions are closest to the design oxygen and methane exit velocities. In fact, the point that simultaneously matches both velocities had a relatively high instability. Relatively high amplitudes are also present where the oxygen exit velocity and OF ratio are matched and where the methane exit velocity and OF ratio are matched. If either of these design points—whether one exit velocity and the OF ratio or both exit velocities—are the proper scaled flow conditions, combustion instability is likely to be seen in the full-scale engine using this injector.

4.4 Chemiluminescence Imaging Analysis

CH* chemiluminescence imaging at a high frame rate provided an interesting perspective of the combustion instability phenomenon. Imaging performed during

the preliminary testing showed clear differences in the flame structure; however, the images were limited in the amount of information they gave due to single phase-synchronization and erratic exposure time. The analysis done in this section looks at the effect of the emissions with respect to classical aspects of high-frequency combustion instability.

4.4.1 Core Flame Structure Changes

The structure of a flame is usually affected by combustion instability. The most obvious change of the flame structure that occurred during this research, mentioned in Section 4.3.1, is flame liftoff that is seen at each setpoint with high-amplitude pressure oscillations. Under stable conditions the flame is attached to the injector lip, and the primary combustion—indicated by the CH^* chemiluminescence—occurs along the fuel-oxidizer interface as expected. When the combustion zone lifts off the injector, the interface shifts from the mixing region parallel to the flow to a finite distance above the injector exit where the combustion becomes more turbulent.

Two setpoints from one test will be examined more closely. The first is a stable flame from early in the test, and the second is an unstable flame from later in the same test after the combustion zone had lifted off the injector. The properties from both of these setpoints are listed in Table 4.23. The stable flame is shown in Figure 4.33. This image is an overlay of two concurrently acquired images: a CH^* chemiluminescence image over a regular high-speed image without a filter that has been converted to a blue color scale. The original unfiltered and filtered images are provided for comparison. The composite image shows the region between where the

Table 4.23: Stable and Unstable Flame Properties

Test	SP#	Transducer	$\dot{m}_{ox}$ [g/s]	$\dot{m}_f$ [g/s]	A_{p-p} [$\%P_c$]	f [kHz]	Mode
3.0	1	P1	0.3926	0.1959	0.33	0.3	-
3.0	7	P2	0.5890	0.1938	1.67	10.3	Unknown
1.5	10	P1	0.5235	0.1217	2.62	2.4	2T

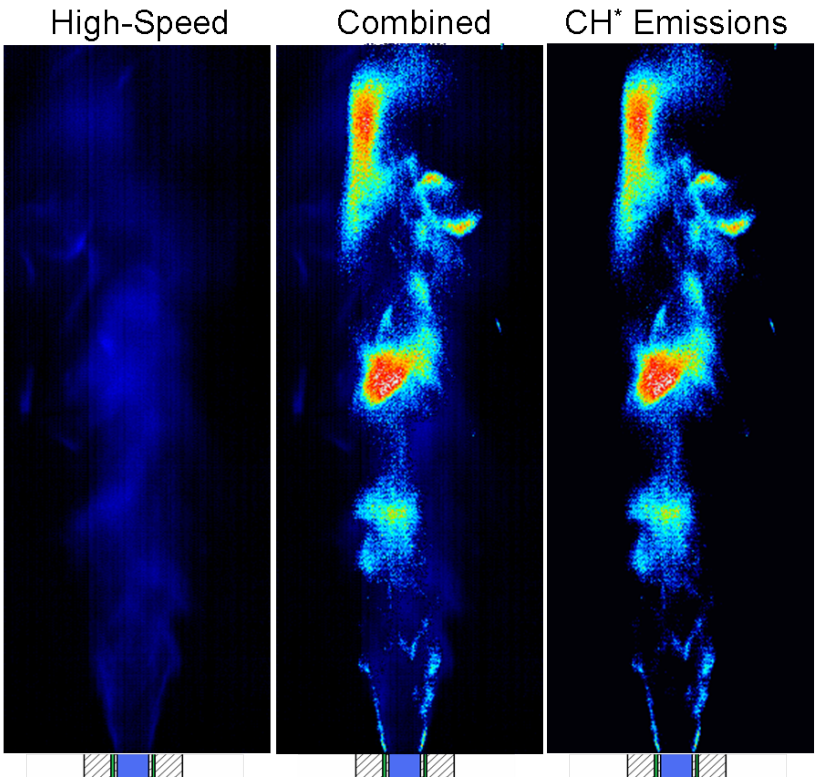

Figure 4.33: Visible and CH* Emissions of a Stable Flame from Test 3.0 SP 1

fuel and oxidizer are ejected as being the primary combustion zone with secondary combustion occurring farther downstream.

Figure 4.34 shows a similar overlay of an unstable flame, which shows the lifted combustion zone. Obviously, this region is far more intense than the interface from the

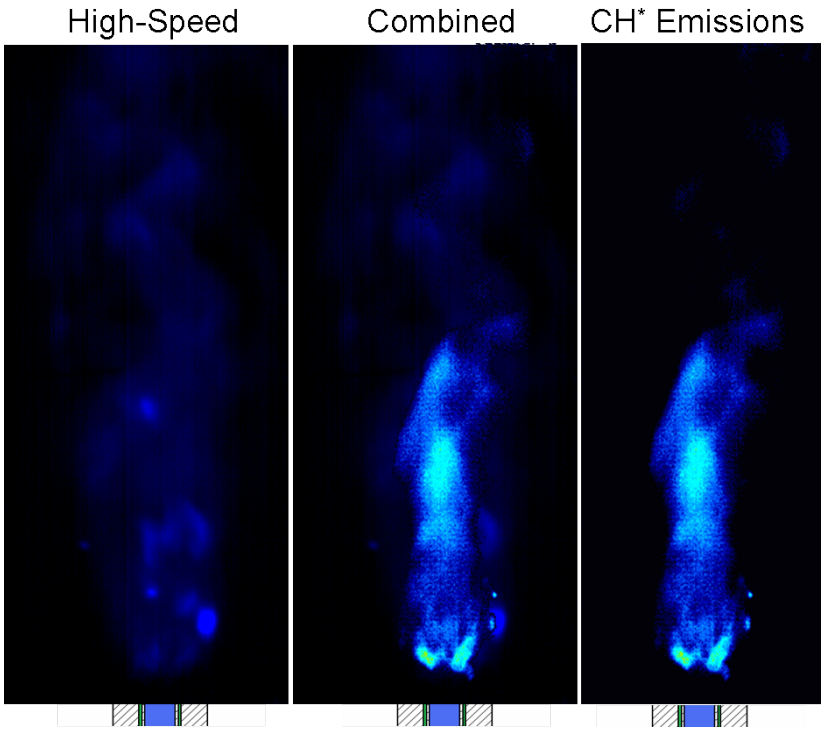

Figure 4.34: Images of an Unstable Flame from Test 3.0 SP 7

stable flame. The region in the unstable flame where chemiluminescence is emitted is much shorter than the actual flame. During unstable combustion the mixing between the fuel and oxidizer is enhanced, causing more complete combustion closer to the injector face. Thus, the chemical reactions required to create chemiluminescence does not occur farther downstream during unstable combustion as it does during stable combustion.

Additionally, high-speed imaging showed that the flame would "pulse" due to vibrations in the propellant feed lines. When the flame was pulsing, the flame would first appear to not exist. The flame would then "catch" near the injector and begin to grow. It would eventually detach, and the top part would finish burning. The flame would then regenerate at the base of the combustion zone, and the sequence would

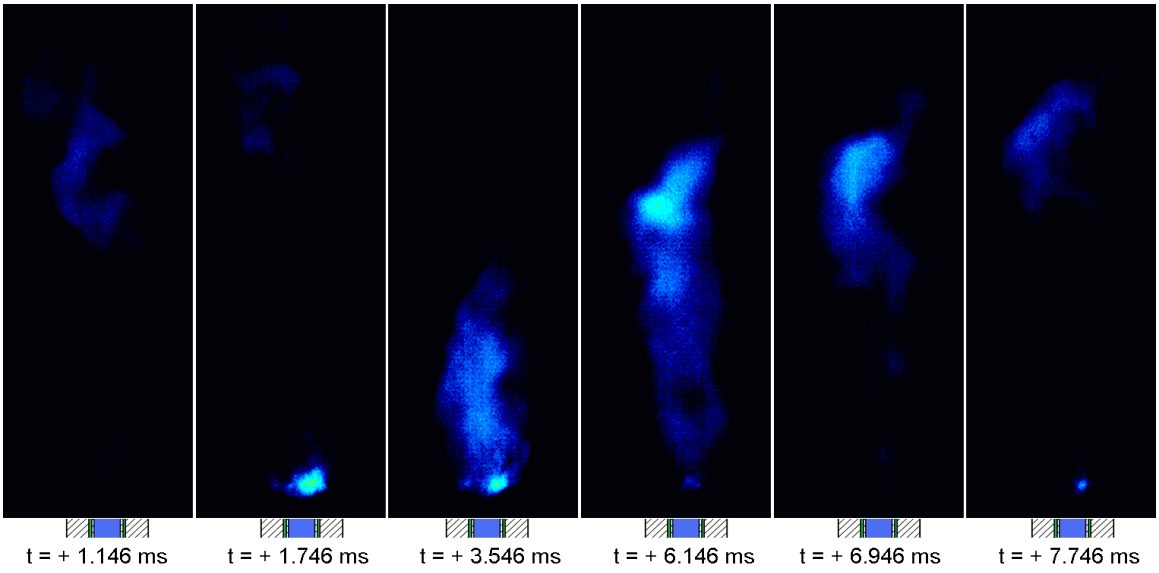

Figure 4.35: Phases of Pulsing Flame from Test 1.5 SP 10

continue. A sequence of images shown in Figure 4.35 shows the different phases of the pulsing flame just described. The image is similar to the image of the vibrating flame shown in Figure 1.6. The properties from this setpoint are listed in Table 4.23. The associated time was taken from the time stamp from each image to indicate the time scale of the process. The period is estimated to be about 6.6 ms, resulting in a frequency of approximately 150 Hz.

4.4.2 Combustion Instability and Heat Release

One aspect of combustion instability that is widely known is the increase of localized heat release. As mentioned previously the heat release must be in-phase with the pressure oscillations for combustion instability to sustain itself. A phase-locked image sequence of the 1R mode from injector location $\frac{r}{r_c}$=0.0 is shown in Figure 4.36. As seen in the figure, the primary combustion zone occurs slightly downstream of

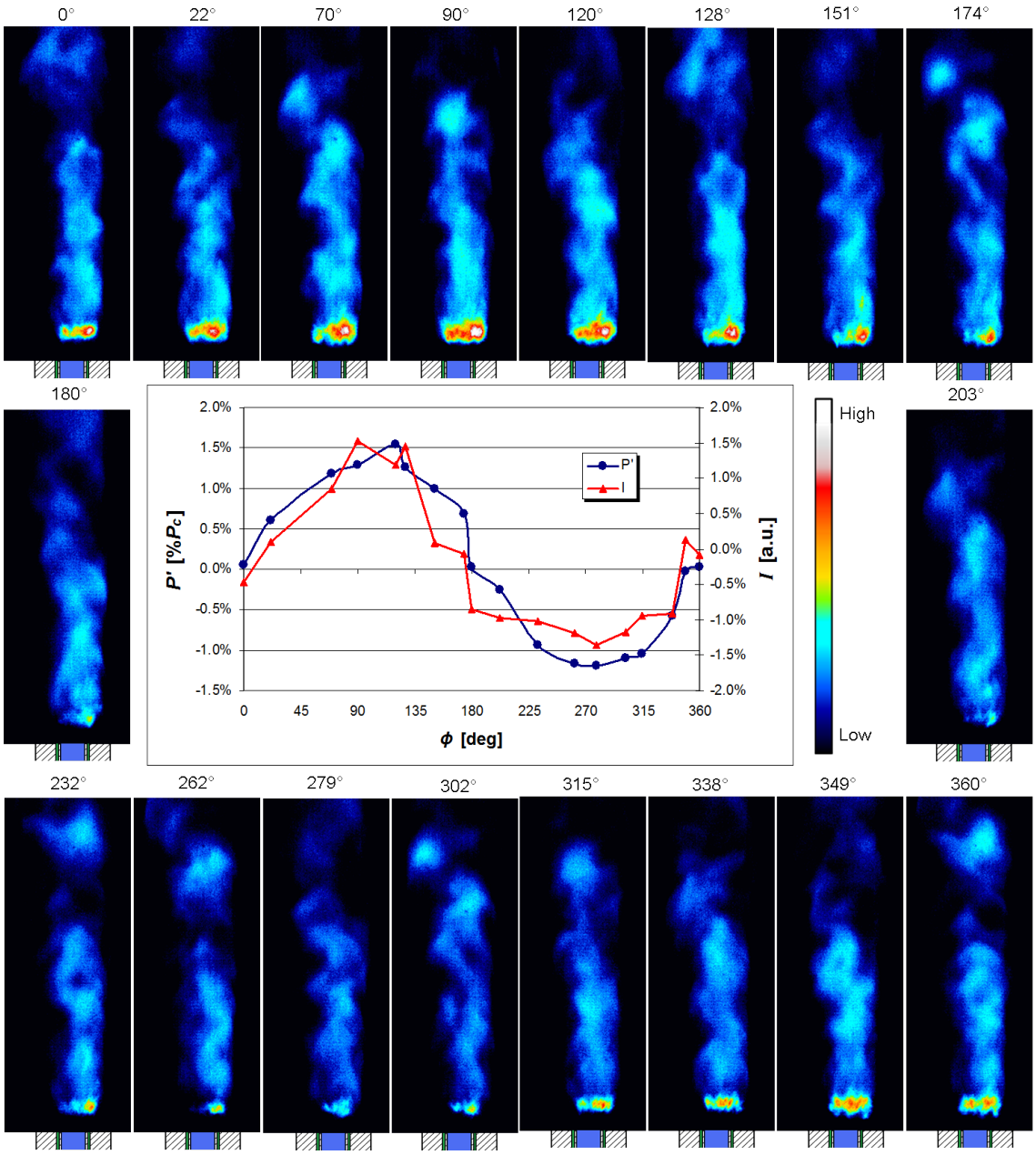

Figure 4.36: CH* Chemiluminescence from Test 2.0 SP 11

the injector exit in a localized area. The combustion zone liftoff is estimated to be 4.1 mm from the injector face. Qualitatively, the intensity of the combustion zone increases as the pressure increases and decreases as the pressure approaches a minimum. In order to quantify the intensity trace, the number of pixels with intensity

values above 150 was calculated for each image. These values were normalized to match the dynamic pressure scale. The two curves show a good relationship. Since CH^* emissions correlate with heat release, these images satisfy Rayleigh's criterion.

4.5 Feed System Response

Five of the setpoints tested were chosen for a repeat test to measure possible feed line oscillations. For these tests, OH^* chemiluminescence instead of CH^* chemiluminescence was imaged for feasibility of future testing. The points selected are described in Table 4.1. The first point is setpoint 7 from Test 3.0. This point was chosen because it matches the oxygen exit velocity and OF ratio from the original LOX/LCH_4 design. Another design point that was considered interesting is setpoint 3 from Test 4.0, which matches both the methane and oxygen design velocities. Both of these flow conditions are considered the primary scaled flow conditions that best simulate the full-scale flow conditions. The other three points saw either high instabilities or problems during testing. Test 4.0 SP 13 would not blow out, but the desired oxygen flow rate was unable to be reached. The flow rate was consistently low. This problem was believed to be caused by pressure oscillations that would reach the mass flow controller, which continuously changed the downstream pressure. The last two setpoints, setpoint 7 from Test 4.5 and setpoint 12 from Test 1.0, were chosen due to relatively high amplitude 2T modes that occurred during testing. It was believed feed line coupling could occur at higher chamber amplitudes.

Two transducers from the chamber, transducers P2 and P6, were moved to the two feed lines for this testing. The other transducers were used in their normal

configuration. The results of the testing, taken from the chamber pressure transducers, are shown in Table 4.24. First, only the general repeatability will be analyzed. The highest amplitude occurred for Test 4.5 SP 7. Comparing with the initial test at this setpoint, the amplitudes are nearly the same, 3.14% to 3.29%, and both had a 2T mode. Test 1.0 SP 12 also stayed relatively consistent with the same 2T mode at a slightly lower amplitude, from 3.52% to 2.92%. Test 3.0 SP 7, the point that was scaled to match the oxygen exit velocity and OF ratio, saw a 2T mode. The primary frequency at this point is different from the same point during the initial testing where a 10.3 kHz frequency was present. The amplitude from the repeated test is 1.23% of chamber pressure, which is similar to the 1.69% P_c amplitude measured previously. The other scaled point, where the fuel and oxidizer design velocities were matched, was stable, with a low peak amplitude well below 1% at a frequency well below 1.0 kHz. This same point saw a 1T1R2L mode at 5.1 kHz with an amplitude of 1.72% P_c in the original testing. The setpoint that could not be reached in the previous testing, Test 4.0 SP 13, could also not be reached for this test. Although the oxygen flow rate was less than desired, the data were recorded anyway. The mode

Table 4.24: Repeat Testing Results

Test	SP#	$\dot{m}_{ox}$ [g/s]	$\dot{m}_f$ [g/s]	A_{p-p} [%P_c]	f [kHz]	Mode	a_{est} [m/s]
3.0	7	0.6108	0.1937	1.23	2.6	2T	449
4.0	3	0.6326	0.2594	0.32	0.3	-	436
4.0	13	1.2652	0.2588	0.93	1.6	1T	396
4.5	7	0.8725	0.2910	3.14	2.3	2T	398
1.0	12	0.9380	0.2903	2.92	2.5	2T	423

was determined to be a 1T mode, although the amplitude is less than 1% of chamber pressure. The estimated speed of sound within the chamber stayed consistent with previous testing.

Overall, the repeated setpoints were somewhat consistent with the initial testing at those flow conditions. Two setpoints saw similar frequencies and amplitudes from the first testing, and another had the same problem in reaching the desired flow rates. The amplitude of one of the remaining setpoints was comparable to the original, but the frequency was much lower. The last setpoint went from being unstable to stable with a large decrease in the measured amplitude. These inconsistencies can be a result of the small time interval when the data is recorded. The frequencies and amplitudes might shift at these setpoints, but the time interval is too small to detect the shift.

FFTs of the transducers in the propellant feed lines show possible feed system coupling with the chamber dynamics. Each setpoint had a common frequency between each feed line and the chamber. Figure 4.37 shows FFTs from transducer P1 and the two propellant feed lines. The common frequency is 2.3 kHz, which is the frequency of the 2T mode. A smaller amplitude frequency of 3.5 kHz is also present in each of the feed lines. It could not be determined what specific mode occurs at this frequency, but it closely resembles the natural frequency of the LOX post, which is estimated to be 3.3 kHz. These common frequencies are a possible indication of feed line coupling.

It was noticed that an audible noise came from the injector at low fuel flow rates. Cold-flow testing was performed to determine the frequency of this noise. A standard microphone was used to measure the sound. Methane was flowed at the

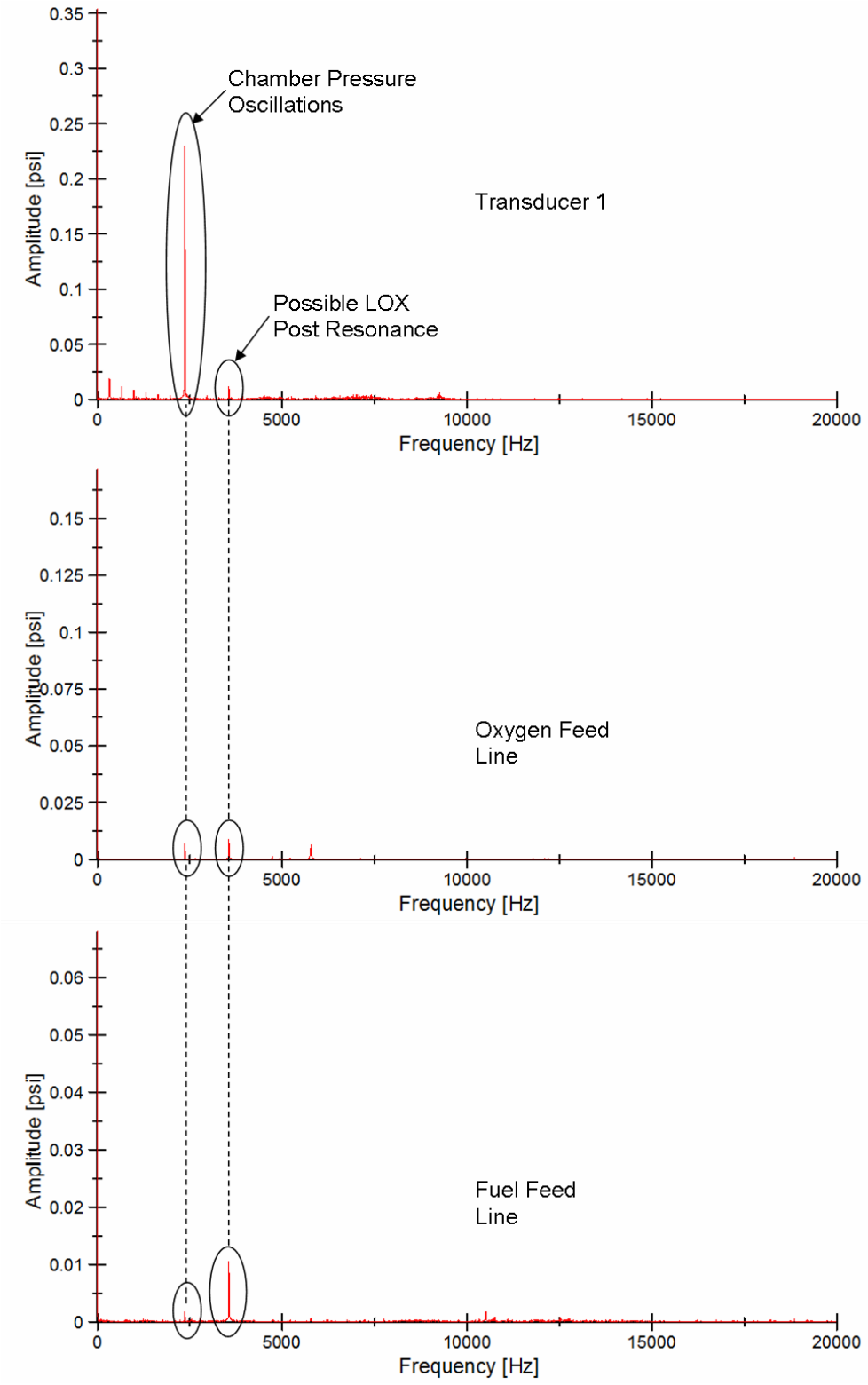

Figure 4.37: Possible Chamber and Feed System Coupling

flow rates associated with Tests 1.0, 1.5, and 2.0. An FFT of no-flow and cold-flow testing of the Test 1.0 flow rate is shown in Figure 4.38, which shows the presence of the first three harmonics of an unknown natural frequency where the 318 Hz second harmonic is the dominant of the three. It is believed that this response could be the cause of the two tests that could not be completed due to flame blowout. This frequency was seen at various setpoints, usually when the combustion was relatively stable and no other high-amplitude frequencies were present. It was also the peak frequency in the repeated test of Test 4.0 SP 3. It is interesting to note that the primary frequency of 155 Hz matches rather well with the reported flame pulsing

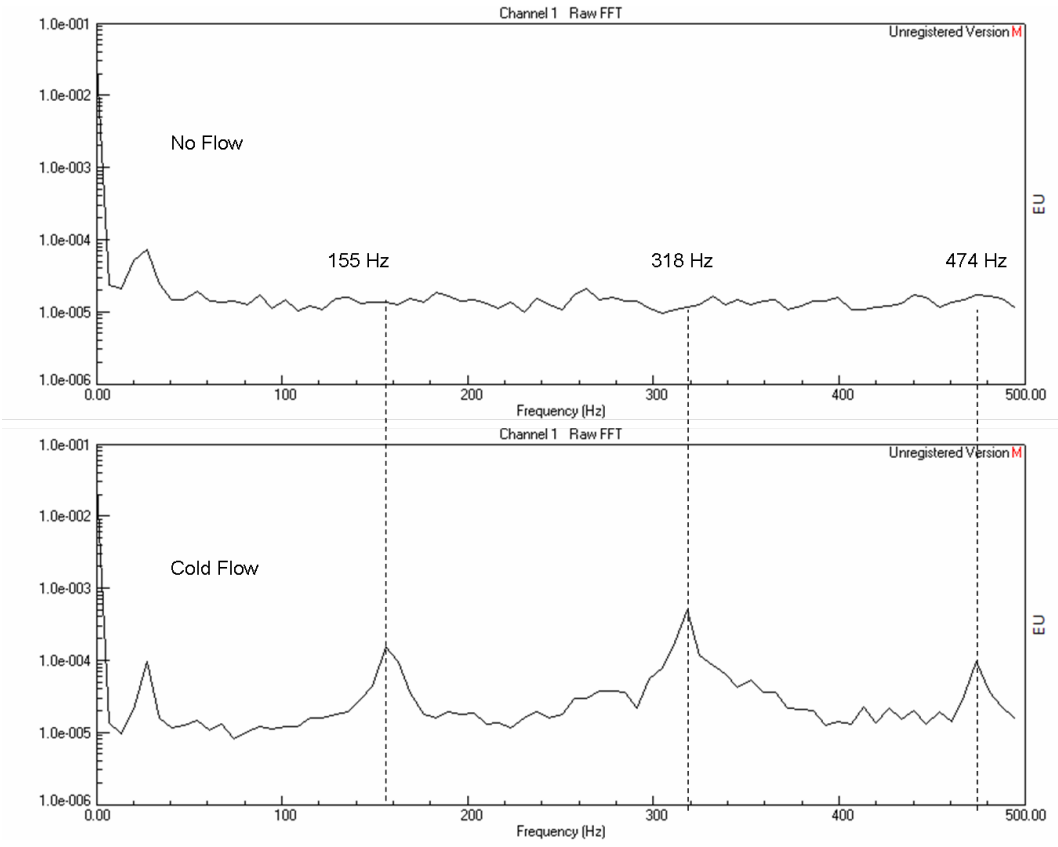

Figure 4.38: Cold-Flow Harmonics at Low Fuel Flow Rates

frequency from Section 4.4.1. It is likely the flame pulsing was the cause of the flame blowout.

As mentioned before OH* chemiluminescence was imaged for this set of tests to determine if it was feasible. Since the light was expected to be much more faint than the CH* chemiluminescence, the sample rate was lowered to 1000 frames per second, and the exposure time was set to 997 μs. Figure 4.39 shows two sample OH* images from the first repeat test—the Test 3.0 SP 7 flow rates—as well as a sample CH* image from the first test at these conditions. The images cannot be phase-locked due to the high exposure time, but they provide interesting information. Obviously, the image is much brighter than the CH* imaging, and it shows the flame bending as a result of the

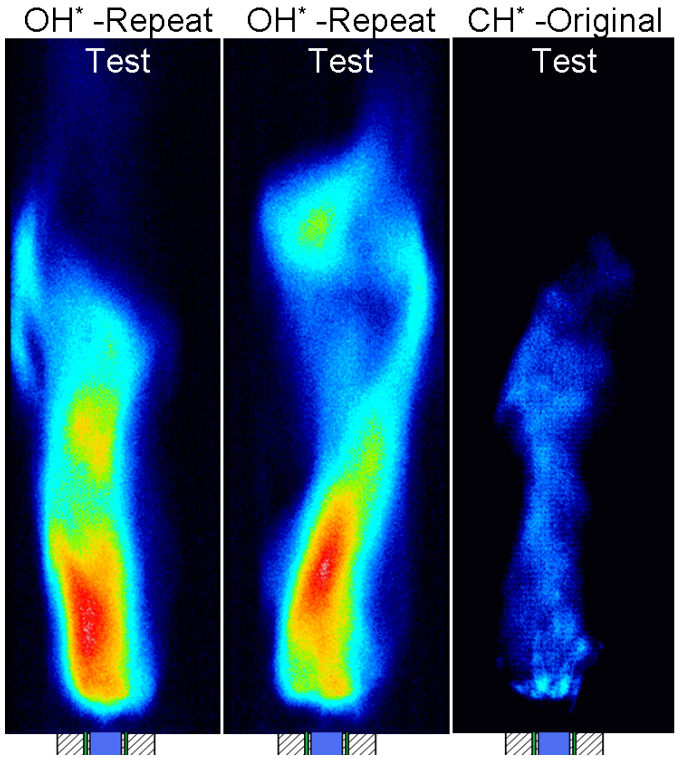

Figure 4.39: OH* and CH* Chemiluminescence from Test 3.0 SP 7

pressure oscillations in the chamber. The OH^* images tend to show the movement of the flame better than the CH^* images. It has been shown that OH^* emissions can be imaged and would likely provide interesting results when compared with CH^* emissions. Both the feed line measurements and OH^* chemiluminescence emissions would provide additional interesting research for testing using this experiment.

CHAPTER 5

CONCLUSIONS

Science is always wrong, it never
solves a problem without creating ten more.

—George Bernard Shaw

5.1 Summary

This research intended to map the instabilities of an injector over a broad range of flow conditions that encompassed the nominal flow conditions. CH^* chemiluminescence emissions were imaged as a measurement of flame structure changes and heat release, an important parameter in sustained combustion instability. A few selected points of interest were tested again to evaluate the general repeatability of the results and to assess additional diagnostic capabilities. Additional diagnostics were implemented to prove they provided useful data in characterizing combustion instability.

A full-scale swirl-coaxial injector was designed based on the operating conditions of a Lunar Ascent Engine from the Constellation program. The injector was tested over a variety of mass flow rate conditions that matched scaling parameters from the full-scale design. It was placed in three positions in the chamber to try to

excite different types of instability modes. For each flow rate condition CH^* chemiluminescence was imaged to determine the change of heat release and flame structure. The instabilities determined from each injector location are listed below.

1. Injector Location $\frac{r}{r_c}$=0: A maximum amplitude of 2.21% P_c was achieved at this location. A 1R and a 1R2L mode were determined to be present, which was expected considering the injector was placed at the antinode of the radial mode.

2. Injector Location $\frac{r}{r_c}$=0.50: The maximum amplitude at this location was 2.01% of chamber pressure. Complex combined modes were present, including a 1T1R2L mode, 2T1R2L mode, and a possible 1T2L mode.

3. Injector Location $\frac{r}{r_c}$=0.75: 3.2% P_c was the highest peak-to-peak amplitude present at this location. The second tangential mode was the dominant mode at this injector position, which is expected when it is placed close to the chamber wall. A relatively high-order mode, a 2R2L mode, was determined to be present. Additional modes that were present were a 2T1R mode and a 1T1R2L mode.

The effective speed of sound was estimated using temperature measurements and calculated based on the frequency and instability mode. Both estimated and calculated values stayed in a reasonable range when considering the injector location. The measured temperatures were highest during the centered injector testing. The lowest temperatures were measured when the injector was closest to the wall. Comparisons between the estimated and calculated speeds of sound had a relative error

of below 15% for most of the points analyzed, although a couple were outside this value. The higher error was caused by higher temperature measurements from the thermocouples at the higher plane. Recalculating the speed of sound using only the lower thermocouples lowered the relative error.

Instabilities did not correlate with the velocity ratio, momentum ratio, or momentum flux ratio. The design exit velocities of both oxygen and methane were the most susceptible to combustion instability, although stable combustion was also seen when these parameters were matched. Matching either of the design velocities and the OF ratio also caused instabilities. Considering the two design flow conditions that would most likely be used saw combustion instability, it may be a problem under full-scale conditions.

CH^* chemiluminescence was shown to indicate heat release by following Rayleigh's criterion that states the heat release should be in phase with the pressure oscillations. Changes in flame structure were also evident, with a lifted combustion zone being the most prominent change. This lifted combustion zone was indicative of high-frequencies instabilities. Vibrations in the propellant feed line produced flame oscillations similar to what was described in the literature. Preliminary OH^* chemiluminescence showed promising results for future testing.

Repeat testing of a few selected flow conditions was performed to measure the propellant feed line dynamic pressure. In terms of general repeatability, similar amplitudes and frequencies were seen for some of the flow conditions, but different results were seen for the others. It is possible that the instability would change in frequency or amplitude, but the small time interval when the data were recorded

was not sufficient to see this shift. The repeat testing also showed that possible feed system coupling was present due to common frequencies in the chamber and each feed line. Additional cold-flow testing showed a low-frequency resonance from the fuel annulus that was the probable cause of flame blowout at low fuel flow rates that disallowed complete testing at those tests. The primary measured frequency was similar to the estimated frequency of the flame oscillations that was calculated based on CH^* chemiluminescence emissions.

5.2 Recommendations

Although this experiment is capable of evaluating injector responses, additional testing and research needs to be performed to better match full-scale conditions. One of the criteria, as mentioned previously, is matching the expected frequency of the first tangential mode. This frequency can be easily estimated using the geometry of the chamber and a chemical equilibrium program to determine the speed of sound inside the chamber. However, in an open combustion chamber the speed of sound varies with chamber size, most likely due to air entrainment. Therefore, hot-fire testing that takes detailed frequency and temperature data needs to be performed using different chamber sizes. This testing should provide an empirical method for scaling the chamber speed of sound. The effect of air entrainment can also be evaluated in conjunction with the different chamber sizes rather easily by adding a removable convergence section to the top of each chamber. Temperature and frequency data from both of the aforementioned tests can provide interesting results: change of speed of

sound with and without the convergence section, addition of a longitudinal mode with the convergence section, and change of instabilities due to air entrainment.

Matching the proper scaling conditions is necessary to achieve an adequate simulation of full-scale results. Unfortunately, scaling has proved to be quite difficult. Detailed testing should be performed that varies the diluent flow rates and propellant temperatures to match different flow rate conditions. For example, a test matrix can be formed that only matches one nominal flow rate. On one axis the mass percentage of diluent can be varied, and the temperature can be varied on the other. The effect of each on stability can be determined to aid in future scaling. The Rocketdyne shear-coaxial injector would be the best injector to use for this testing because it is the simplest and it has historical data that can be used for comparison.

As mentioned previously, the feed line pressure measurements showed interesting results in terms of possible feed line coupling. One improvement that should be made is the location of the fuel feed line pressure transducer. Currently, it is farther from the injector than desirable. Sufficient space exists in the injector housing where it can be implemented almost immediately before the gases exit the injector. Moving the transducer to this location would require a redesign of the injector face pressure transducer locations.

A couple of miscellaneous improvements that can be made would be to add a single-axis translation stage to the experiment and to measure the dynamic mass flow oscillations. The translation stage can be used to quickly determine the effect of the injector position on combustion instability. The mass flow controllers have an analog

measurement capability that can be used to measure the classical injector response in terms of mass flow oscillations and pressure oscillations.

5.3 Future Work

An additional study that would provide interesting and useful information would be to study the effect of the injector type on stability. Since the injector used in this experiment is capable of being used as a shear-coaxial, swirl-coaxial, and dual-swirl injector, it can be tested over the same flow conditions, but with a different configuration. Furthermore, the effect of the LOX post recess on stability can be scrutinized.

Rectangular chambers can be used in place of the cylindrical chambers. One advantage of the rectangular chamber is the removal of radial instability modes that would be present during unstable combustion. Removing one possible component of an instability would greatly improve mode determination. Implementing the high-frequency pressure transducers would be easier compared to the cylindrical chamber. It would also be easier to provide optical accessibility to the chamber.

One of the biggest advantages of using a laboratory-scale, low-pressure experiment is that many types of diagnostics, specifically optical diagnostics, can be implemented relatively inexpensively and safely in comparison to larger, high-pressure experiments. An optical diagnostic similar to that studied in this research that can be used is Laser Induced Fluorescence, or LIF. Shadowgraph and Schlieren images can also be implemented to give useful results. One interesting study involving the Schlieren technique would be to use a glass injector face and take top-down or bottom-

up images of the chamber volume to try to see spatial changes of density, which could yield a visual representation of the mode shape of the instability.

An additional capability that could provide useful results is to implement multiple injector elements to determine the effect injector interaction has on combustion instability. Heat flux gages and coaxial thermocouples can be added to measure heat flux to give a better indication of the energy lost through heat transfer through the chamber wall or the injector face.

APPENDICES

APPENDIX A

TEST PROCEDURES

Russian Methodology Test Procedure

Heated Fuel / Heated Oxidizer
Multiple High-Frequency Pressure Transducers
High-Speed Imaging

Date:_____
Red Team Members:_____
Propellants:_____
Injector:_____

Table 1. Experimental Mass Flow Settings and Ranges

Test #	Methane Mass Flow Rate [g/s]	Oxygen Mass Flow Rate [g/s]	Methane Temp. [C]	Oxygen Temp. [C]	Notes

High Frequency Measurements
Sampling Rate:_____
Number of Samples per Measurement:_____

Shawn Ikard: _____
John Brooks: _____
Brian Sweeney: _____
Dr. Moser: _____
Dr. Frederick: _____
Dr. Lineberry: _____
Tony Hall: _____ **(Test Engineer)**

Campus Police: (256) 824-6911

Rev17 – 9/7/09 – SI

Other operators or Red Team Members not shown on this document must be certified by the Test Engineer

Figure A.1: Page 1 of Experiment Procedures

Injector Manifold Assembly (follow these steps sequentially)

1. Assemble Injector Assembly as in Figure 1 with the following steps
   I. Place cover seal and heat proof lid onto case and secure with short head hex cap screws
   II. Place fire seal and fuel post into heat proof lid
   III. Place cover over fuel post and secure with hex screws
   IV. Insert Teflon seal, spacers, oxygen post, swirl nut, and press plate into holder
   V. Screw press nut into holder until tight
   VI. Place klingersil into case around fuel post
   VII. Place holder seal over holder
   VIII. Place klingersil and fuel sleeve into crevice in holder
   IX. Screw holder into case until tight
2. Slide case with brackets onto mounting plate with fuel inlet facing the fuel feed line
3. Attach case cooling lines
4. Push cover flush with plate and fasten with nuts (apply Fire Barrier silicone)
5. Place cover seal into case groove
6. Mount oxidizer collector onto the case with hex cap screws
7. Attach fuel line and oxidizer line to injector assembly

Test Stand Preparation

- ☐ Roll cart into test cell
- ☐ Attach pressurization air to actuated fire valve air manifold (plastic tubing)
- ☐ Attach the pressurization air to the compressor in the instrumentation room and make sure that the compressor is on auto compress
- ☐ Attach power to actuated fire valve control line
- ☐ Attach main air/oxygen line to the oxidizer fire valve
- ☐ Attach main fuel line to the fuel fire valve
- ☐ Attach fuel purge line to the fuel purge cross (see plumbing schematic appendix for fuel purge tee location)
- ☐ Attach oxidizer purge line to oxidizer purge tee (see plumbing schematic appendix for oxidizer purge tee location)
- ☐ Attach the methane drain line to the dome loader fuel vent line
- ☐ Close the water manifold valves
- ☐ Attach the water line from the instrumentation room to the quick disconnect fitting on the water manifold
- ☐ Ensure that all gates are unlocked and open for safety reasons

Leak Check

Cooling Lines

- ☐ Attach the cooling lines on the cart top to the dynamic pressure transducer cooling jacket
- ☐ Place the drainage line on the tee and the other end in the drain

Figure A.2: Page 2 of Experiment Procedures

- Open water main line in the instrumentation room
- Open the cooling jacket and injector assembly cooling line manifold valves
- Remove electrical tape from injector face
- Ensure that there is no leakage from the H_2O system
  - May wish to inspect injector cavity with flashlight
  - In the event of leakage, reassemble the manifold strictly adhering to the assembly instructions

Igniter Setup

- If using the igniter stand, attach igniter so that it is above the chamber
- Attach blue igniter ground to actuator grounding post
- Attach oxygen line to the igniter
- Attach hydrogen line to the igniter
- Attach red spark plug connection to the spark plug tip on the igniter
- Clamp grounding clamp [from igniter] to the copper plate behind the thrust stand
- Set the secondary oxygen needle valve to the correct setting (Default – 5)
- Set the secondary hydrogen needle valve to the correct setting (Default – 5)

Figure A.3: Page 3 of Experiment Procedures

Instrumentation

Attach the following:

	Description	DAQ Input Location
	Sensotec oxidizer collector static pressure transducer	A2
	Sensotec fuel collector static pressure transducer	A1
	Attach Honeywell (Serial # 1144300) pressure transducer to igniter, plug into DAQ	A3
	Assemble dynamic pressure transducers into cooling jackets on chamber, hook up power system, plug into DAQ See "Sensor Info and Locations v3.xls" for configurations	Un-powered BNC
	Oxygen K-type thermocouple (Marked A)	Thermocouple Input # 1
	Oxidizer Nitrogen K-type thermocouple (Marked B)	Thermocouple Input # 2
	Methane K-type thermocouple (Marked C)	Thermocouple Input # 3
	Fuel Nitrogen K-type thermocouple (Marked D)	Thermocouple Input # 4
	Fuel K-type thermocouple (Marked E)	Thermocouple Input # 5
	Oxidizer Collector K-type thermocouple	Thermocouple Input # 6
	Fuel Collector K-type thermocouple	Thermocouple Input # 7
	Ambient Air K-type thermocouple	Thermocouple Input # 8
	Chamber 1 K-type thermocouple	Thermocouple Input # 9
	Chamber 2 K-type thermocouple	Thermocouple Input # 10
	Chamber 3 K-type thermocouple	Thermocouple Input # 11
	Chamber 4 K-type thermocouple	Thermocouple Input # 12
	Chamber 5 K-type thermocouple	Thermocouple Input # 13
	Chamber 8 K-type thermocouple	Thermocouple Input # 14
	Chamber 9 K-type thermocouple	Thermocouple Input # 15
	PLC plug from electrical enclosure face (*For heater use*)	Un-powered BNC Ch. 8
	Plug in SCRs and Controllers on electrical enclosure face	

(see Figure 2 for further instrumentation location information)

- ☐ Plug in the color coded mass flow controller terminal block into the serial line (black-green-white wire). See Table 2 below.

Table 2. Mass Flow Controller Wiring

	Test Stand	Cart
Serial	Green	Purple
	Black	Yellow
	White	Red

- ☐ Turn on the Controller switch
- ☐ If using the heaters
  - Turn on the SCR switch
  - Input the desired set-points into Controllers
- ☐ Make sure mass flow controllers have the correct settings (gas type [ie. Oxygen→ O2], baud rate [Default – 2400], serial control, etc.) and ensure a set-point of "0"

Figure A.4: Page 4 of Experiment Procedures

- ☐ Set up mirror, if necessary, and position video camera on ground accordingly. Hook up RCA cables and power plug. If relevant, disable camera's Demo Mode.
- ☐ Ensure that the DAQ patches are correct in the instrumentation room, documented in "C:/Control Room Computer/Russian Methodology/Sensor Info and Locations v3.xls" on the control room computer

Miro 4 High-Speed Camera Setup

- ☐ Place high-speed camera into position and attach power cord
- ☐ Attach ethernet cable from camera to computer
- ☐ Attach BNC cable labeled "TRIG" to red wire labeled "Trigger"
- ☐ Attach green wire labeled "Ready" to un-powered BNC Ch. 8
- ☐ Press green power button on camera and open Phantom software
- ☐ Under the "Camera Options" set "Trigger" to "Falling Edge," "Ready sig. ends at" to "Trigger," and "Start in:" to "Wait pretrigger"
- ☐ Check "Restart Recording"
- ☐ Set "Image Range" to the desired range, where image "0" is the first image after trigger
- ☐ Under "Setup and Recording" set the desired exposure time and frame rate
- ☐ Cover lens and click "Current Session Reference" for exposure times less than 1 ms
- ☐ For exposure times greater than 1 ms, click "Options" and "Black Reference"
- ☐ Under "Setup and Recording" check "Cont. rec"
- ☐ Set "Cine file paths and save parameters" to the desired directory and use the symbol "@" to save files after acquisition (e.g. "Test1.0@2")
- ☐ Please note that some of the parameters above will need to change to synchronize the camera(s) differently

Redlake High-Speed Camera Setup

- ☐ Place high-speed camera into position and attach power cord
- ☐ Attach USB cable to camera and to computer
- ☐ Attach BNC cable labeled "TRIG" to camera BNC port labeled "TRIG IN"
- ☐ Attach camera BNC port labeled "SYNC OUT" to un-powered BNC Ch. 7
- ☐ Open MotionPro X Studio software
- ☐ Under the "Record" tab, set the rate to "External," Sync to "Pulse Low," and Trigger Configuration to "Edge Low"
- ☐ Under "Advanced Acquisition Configuration" set the filename, click save and restart recording, and put in the number of restarts needed
- ☐ Please note that some of the parameters above will need to change to synchronize the camera(s) differently

Control Room Settings

- ☐ Ensure PLC times are correct in RUSSIAN3.cxt, referencing "C:/Control Room Computer/Russian Methodology/Russian PLC times.xls"
- ☐ Upload PLC timing values to PLC (RUSSIAN3.cxt)

Figure A.5: Page 5 of Experiment Procedures

Pressurized Lines – Safety Glasses Required

- Will likely need to reset PLC in Instrumentation Room afterwards

- ☐ Make sure test facility area is clear (visual inspection & auditory announcement)
- ☐ With all Red Team members in the control room, use the control board to switch on the ox main, ox primary dome, ox secondary dome, fuel main, fuel primary dome, fuel secondary dome
- ☐ Insert enable plug
- ☐ Press Reset on the control board
- ☐ Press FIRE on the control board
- ☐ Ensure the actuators are functioning properly
- ☐ When zone 2 is complete press the BRB (Big Red Button) to enter zone 4 (approx. 10 sec afterwards)
- ☐ Get walkie-talkies or ensure other distance communication method

ONLY Red Team allowed in test cell area from this point forward

Propellant Line Leak Check

- ☐ Perform if:
  - Cart has been disassembled since last test run
  - It has been longer than a week since last check

See Appendix 1 for leak check procedures

NEVER go out to the test stand without the control board key when propellants are present in the lines

Propellant Line Fill

- ☐ Remove the key from the control board
- ☐ Put up all blockades around the test facility
- ☐ Ensure that the water manifold valves are open and water is running into the drain
- ☐ Slowly open the nitrogen tanks to the nitrogen manifold
- ☐ Slowly open the nitrogen manifold ball valves
- ☐ Ensure that there is sufficient pressure in the manifold (>500 psi). Record in Log.
- ☐ Adjust the pressure settings to the appropriate pressures, according to the Pressure Board Settings Table below; "()" = unoriginal setting now required for testing.

Table 3. Experimental Pressure Settings

Oxygen Ignition	Fuel Ignition	Oxygen Main	Fuel Main
60 psi (75 psi)	60 psi (75 psi)	300 psi	300 psi
Oxygen Ignition Purge	**Fuel Ignition Purge**	**Oxygen Main Purge**	**Fuel Main Purge**
30 psi	30-40 psi	50 psi	50 psi

- ☐ Commence Purge Check Sequence

Figure A.6: Page 6 of Experiment Procedures

Pressurized Lines – Safety Glasses Required

Table 4. Purge Check Sequence

Step	Control Room	Test Cell
1	Open "Mass Flow Control.vi"	
2	Replace key and turn on board	
3	Communication check with the intercom	
4		When ready, tell the control room to start the purge check sequence
5	Switch on fuel primary purge, initiate mass flow controller (0.3g/s)	
6		Confirm injector purge flow
7	Switch off fuel primary purge, set mass flow controller to zero, switch on fuel secondary purge	
8		Confirm igniter purge flow
9	Switch off fuel secondary purge, switch on ox primary purge, initiate mass flow controller (1g/s)	
10		Confirm injector purge flow
11	Switch off ox primary purge, set mass flow controller to zero, switch on ox secondary purge	
12		Confirm igniter purge flow
13	Switch off ox secondary purge	

- ☐ Slowly open the main fuel tanks
- ☐ Slowly open the main fuel manifold ball valves
- ☐ Ensure that there is sufficient pressure in the manifold (>500 psi). Record in Log.
- ☐ Slowly open the hydrogen tank to the secondary fuel manifold
- ☐ Slowly open the secondary fuel manifold ball valve
- ☐ Ensure that there is sufficient pressure in the manifold (>500 psi). Record in Log.
- ☐ Slowly open the oxygen tank to the secondary oxygen manifold
- ☐ Slowly open the secondary oxidizer manifold ball valve
- ☐ Ensure that there is sufficient pressure in the manifold (>500 psi). Record in Log.
- ☐ Slowly open the oxygen tank to the primary oxygen manifold
- ☐ Slowly open the primary oxygen manifold ball valves
- ☐ Ensure that there is sufficient pressure in the manifold (>500 psi). Record in Log.
- ☐ Make sure that the pressure settings are correct on the pressure regulator board and record.

At any point, if a Red Team Member sees a questionable situation he can, and should, call for a solution discussion or experimental shut-down

Firing Sequence*

- ☐ Open LabVIEW 8.0 virtual instrument, "RUSKIE_29.vi", and set all the settings in the appropriate input locations

Figure A.7: Page 7 of Experiment Procedures

Pressurized Lines – Safety Glasses Required

- ☐ Make sure test facility area is clear (visual inspection & auditory announcement)
- ☐ Ensure temperature settings are correct on both Controllers and LabVIEW
- ☐ With all Red Team members in the control room, use the control board to switch on the ox main, ox primary dome, ox secondary dome, fuel main, fuel primary dome, fuel secondary dome
- ☐ For the first firing
  - Fill the cart propellant lines with propellant using "Mass Flow Control.vi" and the manual fire valves
    - Set CH4 flow to 0.3 g/s and switch on "Fuel Primary Fire" valve for 5 seconds. Reset flow to 0 and switch off "Fuel Primary Fire."
    - Set O2 flow to 1 g/s and switch on "Ox Primary Fire" valve for 5 seconds. Reset flow to 0 and switch off "Fuel Primary Fire."
- ☐ If using a custom test number and matrix, input values into C:/Control Room Computer/Russian Methodology/Test Matrices/Test Matrix Custom.txt
  - Standard tests (Test 1.0, 1.5, 2.0, 2.5, 3.0, 3.5, 4.0, 4.5, and 5.0) are built in
- ☐ Run LabVIEW program and enter test number
  - Standard test numbers will load test matrix automatically
  - Custom tests require a non standard test number (numerical value > 0)
  - (To debug program begin with a letter or word in the test number)
- ☐ Ensure that all test stand pressures are correct
  - Watch "Fuel Ign Line"
  - Watch "Ox Main Tank" and "Ox Main Line" pressures
- ☐ Hit record on the DVD recorder
- ☐ Announce the Test Number
- ☐ Press Reset
- ☐ Insert enable plug
- ☐ Press FIRE on the control board
- ☐ When experimental sequence is complete, LabVIEW will say it is ready to purge. At this time manually purge the lines with the BRB.
- ☐ The LabVIEW program will automatically stop when the purge flow is zero.
- ☐ After BRB is pushed, switch off the Fuel and Ox Mains and all four domes.
- ☐ Ensure BRB is returned to upward position
- ☐ Repeat "Firing Sequence" as needed

*Familiarize yourself with failure mode solutions before firing sequence

Shut-Down Sequence

- ☐ Record tank pressures in Propellant Tank Log
- ☐ Close main fuel tanks
- ☐ Vent main fuel manifold
- ☐ Close main fuel manifold ball valves
- ☐ Close main oxygen tanks
- ☐ Vent main oxygen manifold
- ☐ Close main oxygen manifold ball valves
- ☐ Close igniter fuel tank

Figure A.8: Page 8 of Experiment Procedures

Pressurized Lines – Safety Glasses Required

- ☐ Vent igniter fuel manifold
- ☐ Close igniter fuel manifold ball valves
- ☐ Close igniter oxygen tank
- ☐ Vent igniter oxygen manifold
- ☐ Close igniter oxygen manifold ball valves
- ☐ Close nitrogen manifold nitrogen tanks
- ☐ Vent nitrogen manifold
- ☐ Close nitrogen manifold ball valves
- ☐ Ensure all pressures are back to ambient with LabVIEW
- ☐ Turn off water
- ☐ Detach water line and blow out with actuator air line
- ☐ Detach actuator air line from the compressor
- ☐ Detach propellant lines from cart
- ☐ Place chamber on the thrust stand
- ☐ Detach instrumentation and store

Figure A.9: Page 9 of Experiment Procedures

Failure Analysis

FAILURE MODE	SOLUTION	EFFECT
Gas leaks in supply lines	Leak Check	
Power failure	Fuel vent valve releases fuel to drainage	Shut-down sequence when power returns
Missed ignition	Press BRB on the test stand control box and the STOP button on the LabVIEW program	Try sequence once more or adjust PLC timing/ injector ignition operating conditions
Inadvertent Burning of Experiment	Press BRB on the test stand control box and the STOP button on the LabVIEW program	Shut-down sequence and assess damage
Over Pressurization	Press BRB on the test stand control box and the STOP button on the LabVIEW program	Shut-down sequence and assess failure location and possible damage
Mass Flow Control Failure	Press BRB on the test stand control box and the STOP button on the LabVIEW program	Check controller settings and LabVIEW program settings
No Cooling Water	Press BRB on the test stand control box and the STOP button on the LabVIEW program	
Accidental ignition or start of gas flow	Key ignitions, normally closed valves	
Experiment will not stop	Press BRB on the test stand control box and the STOP button on the LabVIEW program, manual shut-off at K-bottle	
Gas leaks in supply lines	Leak check, hydrocarbon meter, forced ventilation	
Nitrogen pressure too low	Ensure sufficient pressure prior to testing	Potential failure to purge; propellants remain in lines
Actuators don't function	Ensure air compressor is on and pressurized	
Overheated Propellants	Press BRB on the test stand control box and the STOP button on the LabVIEW program / LabVIEW Emergency Purge	Potential auto-ignition (537°C for CH_4)

Campus Police: (256) 824-6911

Figure A.10: Page 10 of Experiment Procedures

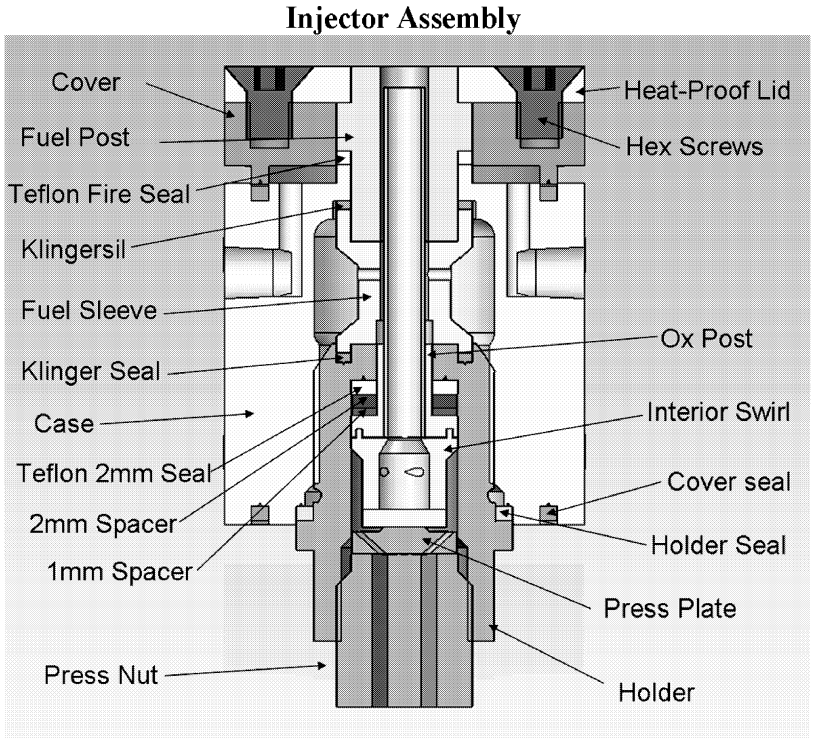

Figure 1. Injector Assembly Schematic.

Figure A.11: Page 11 of Experiment Procedures

Piping Schematic

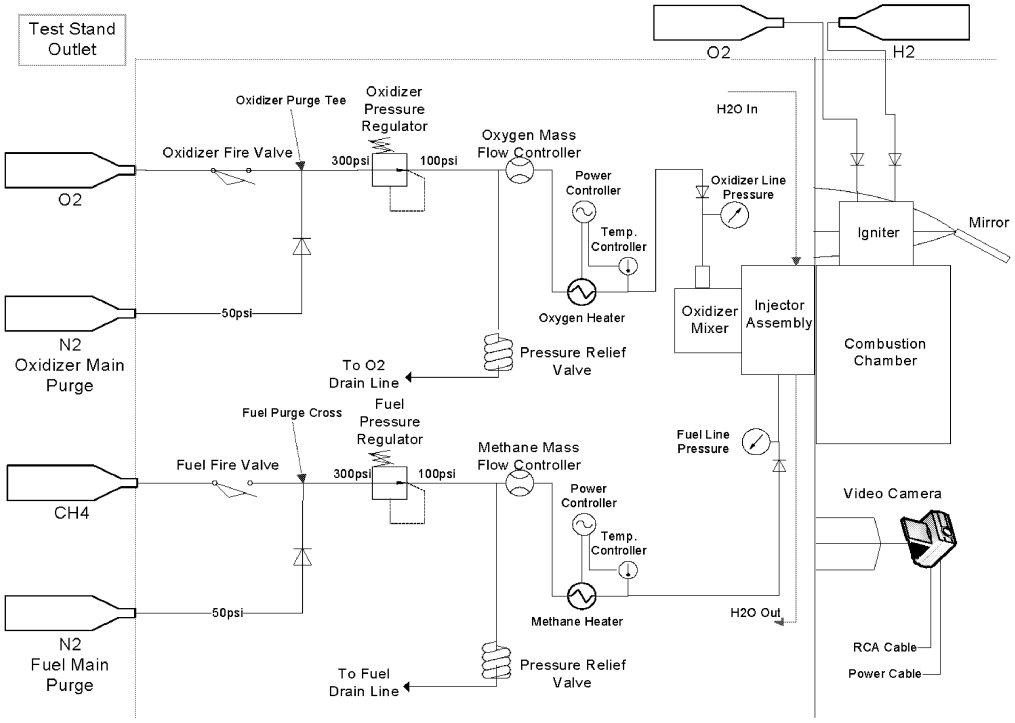

Figure 2. Experimental Piping Schematic

Figure A.12: Page 12 of Experiment Procedures

Appendix 1 – Propellant Line Leak Check

Pressurized Lines – Safety Glasses Required

Table 5. Experimental Pressure Settings

Oxygen Ignition	Fuel Ignition	Oxygen Main	Fuel Main
60 psi (75 psi)	60 psi (75 psi)	300 psi	300 psi
Oxygen Ignition Purge	**Fuel Ignition Purge**	**Oxygen Main Purge**	**Fuel Main Purge**
30 psi	30-40 psi	50 psi	50 psi

- Tighten all fittings and components from the test stand connection to the injector for each line

Fuel Main Line

- Turn on the control board
- Turn on the fuel main, oxidizer main, oxidizer primary dome, fuel primary dome, oxidizer secondary dome, and fuel secondary dome
- Turn on the primary fuel dome switch
- Go outside to the fuel and nitrogen storage area
- Slowly open nitrogen bottles to the nitrogen manifold
- Slowly open manifold ball valves to nitrogen manifold
- Check to make sure there is sufficient pressure in the manifold using the analog gauges
- Set the Experimental Pressure Settings on the pressure regulator board
- Slowly open the nitrogen bottle on the fuel main manifold
- Slowly open the fuel main manifold valve
- Check to make sure there is sufficient pressure in the manifold using the analog gauges
- One red team member must return to the control room, the others go to the test cell

Table 6. Fuel Main Leak Check Procedure

Step	Control Room	Test Cell
1	Open "Mass Flow Control.vi"	
2	Replace key and turn on board	
3	Communication check with the intercom	
4		When ready, tell the control room to actuate the fuel main fire valve
5	Switch on the fuel main fire valve, initiate mass flow controller (.3g/s)	
6		Set cart regulator to 90 psi with flow through the mass flow controller
7		Find leaks with bubble solution
8	Turn off fuel main fire valve, set mass flow controller to zero	
9		Tighten the appropriate fittings
10	Iterate Steps 4-9 until no leaks are present	

Figure A.13: Page 13 of Experiment Procedures

Pressurized Lines – Safety Glasses Required

- Depressurize fuel main manifold

Oxidizer Main Line

- Move the nitrogen tank to the oxidizer main manifold
- Slowly open the nitrogen bottle to the oxidizer main manifold
- Slowly open the oxidizer main manifold valve
- Check to make sure there is sufficient pressure in the manifold using the analog gauges

Table 7. Oxidizer Main Leak Check Procedure

Step	Control Room	Test Cell
1	Open "Mass Flow Control.vi"	
2	Replace key and turn on board	
3	Communication check with the intercom	
4		When ready, tell the control room to actuate the ox main fire valve
5	Switch on the ox main fire valve, initiate mass flow controller (1g/s)	
6		Set cart regulator to 90 psi with flow through the mass flow controller
7		Find leaks with bubble solution
8	Turn off ox main fire valve, set mass flow controller to zero	
9		Tighten the appropriate fittings
10	Iterate Steps 4-9 until no leaks are present	

- Depressurize oxidizer main manifold

Igniter Fuel Line (skip this leak check if the igniter has not been disassembled since the previous experimental session)

- Attach nitrogen to fuel igniter manifold
- Slowly open nitrogen tank
- Slowly open manifold ball valve to fuel igniter manifold
- Check to make sure there is sufficient pressure in the manifold using the analog gauge (≈ 200 psi)
- One red team member must return to the control room, the others go to the test cell

Table 8. Igniter Fuel Leak Check Procedure

Step	Control Room	Test Cell
1	Replace key and turn on board	
2	Communication check with the intercom	
3		When ready, tell the control room to actuate the fuel secondary fire valve
4	Switch on the fuel secondary fire valve	

Figure A.14: Page 14 of Experiment Procedures

Pressurized Lines – Safety Glasses Required

5		Find leaks with bubble solution
6	Turn off fuel secondary fire valve	
7		Tighten the appropriate fittings
8	Iterate Steps 3-7 until no leaks are present	

Igniter Oxygen Line (skip this leak check if the igniter has not been disassembled since the previous experimental session)

- Attach nitrogen to oxygen igniter manifold
- Slowly open nitrogen tank
- Slowly open manifold ball valves to oxygen igniter manifold
- Check to make sure there is sufficient pressure in the manifold using the analog gauge (≈ 200 psi)
- Set the oxygen igniter pressure on the pressure regulator board
- One red team member must return to the control room, the others go to the test cell

Table 9. Igniter Oxygen Leak Check Procedure

Step	Control Room	Test Cell
1	Replace key and turn on board	
2	Communication check with the intercom	
3		When ready, tell the control room to actuate the oxidizer secondary fire valve
4	Switch on the oxidizer secondary fire valve	
5		Find leaks with bubble solution
6	Turn off oxidizer secondary fire valve	
7		Tighten the appropriate fittings
8	Iterate Steps 3-7 until no leaks are present	

Figure A.15: Page 15 of Experiment Procedures

APPENDIX B

INJECTOR DESIGN PROCEDURE AND DRAWINGS

Several important parameters necessary for dimensioning the swirl injector are known before the design process. These parameters are dictated by the mission requirements, propellant selection, etc. Usually the known parameters are the mass flow rate and propellant density. Other properties, such as the pressure drop and desired spray angle, are selected.

The propellant mass flow rates are calculated from given thrust, burn time, and OF ratio.

$$\dot{m}_{\Sigma} = \frac{Th}{gI_{sp}} = \frac{24.465\ kN}{(9.81\ m/s^2)\,(355\ s)} = 7.027\ \frac{kg}{s}$$

$$\Rightarrow \dot{m}_{LOX} = \frac{OF\dot{m}_{\Sigma}}{(OF+1)\,n_{inj}} = \frac{3\,(7,027\ g/s)}{(3+1)\,65} = 81\ g/s$$

$$\Rightarrow \dot{m}_{LCH4} = \frac{\dot{m}_{LOX}}{OF} = \frac{81\ g/s}{3} = 27\ g/s.$$

The calculations for the interior LOX swirl stage begin with calculating the exit velocity from Bernoulli's equation.

$$V_{\Sigma,LOX} = \sqrt{\frac{2\Delta P_{LOX}}{\rho_{LOX}}} = \sqrt{\frac{2\,(345\ kPa)}{1,083\ kg/m^3}} = 25.2\ m/s.$$

The velocity does not correspond to a swirl velocity, but rather a jet velocity. The cross-sectional area and for a jet at this velocity can be calculated.

$$A_{j,LOX} = \frac{\dot{m}_{LOX}}{\rho_{LOX} V_{\Sigma,LOX}} = \frac{81\ g/s}{(1083\ g/m^3)\,(25.2\ m/s)} = 2.968\ mm^2.$$

The non-dimensional parameter a is a parameter that characterizes the swirl injector. It is defined as $a{=}\frac{r_{mk}}{R_n}$, where r_{mk} is the vortex radius of the head end and R_n is the nozzle radius. These values are referenced in Figure B.1.

The non-dimensional parameter a can also be calculated from the spray angle.

$$a_{LOX} = \frac{tan^2\left(\frac{\alpha}{2}\right)}{1 + tan^2\left(\frac{\alpha}{2}\right)} = 0.5.$$

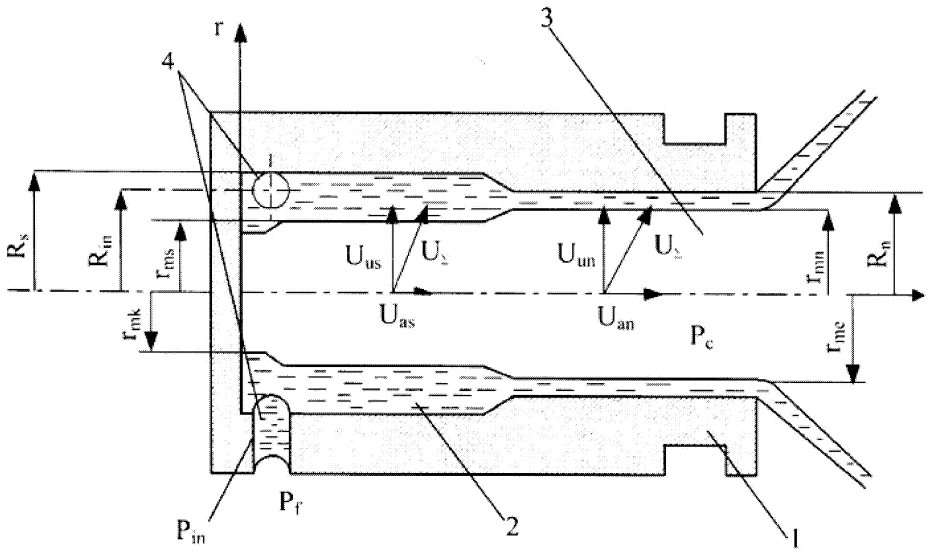

Figure B.1: Swirl Injector Parameters

The fullness factor ϕ is the fractional area of the liquid in the passage and is calculated from a.

$$\sqrt{a_{LOX}} = (1 - \phi_{LOX}) \sqrt{\frac{2}{2 - \phi_{LOX}}}$$

$$\Rightarrow \phi = 0.36.$$

The discharge coefficient is then calculated.

$$\mu_{LOX} = \frac{\phi_{LOX}\sqrt{\phi_{LOX}}}{\sqrt{2 - \phi_{LOX}}} = \frac{0.36\sqrt{0.36}}{2 - 0.36} = 0.168.$$

The nozzle area, radius, and diameter are calculated from the jet area and the discharge coefficient.

$$A_{n,LOX} = \frac{A_{j,LOX}}{\mu_{LOX}} = \frac{2.968\ mm^2}{0.168} = 17.625\ mm^2$$

$$R_{n,LOX} = \sqrt{\frac{A_{n,LOX}}{\pi}} = \sqrt{\frac{17.625\ mm^2}{\pi}} = 2.369\ mm$$

$$d_{n,LOX} = 2R_{n,LOX} = 2\,(2.369\ mm) = 4.737\ mm.$$

The liquid film thickness, normalized by the nozzle radius, is calculated from the fullness factor.

$$\bar{h}_{LOX} = 1 - \sqrt{1 - \phi} = 1 - \sqrt{1 - 0.36} = 0.2$$

$$h_{LOX} = \bar{h}_{LOX} R_{n,LOX} = (0.2)\,(2.369\ mm) = 0.473\ mm.$$

A geometric characteristic parameter of a swirl injector is A, where $A=\frac{\bar{R}_{in}}{A_{in}}$. It can also be calculated from the non-dimensional parameter a.

$$A_{LOX} = \frac{\sqrt{a_{LOX}}}{\mu_{LOX}} = \frac{\sqrt{0.5}}{0.168} = 4.2.$$

The total inlet area and diameter is calculated from this parameter.

$$A_{in,LOX} = \frac{\bar{R}_{in,LOX} A_{n,LOX}}{A_{LOX}} = \frac{(1.2)\,(17.625\ mm^2)}{4.2} = 5.036\ mm^2$$

$$d_{in,LOX} = \sqrt{\frac{4A_{in,LOX}}{\pi n_{inj}}} = \sqrt{\frac{4\,(5.036\ mm^2)}{65\pi}} = 1.266\ mm.$$

The vortex chamber diameter is the sum of the inlet geometry.

$$d_{vc,LOX} = 2\bar{R}_{in,LOX} R_{n,LOX} + d_{in,LOX}$$

$$= 2\,(1.2)\,(2.369\ mm) + 1.266\ mm = 6.951\ mm.$$

The suggested length of the inlet channel is double the inlet diameter.

$$L_{in,LOX} = 2d_{in,LOX} = 2\,(1.266\ mm) = 2.532\ mm.$$

The suggested length of the vortex chamber is 2.5 times the inlet diameter.

$$L_{vc,LOX} = 2.5d_{in,LOX} = 2.5\,(1.266\ mm) = 3.165\ mm.$$

To start the calculations for the exterior fuel swirling stage, a liquid fuel thickness is assumed.

$$h_{LCH4} = 0.3\ mm.$$

The minimum nozzle diameter for the fuel is the summation of the LOX post nozzle diameter, LOX post wall thickness, a desired gap distance between the LOX post nozzle and the LCH$_4$ interface, and the LCH4 film thickness. The area can then be calculated.

$$d_{n,LCH4} = d_{n,LOX} + 2\delta_{wall} + 2\delta_{gap} + 2h_{LCH4}$$

$$= 4.737\ mm + 2\,(0.5\ mm) + 2\,(0.25\ mm) + 2\,(0.3\ mm) = 6.837\ mm$$

$$A_{n,LCH4} = \frac{\pi}{4} d_{n,LCH4}^2 = \frac{\pi}{4}\,(6.837\ mm)^2 = 36.715\ mm^2.$$

The velocity is calculated from Bernoulli's equation.

$$V_{\Sigma,LCH4} = \sqrt{\frac{2\Delta P_{LCH4}}{\rho_{LCH4}}} = \sqrt{\frac{2\,(345\ kPa)}{437\ kg/m^3}} = 39.7\ m/s.$$

The jet area is then calculated.

$$A_{j,LCH4} = \frac{\dot{m}_{LCH4}}{\rho_{LCH4} V_{\Sigma,LCH4}} = \frac{27\ g/s}{(437\ kg/m^3)}\,(39.7\ m/s) = 1.557\ mm^2.$$

The discharge coefficient and fullness factor are then calculated.

$$\mu_{LCH4} = \frac{A_{j,LCH4}}{A_{n,LCH4}} = \frac{1.557\ mm^2}{36.715\ mm^2} = 0.042$$

$$\mu_{LCH4} = \frac{\phi_{LCH4}\sqrt{\phi_{LCH4}}}{\sqrt{2-\phi_{LCH4}}}$$

$$\Rightarrow \phi_{LCH4} = 0.149.$$

The fullness factor is used to recalculate the liquid film thickness. The sequence can be repeated until the values converge. For this design the sequence was repeated once.

$$h_{LCH4,new} = \frac{d_{n,LCH4}}{2}\left(1-\sqrt{1-\phi_{LCH4}}\right)$$

$$= \frac{6.837\ mm}{2}\left(1-\sqrt{1-0.149}\right) = 0.265\ mm.$$

From final dimensions of the recalculated parameters are summarized in Table B.1.

Table B.1: Liquid LCH_4 Parameters

Parameter	Value
$d_{n,LCH4}$	6.768 mm
$A_{n,LCH4}$	35.973 mm^2
μ_{LCH4}	0.043
ϕ_{LCH4}	0.151

The non-dimensional parameter a for the fuel is calculated so the geometric parameter A can be calculated.

$$\sqrt{a_{LCH4}} = (1-\phi_{LCH4})\sqrt{\frac{2}{2-\phi_{LCH4}}} = (1-0.151)\sqrt{\frac{2}{2-0.151}}$$

$$\Rightarrow a_{LCH4} = 0.779$$

$$A_{LCH4} = \frac{\sqrt{a_{LCH4}}}{\mu_{LCH4}} = \frac{0.779}{0.043} = 20.425.$$

The total inlet area and individual inlet diameter for the exterior fuel stage are then calculated.

$$A_{in,LCH4} = \frac{\bar{R}_{in,LCH4} A_{n,LCH4}}{A_{LCH4}} = \frac{1.0\,(35.973\ mm^2)}{20.425} = 1.798\ mm^2$$

$$d_{in,LCH4} = \sqrt{\frac{4A_{in,LCH4}}{\pi n_L CH4}} = \sqrt{\frac{4\,(1.798\ mm^2)}{4\pi}} = 0.756\ mm.$$

The length of the inlet channels are double the diameter.

$$L_{in,LCH4} = 2d_{in,LCH4} = 2\,(0.756\ mm) = 1.513\ mm.$$

The vortex chamber diameter is calculated by summing various dimensions.

$$d_{vc,LCH4} = \bar{R}_{LCH4} d_{n,LCH4} + d_{in,LCH4} = 1.0\,(6.837\ mm) + 0.756\ mm = 6.951\ mm.$$

The suggested length of the vortex chamber is 2.5 times the inlet diameter.

$$L_{vc,LCH4} = 2.5 d_{in,LCH4} = 2.5\,(0.756\ mm) = 3.165\ mm.$$

Once all the dimensions are calculated, the scaling parameters can be calculated. The velocity ratio is the total fuel velocity divided by the total oxygen velocity.

$$VR = \frac{V_{\Sigma,LCH4}}{V_{\Sigma,LOX}} = \frac{39.7\ m/s}{25.2\ m/s} = 1.545.$$

The momentum ratio is the momentum of the fuel divided by the momentum of the oxidizer.

$$MR = \frac{\dot{m}_{LCH4} V_{\Sigma,LCH4}}{\dot{m}_{LOX} V_{\Sigma,LOX}} = \frac{(27\ g/s)\,(39.7\ m/s)}{(81\ g/s)\,(25.2\ m/s)} = 0.515.$$

Then the momentum ratio is calculated.

$$J = \frac{\rho_{LCH4} V_{\Sigma,LCH4}^2}{\rho_{LOX} V_{\Sigma,LOX}^2} = \frac{(437\ kg/m^3)\,(39.7\ m/s)^2}{(1,083\ kg/m^3)\,(25.2\ m/s)^2} = 0.963.$$

Figure B.2 shows a model of the final injector design.

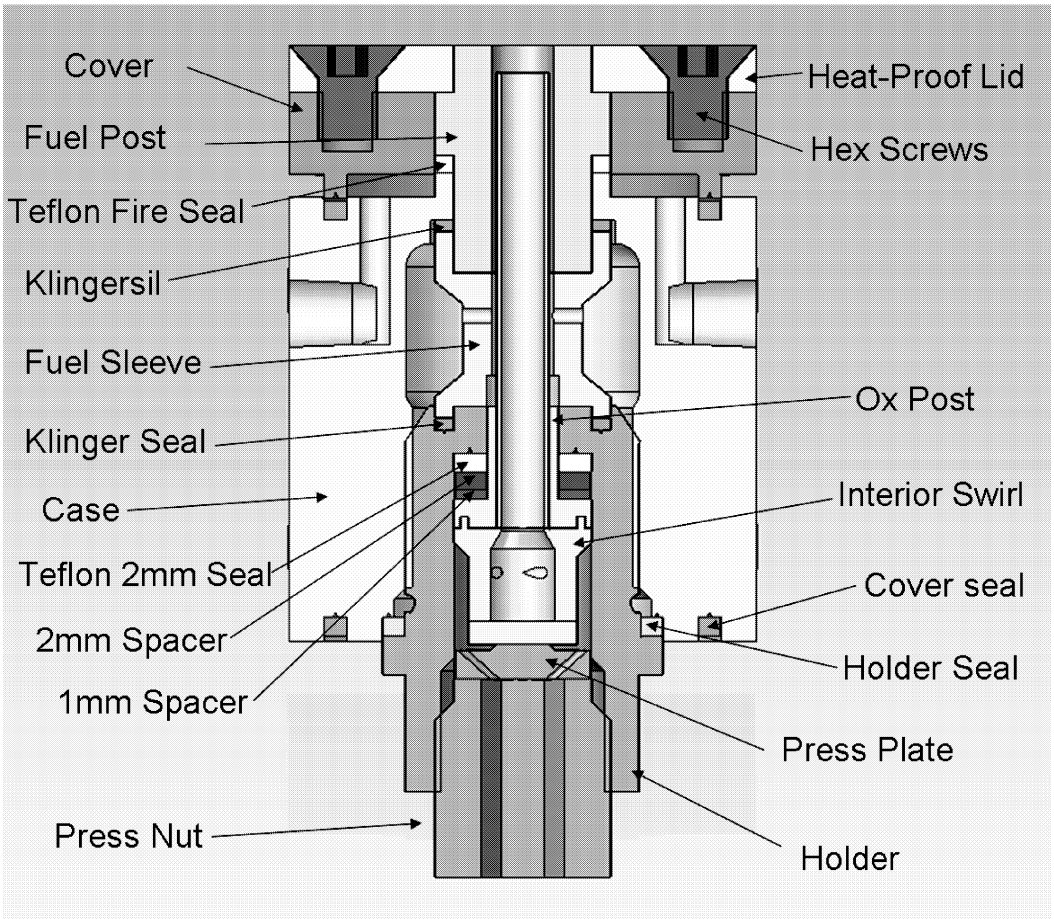

Figure B.2: Swirl-Coaxial Injector

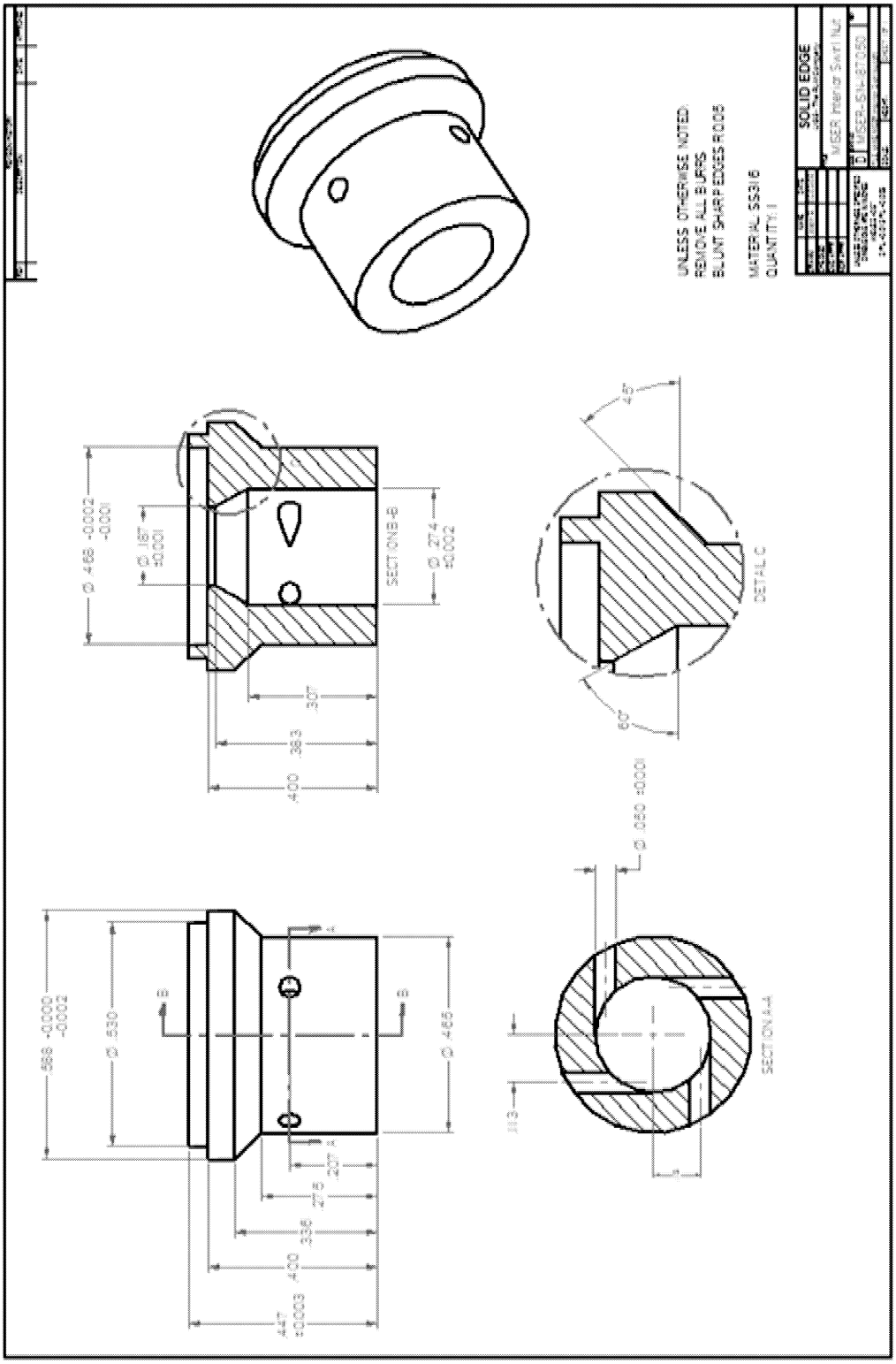

Figure B.3: Drawing of LOX Swirl Nut

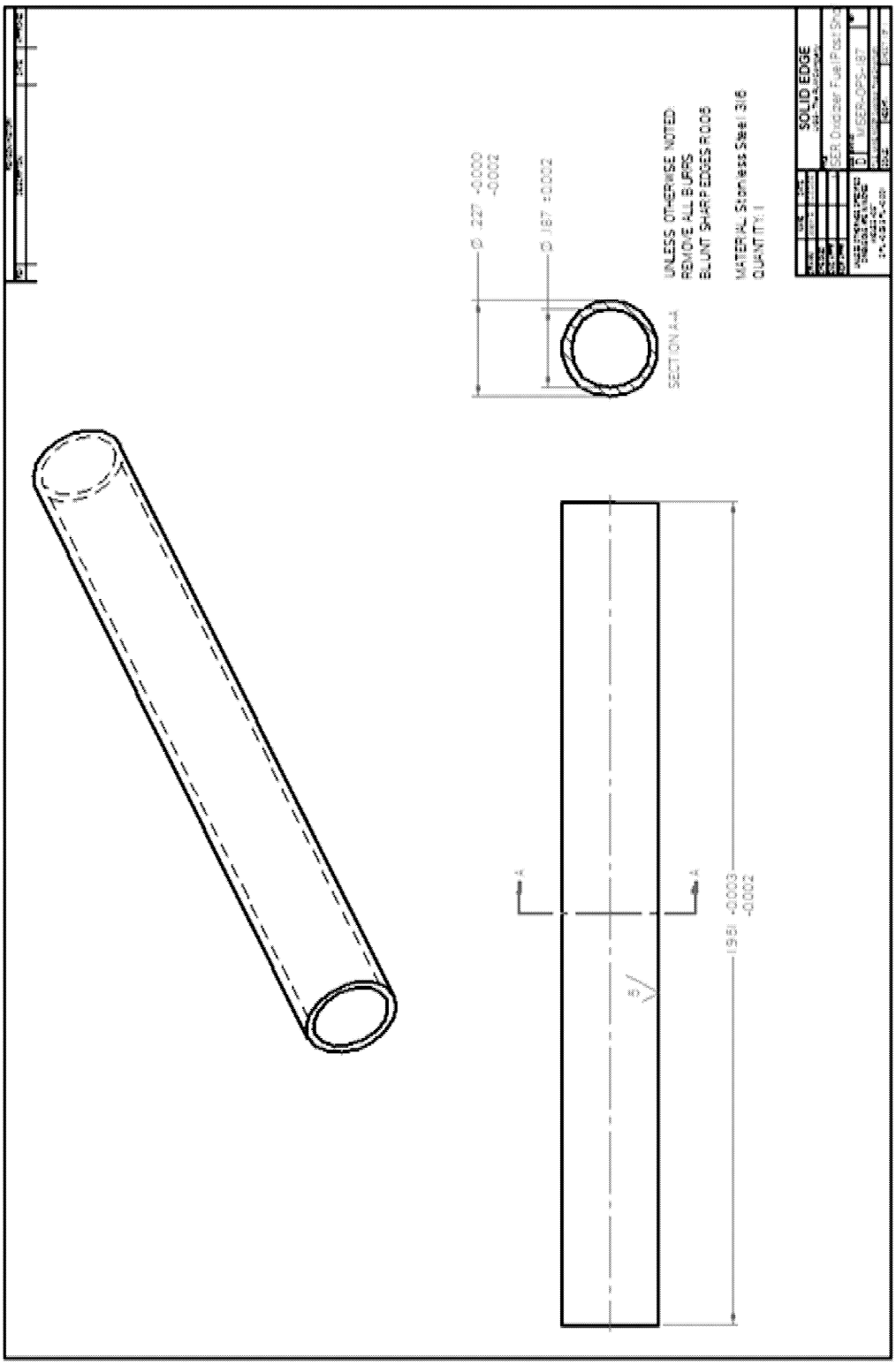

Figure B.4: Drawing of LOX Post

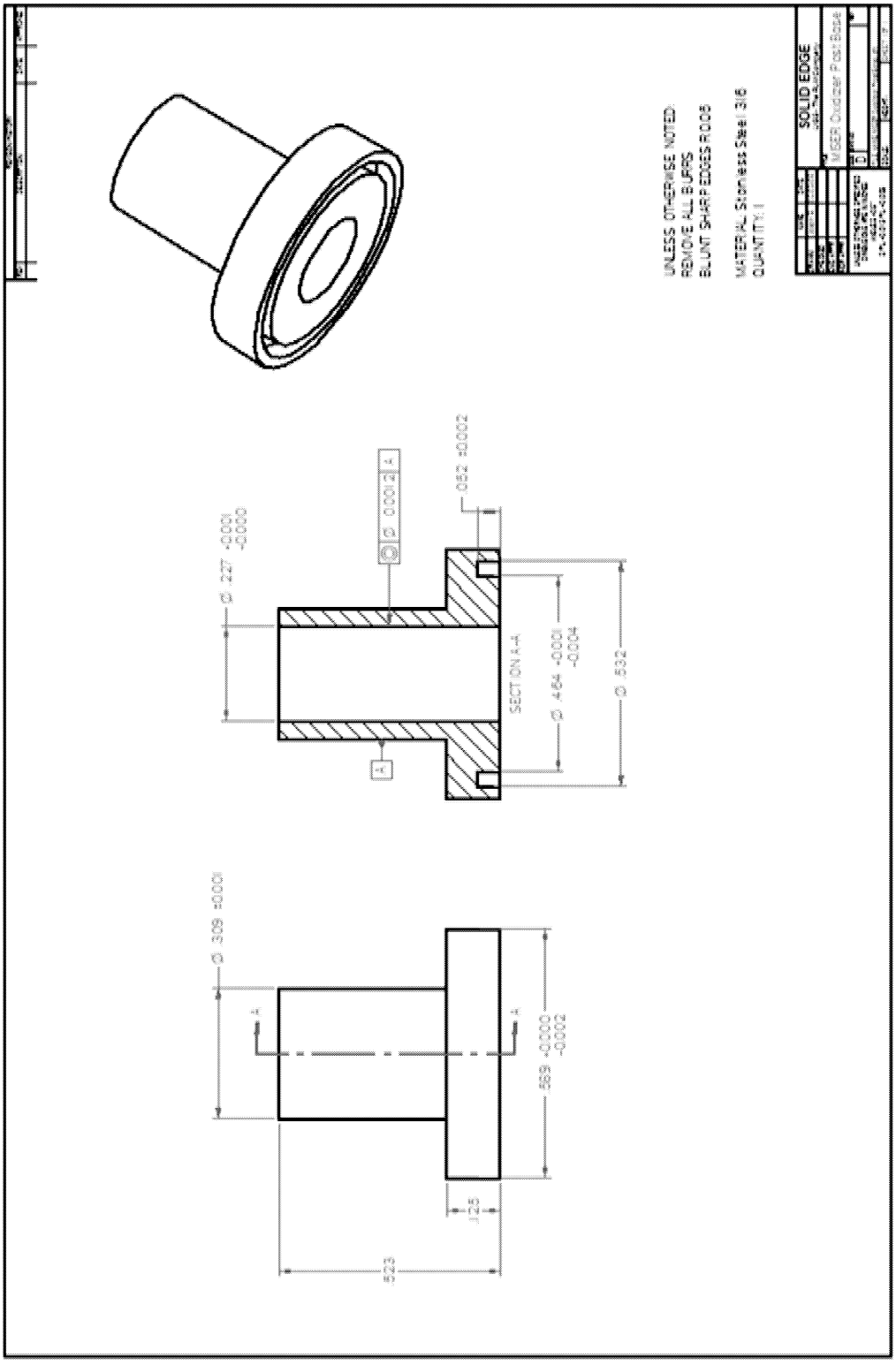

Figure B.5: Drawing of LOX Post Base

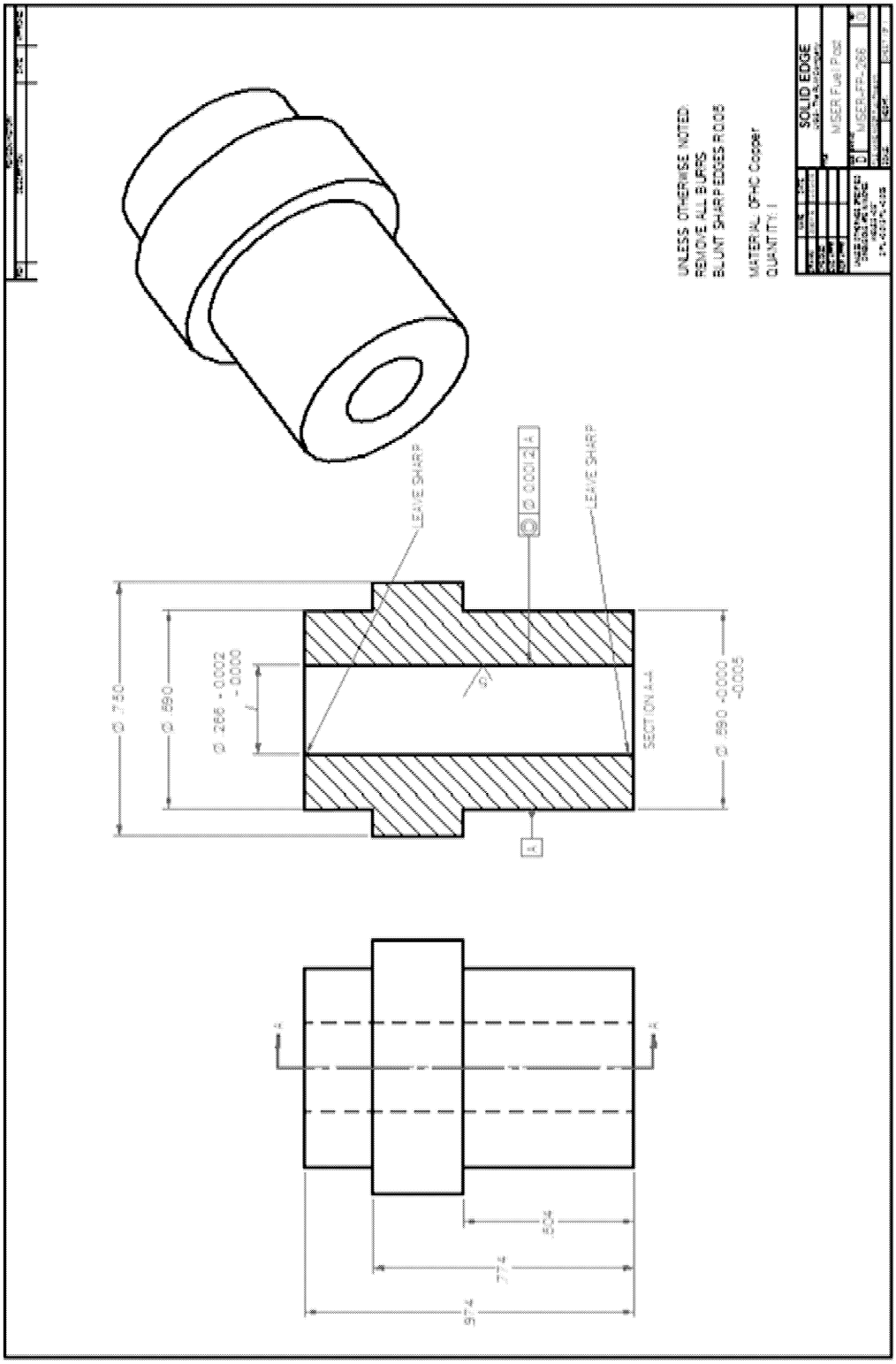

Figure B.6: Drawing of LCH_4 Post

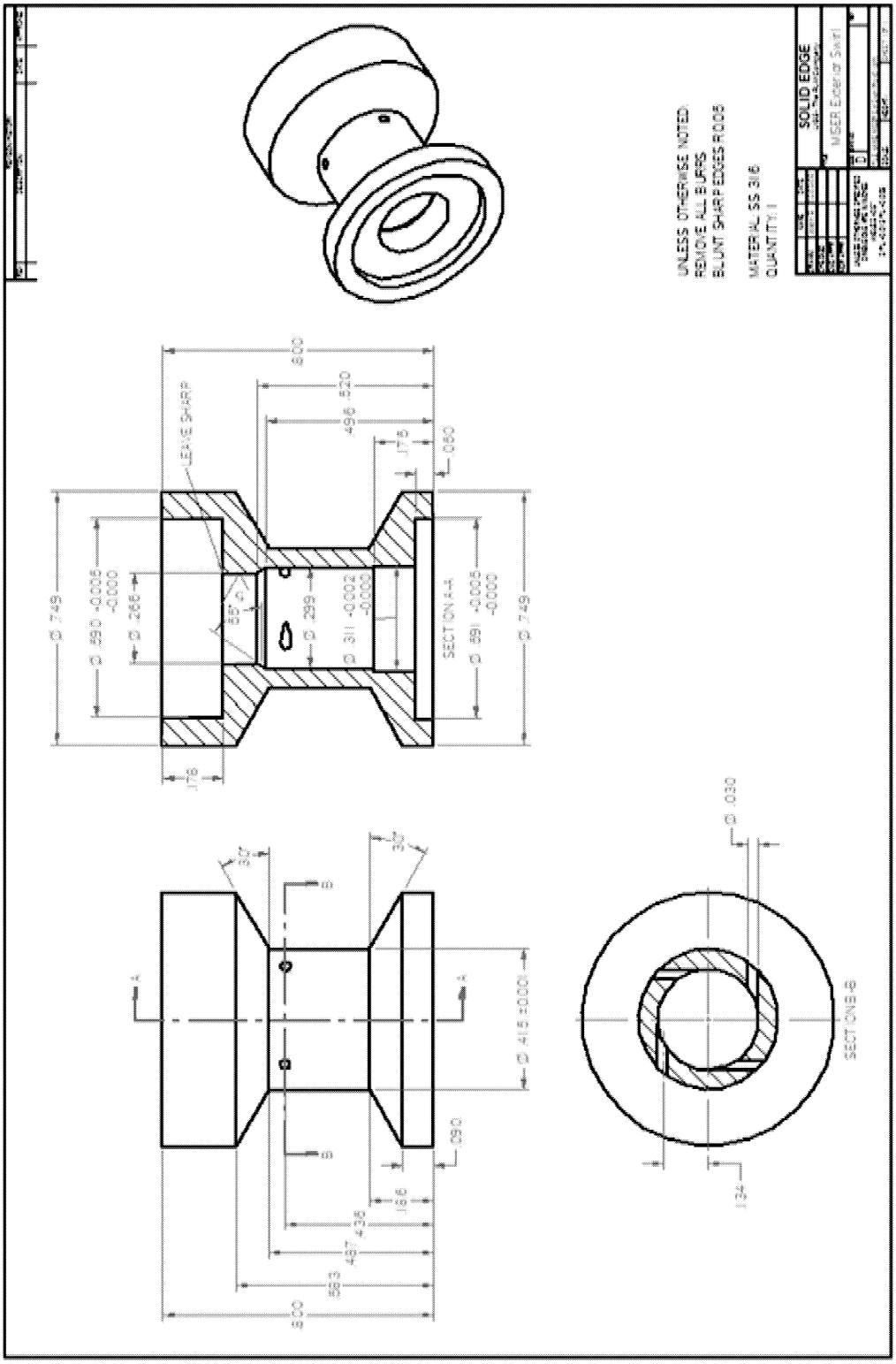

Figure B.7: Drawing of LCH_4 Swirl Nut

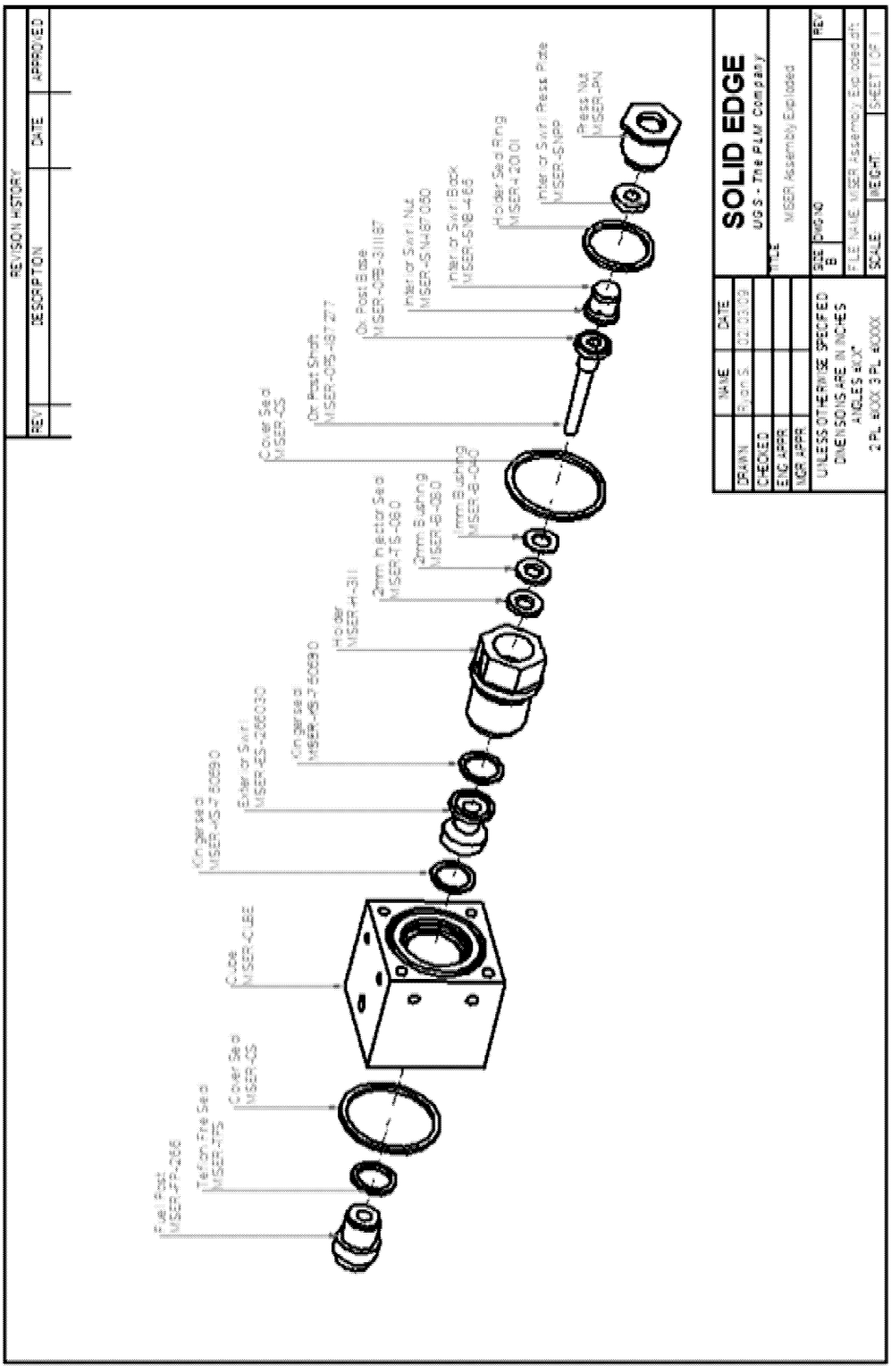

Figure B.8: Exploded View of Injector Assembly

APPENDIX C

EQUIPMENT CALIBRATION SHEETS

CALIBRATION CERTIFICATE

Model:	106B			**Date:**	7/30/2009
Serial #:	11212			**By:**	Jonathan Rappold, Cal. Tech
Description:	Pressure Sensor				
Type:	ICP	**Time Constant:**	1.3 sec	**Station:**	903 Pulse #2 (Test procedure AT601-6)
Sensitivity*:	299.6 mV/PSI 43.46 mV/kPa			**Temp:** **Humidity:**	72 deg F [22deg C] 79 %
Linearity*:	0.2% FS			**Cert #:**	333963
Uncertainty:**	+/- 1 %				

Bias: 4.6 VDC

* Zero based, least-squares straight line.

** Measurement uncertainty represented using a coverage factor of k=2 which provides a level of confidence of approximately 95 %.

Condition of Unit:
As Found: In tolerance
As Left: In tolerance

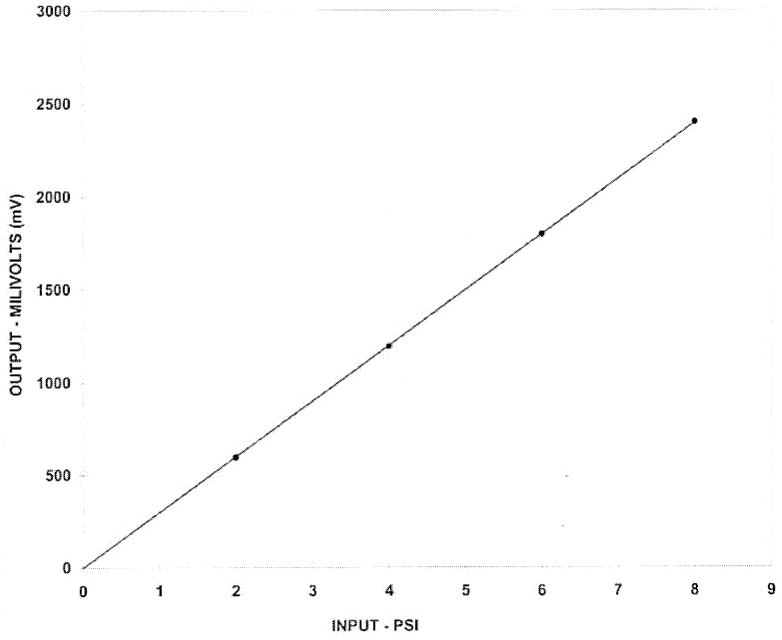

TEST DATA

INPUT (PSI)	OUTPUT (mV)
2.00	595
4.00	1194
6.00	1797
8.00	2401

Notes:
1 STATION #15
2 Calibration is traceable to NIST and is accredited to ISO 17025 and ANSI/NCSL Z540-1-1994.
3 NIST traceability through PCB control # ME127.
4 This certificate may not be reproduced, except in full, without written approval from PCB Piezotronics, Inc.

ACCREDITED
CALIBRATION CERT #1662.01

PCB PIEZOTRONICS INC.
Tel: 716-684-0001 Fax: 716-684-0987 Email: sales@pcb.com
3425 Walden Avenue, Depew NY 14043

ISO 9001 CERTIFIED

Page 1 of 1

Figure C.1: Transducer 1 Calibration Sheet Page 1

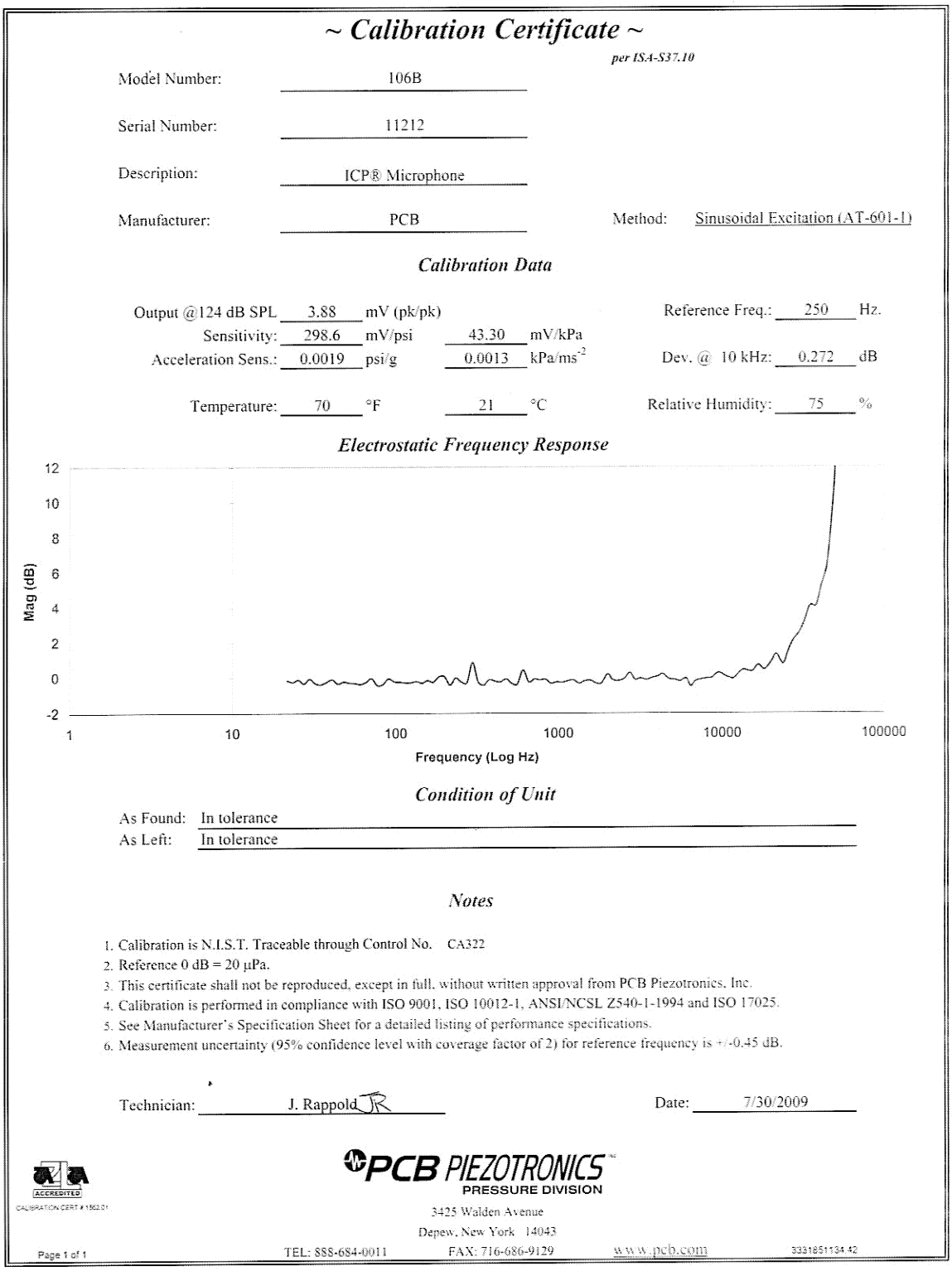

~ Calibration Certificate ~

per ISA-S37.10

Model Number: 106B

Serial Number: 11212

Description: ICP® Microphone

Manufacturer: PCB Method: Sinusoidal Excitation (AT-601-1)

Calibration Data

Output @124 dB SPL 3.88 mV (pk/pk) Reference Freq.: 250 Hz.

Sensitivity: 298.6 mV/psi 43.30 mV/kPa

Acceleration Sens.: 0.0019 psi/g 0.0013 kPa/ms^{-2} Dev. @ 10 kHz: 0.272 dB

Temperature: 70 °F 21 °C Relative Humidity: 75 %

Electrostatic Frequency Response

Condition of Unit

As Found: In tolerance

As Left: In tolerance

Notes

1. Calibration is N.I.S.T. Traceable through Control No. CA322
2. Reference 0 dB = 20 µPa.
3. This certificate shall not be reproduced, except in full, without written approval from PCB Piezotronics, Inc.
4. Calibration is performed in compliance with ISO 9001, ISO 10012-1, ANSI/NCSL Z540-1-1994 and ISO 17025.
5. See Manufacturer's Specification Sheet for a detailed listing of performance specifications.
6. Measurement uncertainty (95% confidence level with coverage factor of 2) for reference frequency is +/-0.45 dB.

Technician: J. Rappold Date: 7/30/2009

ACCREDITED
CALIBRATION CERT. # 1362.01

PCB PIEZOTRONICS
PRESSURE DIVISION
3425 Walden Avenue
Depew, New York 14043
TEL: 888-684-0011 FAX: 716-686-9129 www.pcb.com

Page 1 of 1 3338151134.42

Figure C.2: Transducer 1 Calibration Sheet Page 2

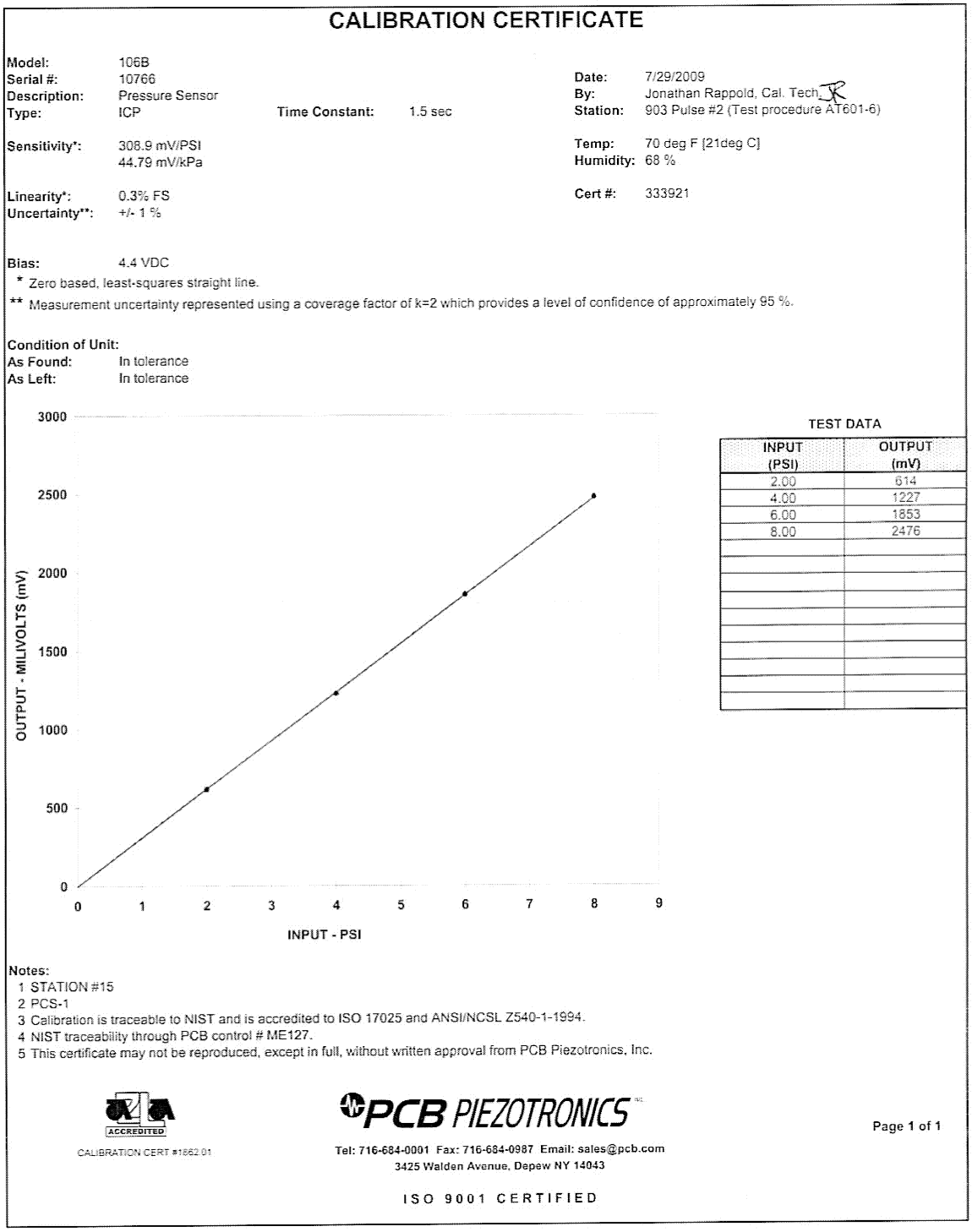

CALIBRATION CERTIFICATE

Model:	106B			**Date:**	7/29/2009
Serial #:	10766			**By:**	Jonathan Rappold, Cal. Tech
Description:	Pressure Sensor				
Type:	ICP	**Time Constant:**	1.5 sec	**Station:**	903 Pulse #2 (Test procedure AT601-6)
Sensitivity*:	308.9 mV/PSI 44.79 mV/kPa			**Temp:** **Humidity:**	70 deg F [21deg C] 68 %
Linearity*:	0.3% FS			**Cert #:**	333921
Uncertainty:**	+/- 1 %				

Bias: 4.4 VDC

* Zero based, least-squares straight line.

** Measurement uncertainty represented using a coverage factor of k=2 which provides a level of confidence of approximately 95 %.

Condition of Unit:
As Found: In tolerance
As Left: In tolerance

TEST DATA

INPUT (PSI)	OUTPUT (mV)
2.00	614
4.00	1227
6.00	1853
8.00	2476

Notes:
1 STATION #15
2 PCS-1
3 Calibration is traceable to NIST and is accredited to ISO 17025 and ANSI/NCSL Z540-1-1994.
4 NIST traceability through PCB control # ME127.
5 This certificate may not be reproduced, except in full, without written approval from PCB Piezotronics, Inc.

ACCREDITED
CALIBRATION CERT #1862.01

PCB PIEZOTRONICS

Tel: 716-684-0001 Fax: 716-684-0987 Email: sales@pcb.com
3425 Walden Avenue, Depew NY 14043

ISO 9001 CERTIFIED

Page 1 of 1

Figure C.3: Transducer 2 Calibration Sheet Page 1

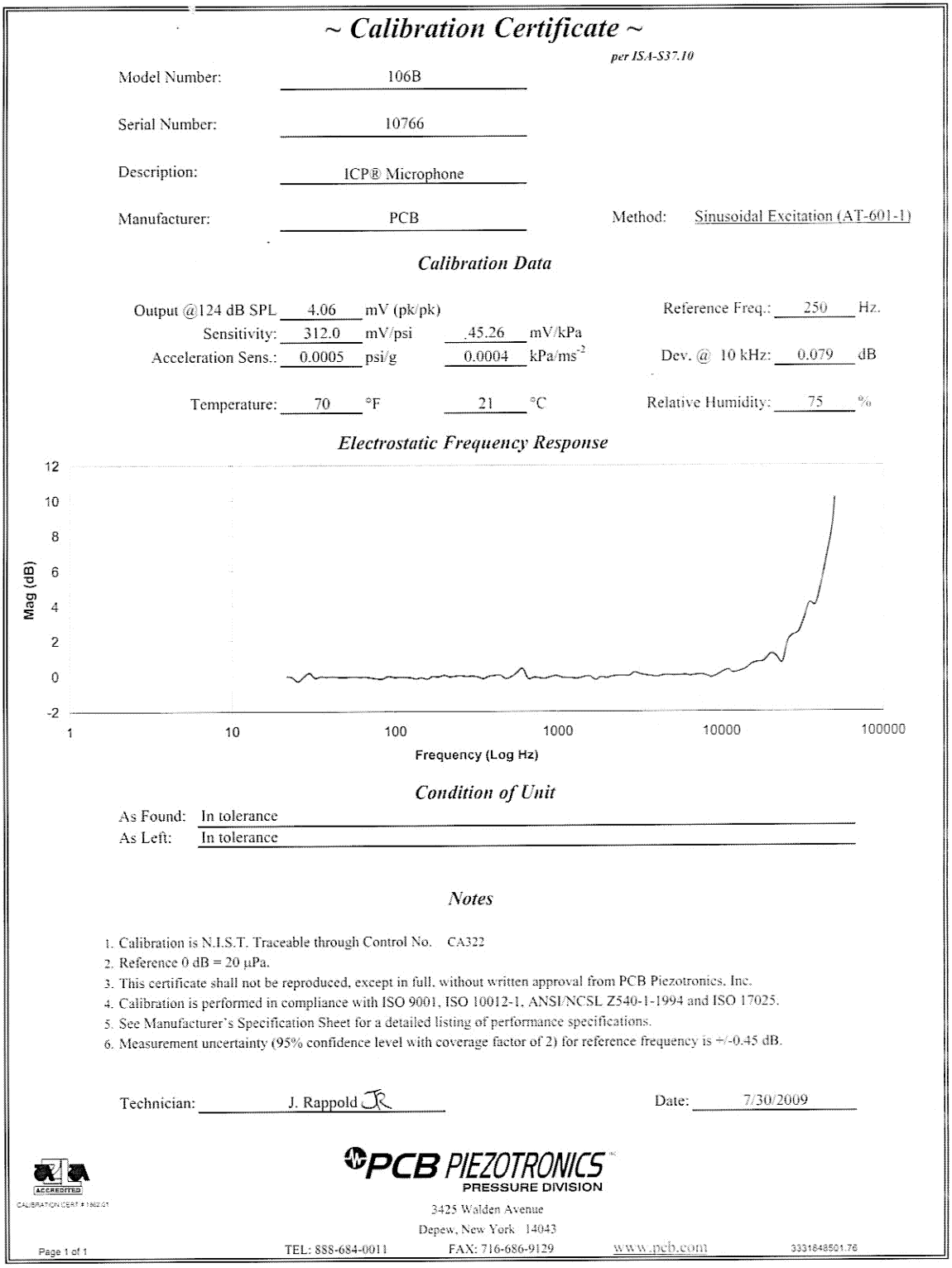

~ Calibration Certificate ~

per ISA-S37.10

Model Number: 106B

Serial Number: 10766

Description: ICP® Microphone

Manufacturer: PCB Method: Sinusoidal Excitation (AT-601-1)

Calibration Data

Output @124 dB SPL 4.06 mV (pk/pk) Reference Freq.: 250 Hz.

Sensitivity: 312.0 mV/psi 45.26 mV/kPa

Acceleration Sens.: 0.0005 psi/g 0.0004 kPa/ms^{-2} Dev. @ 10 kHz: 0.079 dB

Temperature: 70 °F 21 °C Relative Humidity: 75 %

Electrostatic Frequency Response

Condition of Unit

As Found: In tolerance

As Left: In tolerance

Notes

1. Calibration is N.I.S.T. Traceable through Control No. CA322
2. Reference 0 dB = 20 µPa.
3. This certificate shall not be reproduced, except in full, without written approval from PCB Piezotronics, Inc.
4. Calibration is performed in compliance with ISO 9001, ISO 10012-1, ANSI/NCSL Z540-1-1994 and ISO 17025.
5. See Manufacturer's Specification Sheet for a detailed listing of performance specifications.
6. Measurement uncertainty (95% confidence level with coverage factor of 2) for reference frequency is +/-0.45 dB.

Technician: J. Rappold Date: 7/30/2009

ACCREDITED

CALIBRATION CERT # 1862.01

PCB PIEZOTRONICS INC
PRESSURE DIVISION

3425 Walden Avenue
Depew, New York 14043

Page 1 of 1 TEL: 888-684-0011 FAX: 716-686-9129 www.pcb.com 3331848501.76

Figure C.4: Transducer 2 Calibration Sheet Page 2

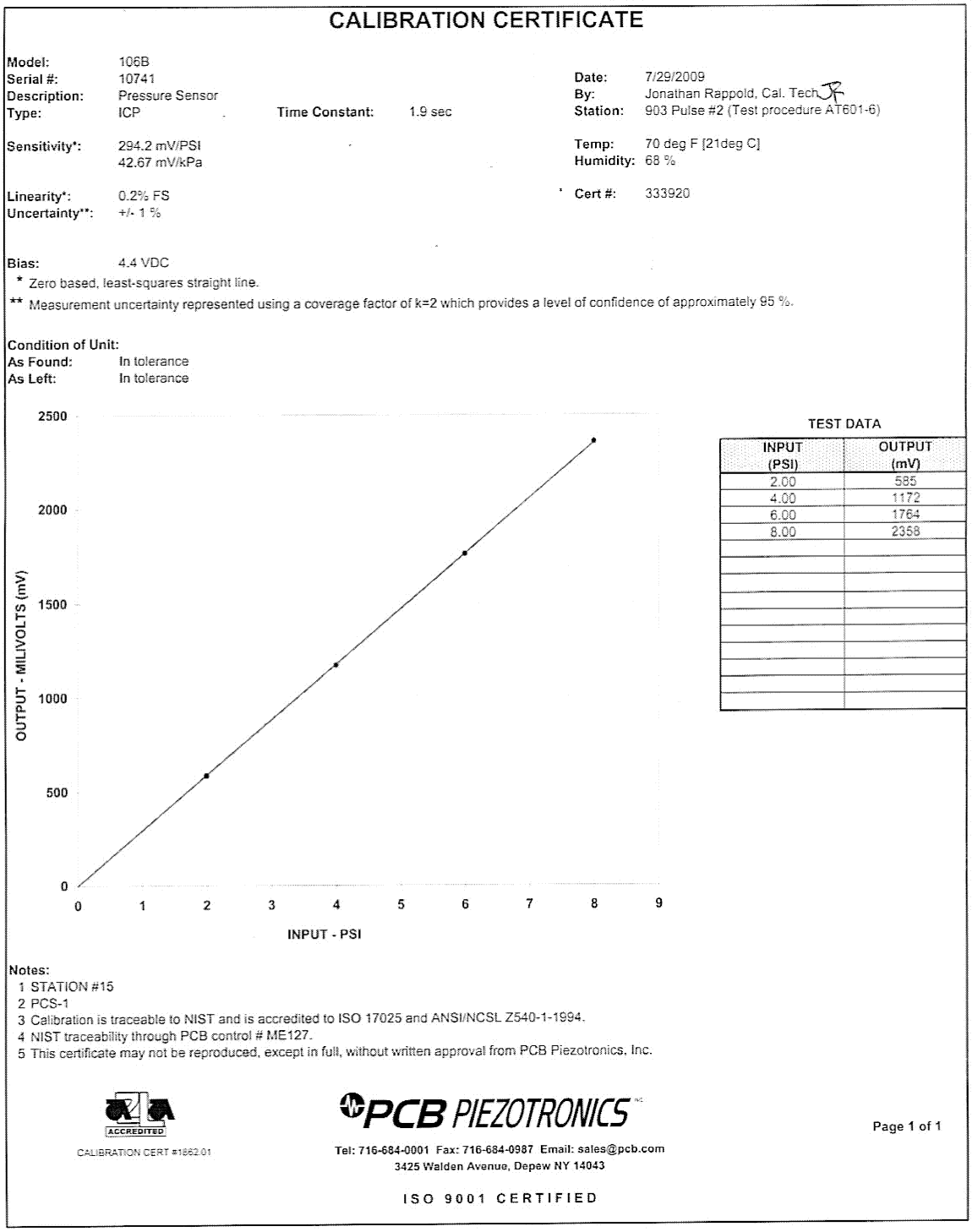

CALIBRATION CERTIFICATE

Model:	106B			**Date:**	7/29/2009
Serial #:	10741			**By:**	Jonathan Rappold, Cal. Tech
Description:	Pressure Sensor				
Type:	ICP	**Time Constant:**	1.9 sec	**Station:**	903 Pulse #2 (Test procedure AT601-6)
Sensitivity*:	294.2 mV/PSI 42.67 mV/kPa			**Temp:** **Humidity:**	70 deg F [21deg C] 68 %
Linearity*:	0.2% FS			**Cert #:**	333920
Uncertainty:**	+/- 1 %				

Bias: 4.4 VDC

* Zero based, least-squares straight line.

** Measurement uncertainty represented using a coverage factor of k=2 which provides a level of confidence of approximately 95 %.

Condition of Unit:
As Found: In tolerance
As Left: In tolerance

TEST DATA

INPUT (PSI)	OUTPUT (mV)
2.00	585
4.00	1172
6.00	1764
8.00	2358

Notes:
1 STATION #15
2 PCS-1
3 Calibration is traceable to NIST and is accredited to ISO 17025 and ANSI/NCSL Z540-1-1994.
4 NIST traceability through PCB control # ME127.
5 This certificate may not be reproduced, except in full, without written approval from PCB Piezotronics, Inc.

ACCREDITED
CALIBRATION CERT #1862.01

PCB PIEZOTRONICS INC.
Tel: 716-684-0001 Fax: 716-684-0987 Email: sales@pcb.com
3425 Walden Avenue, Depew NY 14043

ISO 9001 CERTIFIED

Page 1 of 1

Figure C.5: Transducer 4 Calibration Sheet Page 1

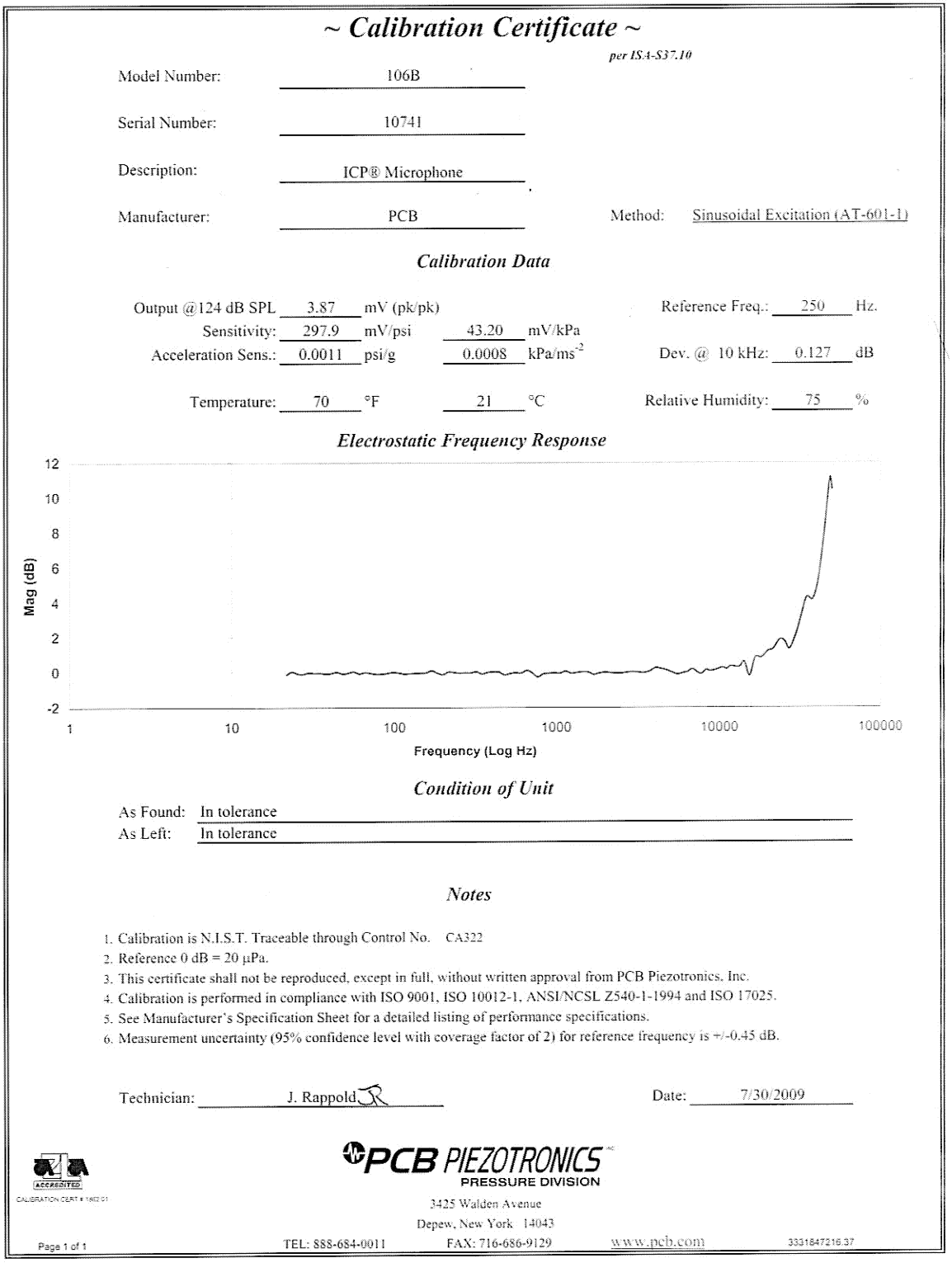

~ Calibration Certificate ~

per ISA-S37.10

Model Number: 106B

Serial Number: 10741

Description: ICP® Microphone

Manufacturer: PCB Method: Sinusoidal Excitation (AT-601-1)

Calibration Data

Output @124 dB SPL 3.87 mV (pk/pk) Reference Freq.: 250 Hz.

Sensitivity: 297.9 mV/psi 43.20 mV/kPa

Acceleration Sens.: 0.0011 psi/g 0.0008 kPa/ms^{-2} Dev. @ 10 kHz: 0.127 dB

Temperature: 70 °F 21 °C Relative Humidity: 75 %

Electrostatic Frequency Response

Condition of Unit

As Found: In tolerance

As Left: In tolerance

Notes

1. Calibration is N.I.S.T. Traceable through Control No. CA322
2. Reference 0 dB = 20 µPa.
3. This certificate shall not be reproduced, except in full, without written approval from PCB Piezotronics, Inc.
4. Calibration is performed in compliance with ISO 9001, ISO 10012-1, ANSI/NCSL Z540-1-1994 and ISO 17025.
5. See Manufacturer's Specification Sheet for a detailed listing of performance specifications.
6. Measurement uncertainty (95% confidence level with coverage factor of 2) for reference frequency is +/-0.45 dB.

Technician: J. Rappold Date: 7/30/2009

ACCREDITED
CALIBRATION CERT # 1562.01

PCB PIEZOTRONICS INC
PRESSURE DIVISION
3425 Walden Avenue
Depew, New York 14043
TEL: 888-684-0011 FAX: 716-686-9129 www.pcb.com

Page 1 of 1 3331847216.37

Figure C.6: Transducer 4 Calibration Sheet Page 2

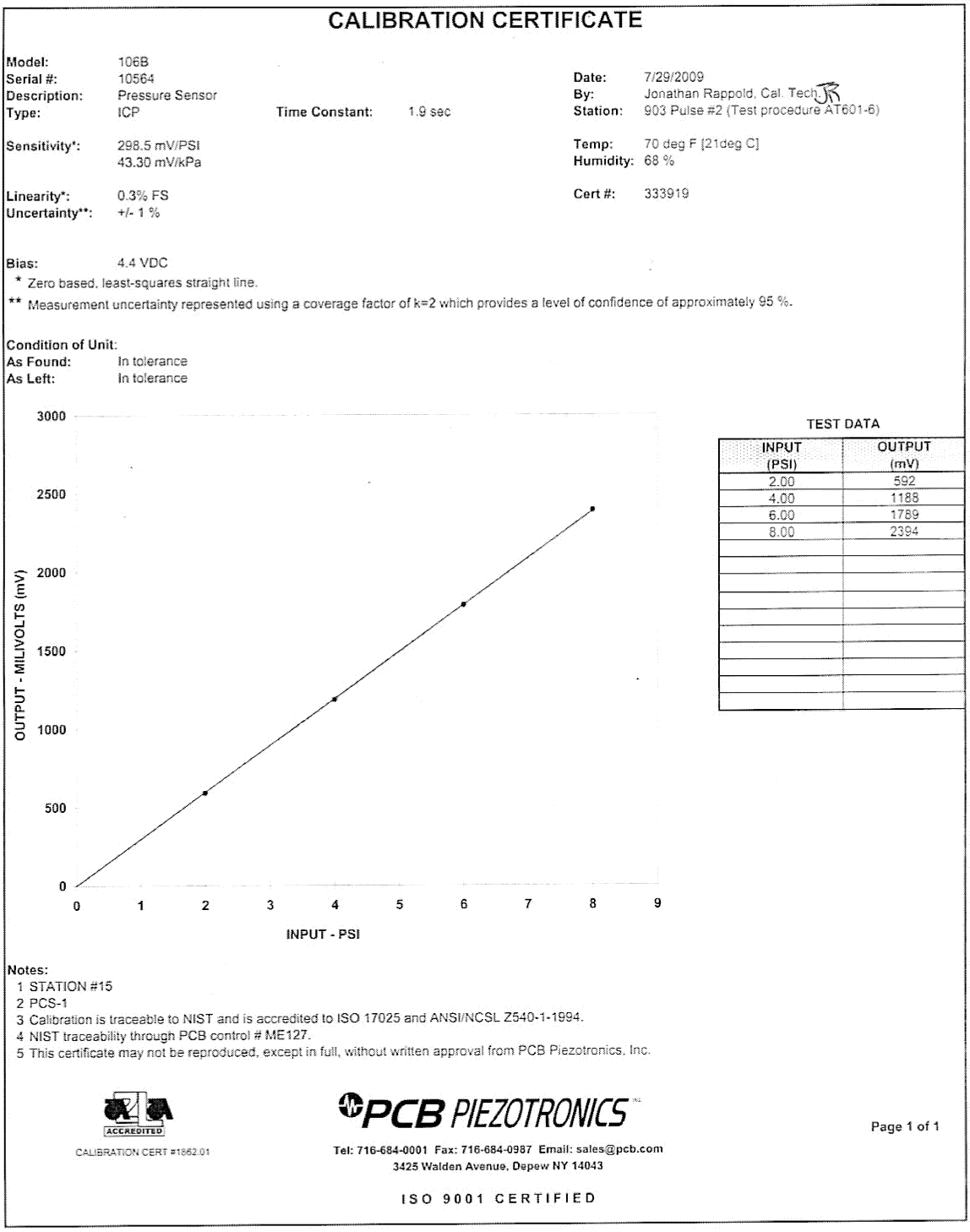

CALIBRATION CERTIFICATE

Model:	106B			**Date:**	7/29/2009
Serial #:	10564			**By:**	Jonathan Rappold, Cal. Tech
Description:	Pressure Sensor				
Type:	ICP	**Time Constant:**	1.9 sec	**Station:**	903 Pulse #2 (Test procedure AT601-6)
Sensitivity*:	298.5 mV/PSI 43.30 mV/kPa			**Temp:** **Humidity:**	70 deg F [21deg C] 68 %
Linearity*:	0.3% FS			**Cert #:**	333919
Uncertainty:**	+/- 1 %				

Bias: 4.4 VDC

* Zero based, least-squares straight line.

** Measurement uncertainty represented using a coverage factor of k=2 which provides a level of confidence of approximately 95 %.

Condition of Unit:
As Found: In tolerance
As Left: In tolerance

TEST DATA

INPUT (PSI)	OUTPUT (mV)
2.00	592
4.00	1188
6.00	1789
8.00	2394

Notes:
1 STATION #15
2 PCS-1
3 Calibration is traceable to NIST and is accredited to ISO 17025 and ANSI/NCSL Z540-1-1994.
4 NIST traceability through PCB control # ME127.
5 This certificate may not be reproduced, except in full, without written approval from PCB Piezotronics, Inc.

ACCREDITED
CALIBRATION CERT #1862.01

PCB PIEZOTRONICS INC.
Tel: 716-684-0001 Fax: 716-684-0987 Email: sales@pcb.com
3425 Walden Avenue, Depew NY 14043

ISO 9001 CERTIFIED

Page 1 of 1

Figure C.7: Transducer 6 Calibration Sheet Page 1

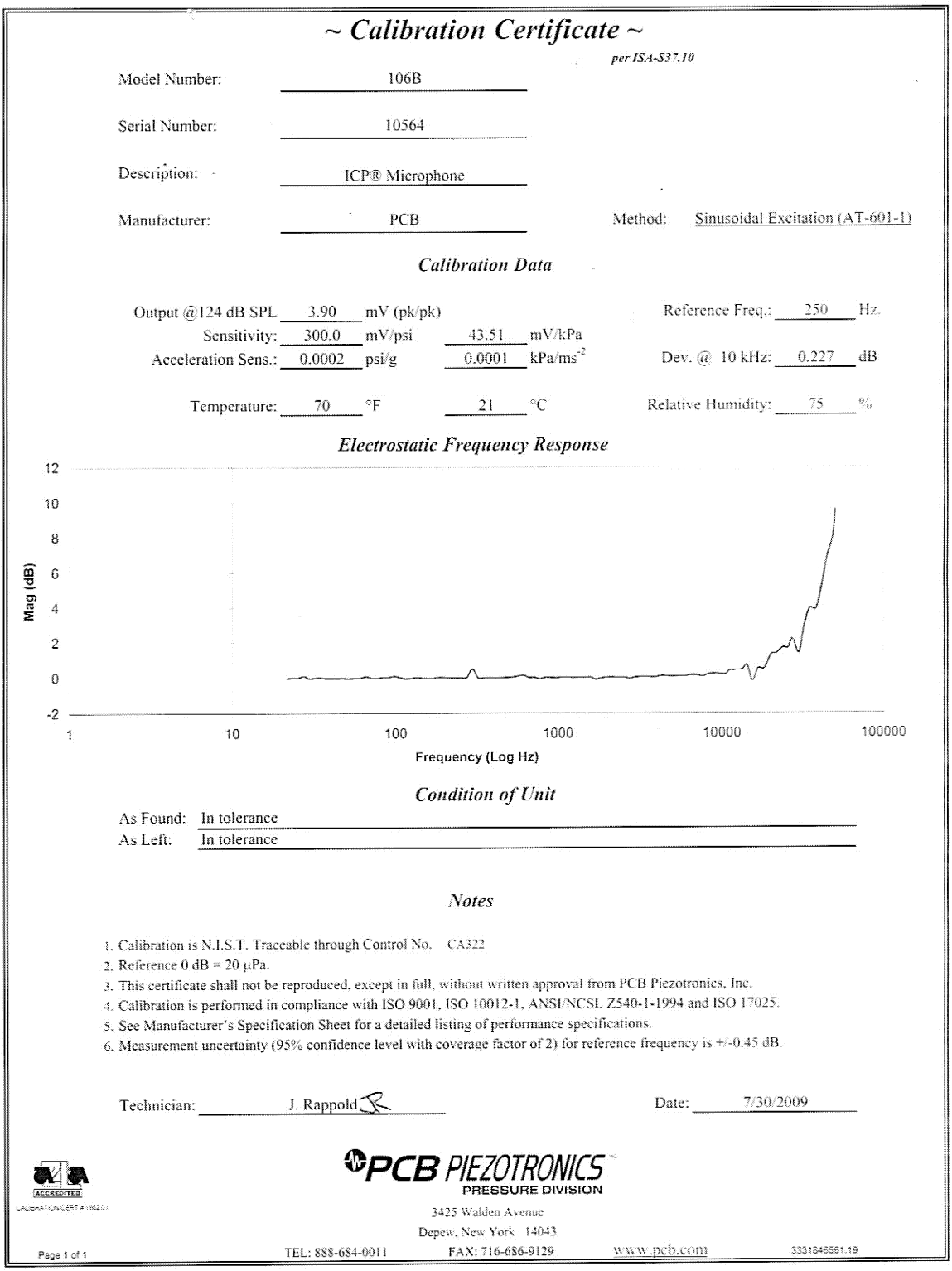

~ Calibration Certificate ~

per ISA-S37.10

Model Number: 106B

Serial Number: 10564

Description: ICP® Microphone

Manufacturer: PCB

Method: Sinusoidal Excitation (AT-601-1)

Calibration Data

Output @124 dB SPL: 3.90 mV (pk/pk)

Sensitivity: 300.0 mV/psi 43.51 mV/kPa

Acceleration Sens.: 0.0002 psi/g 0.0001 kPa/ms^{-2}

Reference Freq.: 250 Hz

Dev. @ 10 kHz: 0.227 dB

Temperature: 70 °F 21 °C

Relative Humidity: 75 %

Electrostatic Frequency Response

Condition of Unit

As Found: In tolerance

As Left: In tolerance

Notes

1. Calibration is N.I.S.T. Traceable through Control No. CA322
2. Reference 0 dB = 20 µPa.
3. This certificate shall not be reproduced, except in full, without written approval from PCB Piezotronics, Inc.
4. Calibration is performed in compliance with ISO 9001, ISO 10012-1, ANSI/NCSL Z540-1-1994 and ISO 17025.
5. See Manufacturer's Specification Sheet for a detailed listing of performance specifications.
6. Measurement uncertainty (95% confidence level with coverage factor of 2) for reference frequency is +/-0.45 dB.

Technician: J. Rappold Date: 7/30/2009

ACCREDITED
CALIBRATION CERT # 1952.01

PCB PIEZOTRONICS
PRESSURE DIVISION
3425 Walden Avenue
Depew, New York 14043
TEL: 888-684-0011 FAX: 716-686-9129 www.pcb.com

Page 1 of 1

3331846561.19

Figure C.8: Transducer 6 Calibration Sheet Page 2

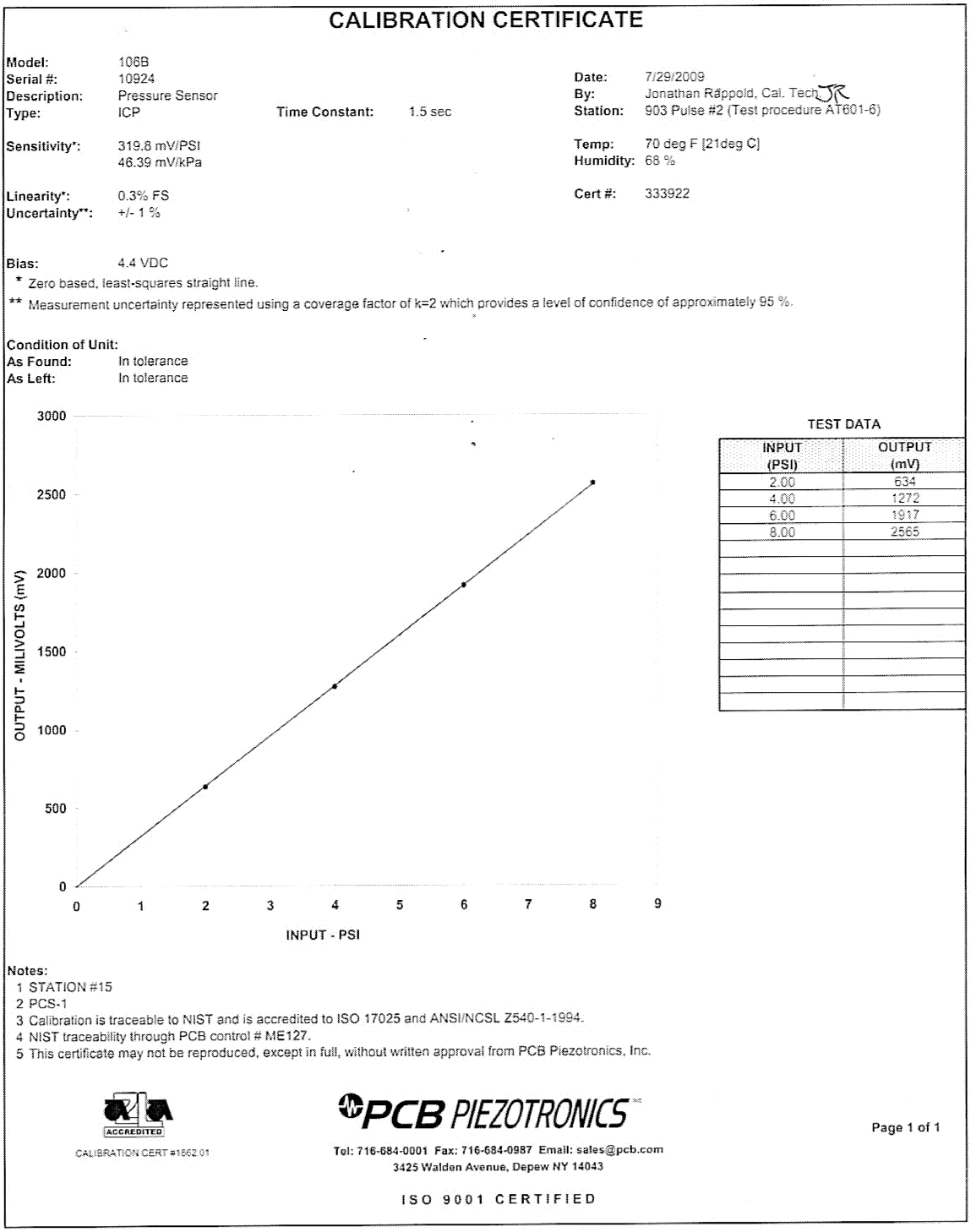

CALIBRATION CERTIFICATE

Model:	106B			**Date:**	7/29/2009
Serial #:	10924			**By:**	Jonathan Rappold, Cal. Tech
Description:	Pressure Sensor				
Type:	ICP	**Time Constant:**	1.5 sec	**Station:**	903 Pulse #2 (Test procedure AT601-6)
Sensitivity*:	319.8 mV/PSI 46.39 mV/kPa			**Temp:** **Humidity:**	70 deg F [21deg C] 68 %
Linearity*:	0.3% FS			**Cert #:**	333922
Uncertainty:**	+/- 1 %				

Bias: 4.4 VDC

* Zero based, least-squares straight line.

** Measurement uncertainty represented using a coverage factor of k=2 which provides a level of confidence of approximately 95 %.

Condition of Unit:
As Found: In tolerance
As Left: In tolerance

TEST DATA

INPUT (PSI)	OUTPUT (mV)
2.00	634
4.00	1272
6.00	1917
8.00	2565

Notes:
1 STATION #15
2 PCS-1
3 Calibration is traceable to NIST and is accredited to ISO 17025 and ANSI/NCSL Z540-1-1994.
4 NIST traceability through PCB control # ME127.
5 This certificate may not be reproduced, except in full, without written approval from PCB Piezotronics, Inc.

ACCREDITED
CALIBRATION CERT #1662.01

PCB PIEZOTRONICS
Tel: 716-684-0001 Fax: 716-684-0987 Email: sales@pcb.com
3425 Walden Avenue, Depew NY 14043

ISO 9001 CERTIFIED

Page 1 of 1

Figure C.9: Transducer 7 Calibration Sheet Page 1

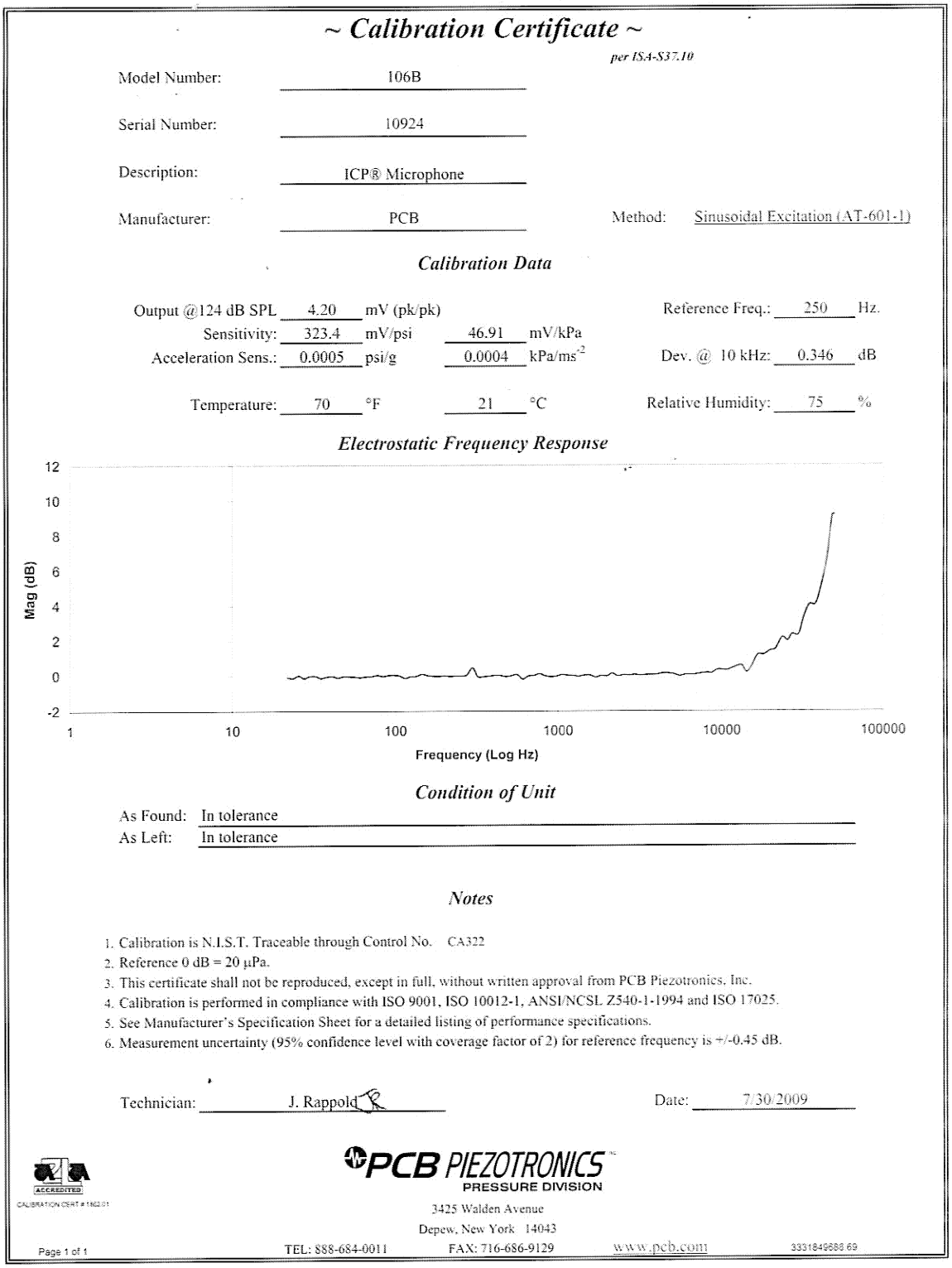

~ Calibration Certificate ~

per ISA-S37.10

Model Number: 106B

Serial Number: 10924

Description: ICP® Microphone

Manufacturer: PCB Method: Sinusoidal Excitation (AT-601-1)

Calibration Data

Output @124 dB SPL 4.20 mV (pk/pk) Reference Freq.: 250 Hz.

Sensitivity: 323.4 mV/psi 46.91 mV/kPa

Acceleration Sens.: 0.0005 psi/g 0.0004 kPa/ms^{-2} Dev. @ 10 kHz: 0.346 dB

Temperature: 70 °F 21 °C Relative Humidity: 75 %

Electrostatic Frequency Response

Condition of Unit

As Found: In tolerance

As Left: In tolerance

Notes

1. Calibration is N.I.S.T. Traceable through Control No. CA322
2. Reference 0 dB = 20 µPa.
3. This certificate shall not be reproduced, except in full, without written approval from PCB Piezotronics, Inc.
4. Calibration is performed in compliance with ISO 9001, ISO 10012-1, ANSI/NCSL Z540-1-1994 and ISO 17025.
5. See Manufacturer's Specification Sheet for a detailed listing of performance specifications.
6. Measurement uncertainty (95% confidence level with coverage factor of 2) for reference frequency is +/-0.45 dB.

Technician: J. Rappold Date: 7/30/2009

ACCREDITED
CALIBRATION CERT # 1952.01

PCB PIEZOTRONICS
PRESSURE DIVISION
3425 Walden Avenue
Depew, New York 14043
TEL: 888-684-0011 FAX: 716-686-9129 www.pcb.com

Page 1 of 1 3331849688.69

Figure C.10: Transducer 7 Calibration Sheet Page 2

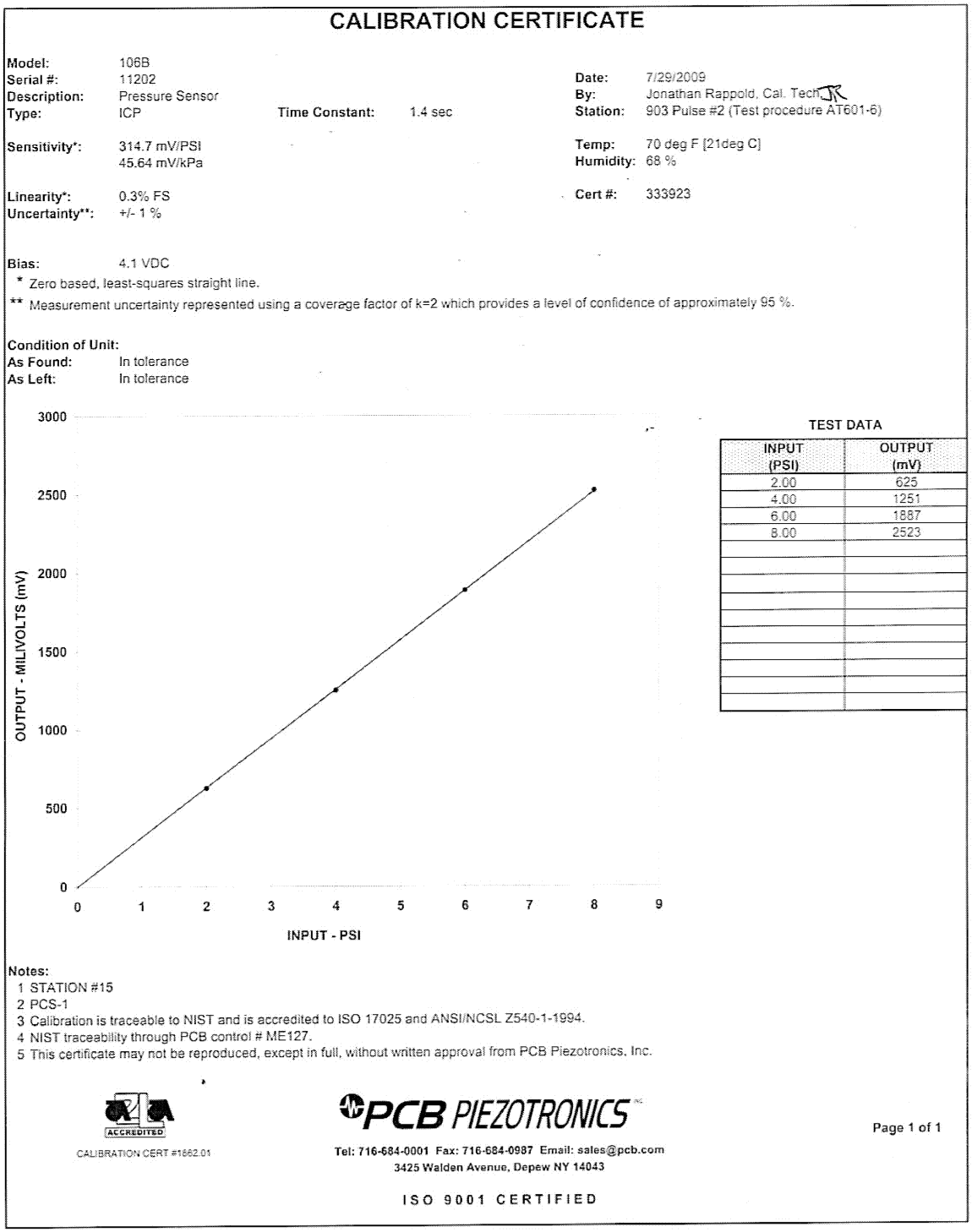

CALIBRATION CERTIFICATE

Model: 106B
Serial #: 11202
Description: Pressure Sensor
Type: ICP
Time Constant: 1.4 sec

Date: 7/29/2009
By: Jonathan Rappold, Cal. Tech
Station: 903 Pulse #2 (Test procedure AT601-6)

Sensitivity*: 314.7 mV/PSI
45.64 mV/kPa

Temp: 70 deg F [21deg C]
Humidity: 68 %

Linearity*: 0.3% FS
Uncertainty**: +/- 1 %

Cert #: 333923

Bias: 4.1 VDC

* Zero based, least-squares straight line.

** Measurement uncertainty represented using a coverage factor of k=2 which provides a level of confidence of approximately 95 %.

Condition of Unit:
As Found: In tolerance
As Left: In tolerance

TEST DATA

INPUT (PSI)	OUTPUT (mV)
2.00	625
4.00	1251
6.00	1887
8.00	2523

Notes:
1 STATION #15
2 PCS-1
3 Calibration is traceable to NIST and is accredited to ISO 17025 and ANSI/NCSL Z540-1-1994.
4 NIST traceability through PCB control # ME127.
5 This certificate may not be reproduced, except in full, without written approval from PCB Piezotronics, Inc.

ACCREDITED
CALIBRATION CERT #1662.01

PCB PIEZOTRONICS INC.
Tel: 716-684-0001 Fax: 716-684-0987 Email: sales@pcb.com
3425 Walden Avenue, Depew NY 14043

ISO 9001 CERTIFIED

Page 1 of 1

Figure C.11: Transducer 8 Calibration Sheet Page 1

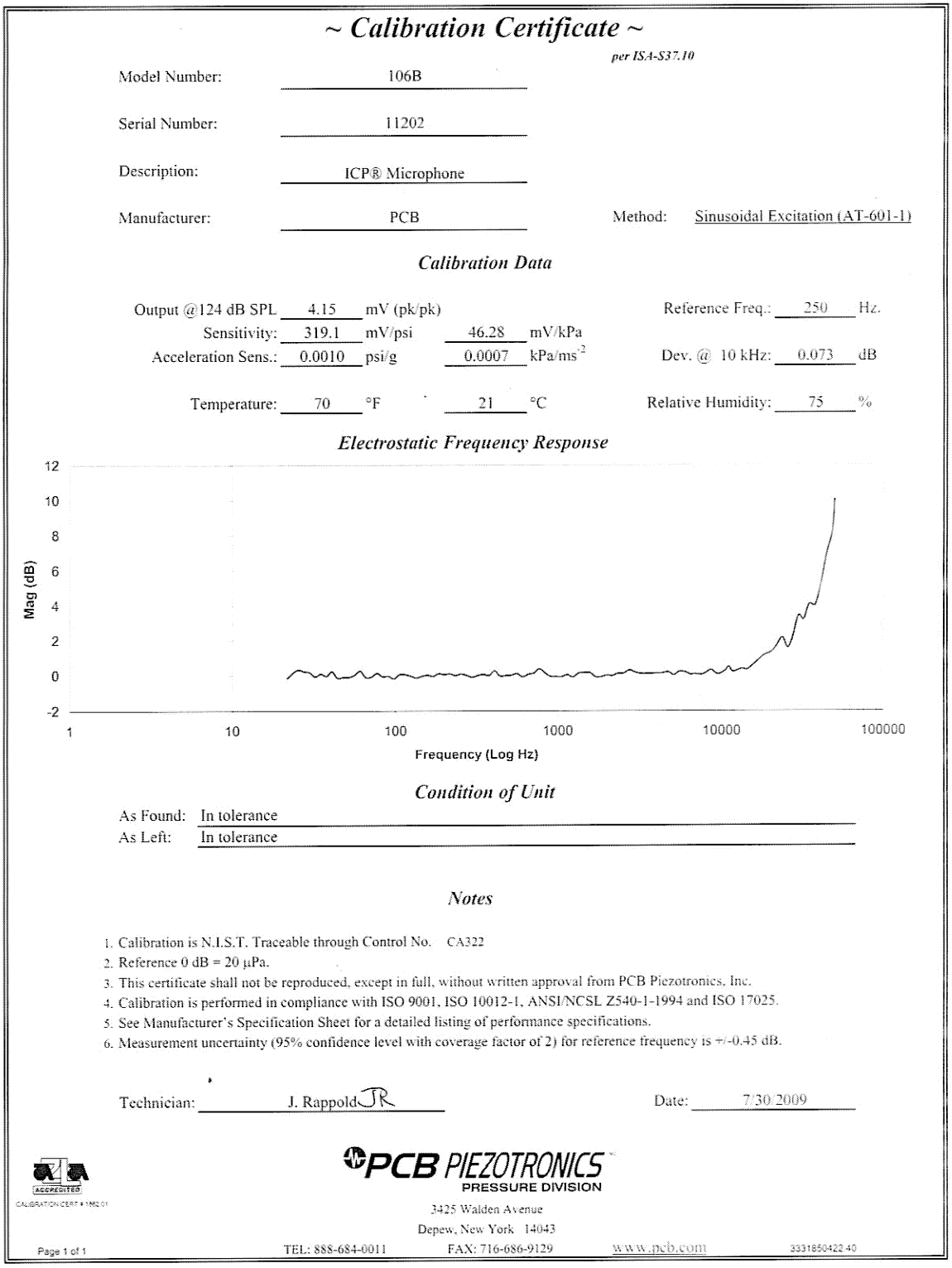

~ Calibration Certificate ~

per ISA-S37.10

Model Number: 106B

Serial Number: 11202

Description: ICP® Microphone

Manufacturer: PCB Method: Sinusoidal Excitation (AT-601-1)

Calibration Data

Output @124 dB SPL 4.15 mV (pk/pk) Reference Freq.: 250 Hz.

Sensitivity: 319.1 mV/psi 46.28 mV/kPa

Acceleration Sens.: 0.0010 psi/g 0.0007 kPa/ms^{-2} Dev. @ 10 kHz: 0.073 dB

Temperature: 70 °F 21 °C Relative Humidity: 75 %

Electrostatic Frequency Response

Condition of Unit

As Found: In tolerance

As Left: In tolerance

Notes

1. Calibration is N.I.S.T. Traceable through Control No. CA322
2. Reference 0 dB = 20 µPa.
3. This certificate shall not be reproduced, except in full, without written approval from PCB Piezotronics, Inc.
4. Calibration is performed in compliance with ISO 9001, ISO 10012-1, ANSI/NCSL Z540-1-1994 and ISO 17025.
5. See Manufacturer's Specification Sheet for a detailed listing of performance specifications.
6. Measurement uncertainty (95% confidence level with coverage factor of 2) for reference frequency is +/-0.45 dB.

Technician: J. Rappold JR Date: 7/30/2009

ACCREDITED
CALIBRATION CERT # 1982.01

PCB PIEZOTRONICS
PRESSURE DIVISION
3425 Walden Avenue
Depew, New York 14043

Page 1 of 1 TEL: 888-684-0011 FAX: 716-686-9129 www.pcb.com 33318S0422.40

Figure C.12: Transducer 8 Calibration Sheet Page 2

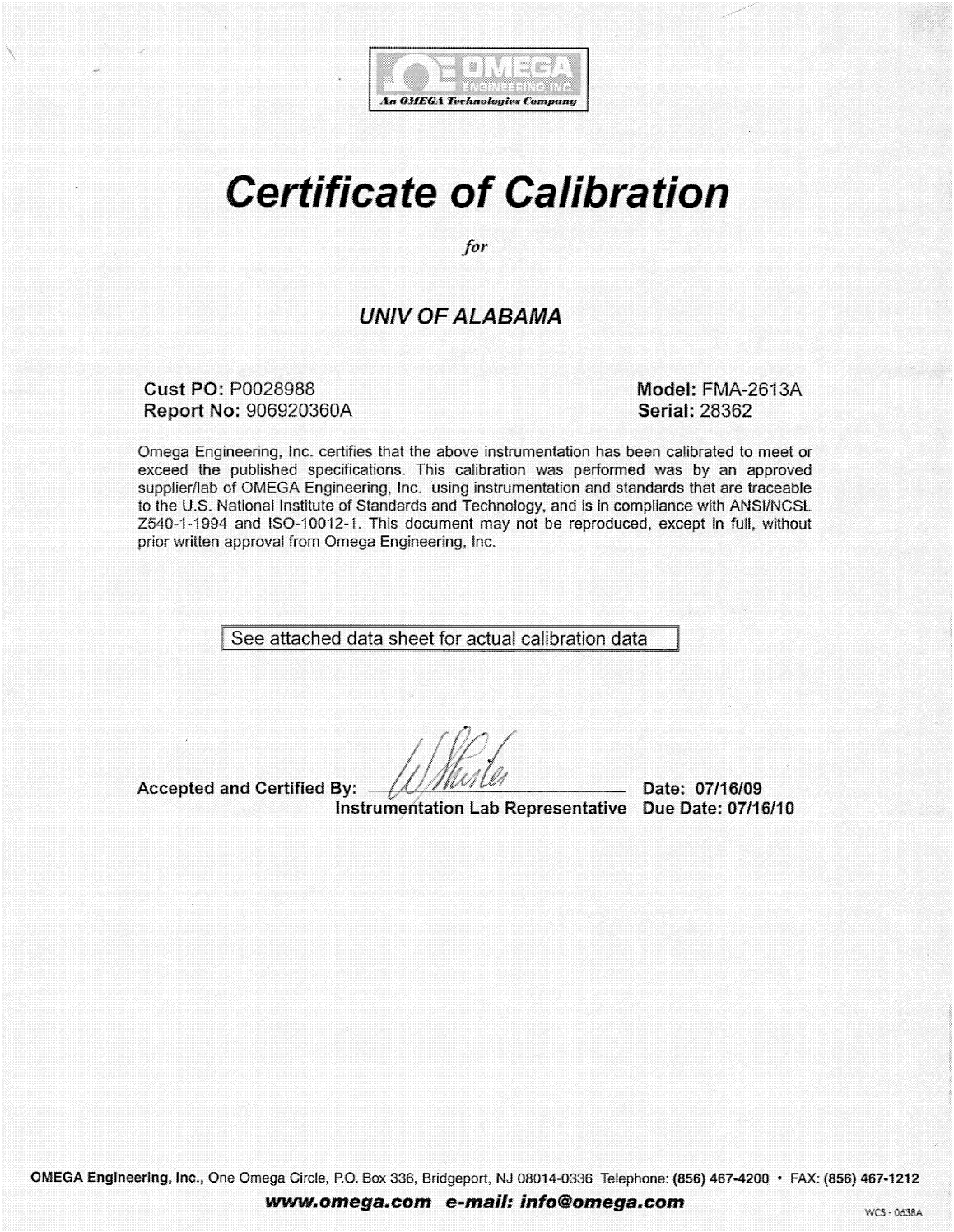

OMEGA ENGINEERING, INC.
An OMEGA Technologies Company

Certificate of Calibration

for

UNIV OF ALABAMA

Cust PO: P0028988
Report No: 906920360A

Model: FMA-2613A
Serial: 28362

Omega Engineering, Inc. certifies that the above instrumentation has been calibrated to meet or exceed the published specifications. This calibration was performed was by an approved supplier/lab of OMEGA Engineering, Inc. using instrumentation and standards that are traceable to the U.S. National Institute of Standards and Technology, and is in compliance with ANSI/NCSL Z540-1-1994 and ISO-10012-1. This document may not be reproduced, except in full, without prior written approval from Omega Engineering, Inc.

See attached data sheet for actual calibration data

Accepted and Certified By: _____ **Date: 07/16/09**
Instrumentation Lab Representative **Due Date: 07/16/10**

OMEGA Engineering, Inc., One Omega Circle, P.O. Box 336, Bridgeport, NJ 08014-0336 Telephone: **(856) 467-4200** • FAX: **(856) 467-1212**
www.omega.com e-mail: info@omega.com

WCS - 0638A

Figure C.13: Oxygen Mass Flow Controller Calibration Sheet Page 1

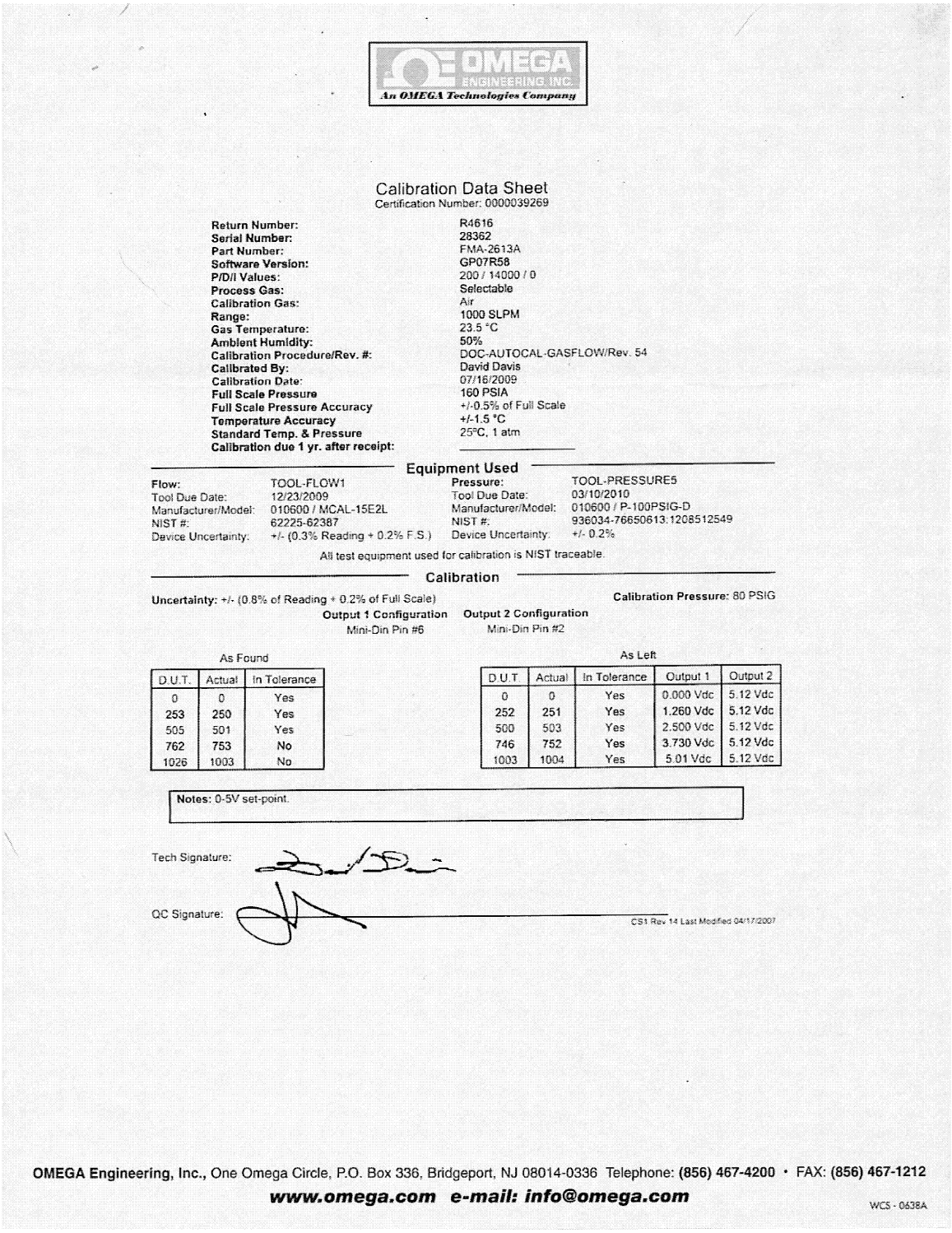

OMEGA ENGINEERING INC.
An OMEGA Technologies Company

Calibration Data Sheet
Certification Number: 0000039269

Return Number:	R4616
Serial Number:	28362
Part Number:	FMA-2613A
Software Version:	GP07R58
P/D/I Values:	200 / 14000 / 0
Process Gas:	Selectable
Calibration Gas:	Air
Range:	1000 SLPM
Gas Temperature:	23.5 °C
Ambient Humidity:	50%
Calibration Procedure/Rev. #:	DOC-AUTOCAL-GASFLOW/Rev. 54
Calibrated By:	David Davis
Calibration Date:	07/16/2009
Full Scale Pressure	160 PSIA
Full Scale Pressure Accuracy	+/-0.5% of Full Scale
Temperature Accuracy	+/-1.5 °C
Standard Temp. & Pressure	25°C, 1 atm
Calibration due 1 yr. after receipt:	

Equipment Used

Flow:	TOOL-FLOW1	**Pressure:**	TOOL-PRESSURE5
Tool Due Date:	12/23/2009	Tool Due Date:	03/10/2010
Manufacturer/Model:	010600 / MCAL-15E2L	Manufacturer/Model:	010600 / P-100PSIG-D
NIST #:	62225-62387	NIST #:	936034-76650613:1208512549
Device Uncertainty:	+/- (0.3% Reading + 0.2% F.S.)	Device Uncertainty:	+/- 0.2%

All test equipment used for calibration is NIST traceable.

Calibration

Uncertainty: +/- (0.8% of Reading + 0.2% of Full Scale) **Calibration Pressure:** 80 PSIG

Output 1 Configuration Mini-Din Pin #6

Output 2 Configuration Mini-Din Pin #2

As Found

D.U.T.	Actual	In Tolerance
0	0	Yes
253	250	Yes
505	501	Yes
762	753	No
1026	1003	No

As Left

D.U.T.	Actual	In Tolerance	Output 1	Output 2
0	0	Yes	0.000 Vdc	5.12 Vdc
252	251	Yes	1.260 Vdc	5.12 Vdc
500	503	Yes	2.500 Vdc	5.12 Vdc
746	752	Yes	3.730 Vdc	5.12 Vdc
1003	1004	Yes	5.01 Vdc	5.12 Vdc

Notes: 0-5V set-point.

Tech Signature:

QC Signature:

CS1 Rev 14 Last Modified 04/17/2007

OMEGA Engineering, Inc., One Omega Circle, P.O. Box 336, Bridgeport, NJ 08014-0336 Telephone: **(856) 467-4200** • FAX: **(856) 467-1212**

www.omega.com e-mail: info@omega.com

WCS - 0638A

Figure C.14: Oxygen Mass Flow Controller Calibration Sheet Page 2

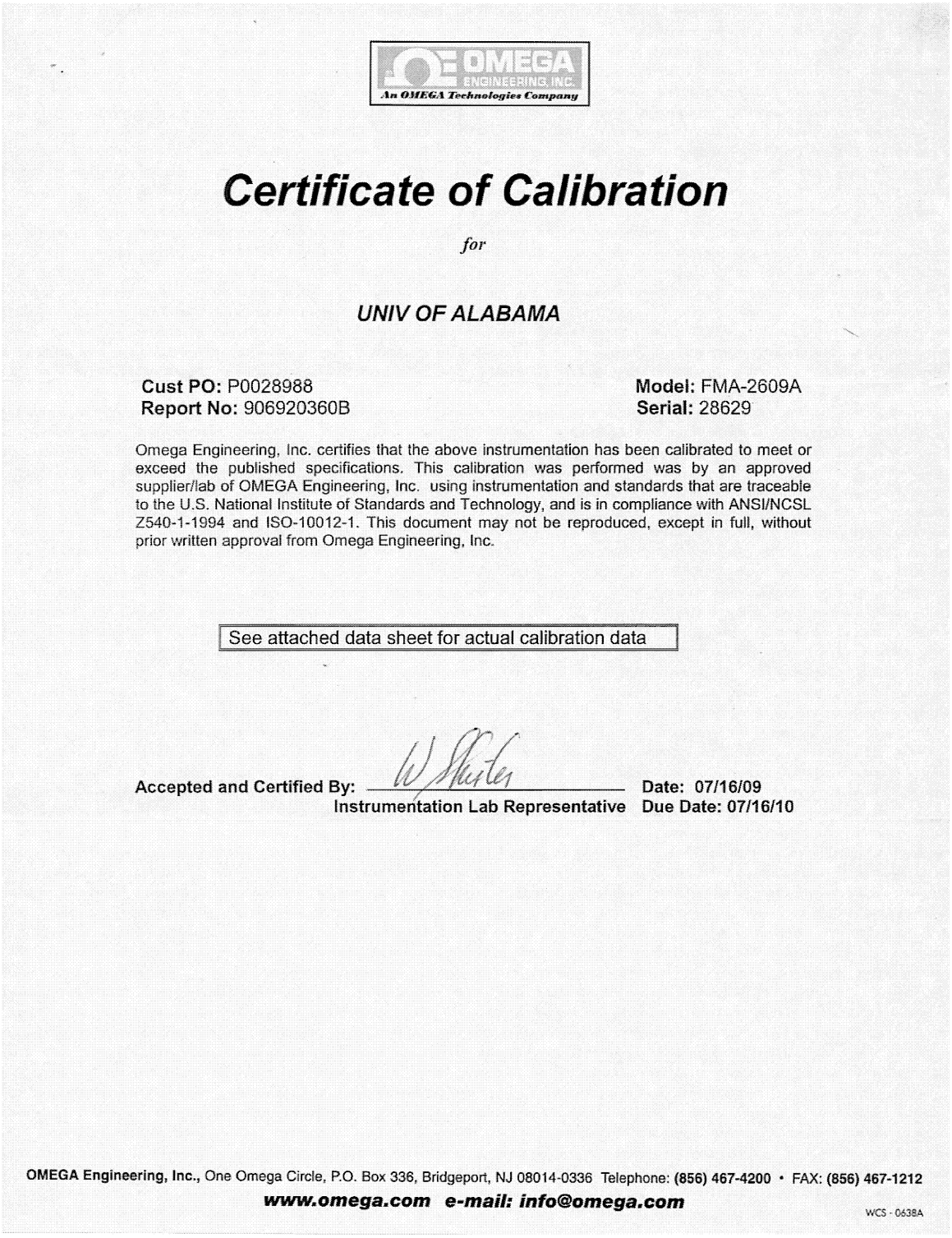

OMEGA ENGINEERING, INC.
An OMEGA Technologies Company

Certificate of Calibration

for

UNIV OF ALABAMA

Cust PO: P0028988
Report No: 906920360B

Model: FMA-2609A
Serial: 28629

Omega Engineering, Inc. certifies that the above instrumentation has been calibrated to meet or exceed the published specifications. This calibration was performed was by an approved supplier/lab of OMEGA Engineering, Inc. using instrumentation and standards that are traceable to the U.S. National Institute of Standards and Technology, and is in compliance with ANSI/NCSL Z540-1-1994 and ISO-10012-1. This document may not be reproduced, except in full, without prior written approval from Omega Engineering, Inc.

See attached data sheet for actual calibration data

Accepted and Certified By: _____ **Date:** 07/16/09
Instrumentation Lab Representative **Due Date:** 07/16/10

OMEGA Engineering, Inc., One Omega Circle, P.O. Box 336, Bridgeport, NJ 08014-0336 Telephone: **(856) 467-4200** • FAX: **(856) 467-1212**
www.omega.com e-mail: info@omega.com

WCS - 0638A

Figure C.15: Methane Mass Flow Controller Calibration Sheet Page 1

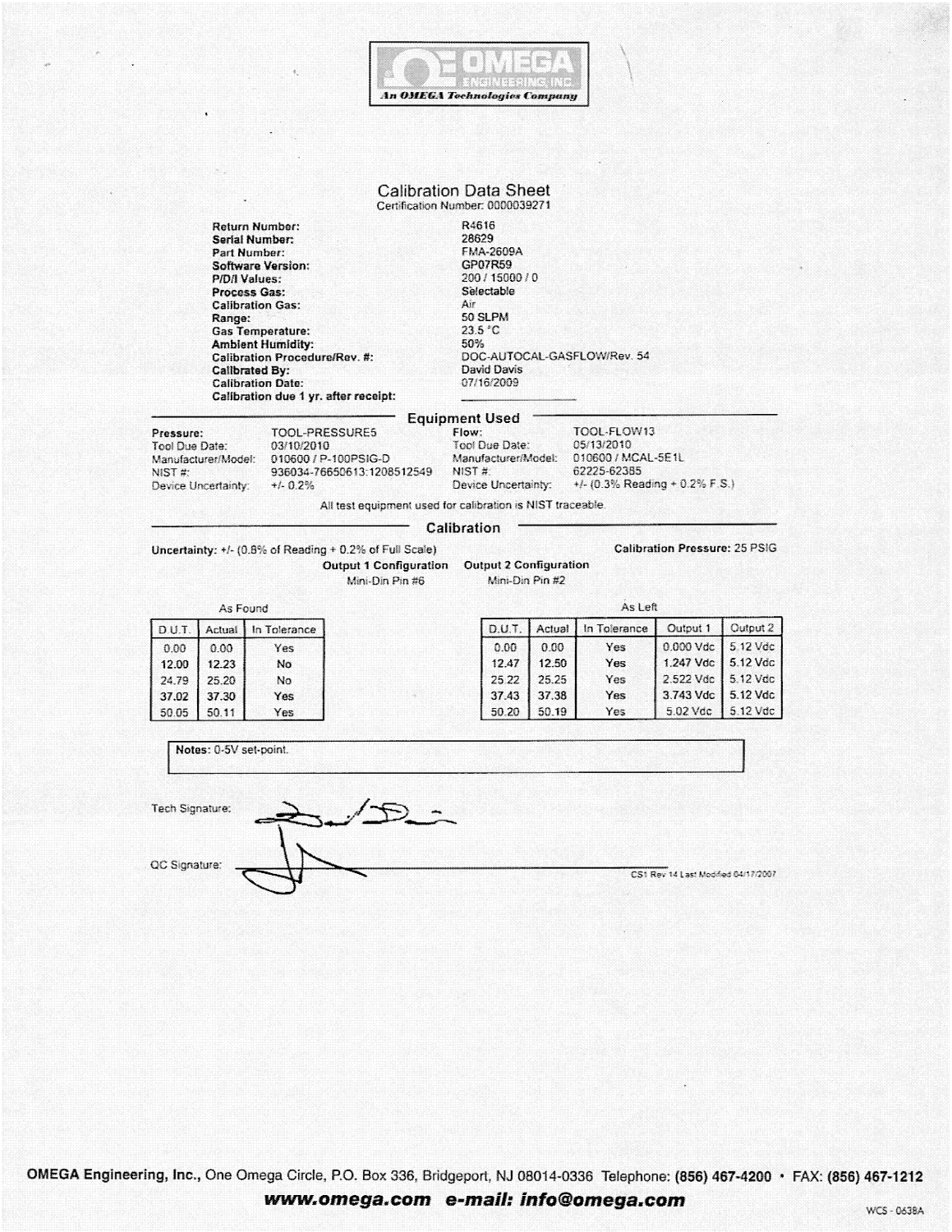

OMEGA ENGINEERING INC.
An OMEGA Technologies Company

Calibration Data Sheet
Certification Number: 0000039271

Return Number:	R4616
Serial Number:	28629
Part Number:	FMA-2609A
Software Version:	GP07R59
P/D/I Values:	200 / 15000 / 0
Process Gas:	Selectable
Calibration Gas:	Air
Range:	50 SLPM
Gas Temperature:	23.5 °C
Ambient Humidity:	50%
Calibration Procedure/Rev. #:	DOC-AUTOCAL-GASFLOW/Rev. 54
Calibrated By:	David Davis
Calibration Date:	07/16/2009
Calibration due 1 yr. after receipt:	

Equipment Used

Pressure:	TOOL-PRESSURE5	**Flow:**	TOOL-FLOW13
Tool Due Date:	03/10/2010	Tool Due Date:	05/13/2010
Manufacturer/Model:	010600 / P-100PSIG-D	Manufacturer/Model:	010600 / MCAL-5E1L
NIST #:	936034-76650613:1208512549	NIST #:	62225-62385
Device Uncertainty:	+/- 0.2%	Device Uncertainty:	+/- (0.3% Reading + 0.2% F.S.)

All test equipment used for calibration is NIST traceable.

Calibration

Uncertainty: +/- (0.6% of Reading + 0.2% of Full Scale) **Calibration Pressure:** 25 PSIG

Output 1 Configuration Mini-Din Pin #6
Output 2 Configuration Mini-Din Pin #2

As Found

D.U.T.	Actual	In Tolerance
0.00	0.00	Yes
12.00	12.23	No
24.79	25.20	No
37.02	37.30	Yes
50.05	50.11	Yes

As Left

D.U.T.	Actual	In Tolerance	Output 1	Output 2
0.00	0.00	Yes	0.000 Vdc	5.12 Vdc
12.47	12.50	Yes	1.247 Vdc	5.12 Vdc
25.22	25.25	Yes	2.522 Vdc	5.12 Vdc
37.43	37.38	Yes	3.743 Vdc	5.12 Vdc
50.20	50.19	Yes	5.02 Vdc	5.12 Vdc

Notes: 0-5V set-point.

Tech Signature:

QC Signature:

CS1 Rev 14 Last Modified 04/17/2007

OMEGA Engineering, Inc., One Omega Circle, P.O. Box 336, Bridgeport, NJ 08014-0336 Telephone: **(856) 467-4200** • FAX: **(856) 467-1212**
www.omega.com e-mail: info@omega.com

WCS - 0638A

Figure C.16: Methane Mass Flow Controller Calibration Sheet Page 2

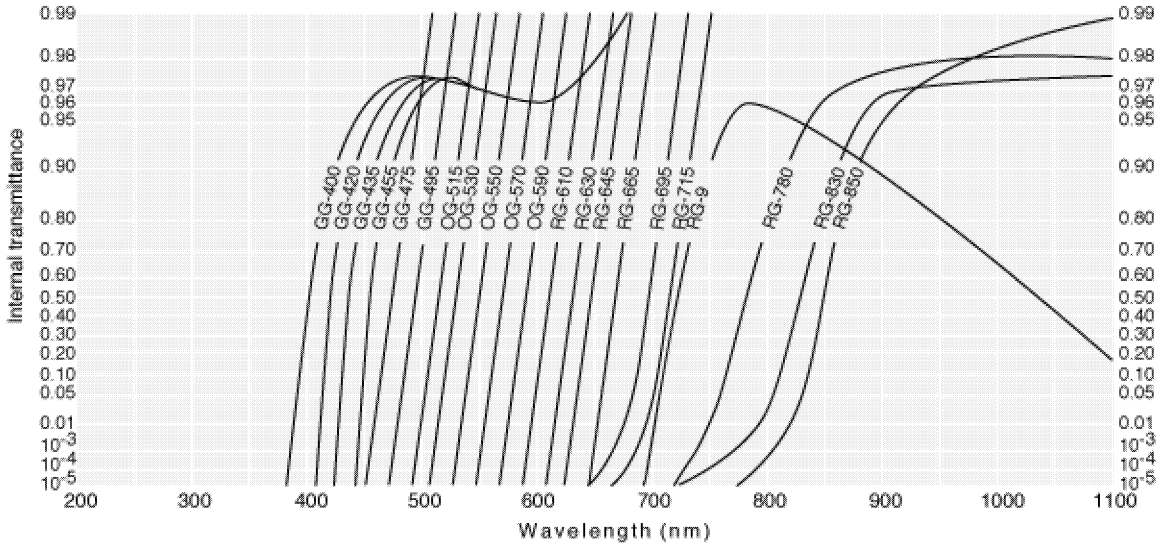

Figure C.17: CH* GG-420 High-Pass Filter Transmittance Curve

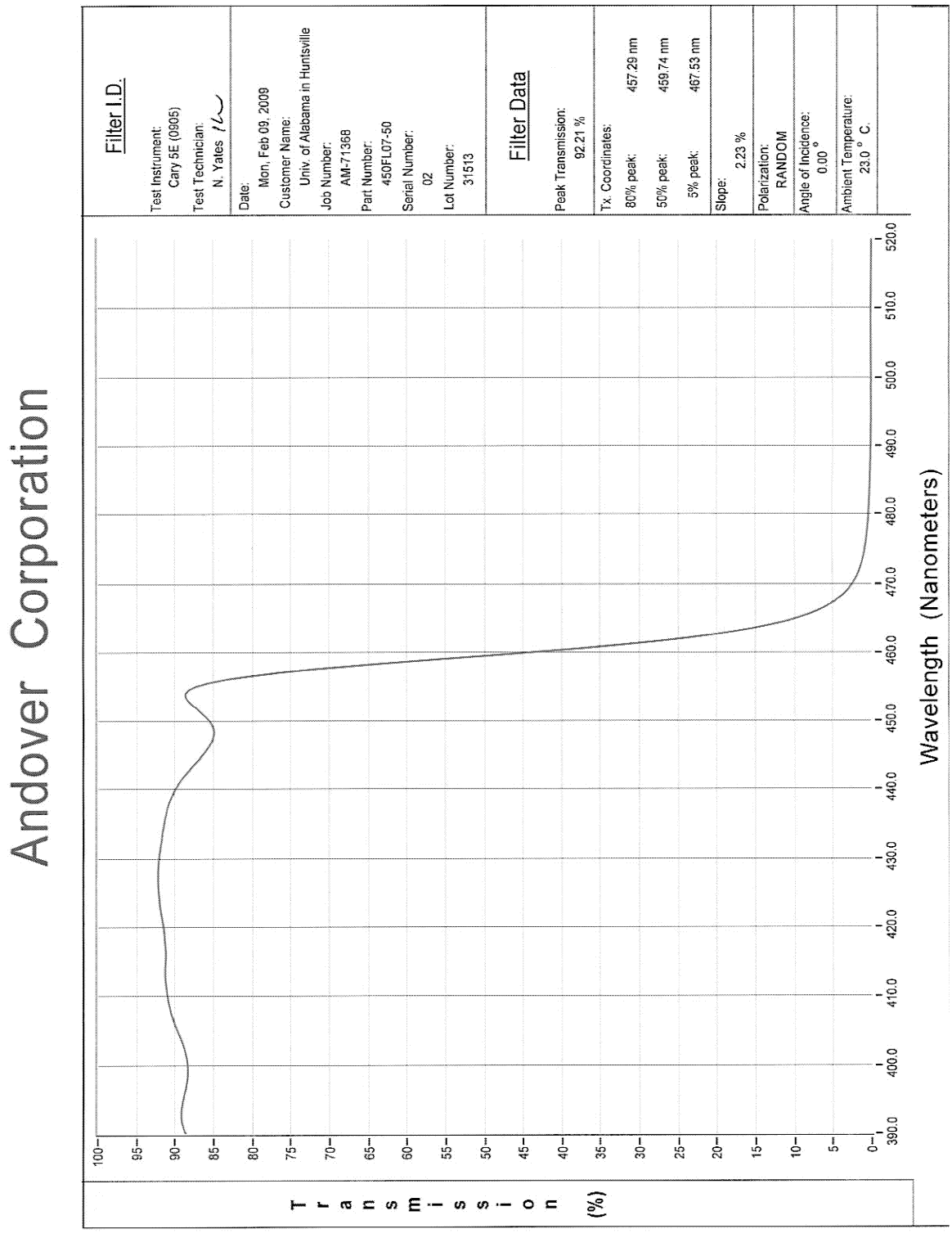

Figure C.18: CH* Low-Pass Filter Transmittance Curve

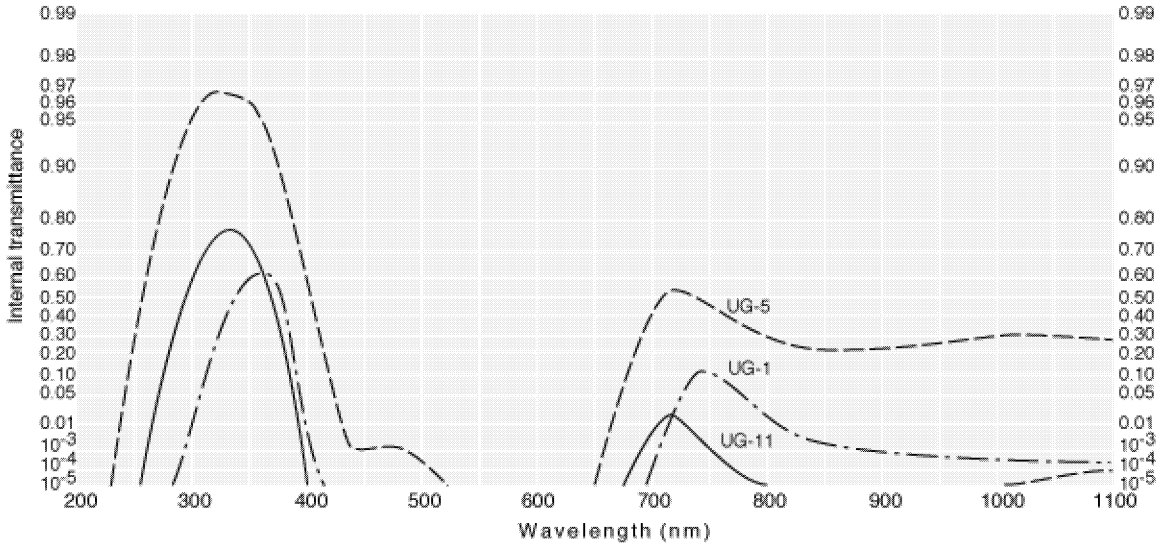

Figure C.19: OH* UG-11 Bandpass Filter Transmittance Curve

APPENDIX D

EQUIPMENT SPECIFICATION SHEETS

MASS AND VOLUMETRIC GAS FLOW CONTROLLERS

For Clean Gases

FMA/FVL-2600A Series
Starts at

$1470

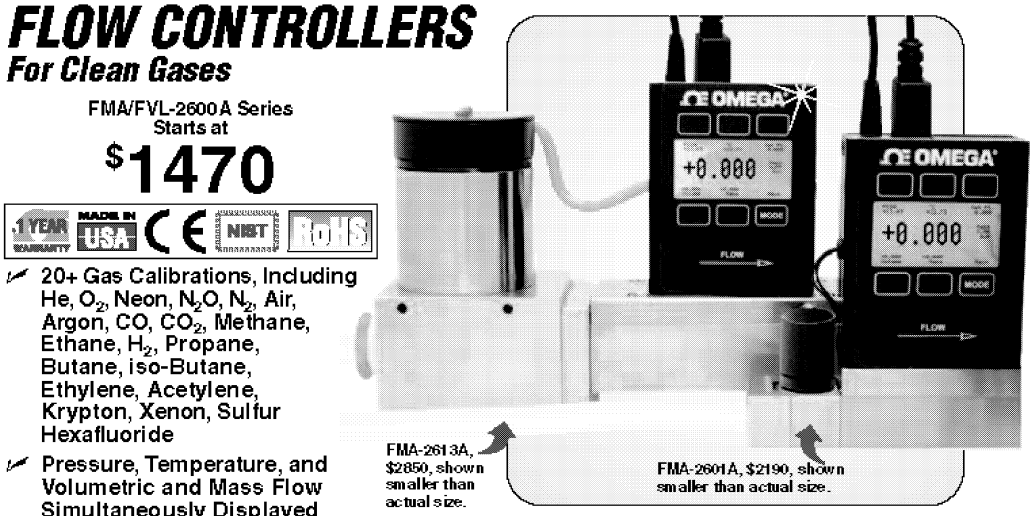

FMA-2613A, $2850, shown smaller than actual size.

FMA-2601A, $2190, shown smaller than actual size.

- 20+ Gas Calibrations, Including He, O_2, Neon, N_2O, N_2, Air, Argon, CO, CO_2, Methane, Ethane, H_2, Propane, Butane, iso-Butane, Ethylene, Acetylene, Krypton, Xenon, Sulfur Hexafluoride
- Pressure, Temperature, and Volumetric and Mass Flow Simultaneously Displayed (FMA-2600A Series)
- Easy-to-Use Pushbutton Interface
- NIST Traceability Standard
- Full Scale Ranges from 0.5 SCCM to 1500 SLM
- Response Time of 50 to 100 ms Typical
- Turndown Ratio of 100:1 Typical
- Position Insensitive
- ±0.8% Reading Accuracy
- RS232 Standard

The FMA-2600A and FVL-2600A Series mass and volumetric flow controllers use the principle of differential pressure within a laminar flow field to determine and control mass flow rate. A laminar flow element (LFE) inside the meter forces the gas into laminar (streamlined) flow. Inside this region, the Poiseuille equation dictates that the volumetric flow rate be linearly related to the pressure drop. A differential pressure sensor is used to measure the pressure drop along a fixed distance of the LFE. This, along with the viscosity of the gas, is used to accurately determine the volumetric flow rate.

Quick Selection Guide

- Operating pressures over 15 psig or with more than a little backpressure, use FMA-2600A Series
- Line temperature or pressure changes, use FMA-2600A Series
- If only basic, digital, and uncompensated volumetric flow is required, use the more economical FVL-2600A Series
- For comparing or running flowmeters or controllers in line, use FMA-2600A Series

Separate absolute temperature and pressure sensors are incorporated and correct the volumetric flow rate to a set of standard conditions. This standardized flow rate is commonly called the mass flow rate and is reported in units such as standard cubic feet per minute (SCFM) or standard liters per minute (SLM).

The controller uses a true proportional valve coupled to the flow body to control flow using the integral PID loop controller. Standard units include a 0 to 5 V output (4 to 20 mA optional) and RS232 communications. The gas-select feature and the setpoints can be adjusted from the front keypad or via RS232 communications. Volumetric flow, mass flow, absolute pressure, and temperature can all be viewed or recorded through the RS232 connection. It is also possible to multi-drop up to 26 units on the same serial connection to a distance of 46 m (150').

The FVL-2600A Series comprises volumetric flow controllers only. They do not measure or correct for absolute pressure or temperature. The FMA-2600A Series is recommended if operating pressure is above 15 psig or if there is any restriction or backpressure in the application.

SPECIFICATIONS

Accuracy: ±(0.8% of reading + 0.2%FS)
Repeatability: ±0.2% FS
Turndown Ratio: 100:1
Control Response Time: 100 ms
Input Control Signal: 0 to 5 Vdc, RS232
Output Signal: 0 to 5 Vdc, RS232
Optional Input/Outputs: 4 to 20 mA, 0 to 10 Vdc
Operating Temperature: -10 to 50°C (14 to 122°F)
Zero Shift: 0.02%/ATM FS/°C
Span Shift: 0.02%/ATM FS/°C
Humidity Range: 0 to 100% RH, non-condensing
Excess Flow Rate: 2.4% FS
Wetted Materials: 303 and 302 SS, FKM, silicone RTV (rubber), glass-reinforced nylon, aluminum, brass, 410 SS, silicone, glass; >250 SLM: 416 SS and nickel replace brass

Figure D.1: Mass Flow Controller Specification Sheet Page 1

Maximum Pressure:
Mass Flow Controllers: 145 psig
Volumetric Flow Controllers: Near atmosphere, 15 psig recommended maximum. Volumetric flowmeters and controllers not certified for accuracy at mass flow rates above the rated flow range of the meter. They are designed for near atmospheric pressure conditions only. The recommended maximum operating pressure is 15 psig
Minimum Differential Pressure Required: 5 SLM and under: 5 psid; 10 to 250 SLM: 15 psid; 500 SLM: 5 psid; 1500 SLM: 10 psid

Dimensions: mm (in)

Flow Range	Height	Length	Depth
0.5 to 50 SCCM	100 (3.9)	89 (3.5)	26.7 (1.05)
100 SCCM to 20 SLM	104.1 (4.1)	92 (3.6)	26.7 (1.05)
50 to 100 SLM	120 (4.7)	185 (7.3)	58 (2.25)
250 SLM	140 (5.5)	188 (7.4)	58 (2.25)
500 to 1500 SLM	140 (5.5)	188 (7.4)	58 (2.25)

Please allow approximately 44.5 mm (1.75") on top of the unit for electrical cable connection.

Supply Current: 0.250 A for 20 SLM and under; 0.75 A for 50 SLM and above (typical)
Supply Voltage: 12 to 30 Vdc for units 20 SLM and smaller; 24 to 30 Vdc for units 50 SLM and larger

Electrical Connections: 8-pin circular mini DIN

MOST POPULAR MODELS HIGHLIGHTED!

To Order *(Specify Model Number)*

Model No. Gas Mass Flow Controller	Price	Model No. Volumetric Gas Flow Controller	Price	Connection	Max Flow Rate
FMA-2601A	**$2190**	**FVL-2601A**	**$2190**	10-32 thread	0.5 SCCM
FMA-2602A	**2190**	**FVL-2602A**	**2190**	10-32 thread	1 SCCM
FMA-2614A	**1950**	**FVL-2614A**	**1950**	10-32 thread	2 SCCM
FMA-2615A	**1950**	**FVL-2615A**	**1950**	10-32 thread	5 SCCM
FMA-2603A	**1710**	**FVL-2603A**	**1710**	10-32 thread	10 SCCM
FMA-2616A	**1710**	**FVL-2616A**	**1710**	10-32 thread	20 SCCM
FMA-2604A	**1710**	**FVL-2604A**	**1710**	10-32 thread	50 SCCM
FMA-2617A	**1470**	**FVL-2617A**	**1470**	⅛ FNPT	100 SCCM
FMA-2618A	**1470**	**FVL-2618A**	**1470**	⅛ FNPT	200 SCCM
FMA-2619A	**1470**	**FVL-2619A**	**1470**	⅛ FNPT	500 SCCM
FMA-2620A	**1470**	**FVL-2620A**	**1470**	⅛ FNPT	1 SLM
FMA-2605A	**1470**	**FVL-2605A**	**1470**	⅛ FNPT	2 SLM
FMA-2606A	**1470**	**FVL-2606A**	**1470**	⅛ FNPT	5 SLM
FMA-2607A	**1470**	**FVL-2607A**	**1470**	⅛ FNPT	10 SLM
FMA-2608A	**1710**	**FVL-2608A**	**1710**	⅛ FNPT	20 SLM
FMA-2609A	**1830**	**FVL-2609A**	**1830**	¼ FNPT	50 SLM
FMA-2610A	**2070**	**FVL-2610A**	**2070**	¼ FNPT	100 SLM
FMA-2611A	**2430**	**FVL-2611A**	**2430**	½ FNPT	250 SLM
FMA-2612A	**2490**	**FVL-2612A**	**2490**	¾ FNPT	500 SLM
FMA-2613A	**2850**	**FVL-2613A**	**2850**	¾ FNPT	1000 SLM
FMA-2621A	**3342**	**FVL-2621A**	**3342**	¾ FNPT	1500 SLM

Accessories for FMA/FVL-2600A Series

Model No.	Price	Description
FMA1600-C1	**$35**	Replacement single-ended 1.83 m (6') 8-pin mini DIN cable connector
FMA1600-C3	**42**	1.83 m (6') adaptor cable with male 8-pin DIN to male DB9
FMA1600-PSU	**80**	Replacement 24 Vdc universal power supply
FMA1600-E1	**84**	220 Vac to 12 Vdc power supply for 20 LPM or less
FMA1600-E2	**146**	220 Vac to 24 Vdc power supply for 50 LPM or greater

Comes complete with NIST certificate, 24 Vdc universal power supply, 1.83 m (6') cable 8-pin mini din connector and operator's manual.
*Add **-(*)**: Please specify gas, inlet/outlet or backpressure, and temperature for custom calibrations.*
*For 4 to 20 mA output, add suffix "**-I**" to model number and **$60** to price.*
*For second channel output of 4 to 20 mA, add suffix "**-I2**" to model number and **$60** to price.*
*For second channel output of 0 to 5V, add suffix "**-V2**" to model number and **$60** to price.*
*Standard "**-I2**" and "**-V2**" options are scaled to the flow rate. For a different secondary ouput scale, add suffix "**-T**" for temperature and suffix "**-P**" for pressure, no additional charge.*
*For 4 to 20 mA input, add suffix "**-IN**" to model number, no additional charge.*
*For totalizer option, add suffix "**-TOT**" to model number and **$120** to price.*
Please specify resolution. This is a 6-digit counter. Examples: For totalizing in liters with 1/100 resolution, the max count would be 9999.99.
For totalizing in liters with 1 liter resolution, the max count would be 999999.
Ordering Examples: FMA-2617A-I2T**, ⅛ FNPT mass gas flow controller with optional second channel output of 4 to 20 mA for temperature, $1470 + 60 = **$1530.
***FMA-2620A**, ⅛ FNPT mass flow controller, **$1470**.*

Recommended Reference Book:
Industrial Flow Measurement,
FW-337, $92.
See Section Y for Additional Books.

Figure D.2: Mass Flow Controller Specification Sheet Page 2

NEW

"T" TYPE AIR PROCESS HEATERS

For In-Line Air and Gas Heating

AHP Series Starts at

$67

MADE IN USA · 1 YEAR WARRANTY

- **⅜, ½ or ¾" Diameters**
- **Exit Air or Gas Temperatures to 540°C (1000°F)**
- **Inlet Air or Gas Temperatures to 121°C (250°F)**
- **For Horizontal Mounting**
- **With or Without NPT Fittings***

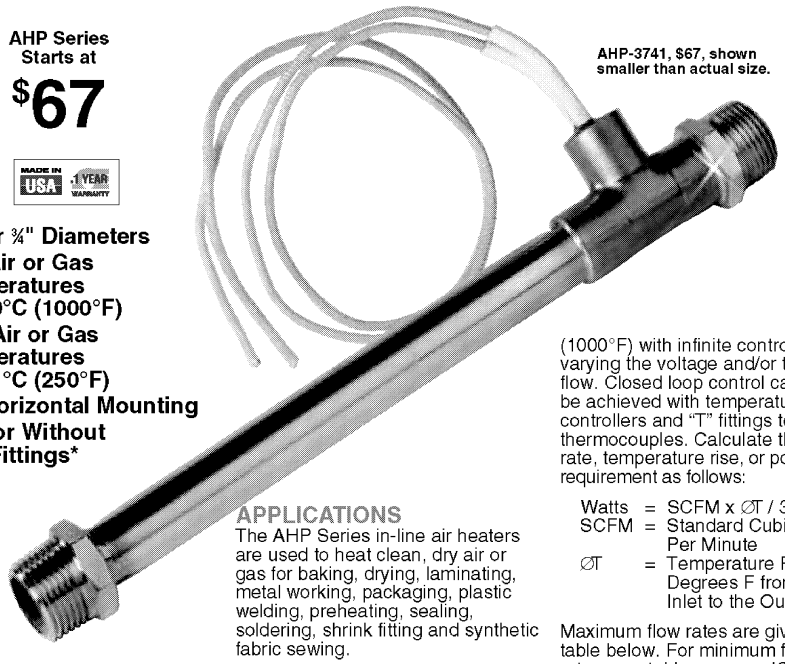

AHP-3741, $67, shown smaller than actual size.

APPLICATIONS

The AHP Series in-line air heaters are used to heat clean, dry air or gas for baking, drying, laminating, metal working, packaging, plastic welding, preheating, sealing, soldering, shrink fitting and synthetic fabric sewing.

AHP series air process heaters provide hot air and gas up to 540°C (1000°F) with infinite control by varying the voltage and/or the air flow. Closed loop control can also be achieved with temperature controllers and "T" fittings to mount thermocouples. Calculate the flow rate, temperature rise, or power requirement as follows:

Watts = SCFM x ∅T / 3
SCFM = Standard Cubic Feet Per Minute
∅T = Temperature Rise in Degrees F from the Inlet to the Outlet

Maximum flow rates are given in the table below. For minimum flow rates, see table on page 120.

MOST POPULAR MODELS HIGHLIGHTED!

To Order *(Specify Model Number)*

Model Number	Volts	Watts	Heated Length mm (in)	Watts/ Inch†	Maximum CFM	Diameter mm (in)	NPT Fitting	Price	Weight g (lb)
120 Vac Models									
AHP-3741	120	200	89 (3½)	57	8	10 (⅜)	¼"	**$67**	82 (0.18)
AHP-5051	120	400	114 (4½)	88	10	13 (½)	⅜"	**80**	113 (0.25)
AHP-7561	120	750	140 (5½)	136	20	19 (¾)	¾"	**105**	308 (0.68)
120/240 Vac Models**									
AHP-3742	120 240	50 200	89 (3½) 89 (3½)	14 57	8 8	10 (⅜)	¼"	**67**	82 (0.18)
AHP-5052	120 240	100 400	11 (4½) 11 (4½)	22 80	10 10	13 (½)	⅜"	**80**	113 (0.25)
AHP-7562	120 240	190 750	14 (5½) 14 (5½)	34 136	20 20	19 (¾)	¾"	**105**	308 (0.68)

** **Note:** To order heaters without NPT fittings add suffix "**-NF**" to model no. price for heaters without fittings is **$44** for **AHP-374** Series, **$54** for **AHP-505** Series, and **$68** for **AHP-756** Series.*
*** These air heaters can be operated on either 120 or 240V. Specifications are shown for operation on both 120 and 240V.*
† Indicates watts per inch of heated length. Use the table above to determine minimum required flow rates. The watts per inch of heated length can be changed by reducing the operating voltage or by ordering a custom made heater.
Ordering Example: AHP-3741/120**, 200 W, 120 Vac "T" Type in-line air/gas heater, **$67.

Figure D.3: Propellant Heaters Specification Sheet Page 1

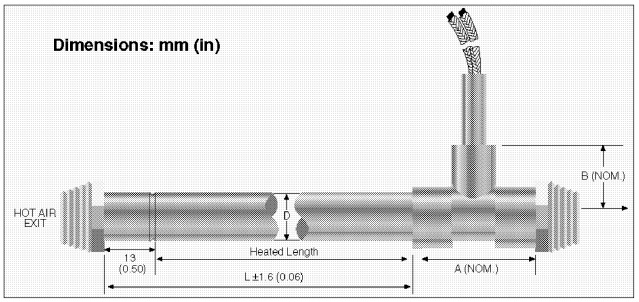

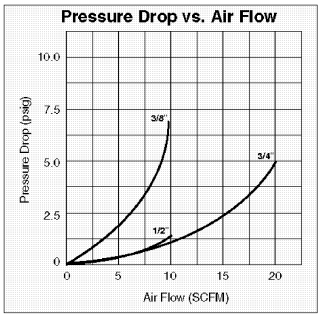

Dimensions: mm (in)

Series	Diameter	Heated Length	L	A	B
AHP-374	9.5 (⅜)	88.9 (3½)	101.6 (4)	7.9 (5/16)	33.3 (1 5/16)
AHP-505	12.7 (½)	114.3 (4½)	127.0 (5)	34.9 (1⅜)	19 (1¾)
AHP-756	19.1 (¾)	139.7 (5½)	152.4 (6)	61.9 (2 7/16)	41.3 (1⅝)

SPECIFICATIONS

Pressure Rating: 80 PSIG
Wattage Tolerance: +5, -10% or better at the voltage specified
Leads:
0.3 m L (1') fiberglass insulated leads

Maximum Watts Per Linear Inch of Heated Length

Minimum CFM Required	⅜" Dia.	½" Dia.	¾" Dia.
1	60	80	120
2	60	80	120
4	100	100	120
6	150	150	150
8	200	200	200
10	-	250	250
15	-	-	375
20	-	-	500

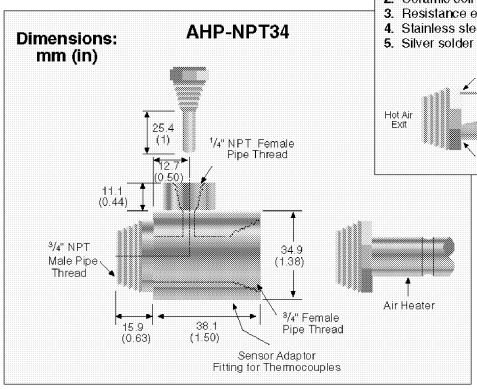

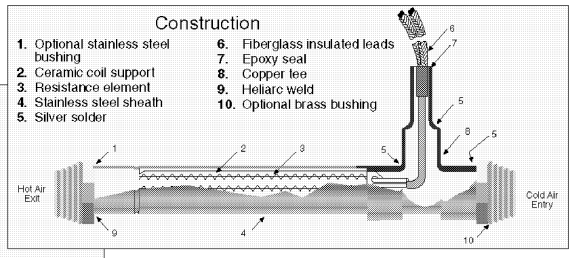

Thermocouple T-Fitting

The AHP-NPT34 fitting can be used with subminiature thermocouple probes (see the OMEGA Complete Temperature Measurement Handbook and Encyclopedia®) and with stainless steel compression fittings (Model SSLK-18-14) to monitor temperature at the outlet of the AHP-756 Series heaters.

Model Number	Price
AHP-NPT34	**$94**

Figure D.4: Propellant Heaters Specification Sheet Page 2

iSeries ⅛ DIN Temperature, Process, and Strain PID Controllers

OMEGA

- High Quality
- 5-Year Warranty
- High Accuracy ±0.5°C (±0.9°F), 0.03% Reading
- User-Friendly, Simple to Configure
- Free Software
- Full Autotune PID Control
- Universal Inputs: RTD, Thermocouple, Process Voltage/Current, Strain
- Totally Programmable Color Displays (Standard)
- Built-InExcitation (Standard)
- 2 Control or Alarm Outputs: DC Pulse, Mechanical Relays, Analog Voltage and Current
- Embedded Internet Connectivity

The OMEGA® CNi8 is a ⅛ DIN size [96 x 48 mm (3.7 x 1.9")] digital panel meter featuring the big iSeries color-changing display. The digits are twice the size of typical ⅛ DIN panel meters. The iSeries meters feature the only LED displays that can be programmed to change color between GREEN, AMBER, and RED at any setpoint or alarm point. The "CNi8" model is available as an extremely accurate programmable digital panel meter with no outputs or with dual outputs for controlling or alarming functions. Other options include isolated programmable analog output, serial communications, MODBUS and Ethernet. The user can easily program the CNi8 for any control or alarming requirement from simple on/off to full autotune PID with a choice of form C SPDT relays, solid state relays, DC pulse, and analog (voltage and current) outputs.

Fully isolated analog output for retransmission of the process value is available in addition to the control and alarm relays (specify model CNi8A33).

The CNi8 covers a broad selection of transducer and transmitter inputs with 2 input models:

Embedded Internet Connectivity!

CNi8 Series Starts at $310

MADE IN USA · 5 YEAR WARRANTY · CE · cULus

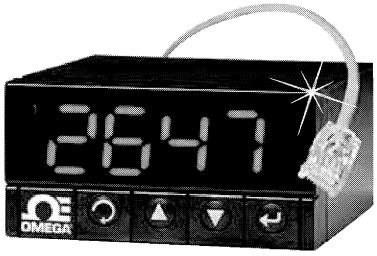

The universal temperature and process instrument (model "i") handles 10 common types of thermocouples, multiple RTD's, and several process (DC) voltage and current ranges. This model also features built-in excitation, 24 Vdc @ 25 mA. With its wide choice of signal inputs, this model is an excellent choice for measuring or controlling temperature with a thermocouple, RTD, or 4 to 20 mA transmitter.

The strain and process instrument (model "iS") measures inputs from load cells, pressure transducers, and most any strain gage sensor as well as process voltage and current ranges. The "iS" has built-in 5 or 10 Vdc excitation for bridge transducers, 5 Vdc @ 40 mA or 10 Vdc @ 60 mA. (Any excitation voltage between 5 and 24 Vdc is available by special order.) This "iS" model supports 4- and 6-wire bridge configurations, ratiometric and non-ratiometric measurements. The "iS" features fast and easy "in process" calibration/scaling of the signal inputs to any engineering units. This model also features 10-point linearization which allows the user to linearize the signal input from extremely nonlinear transducers of all kinds.

Input Type		Range	Accuracy
Universal Process			
Process Voltage		0 to 100 mV, 0 to 1 V, 0 to 10 Vdc	0.03% rdg
Process Current		0 to 20 mA (4 to 20 mA)	0.03% rdg
Excitation		24 V @ 25 mA	—
Universal Strain/Process			
Process Voltage		0 to 100 mV, -100 to 1 V, 0 to 10 Vdc	0.03% rdg
Process Current		0 to 20 mA (4 to 20 mA)	0.03% rdg
Excitation		5 V @ 40 mA, 10 V @ 60 mV	—
Nickel RTD Input (FS Required)			
RTD-1N (Nickel MIL-T-7990B)		0 to 200°C (32 to 392°F)	0.1°C (0.2 °F)
RTD-2N (Nickel MIL-T-7990B)		-40 to 300°C (-40 to 572°F)	0.3°C (0.5 °F)
Temperature			
J	Iron-Constantan	-210 to 760°C (-346 to 1400°F)	0.4°C (0.7°F)
K	CHROMEGA®-ALOMEGA®	-270 to -160°C/-160 to 1372°C (-454 to -256°F/-256 to 2502°F)	1.0°C/0.4°C (1.8°F/0.7°F)
T	Copper-Constantan	-270 to -190°C/-190 to 400°C (-454 to -310°F/-310 to 752°F)	1.0°C/0.4°C (1.8°F/0.7°F)
E	CHROMEGA®-Constantan	-270 to -220°C/-220 to 1000°C (-454 to -364°F/-364 to 1832°F)	1.0°C/0.4°C (1.8°F/0.7°F)
R	Pt/13%Rh-Pt	-50 to 40°C/40 to 1768°C (-58 to 104°F/104 to 3214°F)	1.0°C/0.5°C (1.8°F/0.9°F)
S	Pt/10%Rh-Pt	-50 to 100°C/100 to 1768°C (-58 to 212°F/212 to 3214°F)	1.0°C/0.5°C (1.8°F/0.9°F)
B	30%Rh-Pt/6%Rh-Pt	100 to 640°C/640 to 1820°C (212 to 1184°F/1184 to 3308°F)	1.0°C/0.5°C (1.8°F/0.9°F)
C	5%Re-W/26%Re-W	0 to 2320°C (32 to 4208°F)	0.4°C (0.7°F)
N	Nicrosil-nisil	-250 to -100°C/-100 to 1300°C (-418 to -148°F/-148 to 2372°F)	1.0°C/0.4°C (1.8°F/0.7°F)
L	J DIN	-200 to 900°C (-328 to 1652°F)	0.4°C (0.7°F)
RTD	Pt, 0.00385, 100, 500, 1000	-200 to 900°C (-328 to 1652°F)	0.4°C (0.7°F)
RTD	Pt, 0.00392, 100, 500, 1000	-200 to 850°C (-328 to 1562°F)	0.4°C (0.7°F)

Figure D.5: Power Controllers Specification Sheet Page 1

i.Series Common Specifications (All i/8, i/16, i/32 DIN)

Universal Temperature and Process Input (Model "i")

Accuracy: ±0.5°C temp; 0.03% reading
Resolution: 1°/0.1°; 10 µV process
Temperature Stability:
RTD: 0.04°C/°C
TC @ 25°C (77°F): 0.05°C/°C
Cold Junction Compensation
Process: 50 ppm/°C
NMRR: 60 dB
CMRR: 120 dB
A/D Conversion: Dual slope
Reading Rate: 3 samples/s
Digital Filter: Programmable
Display: 4-digit 9-segment LED 10.2 mm (0.40"); i32, i16, i16D, i8DV 21 mm (0.83"); i8 10.2 mm (0.40") and 21 mm (0.83"); i8DH **RED**, GREEN, and AMBER programmable colors for process variable, setpoint and temperature units
Input Types: Thermocouple, RTD, analog voltage, analog current
Thermocouple Lead Resistance: 100 Ω max
Thermocouple Types (ITS 90): J, K, T, E, R, S, B, C, N, L
RTD Input (ITS 68): 100/500/1000 Ω Pt sensor, 2-, 3- or 4-wire; 0.00385 or 0.00392 curve
Voltage Input: 0 to 100 mV, 0 to 1 V, 0 to 10 Vdc
Input Impedance: 10 MΩ for 100 mV 1 MΩ for 1 or 10 Vdc
Current Input: 0 to 20 mA (5Ω load)
Configuration: Single-ended
Polarity: Unipolar
Step Response: 0.7 sec for 99.9%
Decimal Selection:
Temperature: None, 0.1
Process: None, 0.1, 0.01 or 0.001
Setpoint Adjustment: -1999 to 9999 counts
Span Adjustment: 0.001 to 9999 counts
Offset Adjustment: -1999 to 9999
Excitation (Not included with Communication): 24 Vdc @ 25 mA (not available for low-power option)

Universal Strain and Process Input (Model "iS")

Accuracy: 0.03% reading
Resolution: 10/1µV
Temperature Stability: 50 ppm/°C
NMRR: 60 dB
CMRR: 120 dB
A/D Conversion: Dual slope
Reading Rate: 3 samples/s
Digital Filter: Programmable
Input Types: Analog voltage and current
Voltage Input: 0 to 100 mVdc, -100 mVdc to 1 Vdc, 0 to 10 Vdc
Input Impedance: 10 MΩ for 100 mV; 1 MΩ for 1 V or 10 Vdc
Current Input: 0 to 20 mA (5Ω load)
Linearization Points: Up to 10
Configuration: Single-ended
Polarity: Unipolar
Step Response: 0.7 sec for 99.9%
Decimal Selection: None, 0.1, 0.01 or 0.001
Setpoint Adjustment: -1999 to 9999 counts
Span Adjustment: 0.001 to 9999 counts
Offset Adjustment: -1999 to 9999
Excitation (Optional In Place Of Communication): 5 Vdc @ 40 mA; 10 Vdc @ 60 mA

Control

Action: Reverse (heat) or direct (cool)
Modes: Time and amplitude proportional control; selectable manual or auto PID, proportional, proportional with integral, proportional with derivative and anti-reset Windup, and on/off
Rate: 0 to 399.9 s
Reset: 0 to 3999 s
Cycle Time: 1 to 199 s; set to 0 for on/off
Gain: 0.5 to 100% of span; setpoints 1 or 2
Damping: 0000 to 0008
Soak: 00.00 to 99.59 (HH:MM), or OFF
Ramp to Setpoint: 00.00 to 99.59 (HH:MM), or OFF
Auto Tune: Operator initiated from front panel

Control Output 1 and 2

Relay: 250 Vac or 30 Vdc @ 3 A (Resistive Load); configurable for on/off, PID and ramp and soak
Output 1: SPDT, can be configured as alarm 1 output
Output 2: SPDT, can be configured as alarm 2 output
SSR: 20 to 265 Vac @ 0.05 to 0.5 A (resistive load); continuous
DC Pulse: Non-isolated; 10 Vdc @ 20 mA
Analog Output (Output 1 Only): Non-isolated, proportional 0 to 10 Vdc or 0 to 20 mA; 500 Ω max

Network and Communications

Ethernet: Standards compliance IEEE 802.3 10 Base-T
Supported Protocols: TCP/IP, ARP, HTTPGET
RS232/RS422/RS485: Selectable from menu; both ASCII and MODBUS protocol selectable from menu; programmable 300 to 19.2 Kb; complete programmable setup capability; program to transmit current display, alarm status, min/max, actual measured input value and status
RS485: Addressable from 0 to 199
Connection: Screw terminals

Alarm 1 and 2 (Programmable)

Type: Same as output 1 and 2
Operation: High/low, above/below, band, latch/unlatch, normally open/normally closed and process/deviation; front panel configurations
Analog Output (Programmable): Non-isolated, retransmission 0 to 10 Vdc or 0 to 20 mA, 500 Ω max (output 1 only); accuracy is ± 1% of FS when following conditions are satisfied: input is not scaled below 1% of input FS, analog output is not scaled below 3% of output FS

General

Power: 90 to 240 Vac ±10%, 50 to 400 Hz*, 110 to 375 Vdc, equivalent voltage
Low Voltage Power Option: 24 Vac**, 12 to 36 Vdc for i/8, i/16. 1/32; 20 to 36 Vdc for CNi8DH, CNi8DV, CNi16D from qualified safety approved source

Isolation

Power to Input/Output: 2300 Vac per 1 minute test
For Low Voltage Power Option: 1500 Vac per 1 minute test
Power to Relay/SSR Output: 2300 Vac per 1 minute test
Relay/SSR to Relay/SSR Output: 2300 Vac per 1 minute test
RS232/485 to Input/Output: 500 Vac per 1 minute test
Environmental Conditions:
All Models: 0 to 55°C (32 to 131°F) 90% RH non-condensing
CNi8DV, CNi8DH, CNi16D: 0 to 50°C (32 to 122°F), 90% RH non-condensing (for UL only)
Protection:
CNi32, CNi16, CNi8C: NEMA 4X/ Type 4 (IP65) front bezel
CNi8, CNi8DH, CNi8DV: NEMA 1/Type 1 front bezel
Approvals: UL, C-UL, CE per EN61010-1:2001
Dimensions
i/8 Series: 48 H x 96 W x 127 mm D (1.89 x 3.78 x 5")
i/16 Series: 48 H x 48 W x 127 mm D (1.89 x 1.89 x 5")
i/32 Series: 25.4 H x 48 W x 127 mm D (1.0 x 1.89 x 5")
Panel Cutout
i/8 Series: 45 H x 92 mm W (1.772" x 3.622"), 1/8 DIN
i/16 Series: 45 mm (1.772") square, 1/16 DIN
i/32 Series: 22.5 H x 45 mm W (0.886" x 1.772"), 1/32 DIN
Weight
i/8 Series: 295 g (0.65 lb)
i/16 Series: 159 g (0.35 lb)
i/32 Series: 127 g (0.28 lb)

** No CE compliance above 60 Hz.*
*** Units can be powered safely with 24 Vac power, but no certification for CE/UL are claimed.*

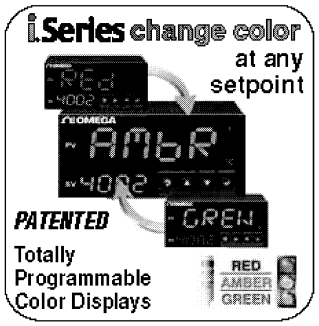

P-22

P

Figure D.6: Power Controllers Specification Sheet Page 2

Figure D.7: PCB Model 106B High-Frequency Pressure Transducer

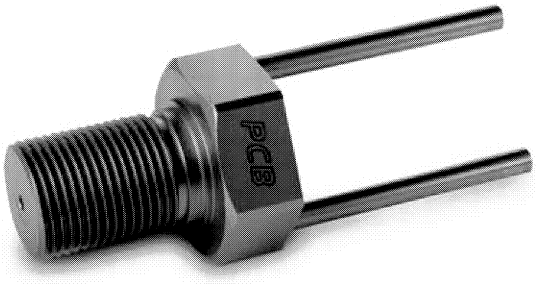

Figure D.8: PCB Model 064B06 Water-cooled Adapter

Model Number 106B

ICP® PRESSURE SENSOR

Revision: Y
ECN #: 29520

Performance	ENGLISH	SI
Measurement Range (for ±2.5V output)	8.3 psi	57.2 kPa
Sensitivity (±15 %)	300 mV/psi	43.5 mV/kPa
Maximum Pressure (step)	200 psi	1379 kPa
Maximum Pressure	2 kpsi	13790 kPa
Resolution	0.1 mpsi	0.000069 kPa [1]
Resonant Frequency	≥60 kHz	≥60 kHz
Rise Time	≤9 µ sec	≤9 µ sec
Low Frequency Response (-5 %)	0.5 Hz	0.5 Hz
Non-Linearity	≤1 % FS	≤1 % FS [2]
Environmental		
Acceleration Sensitivity	≤0.002 psi/g	≤0.0014 kPa/(m/s²)
Temperature Range (Operating)	-65 to +250 °F	-54 to +121 °C
Temperature Coefficient of Sensitivity	≤0.05 %/°F	≤0.09 %/°C
Maximum Flash Temperature	3000 °F	1649 °C
Maximum Shock	2000 g pk	19600 m/s² pk
Electrical		
Output Polarity (Positive Pressure)	Positive	Positive
Discharge Time Constant (at room temp)	≥1 sec	≥1 sec
Excitation Voltage	12 to 30 VDC	12 to 30 VDC
Constant Current Excitation	2 to 20 mA	2 to 20 mA
Output Impedance	≤100 ohm	≤100 ohm
Output Bias Voltage	3 to 8 VDC	3 to 8 VDC
Physical		
Sensing Geometry	Compression	Compression
Sensing Element	Quartz	Quartz
Housing Material	304/304L Stainless Steel	304/304L Stainless Steel
Diaphragm	316L Stainless Steel	316L Stainless Steel
Sealing	Welded Hermetic	Welded Hermetic
Electrical Connector	10-32 Coaxial Jack	10-32 Coaxial Jack
Weight	0.63 oz	18.0 gm

CE [3]

All specifications are at room temperature unless otherwise specified.
In the interest of constant product improvement, we reserve the right to change specifications without notice.
ICP® is a registered trademark of PCB group, Inc.

Optional Versions (Optional versions have identical specifications and accessories as listed for standard model except where noted below. More than one option may be used.)

E - Emration coating

	Emration	Emration
Coating	10^6 ohm	10^8 ohm
Electrical Isolation		

Supplied Accessory: Model 066447 Seal ring, 0.497" OD x 0.437" ID x 0.025" thk, Delrin (for Models E116B and E106B)

J - Ground Isolated [4]

T - TEDS Capable of Digital Memory and Communication Compliant with IEEE P1451.4 [5]

Output Bias Voltage	3.7 to 8.7 VDC	3.7 to 8.7 VDC

W - Water Resistant Cable [5]

Supplied Accessory: Model 060A12 Clamp nut, 9/16-18-2A thd, 9/16" hex (for Models 106B and 116B)

WM - Water Resistant Cable [5]

Supplied Accessory: Model 060A14 Metric clamp nut, M14 x 1.25-6G thd, 14 mm hex, stainless steel (for Models M106B and M116B)

Notes

[1] Typical.
[2] Zero-based, least-squares, straight line method.
[3] See PCB Declaration of Conformance PS023 for details.
[4] Used with optional mounting adaptor.
[5] Clamp nut installed prior to cable attachment.

Supplied Accessories

060A12 Clamp nut, 9/16-18-2A thd, 9/16" hex (1)
060A14 Metric clamp nut, M14 x 1.25-6g thd, 14 mm hex, stainless steel (1)
066437 Seal ring 0.497 OD x 0.437 ID x 0.025 thk Brass (3)

Entered: BLS	Engineer: NJL	Sales: RWM	Approved: RFF	Spec Number
Date: 10/17/2008	Date: 10/02/2008	Date: 10/03/2008	Date: 10/02/2008	106-2010-80

PCB PIEZOTRONICS
PRESSURE DIVISION

3425 Walden Avenue
Depew, NY 14043
UNITED STATES
Phone: 888-684-0011
Fax: 716-686-9129
E-mail: pressure@pcb.com
Web site: www.pcb.com

Figure D.9: PCB Model 106B Specification Sheet

PHANTOM Miro Family

All specifications subject to change Rev October 2006

VISION RESEARCH

Key Features:

Resolution (Pixels): 640x480, 800x600

Maximum full-resolution frame rates of 500fps to 1200fps. (Maximum frame rates at reduced resolutions are as high as 111,000fps)

CMOS active-pixel sensor

Exposure time (shutter speed) as low as 2 microseconds (1/500,000 second)

Built-in LCD touch screen display (on most models)

ISO (ISO-12232 standard): 4800 Mono, 1200 Color

10/100 Ethernet

[illegible]

Compact, lightweight, untethered. The world's first "point and shoot" high-speed cameras.

WHEN IT'S TOO FAST TO SEE, AND TOO IMPORTANT NOT TO™

Compact. Lightweight. Rugged. The perfect balance of resolution, speed, and light-sensitivity. A built-in touch screen display. Battery powered. Flexible triggering. PC connectivity. Removable CompactFlash memory. Everything you need in a high-speed digital imaging system. Whether for product drop testing, biometrics research, automotive crash testing, airborne applications, manufacturing line troubleshooting, or scientific experimentation, our new line of cameras has a model just for you.

Every member of the Phantom Miro family is compact, lightweight, and rugged. Each accepts any standard 1" C-mount lens. Each is packed with the technology and innovation you've come to expect from Vision Research.

With a variety of image sizes (640x480, 800x600) and maximum full-resolution frame rates of **500fps to 1200fps**, you will find a model that matches your need. (Maximum frame rates at reduced resolutions are as high as 111,000fps!)

1

Figure D.10: Vision Research Miro 4 Specification Sheet Page 1

On most Phantom cameras, as you decrease the resolution in increments defined by the Continuously Adjustable Resolution (CAR) specification, you will see an increase in the maximum frame rate that is available to you. This is true on the Phantom Miro cameras with the exception of the Miro 1. The Miro 1 has a fixed resolution of 640x480 pixels and a maximum frame rate of 500 fps. Here are some example frame rates for the rest of the Miro line.

Resolution	Miro 2
640 x 480	1258
512 x 480	1558
512 x 384	1941
512 x 256	2882
512 x 128	5665
512 x 64	10669
320 x 240	4756
256 x 480	2969
256 x 256	5471
256 x 192	7134
256 x 128	10526
256 x 64	19607
128 x 128	16433
128 x 64	32520
64 x 64	46192
32 x 32	86956
32 x16	105263

Resolution	Miro 3 & 4
800 x 600	1265
640 x 480	1949
512 x 512	2252
512 x 384	2986
512 x 256	4429
512 x 128	8583
512 x 64	16194
320 x 240	7155
256 x 512	4132
256 x 256	8146
256 x 128	15325
256 x 64	27586
128 x 128	25477
128 x 64	43010
64 x 64	58823
32 x 32	95238
32 x16	111111

The Phantom Miro's custom-designed CMOS active-pixel sensors have an ISO rating of 4800 (monochrome) ensuring the **light-sensitivity** required in high-speed imaging applications, come in color or monochrome versions.

With shutter speeds as low as 2 microseconds (1/500,000 second), you can **freeze objects in motion**, eliminate blur, and bring out the detail you need for successful motion analysis.

A built-in LCD touch screen display (on most models) allows you to program the camera easily, frame your shot perfectly, and gives you **immediate feedback** on the results of your test or experiment. You can play and rewind in normal or fast mode or step through your movie one frame at a time. Trimming the movie is as easy as setting in-points and out-points prior to saving.

Connect your Phantom Miro camera to a PC using 10/100 Ethernet for camera programming and control, and to retrieve your test images in our efficient cine format for later analysis and processing using the bundled TEMA Starter for Phantom motion analysis software.

Using the Phantom Software you can also **save movies in popular formats** such as Quicktime or AVI, or you can save frames as JPEG or TIFF images. Easily email movies or frames to colleagues.

Take advantage of our **flexible triggering**. When you power-up the camera, it begins taking images at the programmed settings and stores them in a circular buffer in internal memory. Change a setting, and see the impact of the change on the built-in LCD or external monitor immediately. Set up the camera so that a trigger (from external hardware, an on-camera trigger button or software on a connected PC) starts your recording, stops your recording, or records a selectable number of frames before and after the trigger.

Apply the bundled TEMA Starter for Phantom software from Image Systems AB, and you get a **quantitative analysis** as well as a qualitative view of your test results.

All models can be connected to a standard analog video monitor (PAL or NTSC) for real-time monitoring of the camera image or for playback of images stored in the camera's memory.

Use any 1" C-mount lens, or attach your Phantom Miro camera to a microscope or borescope.

Battery power allows you to take shots completely **untethered** from a power source. Field use for animal studies, for example, is now practical. Carry multiple batteries with you for field replacement.

Store images onto removable non-volatile CompactFlash memory (not removable on the Miro 3).

Figure D.11: Vision Research Miro 4 Specification Sheet Page 2

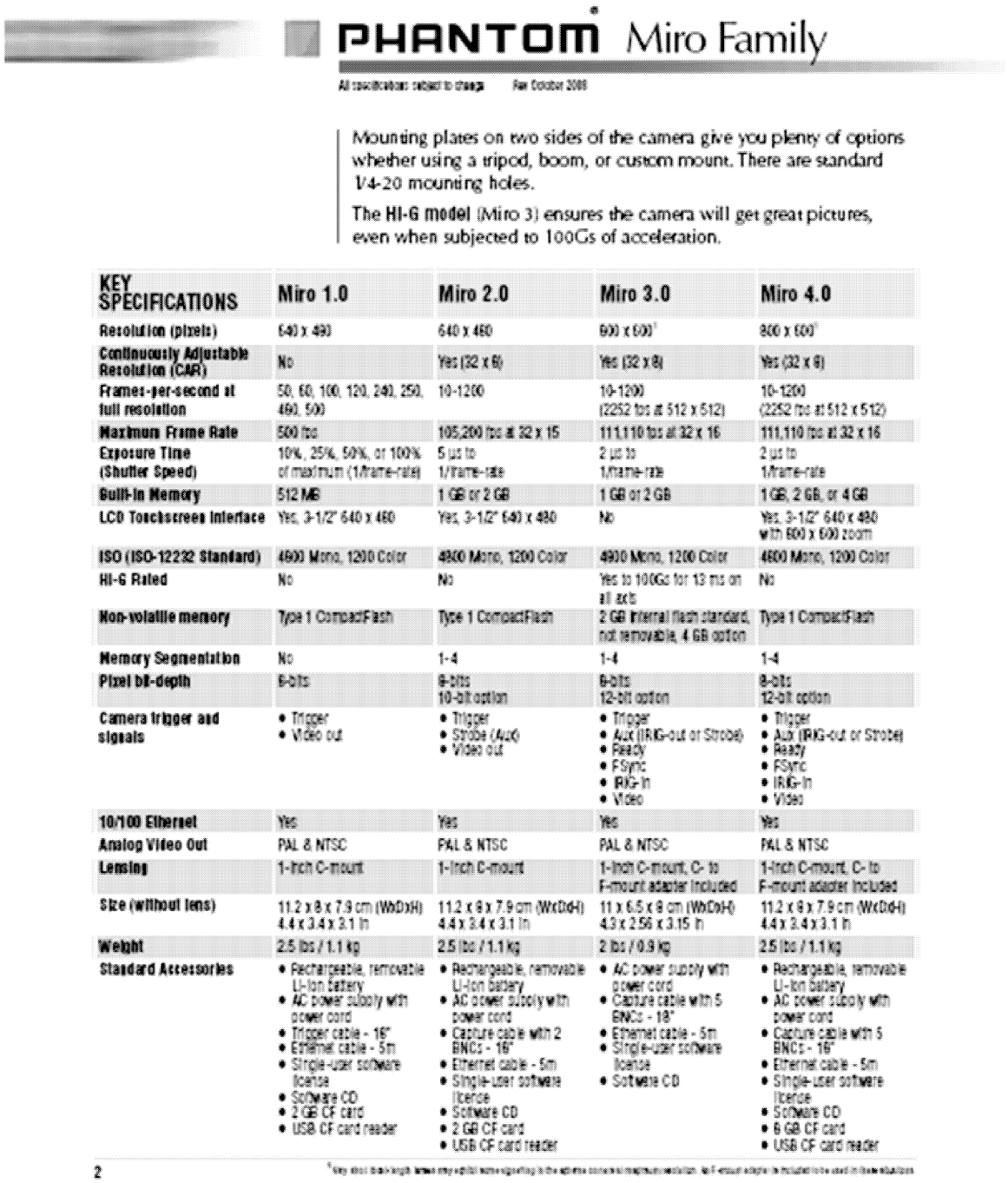

PHANTOM Miro Family

All specifications subject to change Rev October 2006

Mounting plates on two sides of the camera give you plenty of options whether using a tripod, boom, or custom mount. There are standard 1/4-20 mounting holes.

The **HI-G model** (Miro 3) ensures the camera will get great pictures, even when subjected to 100Gs of acceleration.

KEY SPECIFICATIONS	Miro 1.0	Miro 2.0	Miro 3.0	Miro 4.0
Resolution (pixels)	640 x 480	640 x 480	800 x 600[1]	800 x 600[1]
Continuously Adjustable Resolution (CAR)	No	Yes (32 x 8)	Yes (32 x 8)	Yes (32 x 8)
Frames-per-second at full resolution	50, 60, 100, 120, 240, 250, 480, 500	10-1200	10-1200 (2252 fps at 512 x 512)	10-1200 (2252 fps at 512 x 512)
Maximum Frame Rate	500 fps	105,200 fps at 32 x 16	111,110 fps at 32 x 16	111,110 fps at 32 x 16
Exposure Time (Shutter Speed)	10%, 25%, 50%, or 100% of maximum (1/frame-rate)	5 µs to 1/frame-rate	2 µs to 1/frame-rate	2 µs to 1/frame-rate
Built-in Memory	512 MB	1 GB or 2 GB	1 GB or 2 GB	1 GB, 2 GB, or 4 GB
LCD Touchscreen Interface	Yes, 3-1/2" 640 x 480	Yes, 3-1/2" 640 x 480	No	Yes, 3-1/2" 640 x 480 with 800 x 600 zoom
ISO (ISO-12232 Standard)	4800 Mono, 1200 Color	4800 Mono, 1200 Color	4800 Mono, 1200 Color	4800 Mono, 1200 Color
HI-G Rated	No	No	Yes to 100Gs for 13 ms on all axis	No
Non-volatile memory	Type 1 CompactFlash	Type 1 CompactFlash	2 GB internal flash standard, not removable, 4 GB option	Type 1 CompactFlash
Memory Segmentation	No	1-4	1-4	1-4
Pixel bit-depth	8-bits	8-bits 10-bit option	8-bits 12-bit option	8-bits 12-bit option
Camera trigger and signals	• Trigger • Video out	• Trigger • Strobe (Aux) • Video out	• Trigger • Aux (IRIG-out or Strobe) • Ready • FSync • IRIG-in • Video	• Trigger • Aux (IRIG-out or Strobe) • Ready • FSync • IRIG-in • Video
10/100 Ethernet	Yes	Yes	Yes	Yes
Analog Video Out	PAL & NTSC	PAL & NTSC	PAL & NTSC	PAL & NTSC
Lensing	1-inch C-mount	1-inch C-mount	1-inch C-mount, C- to F-mount adapter included	1-inch C-mount, C- to F-mount adapter included
Size (without lens)	11.2 x 8 x 7.9 cm (WxDxH) 4.4 x 3.4 x 3.1 in	11.2 x 8 x 7.9 cm (WxDxH) 4.4 x 3.4 x 3.1 in	11 x 6.5 x 8 cm (WxDxH) 4.3 x 2.56 x 3.15 in	11.2 x 8 x 7.9 cm (WxDxH) 4.4 x 3.4 x 3.1 in
Weight	2.5 lbs / 1.1 kg	2.5 lbs / 1.1 kg	2 lbs / 0.9 kg	2.5 lbs / 1.1 kg
Standard Accessories	• Rechargeable, removable Li-Ion battery • AC power supply with power cord • Trigger cable - 16" • Ethernet cable - 5m • Single-user software license • Software CD • 2 GB CF card • USB CF card reader	• Rechargeable, removable Li-Ion battery • AC power supply with power cord • Capture cable with 2 BNCs - 16" • Ethernet cable - 5m • Single-user software license • Software CD • 2 GB CF card • USB CF card reader	• AC power supply with power cord • Capture cable with 5 BNCs - 18" • Ethernet cable - 5m • Single-user software license • Software CD	• Rechargeable, removable Li-Ion battery • AC power supply with power cord • Capture cable with 5 BNCs - 16" • Ethernet cable - 5m • Single-user software license • Software CD • 8 GB CF card • USB CF card reader

2

[1] Key pixel data is only available when using optical lens adapter (supplied) to the optical camera's magnification electronics. An F-mount adapter is included in the unit in these situations.

Figure D.12: Vision Research Miro 4 Specification Sheet Page 3

PHANTOM Miro Family

ADDITIONAL SPECIFICATIONS	Miro 1.0	Miro 2.0	Miro 3.0	Miro 4.0
External Power	12 - 30 VDC 12W	12 - 30 VDC 12W	15 - 30 VDC 12W	12 - 30 VDC 12W
Operating Temperature	10°C to 40°C	10°C to 40°C	0°C to 50°C	10°C to 40°C
Storage Temperature	-20°C to 35°C with battery -25°C to 60°C without battery	-20°C to 35°C with battery -25°C to 60°C without battery	-20°C to 35°C	-20°C to 35°C with battery -25°C to 60°C without battery
Battery	Removable, replaceable Li-Ion 7.4V BP-511	Removable, replaceable Li-Ion 7.4V BP-511	Internal Li-polymer, 11.1V	Removable, replaceable Li-Ion 7.4V BP-511
Typical battery use time between charges	30 minutes[1]	30 minutes[1]	45 minutes[1]	30 minutes[1]
Recording time at full resolution, 500 fps, maximum built-in memory and 8-bit depth	2.4 seconds	13.9 seconds	8.9 seconds	17.8 seconds

MIRO

Focused

Since 1950 Vision Research has been creating, designing, and manufacturing high-speed cameras. Our single focus is to invent, build, and support the most advanced cameras possible.

VISION RESEARCH

Vision Research
100 Dey Road
Wayne, NJ 07470 USA
+1.973.696.4500
phantom@visionresearch.com
www.visionresearch.com

An AMETEK Company

PHANTOM

4

Figure D.13: Vision Research Miro 4 Specification Sheet Page 4

REDLAKE

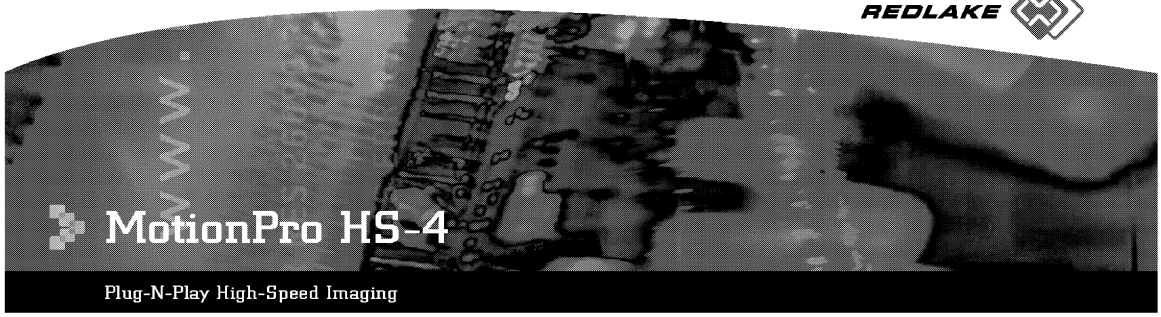

MotionPro HS-4

Plug-N-Play High-Speed Imaging

Redlake's *MotionPro*® HS-4 high-speed motion camera combines excellent resolution to frame rate performance, along with the advanced features you require for accurate high-speed motion analysis on your PC or Mac laptop or desktop computer. The blazing speed of the *MotionPro*® HS-4 of over 5000 fps at 512 x 512 is perfect for research and development labs and airbag testing applications.

With the *MotionPro*® HS-4 camera integration could not be simpler. Just install the software, connect one or more HS Series cameras to USB 2.0 ports or hub, and you are ready to capture high-speed digital imagery. Control the camera system with the feature-rich MotionPro Central software or use the LabVIEW™ or MATLAB® plug-in. To create your own control software, a SDK is included.

The extensive image processing algorithms include binning (2x2, 3x3, and 4x4), filtering, advanced color control, and programmable LUT enable you to maximize the image quality under various lighting conditions.

Image capture with *MotionPro*® HS-4 camera may be initiated via software or a wide variety of external triggers including optical, acoustic, or electrical, as well as simple hand-held switches. Flexible recording options allow the user to capture pre-selected numbers of frames before and/or after receiving a trigger or to employ a double-exposure mode, which, with a 100 nanoseconds inter-frame time, is perfect for motion analysis on objects moving at very high speeds. Memory may be divided into multiple sessions with or without automatic download to assure no event is missed.

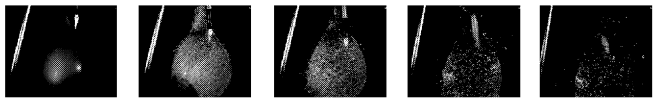

Features

- Up to 512 x 512 resolution color or mono
- Fast frame rates over 5000 fps at full resolution to over 140,000 fps at reduced resolution
- Supports up to 3 seconds record time at full resolution
- LabVIEW™ and MATLAB® plug-ins
- 100 nanosecond inter-frame time in double exposure mode for the capture and analysis of high speed events
- FlexROI™ Configurable Region of Interest for selection of precise field of view to maximize performance

Applications

- Microscopy
- Automotive Airbag Safety Testing
- Biomechanical Research
- Fluid Dynamics Research (PIV)

ISO 9001 Registered

officially licensed by NASCAR

www.redlake.com

Figure D.14: Redlake HS-4 Specification Sheet Page 1

Performance Specifications

CMOS Imager

Sensor Array	Area Array with 16µm x 16 µm pixels, color or monochrome
Image Resolution	Up to 512 x 512 at 5000 fps
Dynamic Range	59 dB at sensor

Memory and Record Rates

On-Board Storage	4 GB
Recording Rates	Selectable, up to 140,000 fps
Playback Rates	User selectable

Camera Control

Shutter	Global Electronic Shutter variable to 1µs, optional 100 nanosecond exposure*
Trigger Frame	Variable position from start to the maximum available frame capacity
Trigger Mode	CMOS level (3.3v) via BNC connectors
Time Stamp	Each frame

Software

Control Software	MotionPro Central, Windows 2000, XP, Mac OS X compatible
Image Processing Algorithms	Binning, filtering, advance color control, and programmable LUT
Plug-ins	LabVIEW™ for PC; MATLAB® for PC and Mac; Twain Driver for PC and Mac
File Formats	TIFF, BMP, PNG, MRF, MCF, AVI, BLD, MPEG, and MOV (Mac only)

Mechanical Description

Camera Size	Dimensions: 3.7"(H) x 3.7 "(W) x 6.4" (L) 95 x 95 x 162mm); Weight: 4.2 lbs (1.9Kg)
Camera to PC Interface	USB 2.0 Sync I/O; Trigger In; Power
Camera Cable Lengths	Camera to PC: up to 90 ft (30m) with option extension cables
Lens Compatibility	1" C-mount
Lens Mount	C-mount, F-mount adapter (Nikon or Canon)

Synchronization

Synchronization (USB Hub Optional)	All cameras are synchronized with each other using an external sync pulse on 3.3v CMOS BNC connector

Environmental

Camera Power	+24 vdc (100-240 VAC, 50-60 Hz ac/dc convertor)
Operating Temperature	+5°C to +40°C Ambient (0°F to 122°F)
Emission/Safety	CE approved, FCC Class B compliant, UL listed

*MotionPro SI-4

Note: Specifications are subject to change without notice

Sample Frame Rates

Vertical Resolution	Max. Horiz. Resolution = 512
512	>5000
256	>10,000
128	>20,000
64	>35,000
32	>75,000
16	>140,000

Note: Horizontal resolution does not affect frame rate performance.
All HS cameras can record at any frame rate at full horizontal resolution.

Accessories

HS Timing Hub	USB digital interface, integrated control software with 8 outputs, 2 inputs
USB Repeater	For use up to 15m

Spectral Range

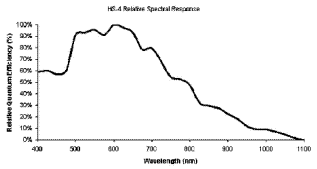

Camera Back

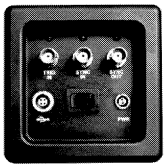

Input/Output
Trig In
Sync In
Sync Out
USB 2.0 Interface
DC Power

Distributed by DEL Imaging Systems

1781 Highland Avenue, Cheshire, CT 06410

Phone: (203) 250-1545 info@delimaging.com www.delimaging.com

Worldwide Sales and Support

www.redlake.com

ISO 9001 Registered

Americas
tel: +1-800-462-4307
tel: +1-858-481-8182
sales@redlake.com

Asia Pacific
tel: +65-6293-4758
salesASPAC@redlake.com

Europe, Africa, Middle East
tel: +31-347-324989
salesEurope@redlake.com

Japan
tel: +81-3-5639-2770
salesJapan@redlake.com

REDLAKE

Figure D.15: Redlake HS-4 Specification Sheet Page 2

Figure D.16: Nikor UV lens

Table D.1: Features of UV Lens

Feature	Value
Color Corrected	250 nm - 650 nm
Focal Length	105 mm
Aperture	f/4.5 - f/32
Apochromatic	Apochromatic
Macro Lens	Macro Lens
Manual Focus	0.5 m - Infinity
Mount	Nikon F-Mount
Filter Mount	52 mm Thread

Figure D.17: UV Lens Specification Sheet Page 1

Figure D.18: UV Lens Specification Sheet Page 2

Figure D.19: UV Lens Specification Sheet Page 3

Figure D.20: UV Lens Specification Sheet Page 4

Figure D.21: UV Lens Specification Sheet Page 5

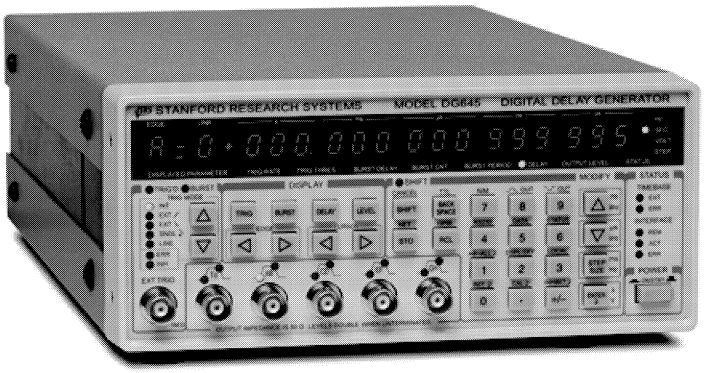

Figure D.22: SRS Digital Delay Generator

DG645 Specifications

Delays

Channels	4 independent pulses controlled in position and width. 8 delay channels available as an option (see *Output Options*).
Range	0 to 2000 s
Resolution	5 ps
Accuracy	1 ns + (timebase error × delay)
Jitter (rms)	
Ext. trig. to any output	<25 ps + (timebase jitter × delay)
T_0 to any output	<15 ps + (timebase jitter × delay)
Trigger delay	85 ns (ext. trig. to T_0 output)

Timebases

Model #	Type	Jitter (s/s)	Stability (20 to 30 °C)	Aging (ppm/yr)
Std.	crystal	10^{-8}	2×10^{-6}	5
Opt. 4	OCXO	10^{-11}	1×10^{-9}	0.2
Opt. 5	Rb	10^{-11}	1×10^{-10}	0.0005

External input	10 MHz ± 10 ppm, sine >0.5 Vpp, 1 kΩ impedance
Output	10 MHz, 2 Vpp sine into 50 Ω

External Trigger

Rate	DC to 1/(100 ns + longest delay) (maximum of 10 MHz)
Threshold	±3.50 VDC
Slope	Trigger on rising or falling edge
Impedance	1 MΩ + 15 pF

Internal Rate Generator

Trigger modes	Continuous, line or single shot
Rate	100 µHz to 10 MHz
Resolution	1 µHz
Accuracy	Same as timebase
Jitter (rms)	<25 ps (10 MHz/N trigger rate) <100 ps (other trigger rates)

Burst Generator

Trigger to first T_0	
Range	0 to 2000 s
Resolution	5 ps
Period between pulses	
Range	100 ns to 42.9 s
Resolution	10 ns
Delay cycles per burst	1 to $2^{32} - 1$

Outputs (T_0, AB, CD, EF, and GH)

Source impedance	50 Ω
Transition time	<2 ns
Overshoot	<100 mV + 10 % of pulse amplitude
Offset	±2 V
Amplitude	0.5 to 5.0 V (level + offset <6.0 V)
Accuracy	100 mV + 5 % of pulse amplitude

General

Computer interfaces	GPIB (IEEE-488.2), RS-232, and Ethernet. All instrument functions can be controlled through the interfaces.
Non-volatile memory	Nine sets of instrument configurations can be stored and recalled.
Power	<100 W, 90 to 264 VAC, 47 Hz to 63 Hz
Dimensions	8.5 × 3.5 × 13 (WHD)
Weight	9 lbs.
Warranty	One year parts and labor on defects in materials & workmanship

Output Options

Option 1 (8 Delay Outputs on Rear Panel)

Outputs (BNC)	T_0, A, B, C, D, E, F, G and H
Source impedance	50 Ω
Transition time	<1 ns
Overshoot	<100 mV
Level	+5 V CMOS logic
Pulse characteristics	
Rising edge	At programmed delay
Falling edge	25 ns after longest delay

Option 2 (8 High-Voltage Delay Outputs on Rear Panel)

Outputs (BNC)	T_0, A, B, C, D, E, F, G and H
Source impedance	50 Ω
Transition time	<5 ns
Levels	0 to 30 V into high impedance 0 to 15 V into 50 Ω (amplitude decreases by 1 %/kHz)
Pulse Characteristics	
Rising Edge	At programmed delay
Falling Edge	100 ns after the rising edge

Option 3 (Combinatorial Outputs on Rear Panel)

Outputs (BNC)	T_0, AB, CD, EF, GH, (AB + CD), (EF + GH), (AB + CD + EF), (AB + CD + EF + GH)
Source impedance	50 Ω
Transition time	<1 ns
Overshoot	<100 mV + 10 % of pulse amplitude
Pulse characteristics	
T_0, AB, CD, EF, GH	Logic high for time between delays
(AB+CD), (EF+GH)	Two pulses created by the logic OR of the given channels
(AB+CD+EF)	Three pulses created by the logic OR of the given channels
(AB+CD+EF+GH)	Four pulses created by the logic OR of the given channels

Option SRD1 (Fast Rise Time Module)

Rise time	<100 ps
Fall time	<3 ns
Offset	0.8 V to 1.1 V
Amplitude	0.5 V to 5.0 V
Load	50 Ω

SRS Stanford Research Systems

phone: (408)744-9040
www.thinkSRS.com

Figure D.23: Digital Delay Generator Specification Sheet

APPENDIX E

FILE NAMES

Table E.1: Raw Data File Names: Preliminary Testing at $\frac{r}{r_c}$=67%

SP	File Path	Raw Data File Name	Description
1	/20090706	Test 6_1_0_Cam.txt	Camera Signals File
1	/20090706	Test 6_1_0_HF.txt	High-Frequency Data File
1	/20090706	Test 6_1_0_LF.xls	Low-Frequency Data File
2	/20090706	Test 6_2_0_Cam.txt	Camera Signals File
2	/20090706	Test 6_2_0_HF.txt	High-Frequency Data File
2	/20090706	Test 6_2_0_LF.xls	Low-Frequency Data File
3	/20090706	Test 8_3_0_Cam.txt	Camera Signals File
3	/20090706	Test 8_3_0_HF.txt	High-Frequency Data File
3	/20090706	Test 8_3_0_LF.xls	Low-Frequency Data File
4	/20090706	Test 11_4_0_Cam.txt	Camera Signals File
4	/20090706	Test 11_4_0_HF.txt	High-Frequency Data File
4	/20090706	Test 11_4_0_LF.xls	Low-Frequency Data File
5	/20090706	Test 11_5_0_Cam.txt	Camera Signals File
5	/20090706	Test 11_5_0_HF.txt	High-Frequency Data File
5	/20090706	Test 11_5_0_LF.xls	Low-Frequency Data File
6	/20090706	Test 11_6_0_Cam.txt	Camera Signals File
6	/20090706	Test 11_6_0_HF.txt	High-Frequency Data File
6	/20090706	Test 11_6_0_LF.xls	Low-Frequency Data File
7	/20090706	Test 11_7_0_Cam.txt	Camera Signals File
7	/20090706	Test 11_7_0_HF.txt	High-Frequency Data File
7	/20090706	Test 11_7_0_LF.xls	Low-Frequency Data File
8	/20090706	Test 11_8_0_Cam.txt	Camera Signals File
8	/20090706	Test 11_8_0_HF.txt	High-Frequency Data File
8	/20090706	Test 11_8_0_LF.xls	Low-Frequency Data File
9	/20090706	Test 11_9_0_Cam.txt	Camera Signals File
9	/20090706	Test 11_9_0_HF.txt	High-Frequency Data File
9	/20090706	Test 11_9_0_LF.xls	Low-Frequency Data File
10	/20090706	Test 11_10_0_Cam.txt	Camera Signals File
10	/20090706	Test 11_10_0_HF.txt	High-Frequency Data File
10	/20090706	Test 11_10_0_LF.xls	Low-Frequency Data File
11	/20090706	Test 11_11_0_Cam.txt	Camera Signals File
11	/20090706	Test 11_11_0_HF.txt	High-Frequency Data File
11	/20090706	Test 11_11_0_LF.xls	Low-Frequency Data File
12	/20090706	Test 11_12_0_Cam.txt	Camera Signals File
12	/20090706	Test 11_12_0_HF.txt	High-Frequency Data File
12	/20090706	Test 11_12_0_LF.xls	Low-Frequency Data File

Table E.2: Raw Data File Names: Tests 1.0-2.5 at $\frac{r}{r_c}$=0%

Test	File Path	Raw Data File Name	Description
1.0	/Sep.14.2009/Center	Test 1.0A.12.47.Camera.tdm	Measurement File Header
1.0	/Sep.14.2009/Center	Test 1.0A.12.47.Camera.tdx	Measurement Data File
1.0	/Sep.14.2009/Center	Test 1.0A.12.47.Chamber.tdm	Measurement File Header
1.0	/Sep.14.2009/Center	Test 1.0A.12.47.Camera.tdx	Measurement Data File
1.0	/Sep.14.2009/Center	Test 1.0A.12.47.Test Stand.tdm	Measurement File Header
1.0	/Sep.14.2009/Center	Test 1.0A.12.47.Test Stand.tdx	Measurement Data File
1.5	/Sep.14.2009/Center	Test 1.5C.13.17.Camera.tdm	Measurement File Header
1.5	/Sep.14.2009/Center	Test 1.5C.13.17.Camera.tdx	Measurement Data File
1.5	/Sep.14.2009/Center	Test 1.5C.13.17.Chamber.tdm	Measurement File Header
1.5	/Sep.14.2009/Center	Test 1.5C.13.17.Chamber.tdx	Measurement Data File
1.5	/Sep.14.2009/Center	Test 1.5C.13.17.Test Stand.tdm	Measurement File Header
1.5	/Sep.14.2009/Center	Test 1.5C.13.17.Test Stand.tdx	Measurement Data File
2.0	/Sep.14.2009/Center	Test 2.0B.16.40.Camera.tdm	Measurement File Header
2.0	/Sep.14.2009/Center	Test 2.0B.16.40.Camera.tdx	Measurement Data File
2.0	/Sep.14.2009/Center	Test 2.0B.16.40.Chamber.tdm	Measurement File Header
2.0	/Sep.14.2009/Center	Test 2.0B.16.40.Chamber.tdx	Measurement Data File
2.0	/Sep.14.2009/Center	Test 2.0B.16.40.Test Stand.tdm	Measurement File Header
2.0	/Sep.14.2009/Center	Test 2.0B.16.40.Test Stand.tdx	Measurement Data File
2.5	/Sep.14.2009/Center	Test 2.5B.16.21.Camera.tdm	Measurement File Header
2.5	/Sep.14.2009/Center	Test 2.5B.16.21.Camera.tdx	Measurement Data File
2.5	/Sep.14.2009/Center	Test 2.5B.16.21.Chamber.tdm	Measurement File Header
2.5	/Sep.14.2009/Center	Test 2.5B.16.21.Chamber.tdx	Measurement Data File
2.5	/Sep.14.2009/Center	Test 2.5B.16.21.Test Stand.tdm	Measurement File Header
2.5	/Sep.14.2009/Center	Test 2.5B.16.21.Test Stand.tdx	Measurement Data File

Table E.3: Raw Data File Names: Tests 3.0-4.5 at $\frac{r}{r_c}$=0%

Test	File Path	Raw Data File Name	Description
3.0	/Sep.14.2009/Center	Test 3.0A.13.35.Camera.tdm	Measurement File Header
3.0	/Sep.14.2009/Center	Test 3.0A.13.35.Camera.tdx	Measurement Data File
3.0	/Sep.14.2009/Center	Test 3.0A.13.35.Chamber.tdm	Measurement File Header
3.0	/Sep.14.2009/Center	Test 3.0A.13.35.Chamber.tdx	Measurement Data File
3.0	/Sep.14.2009/Center	Test 3.0A.13.35.Test Stand.tdm	Measurement File Header
3.0	/Sep.14.2009/Center	Test 3.0A.13.35.Test Stand.tdx	Measurement Data File
3.5	/Sep.14.2009/Center	Test 3.5A.13.47.Camera.tdm	Measurement File Header
3.5	/Sep.14.2009/Center	Test 3.5A.13.47.Camera.tdx	Measurement Data File
3.5	/Sep.14.2009/Center	Test 3.5A.13.47.Chamber.tdm	Measurement File Header
3.5	/Sep.14.2009/Center	Test 3.5A.13.47.Chamber.tdx	Measurement Data File
3.5	/Sep.14.2009/Center	Test 3.5A.13.47.Test Stand.tdm	Measurement File Header
3.5	/Sep.14.2009/Center	Test 3.5A.13.47.Test Stand.tdx	Measurement Data File
4.0	/Sep.14.2009/Center	Test 4.0A.13.57.Camera.tdm	Measurement File Header
4.0	/Sep.14.2009/Center	Test 4.0A.13.57.Camera.tdx	Measurement Data File
4.0	/Sep.14.2009/Center	Test 4.0A.13.57.Chamber.tdm	Measurement File Header
4.0	/Sep.14.2009/Center	Test 4.0A.13.57.Chamber.tdx	Measurement Data File
4.0	/Sep.14.2009/Center	Test 4.0A.13.57.Test Stand.tdm	Measurement File Header
4.0	/Sep.14.2009/Center	Test 4.0A.13.57.Test Stand.tdx	Measurement Data File
4.5	/Sep.14.2009/Center	Test 4.5A.14.06.Camera.tdm	Measurement File Header
4.5	/Sep.14.2009/Center	Test 4.5A.14.06.Camera.tdx	Measurement Data File
4.5	/Sep.14.2009/Center	Test 4.5A.14.06.Chamber.tdm	Measurement File Header
4.5	/Sep.14.2009/Center	Test 4.5A.14.06.Chamber.tdx	Measurement Data File
4.5	/Sep.14.2009/Center	Test 4.5A.14.06.Test Stand.tdm	Measurement File Header
4.5	/Sep.14.2009/Center	Test 4.5A.14.06.Test Stand.tdx	Measurement Data File

Table E.4: Raw Data File Names: Tests 1.0-2.5 at $\frac{r}{r_c}$=50%

Test	File Path	Raw Data File Name	Description
1.0	/Sep.18.2009/50 Percent	Test 1.0A.17.10.Camera.tdm	Measurement File Header
1.0	/Sep.18.2009/50 Percent	Test 1.0A.17.10.Camera.tdx	Measurement Data File
1.0	/Sep.18.2009/50 Percent	Test 1.0A.17.10.Chamber.tdm	Measurement File Header
1.0	/Sep.18.2009/50 Percent	Test 1.0A.17.10.Chamber.tdx	Measurement Data File
1.0	/Sep.18.2009/50 Percent	Test 1.0A.17.10.Test Stand.tdm	Measurement File Header
1.0	/Sep.18.2009/50 Percent	Test 1.0A.17.10.Test Stand.tdx	Measurement Data File
1.5	/Sep.18.2009/50 Percent	Test 1.5A.17.00.Camera.tdm	Measurement File Header
1.5	/Sep.18.2009/50 Percent	Test 1.5A.17.00.Camera.tdx	Measurement Data File
1.5	/Sep.18.2009/50 Percent	Test 1.5A.17.00.Chamber.tdm	Measurement File Header
1.5	/Sep.18.2009/50 Percent	Test 1.5A.17.00.Chamber.tdx	Measurement Data File
1.5	/Sep.18.2009/50 Percent	Test 1.5A.17.00.Test Stand.tdm	Measurement File Header
1.5	/Sep.18.2009/50 Percent	Test 1.5A.17.00.Test Stand.tdx	Measurement Data File
2.0	/Sep.18.2009/50 Percent	Test 2.0B.17.21.Camera.tdm	Measurement File Header
2.0	/Sep.18.2009/50 Percent	Test 2.0B.17.21.Camera.tdx	Measurement Data File
2.0	/Sep.18.2009/50 Percent	Test 2.0B.17.21.Chamber.tdm	Measurement File Header
2.0	/Sep.18.2009/50 Percent	Test 2.0B.17.21.Chamber.tdx	Measurement Data File
2.0	/Sep.18.2009/50 Percent	Test 2.0B.17.21.Test Stand.tdm	Measurement File Header
2.0	/Sep.18.2009/50 Percent	Test 2.0B.17.21.Test Stand.tdx	Measurement Data File
2.5	/Sep.18.2009/50 Percent	Test 2.5A.16.37.Camera.tdm	Measurement File Header
2.5	/Sep.18.2009/50 Percent	Test 2.5A.16.37.Camera.tdx	Measurement Data File
2.5	/Sep.18.2009/50 Percent	Test 2.5A.16.37.Chamber.tdm	Measurement File Header
2.5	/Sep.18.2009/50 Percent	Test 2.5A.16.37.Chamber.tdx	Measurement Data File
2.5	/Sep.18.2009/50 Percent	Test 2.5A.16.37.Test Stand.tdm	Measurement File Header
2.5	/Sep.18.2009/50 Percent	Test 2.5A.16.37.Test Stand.tdx	Measurement Data File

Table E.5: Raw Data File Names: Tests 3.0-4.5 at $\frac{r}{r_c}$=50%

Test	File Path	Raw Data File Name	Description
3.0	/Sep.18.2009/50 Percent	Test 3.0F.15.50.Camera.tdm	Measurement File Header
3.0	/Sep.18.2009/50 Percent	Test 3.0F.15.50.Camera.tdx	Measurement Data File
3.0	/Sep.18.2009/50 Percent	Test 3.0F.15.50.Chamber.tdm	Measurement File Header
3.0	/Sep.18.2009/50 Percent	Test 3.0F.15.50.Chamber.tdx	Measurement Data File
3.0	/Sep.18.2009/50 Percent	Test 3.0F.15.49.Test Stand.tdm	Measurement File Header
3.0	/Sep.18.2009/50 Percent	Test 3.0F.15.49.Test Stand.tdx	Measurement Data File
3.5	/Sep.18.2009/50 Percent	Test 3.5A.16.02.Camera.tdm	Measurement File Header
3.5	/Sep.18.2009/50 Percent	Test 3.5A.16.02.Camera.tdx	Measurement Data File
3.5	/Sep.18.2009/50 Percent	Test 3.5A.16.02.Chamber.tdm	Measurement File Header
3.5	/Sep.18.2009/50 Percent	Test 3.5A.16.02.Chamber.tdx	Measurement Data File
3.5	/Sep.18.2009/50 Percent	Test 3.5A.16.02.Test Stand.tdm	Measurement File Header
3.5	/Sep.18.2009/50 Percent	Test 3.5A.16.02.Test Stand.tdx	Measurement Data File
4.0	/Sep.18.2009/50 Percent	Test 4.0A.16.15.Camera.tdm	Measurement File Header
4.0	/Sep.18.2009/50 Percent	Test 4.0A.16.15.Camera.tdx	Measurement Data File
4.0	/Sep.18.2009/50 Percent	Test 4.0A.16.15.Chamber.tdm	Measurement File Header
4.0	/Sep.18.2009/50 Percent	Test 4.0A.16.15.Chamber.tdx	Measurement Data File
4.0	/Sep.18.2009/50 Percent	Test 4.0A.16.15.Test Stand.tdm	Measurement File Header
4.0	/Sep.18.2009/50 Percent	Test 4.0A.16.15.Test Stand.tdx	Measurement Data File
4.5	/Sep.18.2009/50 Percent	Test 4.5A.16.26.Camera.tdm	Measurement File Header
4.5	/Sep.18.2009/50 Percent	Test 4.5A.16.26.Camera.tdx	Measurement Data File
4.5	/Sep.18.2009/50 Percent	Test 4.5A.16.26.Chamber.tdm	Measurement File Header
4.5	/Sep.18.2009/50 Percent	Test 4.5A.16.26.Chamber.tdx	Measurement Data File
4.5	/Sep.18.2009/50 Percent	Test 4.5A.16.26.Test Stand.tdm	Measurement File Header
4.5	/Sep.18.2009/50 Percent	Test 4.5A.16.26.Test Stand.tdx	Measurement Data File

Table E.6: Raw Data File Names: Tests 1.0-2.5 at $\frac{r}{r_c}$=75%

Test	File Path	Raw Data File Name	Description
1.0	/Sep.15.2009/75 Percent	Test 1.0B.17.30.Camera.tdm	Measurement File Header
1.0	/Sep.15.2009/75 Percent	Test 1.0B.17.30.Camera.tdx	Measurement Data File
1.0	/Sep.15.2009/75 Percent	Test 1.0B.17.30.Chamber.tdm	Measurement File Header
1.0	/Sep.15.2009/75 Percent	Test 1.0B.17.30.Chamber.tdx	Measurement Data File
1.0	/Sep.15.2009/75 Percent	Test 1.0B.17.30.Test Stand.tdm	Measurement File Header
1.0	/Sep.15.2009/75 Percent	Test 1.0B.17.30.Test Stand.tdx	Measurement Data File
1.5	/Sep.18.2009/75 Percent	Test 1.5C.17.41.Camera.tdm	Measurement File Header
1.5	/Sep.18.2009/75 Percent	Test 1.5C.17.41.Camera.tdx	Measurement Data File
1.5	/Sep.18.2009/75 Percent	Test 1.5C.17.41.Chamber.tdm	Measurement File Header
1.5	/Sep.18.2009/75 Percent	Test 1.5C.17.41.Chamber.tdx	Measurement Data File
1.5	/Sep.18.2009/75 Percent	Test 1.5C.17.41.Test Stand.tdm	Measurement File Header
1.5	/Sep.18.2009/75 Percent	Test 1.5C.17.41.Test Stand.tdx	Measurement Data File
2.0	/Sep.18.2009/75 Percent	Test 2.0B.17.57.Camera.tdm	Measurement File Header
2.0	/Sep.18.2009/75 Percent	Test 2.0B.17.57.Camera.tdx	Measurement Data File
2.0	/Sep.18.2009/75 Percent	Test 2.0B.17.57.Chamber.tdm	Measurement File Header
2.0	/Sep.18.2009/75 Percent	Test 2.0B.17.57.Chamber.tdx	Measurement Data File
2.0	/Sep.18.2009/75 Percent	Test 2.0B.17.57.Test Stand.tdm	Measurement File Header
2.0	/Sep.18.2009/75 Percent	Test 2.0B.17.57.Test Stand.tdx	Measurement Data File
2.5	/Sep.15.2009/75 Percent	Test 2.5A.15.27.Camera.tdm	Measurement File Header
2.5	/Sep.15.2009/75 Percent	Test 2.5A.15.27.Camera.tdx	Measurement Data File
2.5	/Sep.15.2009/75 Percent	Test 2.5A.15.27.Chamber.tdm	Measurement File Header
2.5	/Sep.15.2009/75 Percent	Test 2.5A.15.27.Chamber.tdx	Measurement Data File
2.5	/Sep.15.2009/75 Percent	Test 2.5A.15.27.Test Stand.tdm	Measurement File Header
2.5	/Sep.15.2009/75 Percent	Test 2.5A.15.27.Test Stand.tdx	Measurement Data File

Table E.7: Raw Data File Names: Tests 3.0-4.5 at $\frac{r}{r_c}$=75%

Test	File Path	Raw Data File Name	Description
3.0	/Sep.15.2009/75 Percent	Test 3.0B.15.17.Camera.tdm	Measurement File Header
3.0	/Sep.15.2009/75 Percent	Test 3.0B.15.17.Camera.tdx	Measurement Data File
3.0	/Sep.15.2009/75 Percent	Test 3.0B.15.17.Chamber.tdm	Measurement File Header
3.0	/Sep.15.2009/75 Percent	Test 3.0B.15.17.Chamber.tdx	Measurement Data File
3.0	/Sep.15.2009/75 Percent	Test 3.0B.15.17.Test Stand.tdm	Measurement File Header
3.0	/Sep.15.2009/75 Percent	Test 3.0B.15.17.Test Stand.tdx	Measurement Data File
3.5	/Sep.15.2009/75 Percent	Test 3.5A.14.50.Camera.tdm	Measurement File Header
3.5	/Sep.15.2009/75 Percent	Test 3.5A.14.50.Camera.tdx	Measurement Data File
3.5	/Sep.15.2009/75 Percent	Test 3.5A.14.50.Chamber.tdm	Measurement File Header
3.5	/Sep.15.2009/75 Percent	Test 3.5A.14.50.Chamber.tdx	Measurement Data File
3.5	/Sep.15.2009/75 Percent	Test 3.5A.14.50.Test Stand.tdm	Measurement File Header
3.5	/Sep.15.2009/75 Percent	Test 3.5A.14.50.Test Stand.tdx	Measurement Data File
4.0	/Sep.15.2009/75 Percent	Test 4.0A.14.37.Camera.tdm	Measurement File Header
4.0	/Sep.15.2009/75 Percent	Test 4.0A.14.37.Camera.tdx	Measurement Data File
4.0	/Sep.15.2009/75 Percent	Test 4.0A.14.37.Chamber.tdm	Measurement File Header
4.0	/Sep.15.2009/75 Percent	Test 4.0A.14.37.Chamber.tdx	Measurement Data File
4.0	/Sep.15.2009/75 Percent	Test 4.0A.14.37.Test Stand.tdm	Measurement File Header
4.0	/Sep.15.2009/75 Percent	Test 4.0A.14.37.Test Stand.tdx	Measurement Data File
4.5	/Sep.15.2009/75 Percent	Test 4.5A.16.09.Camera.tdm	Measurement File Header
4.5	/Sep.15.2009/75 Percent	Test 4.5A.16.09.Camera.tdx	Measurement Data File
4.5	/Sep.15.2009/75 Percent	Test 4.5A.16.09.Chamber.tdm	Measurement File Header
4.5	/Sep.15.2009/75 Percent	Test 4.5A.16.09.Chamber.tdx	Measurement Data File
4.5	/Sep.15.2009/75 Percent	Test 4.5A.16.09.Test Stand.tdm	Measurement File Header
4.5	/Sep.15.2009/75 Percent	Test 4.5A.16.09.Test Stand.tdx	Measurement Data File

Table E.8: Raw Image File Folders: Tests 1.0-4.5 at $\frac{r}{r_c}$=0%

Test	File Path	Description
1.0	/Sep.14.2009/Center/0914M4/Test 1.0A	CH* High-Speed Images
1.0	/Sep.14.2009/Center/0914RL/Test 1.0A	High-Speed Images
1.5	/Sep.14.2009/Center/0914M4/Test 1.5C	CH* High-Speed Images
1.5	/Sep.14.2009/Center/0914RL/Test 1.5C	High-Speed Images
2.0	/Sep.14.2009/Center/0914M4/Test 2.0B	CH* High-Speed Images
2.0	/Sep.14.2009/Center/0914RL/Test 2.0B	High-Speed Images
2.5	/Sep.14.2009/Center/0914M4/Test 2.5B	CH* High-Speed Images
2.5	/Sep.14.2009/Center/0914RL/Test 2.5B	High-Speed Images
3.0	/Sep.14.2009/Center/0914M4/Test 3.0A	CH* High-Speed Images
3.0	/Sep.14.2009/Center/0914RL/Test 3.0A	High-Speed Images
3.5	/Sep.14.2009/Center/0914M4/Test 3.5A	CH* High-Speed Images
3.5	/Sep.14.2009/Center/0914RL/Test 3.5A	High-Speed Images
4.0	/Sep.14.2009/Center/0914M4/Test 4.0A	CH* High-Speed Images
4.0	/Sep.14.2009/Center/0914RL/Test 4.0A	High-Speed Images
4.5	/Sep.14.2009/Center/0914M4/Test 4.5A	CH* High-Speed Images
4.5	/Sep.14.2009/Center/0914RL/Test 4.5A	High-Speed Images

Table E.9: Raw Image File Folders: Tests 1.0-4.5 at $\frac{r}{r_c}$=50%

Test	File Path	Description
1.0	/Sep.18.2009/50 Percent/0918M4/Test 1.0A	CH* High-Speed Images
1.0	/Sep.18.2009/50 Percent/0918RL/Test 1.0A	High-Speed Images
1.5	/Sep.18.2009/50 Percent/0918M4/Test 1.5A	CH* High-Speed Images
1.5	/Sep.18.2009/50 Percent/0918RL/Test 1.5A	High-Speed Images
2.0	/Sep.18.2009/50 Percent/0918M4/Test 2.0B	CH* High-Speed Images
2.0	/Sep.18.2009/50 Percent/0918RL/Test 2.0B	High-Speed Images
2.5	/Sep.18.2009/50 Percent/0918M4/Test 2.5A	CH* High-Speed Images
2.5	/Sep.18.2009/50 Percent/0918RL/Test 2.5A	High-Speed Images
3.0	/Sep.18.2009/50 Percent/0918M4/Test 3.0F	CH* High-Speed Images
3.0	/Sep.18.2009/50 Percent/0918RL/Test 3.0F	High-Speed Images
3.5	/Sep.18.2009/50 Percent/0918M4/Test 3.5A	CH* High-Speed Images
3.5	/Sep.18.2009/50 Percent/0918RL/Test 3.5A	High-Speed Images
4.0	/Sep.18.2009/50 Percent/0918M4/Test 4.0A	CH* High-Speed Images
4.0	/Sep.18.2009/50 Percent/0918RL/Test 4.0A	High-Speed Images
4.5	/Sep.18.2009/50 Percent/0918M4/Test 4.5A	CH* High-Speed Images
4.5	/Sep.18.2009/50 Percent/0918RL/Test 4.5A	High-Speed Images

Table E.10: Raw Image File Folders: Tests 1.0-4.5 at $\frac{r}{r_c}$=75%

Test	File Path	Description
1.0	/Sep.15.2009/75 Percent/0915M4/Test 1.0B	CH* High-Speed Images
1.0	/Sep.15.2009/75 Percent/0915RL/Test 1.0B	High-Speed Images
1.5	/Sep.18.2009/75 Percent/0918M4/Test 1.5C	CH* High-Speed Images
1.5	/Sep.18.2009/75 Percent/0918RL/Test 1.5C	High-Speed Images
2.0	/Sep.18.2009/75 Percent/0918M4/Test 2.0B	CH* High-Speed Images
2.0	/Sep.18.2009/75 Percent/0918RL/Test 2.0B	High-Speed Images
2.5	/Sep.15.2009/75 Percent/0915M4/Test 2.5A	CH* High-Speed Images
2.5	/Sep.15.2009/75 Percent/0915RL/Test 2.5A	High-Speed Images
3.0	/Sep.15.2009/75 Percent/0915M4/Test 3.0B	CH* High-Speed Images
3.0	/Sep.15.2009/75 Percent/0915RL/Test 3.0B	High-Speed Images
3.5	/Sep.15.2009/75 Percent/0915M4/Test 3.5A	CH* High-Speed Images
3.5	/Sep.15.2009/75 Percent/0915RL/Test 3.5A	High-Speed Images
4.0	/Sep.15.2009/75 Percent/0915M4/Test 4.0A	CH* High-Speed Images
4.0	/Sep.15.2009/75 Percent/0915RL/Test 4.0A	High-Speed Images
4.5	/Sep.15.2009/75 Percent/0915M4/Test 4.5A	CH* High-Speed Images
4.5	/Sep.15.2009/75 Percent/0915RL/Test 4.5A	High-Speed Images

Table E.11: Raw Data File Names: Tests 3.0-4.5 at $\frac{r}{r_c}$=75%

Test	SP	File Path	Raw Data File Name	Description
3.0	7	/Sep.22.2009/75 Percent	Test 5.0A.13.01.Camera.tdm	Measurement File Header
3.0	7	/Sep.22.2009/75 Percent	Test 5.0A.13.01.Camera.tdx	Measurement Data File
3.0	7	/Sep.22.2009/75 Percent	Test 5.0A.13.01.Chamber.tdm	Measurement File Header
3.0	7	/Sep.22.2009/75 Percent	Test 5.0A.13.01.Chamber.tdx	Measurement Data File
3.0	7	/Sep.22.2009/75 Percent	Test 5.0A.13.01.Test Stand.tdm	Measurement File Header
3.0	7	/Sep.22.2009/75 Percent	Test 5.0A.13.01.Test Stand.tdx	Measurement Data File
4.0	3	/Sep.22.2009/75 Percent	Test 5.0B.13.18.Camera.tdm	Measurement File Header
4.0	3	/Sep.22.2009/75 Percent	Test 5.0B.13.18.Camera.tdx	Measurement Data File
4.0	3	/Sep.22.2009/75 Percent	Test 5.0B.13.18.Chamber.tdm	Measurement File Header
4.0	3	/Sep.22.2009/75 Percent	Test 5.0B.13.18.Chamber.tdx	Measurement Data File
4.0	3	/Sep.22.2009/75 Percent	Test 5.0B.13.18.Test Stand.tdm	Measurement File Header
4.0	3	/Sep.22.2009/75 Percent	Test 5.0B.13.18.Test Stand.tdx	Measurement Data File
4.0	13	/Sep.22.2009/75 Percent	Test 5.0J.13.54.Camera.tdm	Measurement File Header
4.0	13	/Sep.22.2009/75 Percent	Test 5.0J.13.54.Camera.tdx	Measurement Data File
4.0	13	/Sep.22.2009/75 Percent	Test 5.0J.13.54.Chamber.tdm	Measurement File Header
4.0	13	/Sep.22.2009/75 Percent	Test 5.0J.13.54.Chamber.tdx	Measurement Data File
4.0	13	/Sep.22.2009/75 Percent	Test 5.0J.13.54.Test Stand.tdm	Measurement File Header
4.0	13	/Sep.22.2009/75 Percent	Test 5.0J.13.54.Test Stand.tdx	Measurement Data File
4.5	7	/Sep.22.2009/75 Percent	Test 5.0K.14.01.Camera.tdm	Measurement File Header
4.5	7	/Sep.22.2009/75 Percent	Test 5.0K.14.01.Camera.tdx	Measurement Data File
4.5	7	/Sep.22.2009/75 Percent	Test 5.0K.14.01.Chamber.tdm	Measurement File Header
4.5	7	/Sep.22.2009/75 Percent	Test 5.0K.14.01.Chamber.tdx	Measurement Data File
4.5	7	/Sep.22.2009/75 Percent	Test 5.0K.14.01.Test Stand.tdm	Measurement File Header
4.5	7	/Sep.22.2009/75 Percent	Test 5.0K.14.01.Test Stand.tdx	Measurement Data File
1.0	12	/Sep.22.2009/75 Percent	Test 5.0M.14.18.Camera.tdm	Measurement File Header
1.0	12	/Sep.22.2009/75 Percent	Test 5.0M.14.18.Camera.tdx	Measurement Data File
1.0	12	/Sep.22.2009/75 Percent	Test 5.0M.14.18.Chamber.tdm	Measurement File Header
1.0	12	/Sep.22.2009/75 Percent	Test 5.0M.14.18.Chamber.tdx	Measurement Data File
1.0	12	/Sep.22.2009/75 Percent	Test 5.0M.14.18.Test Stand.tdm	Measurement File Header
1.0	12	/Sep.22.2009/75 Percent	Test 5.0M.14.18.Test Stand.tdx	Measurement Data File

Table E.12: Raw Image File Folders: Repeated Tests at $\frac{r}{r_c}$=75%

Test	SP	File Path	Description
3.0	7	/Sep.22.2009/75 Percent/0922M4/Test 5.0A	OH* High-Speed Images
3.0	7	/Sep.22.2009/75 Percent/0922RL/Test 5.0A	High-Speed Images
4.0	3	/Sep.22.2009/75 Percent/0922M4/Test 5.0B	OH* High-Speed Images
4.0	3	/Sep.22.2009/75 Percent/0922RL/Test 5.0B	High-Speed Images
4.0	13	/Sep.22.2009/75 Percent/0922M4/Test 5.0J	OH* High-Speed Images
4.0	13	/Sep.22.2009/75 Percent/0922RL/Test 5.0J	High-Speed Images
4.5	7	/Sep.22.2009/75 Percent/0922M4/Test 5.0K	OH* High-Speed Images
4.5	7	/Sep.22.2009/75 Percent/0922RL/Test 5.0K	High-Speed Images
1.0	12	/Sep.22.2009/75 Percent/0922M4/Test 5.0M	OH* High-Speed Images
1.0	12	/Sep.22.2009/75 Percent/0922RL/Test 5.0M	High-Speed Images

Table E.13: Raw Data File Names: Cold Flow Testing at $\frac{r}{r_c}$=75%

Test	SP	File Path	Raw Data File Name	Description
-	-	/Sep.24.2009/Cold Flow	CH4only_ZeroPoint_HF.xls	High-Frequency Data
-	-	/Sep.24.2009/Cold Flow	CH4only_ZeroPoint_LF.xls	Low-Frequency Data
1.0	-	/Sep.24.2009/Cold Flow	CH4only_Test1.0fuel_HF.xls	High-Frequency Data
1.0	-	/Sep.24.2009/Cold Flow	CH4only_Test1.0fuel_LF.xls	Low-Frequency Data
1.5	-	/Sep.24.2009/Cold Flow	CH4only_Test1.5fuel_HF.xls	High-Frequency Data
1.5	-	/Sep.24.2009/Cold Flow	CH4only_Test1.5fuel_LF.xls	Low-Frequency Data
1.5	8	/Sep.24.2009/Cold Flow	02only_Test1.5SP8ox_HF.xls	High-Frequency Data
1.5	8	/Sep.24.2009/Cold Flow	02only_Test1.5SP8ox_LF.xls	Low-Frequency Data
2.0	-	/Sep.24.2009/Cold Flow	CH4only_Test2.0fuel_HF.xls	High-Frequency Data
2.0	-	/Sep.24.2009/Cold Flow	CH4only_Test2.0fuel_LF.xls	Low-Frequency Data
2.0	8	/Sep.24.2009/Cold Flow	02only_Test2.0SP8ox_HF.xls	High-Frequency Data
2.0	8	/Sep.24.2009/Cold Flow	02only_Test2.0SP8ox_LF.xls	Low-Frequency Data
4.0	13	/Sep.24.2009/Cold Flow	02only_Test4.0SP13ox_HF.xls	High-Frequency Data
4.0	13	/Sep.24.2009/Cold Flow	02only_Test4.0SP13ox_LF.xls	Low-Frequency Data

Table E.14: Experiment and Analysis Code File Names

File Name	Description
RUSKIE_29.vi	Experiment Control Program
AUTO_OPEN.VBS	Opens Analysis Toolbar
load_user_interface.VBS	Loads Analysis Command File
RMAnalysis_REV03.SUD	Command File
AvgTempFinder.VBS	Analyzes Temperature Data
Stability_Map_65_horbar_mass_volume.m	Creates Stability Map

APPENDIX F

TABULATED DATA

Table F.1: Test Matrix: Tests 1.0-2.0

Test	SP	$\dot{m}_f$ $[g/s]$	$\dot{m}_{ox}$ $[g/s]$	ϕ	OF	VR	MR	J
1.0	1	0.1091	0.2183	2.00	2.0	1.736	0.868	1.511
1.0	2	0.1091	0.2362	1.85	2.2	1.604	0.741	1.290
1.0	3	0.1091	0.2452	1.78	2.2	1.545	0.687	1.197
1.0	4	0.1091	0.2701	1.62	2.5	1.403	0.567	0.986
1.0	5	0.1091	0.2834	1.54	2.6	1.337	0.515	0.896
1.0	6	0.1091	0.3052	1.43	2.8	1.241	0.444	0.772
1.0	7	0.1091	0.3274	1.33	3.0	1.157	0.386	0.671
1.0	8	0.1091	0.3699	1.18	3.4	1.024	0.302	0.526
1.0	9	0.1091	0.3954	1.10	3.6	0.958	0.264	0.460
1.0	10	0.1091	0.4365	1.00	4.0	0.868	0.217	0.378
1.0	11	0.1091	0.4644	0.94	4.3	0.816	0.192	0.334
1.0	12	0.1091	0.5203	0.84	4.8	0.728	0.153	0.266
1.0	13	0.1091	0.5820	0.75	5.3	0.651	0.122	0.212
1.5	1	0.1220	0.2441	2.00	2.0	1.736	0.868	1.511
1.5	2	0.1220	0.2641	1.85	2.2	1.604	0.741	1.290
1.5	3	0.1220	0.2742	1.78	2.2	1.545	0.687	1.197
1.5	4	0.1220	0.3021	1.62	2.5	1.403	0.567	0.986
1.5	5	0.1220	0.3170	1.54	2.6	1.337	0.515	0.896
1.5	6	0.1220	0.3413	1.43	2.8	1.241	0.444	0.772
1.5	7	0.1220	0.3661	1.33	3.0	1.157	0.386	0.671
1.5	8	0.1220	0.4137	1.18	3.4	1.024	0.302	0.526
1.5	9	0.1220	0.4421	1.10	3.6	0.958	0.264	0.460
1.5	10	0.1220	0.4881	1.00	4.0	0.868	0.217	0.378
1.5	11	0.1220	0.5193	0.94	4.3	0.816	0.192	0.334
1.5	12	0.1220	0.5818	0.84	4.8	0.728	0.153	0.266
1.5	13	0.1220	0.6508	0.75	5.3	0.651	0.122	0.212
2.0	1	0.1455	0.2911	2.00	2.0	1.736	0.868	1.511
2.0	2	0.1455	0.3150	1.85	2.2	1.604	0.741	1.290
2.0	3	0.1455	0.3271	1.78	2.2	1.545	0.687	1.197
2.0	4	0.1455	0.3602	1.62	2.5	1.403	0.567	0.986
2.0	5	0.1455	0.3780	1.54	2.6	1.337	0.515	0.896
2.0	6	0.1455	0.4071	1.43	2.8	1.241	0.444	0.772
2.0	7	0.1455	0.4366	1.33	3.0	1.157	0.386	0.671
2.0	8	0.1455	0.4933	1.18	3.4	1.024	0.302	0.526
2.0	9	0.1455	0.5273	1.10	3.6	0.958	0.264	0.460
2.0	10	0.1455	0.5822	1.00	4.0	0.868	0.217	0.378
2.0	11	0.1455	0.6193	0.94	4.3	0.816	0.192	0.334
2.0	12	0.1455	0.6939	0.84	4.8	0.728	0.153	0.266
2.0	13	0.1455	0.7762	0.75	5.3	0.651	0.122	0.212

Table F.2: Test Matrix: Tests 2.5-3.5

Test	SP	$\dot{m}_f$ $[g/s]$	$\dot{m}_{ox}$ $[g/s]$	ϕ	OF	VR	MR	J
2.5	1	0.1717	0.3433	2.00	2.0	1.736	0.868	1.511
2.5	2	0.1717	0.3716	1.85	2.2	1.604	0.741	1.290
2.5	3	0.1717	0.3858	1.78	2.2	1.545	0.687	1.197
2.5	4	0.1717	0.4249	1.62	2.5	1.403	0.567	0.986
2.5	5	0.1717	0.4459	1.54	2.6	1.337	0.515	0.896
2.5	6	0.1717	0.4802	1.43	2.8	1.241	0.444	0.772
2.5	7	0.1717	0.5150	1.33	3.0	1.157	0.386	0.671
2.5	8	0.1717	0.5819	1.18	3.4	1.024	0.302	0.526
2.5	9	0.1717	0.6220	1.10	3.6	0.958	0.264	0.460
2.5	10	0.1717	0.6867	1.00	4.0	0.868	0.217	0.378
2.5	11	0.1717	0.7305	0.94	4.3	0.816	0.192	0.334
2.5	12	0.1717	0.8185	0.84	4.8	0.728	0.153	0.266
2.5	13	0.1717	0.9156	0.75	5.3	0.651	0.122	0.212
3.0	1	0.1940	0.3880	2.00	2.0	1.736	0.868	1.511
3.0	2	0.1940	0.4199	1.85	2.2	1.604	0.741	1.290
3.0	3	0.1940	0.4359	1.78	2.2	1.545	0.687	1.197
3.0	4	0.1940	0.4801	1.62	2.5	1.403	0.567	0.986
3.0	5	0.1940	0.5038	1.54	2.6	1.337	0.515	0.896
3.0	6	0.1940	0.5426	1.43	2.8	1.241	0.444	0.772
3.0	7	0.1940	0.5819	1.33	3.0	1.157	0.386	0.671
3.0	8	0.1940	0.6576	1.18	3.4	1.024	0.302	0.526
3.0	9	0.1940	0.7028	1.10	3.6	0.958	0.264	0.460
3.0	10	0.1940	0.7759	1.00	4.0	0.868	0.217	0.378
3.0	11	0.1940	0.8254	0.94	4.3	0.816	0.192	0.334
3.0	12	0.1940	0.9248	0.84	4.8	0.728	0.153	0.266
3.0	13	0.1940	1.0345	0.75	5.3	0.651	0.122	0.212
3.5	1	0.2242	0.4483	2.00	2.0	1.736	0.868	1.511
3.5	2	0.2242	0.4852	1.85	2.2	1.604	0.741	1.290
3.5	3	0.2242	0.5037	1.78	2.2	1.545	0.687	1.197
3.5	4	0.2242	0.5548	1.62	2.5	1.403	0.567	0.986
3.5	5	0.2242	0.5822	1.54	2.6	1.337	0.515	0.896
3.5	6	0.2242	0.6270	1.43	2.8	1.241	0.444	0.772
3.5	7	0.2242	0.6725	1.33	3.0	1.157	0.386	0.671
3.5	8	0.2242	0.7599	1.18	3.4	1.024	0.302	0.526
3.5	9	0.2242	0.8122	1.10	3.6	0.958	0.264	0.460
3.5	10	0.2242	0.8966	1.00	4.0	0.868	0.217	0.378
3.5	11	0.2242	0.9539	0.94	4.3	0.816	0.192	0.334
3.5	12	0.2242	1.0687	0.84	4.8	0.728	0.153	0.266
3.5	13	0.2242	1.1955	0.75	5.3	0.651	0.122	0.212

Table F.3: Test Matrix: Tests 4.0-4.5

Test	SP	$\dot{m}_f$ $[g/s]$	$\dot{m}_{ox}$ $[g/s]$	ϕ	OF	VR	MR	J
4.0	1	0.2590	0.5180	2.00	2.0	1.736	0.868	1.511
4.0	2	0.2590	0.5606	1.85	2.2	1.604	0.741	1.290
4.0	3	0.2590	0.5820	1.78	2.2	1.545	0.687	1.197
4.0	4	0.2590	0.6411	1.62	2.5	1.403	0.567	0.986
4.0	5	0.2590	0.6727	1.54	2.6	1.337	0.515	0.896
4.0	6	0.2590	0.7245	1.43	2.8	1.241	0.444	0.772
4.0	7	0.2590	0.7770	1.33	3.0	1.157	0.386	0.671
4.0	8	0.2590	0.8780	1.18	3.4	1.024	0.302	0.526
4.0	9	0.2590	0.9384	1.10	3.6	0.958	0.264	0.460
4.0	10	0.2590	1.0360	1.00	4.0	0.868	0.217	0.378
4.0	11	0.2590	1.1021	0.94	4.3	0.816	0.192	0.334
4.0	12	0.2590	1.2348	0.84	4.8	0.728	0.153	0.266
4.0	13	0.2590	1.3813	0.75	5.3	0.651	0.122	0.212
4.5	1	0.2910	0.5819	2.00	2.0	1.736	0.868	1.511
4.5	2	0.2910	0.6298	1.85	2.2	1.604	0.741	1.290
4.5	3	0.2910	0.6539	1.78	2.2	1.545	0.687	1.197
4.5	4	0.2910	0.7202	1.62	2.5	1.403	0.567	0.986
4.5	5	0.2910	0.7558	1.54	2.6	1.337	0.515	0.896
4.5	6	0.2910	0.8139	1.43	2.8	1.241	0.444	0.772
4.5	7	0.2910	0.8729	1.33	3.0	1.157	0.386	0.671
4.5	8	0.2910	0.9863	1.18	3.4	1.024	0.302	0.526
4.5	9	0.2910	1.0542	1.10	3.6	0.958	0.264	0.460
4.5	10	0.2910	1.1639	1.00	4.0	0.868	0.217	0.378
4.5	11	0.2910	1.2382	0.94	4.3	0.816	0.192	0.334
4.5	12	0.2910	1.3872	0.84	4.8	0.728	0.153	0.266
4.5	13	0.2910	1.5518	0.75	5.3	0.651	0.122	0.212

Table F.4: Data: Tests 1.0-2.0 for $\frac{r}{r_c}$=0%

$\dot{m}_f$ [g/s]	$\dot{m}_{ox}$ [g/s]	A_{P1} [psig]	f_{P1} [Hz]	A_{P2} [psig]	f_{P2} [Hz]	A_{P4} [psig]	f_{P4} [Hz]	A_{P6} [psig]	f_{P6} [Hz]	A_{P8} [psig]	f_{P8} [Hz]
0.1095	0.2181	0.017	318	0.011	3469	0.013	3469	0.013	3469	0.012	3469
0.1093	0.2399	0.018	318	0.010	3469	0.012	3469	0.012	3469	0.011	3469
0.1092	0.2399	0.019	318	0.011	3469	0.012	3469	0.012	3469	0.012	3469
0.1092	0.2836	0.037	8543	0.030	8557	0.028	5820	0.010	5826	0.026	5826
0.1097	0.3054	0.032	6077	0.027	6077	0.016	6084	0.013	3462	0.022	6077
0.1092	0.3054	0.024	6111	0.022	6111	0.024	6118	0.009	3462	0.013	6118
0.1093	0.3272	0.027	6307	0.018	6301	0.045	6301	0.013	3455	0.021	6301
0.1093	0.3926	0.017	318	0.007	3455	0.008	3455	0.008	3455	0.008	3455
0.1092	0.3926	0.018	318	0.011	3455	0.012	3455	0.012	3455	0.012	3455
0.1090	0.4581	0.019	318	0.011	3455	0.013	3455	0.013	3455	0.012	3455
0.1095	0.4799	0.018	318	0.008	3448	0.009	3448	0.009	3448	0.008	3448
0.1093	0.5235	0.023	318	0.016	3347	0.013	3347	0.012	3448	0.011	3448
0.1090	0.5890	0.019	318	0.016	10332	0.011	3448	0.011	3448	0.011	3448
0.1222	0.2399	0.023	318	0.011	3415	0.011	3415	0.012	3415	0.011	3415
0.1221	0.2618	0.019	318	0.011	3415	0.012	3415	0.013	3415	0.012	3415
0.1220	0.2836	0.019	318	0.009	3415	0.010	3415	0.010	3415	0.009	3415
0.1223	0.3054	0.019	318	0.007	3408	0.009	3408	0.009	3408	0.008	3408
0.1220	0.3272	0.025	318	0.009	3401	0.011	3401	0.011	3401	0.010	3401
0.1224	0.3490	0.021	318	0.008	3394	0.009	3394	0.009	3394	0.009	3394
0.1217	0.3708	0.024	318	0.008	3381	0.010	3381	0.010	3381	0.009	3381
0.1458	0.2836	0.022	318	0.011	3381	0.013	3381	0.013	3381	0.011	3381
0.1468	0.3272	0.022	318	0.012	3374	0.013	3374	0.013	3374	0.012	3374
0.1452	0.3490	0.017	318	0.008	3367	0.010	3367	0.009	3367	0.008	3367
0.1452	0.3708	0.017	318	0.011	3367	0.013	3367	0.013	3367	0.013	6816
0.1464	0.3926	0.021	318	0.011	3381	0.013	3381	0.013	3381	0.012	3381
0.1478	0.4145	0.015	318	0.011	3394	0.013	3394	0.012	3394	0.011	3394
0.1455	0.4363	0.015	318	0.008	3401	0.010	3401	0.009	3401	0.009	3401
0.1451	0.5017	0.016	318	0.011	3415	0.013	3415	0.013	3415	0.037	9776
0.1453	0.5235	0.019	318	0.011	3421	0.013	3421	0.013	3421	0.012	3421
0.1455	0.5890	0.015	318	0.015	3713	0.013	3428	0.013	3428	0.012	3428
0.1458	0.6108	0.162	3171	0.160	3171	0.041	3171	0.013	3123	0.021	3171
0.1454	0.6980	0.159	3130	0.155	3130	0.040	3130	0.016	3130	0.015	3130
0.1457	0.7853	0.086	3198	0.093	3198	0.061	3198	0.015	3198	0.012	3198

Table F.5: Data: Tests 2.5-3.5 for $\frac{r}{r_c}$=0%

$\dot{m}_f$ [g/s]	$\dot{m}_{ox}$ [g/s]	A_{P1} [psig]	f_{P1} [Hz]	A_{P2} [psig]	f_{P2} [Hz]	A_{P4} [psig]	f_{P4} [Hz]	A_{P6} [psig]	f_{P6} [Hz]	A_{P8} [psig]	f_{P8} [Hz]
0.1713	0.3272	0.019	318	0.011	3374	0.013	3374	0.012	3374	0.011	3374
0.1721	0.3708	0.023	318	0.012	3374	0.013	3374	0.013	3374	0.011	3374
0.1717	0.3926	0.018	318	0.010	3381	0.012	3381	0.012	3381	0.010	3381
0.1717	0.4581	0.019	318	0.009	3374	0.010	3374	0.010	3374	0.009	3374
0.1717	0.4363	0.018	318	0.011	3367	0.013	3367	0.013	3367	0.011	3367
0.1720	0.4799	0.020	318	0.010	3360	0.011	3360	0.011	3360	0.010	3360
0.1713	0.5235	0.017	318	0.009	3347	0.010	3347	0.010	3347	0.011	9844
0.1715	0.5890	0.019	318	0.011	3340	0.013	3340	0.013	3340	0.012	3340
0.1712	0.6326	0.018	318	0.011	3347	0.022	10305	0.013	3347	0.012	3347
0.1717	0.6980	0.119	3144	0.110	3144	0.072	3144	0.012	3144	0.010	3367
0.1712	0.7417	0.130	3191	0.124	3191	0.079	3191	0.018	5820	0.012	3191
0.1716	0.8289	0.074	3469	0.075	3469	0.017	3469	0.011	3394	0.022	9302
0.1721	0.9162	0.030	3428	0.027	3428	0.014	3408	0.011	3408	0.015	9465
0.1943	0.3926	0.024	318	0.011	3415	0.013	3415	0.013	3415	0.013	3415
0.1939	0.4145	0.020	318	0.008	3415	0.009	3415	0.009	3415	0.009	3415
0.1936	0.4363	0.020	318	0.008	3415	0.009	3415	0.009	3415	0.009	3415
0.1939	0.4799	0.025	318	0.008	3401	0.009	3401	0.009	3401	0.008	3401
0.1944	0.5235	0.055	3252	0.047	3252	0.032	3252	0.010	3381	0.010	9824
0.1943	0.5453	0.034	9993	0.023	10278	0.037	9993	0.013	3367	0.027	9857
0.1939	0.5890	0.024	3597	0.015	3597	0.010	3597	0.010	3354	0.096	9769
0.1936	0.6544	0.021	10447	0.103	10454	0.016	10589	0.012	3354	0.026	10589
0.1936	0.7198	0.105	3225	0.092	3225	0.064	3225	0.021	3225	0.011	3347
0.1939	0.7635	0.120	3340	0.091	3340	0.064	3340	0.014	6050	0.029	9390
0.1944	0.8289	0.077	3543	0.064	3543	0.033	3536	0.013	3543	0.020	9580
0.1932	0.9380	0.031	3455	0.025	3455	0.024	3455	0.011	3340	0.011	3340
0.1939	1.0470	0.061	3421	0.048	3421	0.037	3421	0.009	3421	0.013	9478
0.2243	0.4581	0.015	318	0.008	3428	0.009	3428	0.009	3428	0.008	3428
0.2240	0.4799	0.019	318	0.008	3435	0.009	3435	0.009	3435	0.009	3435
0.2244	0.5017	0.016	318	0.009	3442	0.010	3442	0.010	3442	0.010	3442
0.2237	0.5671	0.029	3577	0.020	3577	0.011	3570	0.009	3442	0.027	9763
0.2241	0.5890	0.020	318	0.025	10135	0.020	10101	0.013	3442	0.012	3442
0.2242	0.6326	0.017	318	0.029	10366	0.012	10460	0.009	3435	0.022	10454
0.2249	0.6762	0.022	318	0.013	10609	0.032	10677	0.042	10677	0.057	10677
0.2240	0.7635	0.072	3252	0.062	3252	0.046	3252	0.018	5935	0.017	5935
0.2240	0.8289	0.065	3536	0.054	3536	0.046	9376	0.012	3442	0.055	9383
0.2241	0.9162	0.039	9255	0.026	3787	0.043	9343	0.020	9607	0.049	9410
0.2248	0.9598	0.023	9546	0.017	9749	0.034	9729	0.013	3435	0.084	9742
0.2241	1.0689	0.018	318	0.013	5840	0.022	5840	0.010	3435	0.018	5847
0.2240	1.1997	0.058	9200	0.011	3435	0.054	9478	0.024	9485	0.041	9559

Table F.6: Data: Tests 4.0-4.5 for $\frac{r}{r_c}$=0%

$\dot{m}_f$ [g/s]	$\dot{m}_{ox}$ [g/s]	A_{P1} [psig]	f_{P1} [Hz]	A_{P2} [psig]	f_{P2} [Hz]	A_{P4} [psig]	f_{P4} [Hz]	A_{P6} [psig]	f_{P6} [Hz]	A_{P8} [psig]	f_{P8} [Hz]
0.2587	0.5235	0.019	318	0.011	3421	0.013	3421	0.013	3421	0.011	3421
0.2584	0.5671	0.024	318	0.011	3421	0.013	3421	0.012	3421	0.011	3421
0.2589	0.5671	0.020	318	0.040	10237	0.028	10135	0.016	10156	0.012	10223
0.2593	0.6544	0.024	318	0.035	10555	0.062	10555	0.019	10670	0.032	10555
0.2588	0.6762	0.024	318	0.011	10616	0.062	10670	0.027	10677	0.036	10664
0.2590	0.7198	0.129	3340	0.120	3340	0.069	3340	0.011	3340	0.008	3374
0.2593	0.7853	0.095	3455	0.083	3455	0.059	3455	0.011	3367	0.033	9255
0.2591	0.8943	0.052	3706	0.046	3706	0.041	9749	0.016	9749	0.110	9749
0.2594	0.9598	0.028	9187	0.014	12432	0.018	9688	0.012	3367	0.024	9688
0.2590	1.0252	0.056	4018	0.033	4018	0.028	4018	0.013	3374	0.011	3374
0.2588	1.1125	0.022	318	0.030	5786	0.082	6009	0.018	6077	0.053	5786
0.2583	1.2434	0.040	9546	0.013	3774	0.060	6545	0.021	9546	0.052	9261
0.2594	1.3742	0.020	318	0.008	7012	0.098	6619	0.021	6606	0.040	6619
0.2903	0.5890	0.016	318	0.007	3435	0.008	3435	0.008	3435	0.007	3435
0.2906	0.6326	0.019	318	0.007	3442	0.009	3442	0.008	3442	0.007	3442
0.2909	0.6544	0.016	318	0.011	10582	0.063	10582	0.010	3442	0.027	10582
0.2906	0.7198	0.016	318	0.011	3442	0.047	9722	0.015	10711	0.036	9614
0.2909	0.7853	0.069	3408	0.060	3408	0.033	3408	0.014	3442	0.012	9105
0.2910	0.8289	0.082	3564	0.068	3564	0.044	9397	0.013	9471	0.068	9397
0.2916	0.8725	0.028	3672	0.033	3672	0.062	9681	0.013	3442	0.028	9681
0.2910	1.0034	0.022	318	0.014	10250	0.027	10142	0.012	3442	0.011	3442
0.2908	1.0689	0.021	318	0.011	3442	0.014	3442	0.013	3442	0.011	3442
0.2909	1.1343	0.019	318	0.008	3435	0.024	9695	0.008	3435	0.022	9702
0.2902	1.2652	0.022	318	0.008	3435	0.011	11395	0.009	3435	0.010	14837
0.2933	1.3742	0.023	6565	0.013	6565	0.093	6565	0.031	6565	0.063	6565
0.2911	1.5269	0.152	3801	0.138	3801	0.072	3801	0.025	3801	0.016	3801

Table F.7: Data: Tests 1.0-2.0 for $\frac{r}{r_c}$=50%

$\dot{m}_f$ [g/s]	$\dot{m}_{ox}$ [g/s]	A_{P1} [psig]	f_{P1} [Hz]	A_{P2} [psig]	f_{P2} [Hz]	A_{P4} [psig]	f_{P4} [Hz]	A_{P6} [psig]	f_{P6} [Hz]	A_{P7} [psig]	f_{P7} [Hz]	A_{P8} [psig]	f_{P8} [Hz]
0.1087	0.2181	0.019	325	0.009	3618	0.010	3618	0.010	3618	0.006	3618	0.010	3618
0.1094	0.2399	0.025	325	0.009	3618	0.010	3618	0.010	3618	0.007	3618	0.010	3618
0.1089	0.2399	0.020	325	0.010	3611	0.011	3611	0.012	3611	0.007	3611	0.011	3611
0.1086	0.2618	0.025	325	0.010	3597	0.011	3597	0.011	3597	0.007	3597	0.011	3597
0.1092	0.2836	0.021	325	0.008	3577	0.009	3577	0.009	3577	0.006	3577	0.009	3577
0.1086	0.3272	0.026	325	0.010	3564	0.012	3564	0.012	3564	0.007	3564	0.011	3564
0.1089	0.3272	0.025	325	0.009	3557	0.011	3557	0.011	3557	0.007	3557	0.010	3557
0.1090	0.4145	0.025	325	0.011	1592	0.011	3536	0.012	3536	0.007	3536	0.011	3536
0.1090	0.3926	0.025	325	0.010	3536	0.012	3536	0.012	3536	0.008	3536	0.011	3536
0.1093	0.4363	0.020	325	0.008	3530	0.010	3530	0.010	3530	0.006	3530	0.009	3530
0.1092	0.4799	0.020	325	0.011	1606	0.011	3523	0.012	3523	0.007	3523	0.011	3523
0.1088	0.5453	0.020	325	0.016	1653	0.011	3516	0.012	3516	0.007	3516	0.011	3516
0.1090	0.5671	0.018	325	0.022	1660	0.011	1660	0.012	3509	0.007	3509	0.011	3509
0.1222	0.2399	0.025	325	0.010	3543	0.011	3543	0.012	3543	0.007	3543	0.011	3543
0.1220	0.2618	0.020	325	0.010	3536	0.011	3536	0.012	3536	0.007	3536	0.011	3536
0.1217	0.2618	0.025	325	0.007	3523	0.008	3523	0.008	3523	0.005	3523	0.008	3523
0.1221	0.3054	0.023	325	0.008	3523	0.010	3523	0.010	3523	0.006	3523	0.009	3523
0.1224	0.3054	0.023	325	0.007	3516	0.008	3516	0.009	3516	0.005	3516	0.008	3516
0.1219	0.3490	0.018	325	0.010	3509	0.011	3509	0.012	3509	0.007	3509	0.011	3509
0.1219	0.3926	0.021	325	0.011	1599	0.011	3509	0.012	3509	0.007	3509	0.011	3509
0.1219	0.4145	0.016	325	0.007	3509	0.008	3509	0.009	3509	0.005	3509	0.008	3509
0.1222	0.4363	0.014	332	0.014	1640	0.008	3516	0.009	3516	0.005	3516	0.008	3516
0.1219	0.5017	0.014	332	0.009	3509	0.011	7154	0.010	3509	0.006	3509	0.010	3509
0.1219	0.5235	0.018	332	0.009	3516	0.040	7811	0.012	3516	0.007	7906	0.010	3516
0.1223	0.5890	0.020	332	0.018	7859	0.054	7900	0.012	7974	0.011	7974	0.009	7859
0.1222	0.6762	0.016	332	0.014	1741	0.010	3543	0.011	3543	0.007	3543	0.010	3543
0.1451	0.2836	0.018	332	0.010	3604	0.011	3604	0.012	3604	0.007	3604	0.011	3604
0.1455	0.3054	0.018	332	0.009	3611	0.010	3611	0.010	3611	0.006	3611	0.010	3611
0.1454	0.3272	0.022	332	0.009	3625	0.010	3625	0.010	3625	0.007	3625	0.010	3625
0.1455	0.3272	0.021	332	0.010	3631	0.011	3631	0.011	3631	0.007	3631	0.011	3631
0.1453	0.3708	0.019	332	0.009	3638	0.010	3638	0.010	3638	0.007	3638	0.010	3638
0.1453	0.4145	0.016	332	0.008	3645	0.009	3645	0.009	3645	0.006	3645	0.008	3645
0.1459	0.4145	0.015	332	0.010	3645	0.011	3645	0.012	3645	0.007	3645	0.011	3645
0.1455	0.5235	0.017	325	0.020	5555	0.022	7764	0.013	3645	0.008	3645	0.011	3645
0.1448	0.5235	0.015	325	0.021	5454	0.017	5454	0.011	3638	0.007	3638	0.015	10833
0.1456	0.5890	0.019	325	0.013	7859	0.069	7859	0.013	7859	0.027	7859	0.010	3638
0.1455	0.6108	0.017	325	0.010	3638	0.050	7879	0.012	3638	0.007	3638	0.011	3638
0.1455	0.7198	0.017	325	0.016	5677	0.011	5677	0.010	3631	0.007	3631	0.010	3631
0.1456	0.8071	0.025	2541	0.016	2541	0.037	7344	0.012	2541	0.006	3631	0.009	3631

Table F.8: Data: Tests 2.5-3.5 for $\frac{r}{r_c}$=50%

$\dot{m}_f$ [g/s]	$\dot{m}_{ox}$ [g/s]	A_{P1} [psig]	f_{P1} [Hz]	A_{P2} [psig]	f_{P2} [Hz]	A_{P4} [psig]	f_{P4} [Hz]	A_{P6} [psig]	f_{P6} [Hz]	A_{P7} [psig]	f_{P7} [Hz]	A_{P8} [psig]	f_{P8} [Hz]
0.1712	0.3272	0.020	332	0.008	3557	0.009	3557	0.009	3557	0.006	3557	0.009	3557
0.1722	0.3708	0.015	332	0.007	3570	0.008	3570	0.008	3570	0.005	3570	0.008	3570
0.1712	0.3708	0.015	332	0.009	3584	0.010	3584	0.010	3584	0.006	3584	0.010	3584
0.1715	0.4581	0.018	332	0.010	3597	0.011	3597	0.011	3597	0.007	3597	0.011	3597
0.1713	0.4581	0.017	325	0.009	1748	0.010	3604	0.010	3604	0.006	3604	0.010	3604
0.1718	0.5017	0.014	332	0.008	3611	0.009	3611	0.010	3611	0.006	3611	0.009	3611
0.1717	0.5017	0.018	325	0.015	7954	0.043	7947	0.026	8143	0.010	7954	0.010	3618
0.1717	0.5890	0.020	325	0.017	5874	0.028	5881	0.022	5874	0.005	3618	0.032	11761
0.1717	0.6326	0.016	325	0.013	5718	0.026	8103	0.034	8150	0.007	3625	0.010	3625
0.1717	0.7198	0.051	5359	0.061	5352	0.080	5359	0.038	5359	0.020	10711	0.015	5359
0.1717	0.7198	0.021	325	0.019	5542	0.032	5542	0.022	5488	0.006	10969	0.010	3625
0.1719	0.8507	0.018	325	0.007	5779	0.011	5718	0.007	3618	0.005	3618	0.007	3618
0.1717	0.9380	0.019	325	0.031	5386	0.034	5379	0.013	5386	0.007	3618	0.017	10745
0.1939	0.3708	0.025	325	0.010	3509	0.011	3509	0.012	3509	0.007	3509	0.011	3509
0.1939	0.4363	0.020	325	0.009	3509	0.010	3509	0.010	3509	0.006	3509	0.010	3509
0.1942	0.4363	0.023	325	0.009	3509	0.010	3509	0.011	3509	0.007	3509	0.010	3509
0.1937	0.4799	0.022	325	0.013	1653	0.017	1653	0.010	3509	0.006	3509	0.009	3509
0.1940	0.5017	0.018	325	0.006	3509	0.007	1687	0.008	3509	0.005	3509	0.007	3509
0.1941	0.5453	0.019	325	0.011	5494	0.019	5583	0.012	3503	0.007	3503	0.010	3503
0.1940	0.5890	0.049	2635	0.041	2635	0.034	5454	0.024	2635	0.015	2635	0.011	3503
0.1942	0.6980	0.015	332	0.020	5494	0.045	5494	0.008	5494	0.005	3509	0.008	3509
0.1941	0.6980	0.016	332	0.017	5643	0.045	5643	0.010	3509	0.006	3509	0.009	3509
0.1939	0.7853	0.021	332	0.029	8834	0.039	8916	0.012	3509	0.060	8990	0.011	3509
0.1947	0.8507	0.029	5467	0.057	5467	0.029	5610	0.031	5467	0.006	3523	0.020	10935
0.1935	0.9380	0.017	332	0.030	5650	0.013	5650	0.007	5650	0.005	3536	0.008	3536
0.1939	1.0470	0.148	5406	0.143	5406	0.083	5420	0.070	5406	0.018	12141	0.044	10847
0.2250	0.4581	0.022	325	0.010	1673	0.009	3564	0.010	3564	0.006	3564	0.009	3564
0.2239	0.5017	0.026	325	0.007	3550	0.008	3550	0.009	3550	0.005	3550	0.008	3550
0.2243	0.5235	0.026	325	0.009	3557	0.010	3557	0.010	3557	0.006	3557	0.010	3557
0.2240	0.5453	0.026	325	0.009	3550	0.009	3550	0.010	3550	0.006	3550	0.010	3550
0.2241	0.5890	0.028	2893	0.013	2893	0.012	2893	0.011	3543	0.007	3543	0.010	3543
0.2236	0.6326	0.021	325	0.014	5515	0.018	5461	0.012	5461	0.005	3530	0.009	5461
0.2240	0.6980	0.023	5454	0.055	5454	0.057	5454	0.026	5454	0.007	3523	0.011	3523
0.2245	0.7635	0.025	325	0.019	5826	0.054	5833	0.009	5833	0.009	5833	0.016	5833
0.2241	0.8289	0.023	325	0.016	5562	0.017	5799	0.029	5779	0.007	11572	0.009	3503
0.2242	0.8943	0.080	2683	0.062	2683	0.060	5542	0.034	2683	0.017	2683	0.010	3496
0.2242	0.9816	0.019	325	0.010	3489	0.024	10034	0.019	5684	0.007	3489	0.020	11199
0.2243	1.0689	0.077	5765	0.051	5765	0.078	5765	0.052	5765	0.015	5765	0.039	11517
0.2240	1.1779	0.049	5671	0.033	5671	0.020	8448	0.056	5671	0.012	10664	0.046	11172

Table F.9: Data: Tests 4.0-4.5 for $\frac{r}{r_c}$=50%

$\dot{m}_f$ [g/s]	$\dot{m}_{ox}$ [g/s]	A_{P1} [psig]	f_{P1} [Hz]	A_{P2} [psig]	f_{P2} [Hz]	A_{P4} [psig]	f_{P4} [Hz]	A_{P6} [psig]	f_{P6} [Hz]	A_{P7} [psig]	f_{P7} [Hz]	A_{P8} [psig]	f_{P8} [Hz]
0.2590	0.5453	0.025	325	0.008	3597	0.009	3597	0.009	3597	0.006	3597	0.009	3597
0.2595	0.5671	0.021	325	0.007	1775	0.007	3577	0.008	3577	0.005	3577	0.007	3577
0.2588	0.5890	0.026	325	0.010	3557	0.011	5034	0.012	5013	0.007	3557	0.011	3557
0.2585	0.6544	0.026	325	0.007	3557	0.014	5711	0.009	3557	0.009	11375	0.008	11395
0.2588	0.6544	0.026	325	0.010	3557	0.011	3557	0.011	3557	0.011	11389	0.011	3557
0.2593	0.7417	0.035	5616	0.028	5616	0.023	8387	0.034	5616	0.011	5616	0.012	11233
0.2595	0.7853	0.021	325	0.024	6009	0.038	9092	0.020	6009	0.011	12046	0.033	6009
0.2593	0.8943	0.043	5461	0.036	5461	0.023	5481	0.032	5461	0.008	2656	0.011	3543
0.2585	0.9598	0.045	5616	0.070	5610	0.029	8408	0.052	5610	0.012	5610	0.032	11226
0.2586	1.0470	0.058	5501	0.069	5501	0.020	5508	0.059	5501	0.010	11009	0.014	264
0.2595	1.1125	0.072	5623	0.119	5623	0.016	8381	0.092	5623	0.026	5623	0.035	11240
0.2575	1.1997	0.037	5515	0.048	5508	0.017	8299	0.031	5650	0.015	11416	0.028	108
0.2914	0.6326	0.020	325	0.012	1768	0.009	3631	0.010	3631	0.006	3631	0.009	3631
0.2907	0.6544	0.017	325	0.010	3625	0.074	5583	0.011	5583	0.007	3625	0.013	5583
0.2916	0.6544	0.019	325	0.009	3625	0.031	5569	0.011	3625	0.007	3625	0.010	3625
0.2911	0.7635	0.019	325	0.010	3625	0.032	5969	0.012	3625	0.007	3625	0.011	3625
0.2919	0.7635	0.020	325	0.010	3625	0.034	6131	0.012	3625	0.007	3625	0.011	3625
0.2911	0.8289	0.020	325	0.013	5596	0.063	5596	0.043	5596	0.010	5596	0.025	11212
0.2912	0.8725	0.020	325	0.013	5623	0.043	5623	0.024	5623	0.007	3618	0.022	11240
0.2911	1.0034	0.044	5535	0.056	5535	0.075	5535	0.057	5535	0.011	11050	0.029	11104
0.2910	1.0689	0.028	5610	0.043	5610	0.026	8401	0.043	5643	0.014	11301	0.041	11124
0.2905	1.1779	0.026	325	0.042	5650	0.024	9153	0.024	5630	0.020	10325	0.034	11395
0.2920	1.1997	0.022	325	0.019	1660	0.012	3577	0.012	3577	0.010	11321	0.056	11341

Table F.10: Data: Tests 1.0-2.0 for $\frac{r}{r_c}$=75%

$\dot{m}_f$ [g/s]	$\dot{m}_{ox}$ [g/s]	A_{P1} [psig]	f_{P1} [Hz]	A_{P2} [psig]	f_{P2} [Hz]	A_{P4} [psig]	f_{P4} [Hz]	A_{P6} [psig]	f_{P6} [Hz]	A_{P7} [psig]	f_{P7} [Hz]	A_{P8} [psig]	f_{P8} [Hz]
0.1090	0.1963	0.021	318	0.010	3428	0.012	3428	0.011	3428	0.007	3428	0.010	3428
0.1089	0.2399	0.022	318	0.009	3428	0.010	3428	0.010	3428	0.006	3428	0.009	3428
0.1090	0.2399	0.022	318	0.010	3421	0.022	5061	0.011	3421	0.007	3421	0.010	3421
0.1093	0.2618	0.023	318	0.008	3415	0.010	3415	0.009	3415	0.006	3415	0.008	3415
0.1092	0.2836	0.019	318	0.036	5969	0.063	5962	0.012	3415	0.008	5962	0.023	5955
0.1093	0.3054	0.024	318	0.030	5718	0.019	5718	0.009	3401	0.008	1802	0.012	5718
0.1092	0.3272	0.024	318	0.070	5948	0.095	5948	0.011	3387	0.010	5948	0.025	5948
0.1089	0.3708	0.147	2466	0.076	2466	0.039	2466	0.070	2466	0.126	2466	0.029	2466
0.1092	0.4145	0.024	318	0.012	5095	0.030	5081	0.009	3354	0.010	2602	0.008	6768
0.1090	0.4363	0.020	318	0.007	3340	0.011	9559	0.008	3340	0.005	1856	0.007	3340
0.1087	0.4581	0.024	318	0.010	3354	0.042	6856	0.011	3354	0.007	1646	0.037	6856
0.1089	0.5235	0.259	2419	0.163	2419	0.031	2419	0.095	2419	0.225	2419	0.053	2419
0.1093	0.5890	0.023	318	0.013	1626	0.012	1626	0.010	3354	0.016	1626	0.009	3354
0.1221	0.2399	0.020	325	0.007	3570	0.009	3570	0.009	3570	0.005	3570	0.008	3570
0.1223	0.2618	0.021	325	0.008	3564	0.010	3564	0.010	3564	0.006	3564	0.009	3564
0.1220	0.2836	0.021	325	0.010	3564	0.013	3564	0.012	3564	0.008	3564	0.011	3564
0.1216	0.3054	0.020	325	0.010	3543	0.012	3543	0.012	3543	0.007	3543	0.011	3543
0.1221	0.3490	0.020	325	0.010	3530	0.012	3530	0.012	3530	0.007	3530	0.011	3530
0.1219	0.3272	0.023	325	0.011	3523	0.013	3523	0.013	3523	0.008	3523	0.012	3523
0.1223	0.3708	0.018	325	0.011	3523	0.013	3523	0.013	3523	0.008	3523	0.012	3523
0.1216	0.4581	0.018	325	0.018	1551	0.027	6782	0.010	3523	0.006	3523	0.009	3523
0.1220	0.4145	0.030	4356	0.034	4356	0.020	5183	0.011	3523	0.007	3523	0.016	5183
0.1217	0.5235	0.192	2392	0.119	2392	0.054	2392	0.081	2392	0.019	2392	0.011	3523
0.1222	0.5017	0.235	2398	0.138	2398	0.099	2398	0.084	2398	0.020	2398	0.016	9586
0.1220	0.5890	0.014	332	0.021	1579	0.011	1579	0.010	3509	0.006	3509	0.009	3509
0.1219	0.6762	0.016	332	0.012	1565	0.017	7805	0.012	3516	0.007	3516	0.011	3516
0.1440	0.2836	0.021	325	0.046	5935	0.044	5935	0.011	3570	0.009	461	0.011	3570
0.1461	0.3054	0.025	325	0.024	5948	0.031	5948	0.012	3564	0.007	467	0.011	3564
0.1451	0.3272	0.020	325	0.022	6070	0.059	6070	0.012	3543	0.008	467	0.011	3543
0.1459	0.3490	0.020	325	0.012	6118	0.038	6118	0.012	3536	0.008	461	0.011	3536
0.1456	0.3708	0.038	2588	0.019	2588	0.025	6924	0.018	2588	0.007	3530	0.010	3530
0.1454	0.4363	0.018	325	0.014	5501	0.040	5345	0.009	3523	0.007	467	0.008	3523
0.1453	0.4363	0.018	325	0.035	5156	0.019	5162	0.008	3516	0.007	312	0.011	5162
0.1454	0.5017	0.016	325	0.022	1673	0.024	1673	0.015	1673	0.008	467	0.011	5223
0.1462	0.5453	0.014	325	0.010	3523	0.013	3523	0.012	3523	0.008	3523	0.011	3523

Table F.11: Data: Tests 2.5-3.5 for $\frac{r}{r_c}$=75%

$\dot{m}_f$ [g/s]	$\dot{m}_{ox}$ [g/s]	A_{P1} [psig]	f_{P1} [Hz]	A_{P2} [psig]	f_{P2} [Hz]	A_{P4} [psig]	f_{P4} [Hz]	A_{P6} [psig]	f_{P6} [Hz]	A_{P7} [psig]	f_{P7} [Hz]	A_{P8} [psig]	f_{P8} [Hz]
0.1717	0.3272	0.017	318	0.010	3442	0.012	3442	0.011	3442	0.007	3442	0.010	3442
0.1717	0.3708	0.018	318	0.010	3442	0.012	3442	0.011	3442	0.007	3442	0.010	3442
0.1717	0.3926	0.018	318	0.007	3442	0.008	3442	0.008	3442	0.012	1687	0.007	3442
0.1715	0.4363	0.018	318	0.007	3435	0.009	3435	0.008	3435	0.012	1701	0.008	3435
0.1711	0.4581	0.023	318	0.009	3435	0.011	3435	0.011	3435	0.008	1646	0.010	3435
0.1719	0.4799	0.019	318	0.009	3428	0.011	3428	0.011	3428	0.009	1680	0.010	3428
0.1717	0.5235	0.020	318	0.067	5291	0.068	5291	0.008	3421	0.020	5291	0.032	5291
0.1717	0.5890	0.020	318	0.064	5183	0.056	5183	0.012	3421	0.025	5183	0.028	5183
0.1719	0.6326	0.025	10393	0.011	10393	0.045	10393	0.018	10393	0.010	10393	0.011	10406
0.1722	0.6762	0.093	3340	0.055	3340	0.026	3340	0.055	3340	0.045	3340	0.024	3340
0.1718	0.7417	0.025	318	0.012	5657	0.016	5657	0.030	5657	0.025	5657	0.014	5657
0.1719	0.8289	0.022	9573	0.014	3611	0.012	11639	0.018	3611	0.016	3611	0.029	11639
0.1718	0.9380	0.065	3381	0.027	3387	0.015	3381	0.042	3381	0.030	3381	0.019	3381
0.1959	0.3926	0.024	318	0.009	3360	0.011	3360	0.011	3360	0.007	3360	0.010	3360
0.1943	0.4581	0.020	318	0.009	3347	0.012	3347	0.011	3347	0.007	3347	0.010	3347
0.1941	0.4363	0.020	318	0.009	3333	0.011	3333	0.011	3333	0.007	3333	0.010	3333
0.1938	0.5017	0.019	318	0.011	1606	0.010	1606	0.008	3333	0.013	1606	0.008	3333
0.1938	0.5017	0.023	318	0.009	3326	0.011	3326	0.011	3326	0.008	1579	0.010	3326
0.1941	0.5671	0.116	2534	0.069	2534	0.015	2534	0.048	2534	0.079	2534	0.010	2534
0.1938	0.5890	0.022	318	0.122	10345	0.057	5176	0.012	5169	0.025	5169	0.008	3333
0.1935	0.6762	0.018	318	0.008	3347	0.022	10569	0.027	10596	0.006	4695	0.009	3347
0.1941	0.6980	0.087	3394	0.073	3394	0.079	3394	0.035	3401	0.079	3394	0.010	3340
0.1937	0.7853	0.032	3435	0.025	2527	0.024	11185	0.027	3435	0.027	3435	0.008	3340
0.1938	0.8507	0.035	9444	0.009	3347	0.054	9444	0.012	9444	0.009	1660	0.015	9458
0.1939	0.9380	0.020	3435	0.040	1592	0.058	11124	0.015	3435	0.044	1592	0.012	11131
0.1937	1.0252	0.017	318	0.024	1551	0.027	5942	0.012	3394	0.019	1551	0.007	3394
0.2242	0.4581	0.019	325	0.009	3435	0.025	7696	0.009	3435	0.012	1701	0.008	3435
0.2242	0.4799	0.015	325	0.010	3442	0.012	3442	0.011	3442	0.007	3442	0.014	9600
0.2240	0.5235	0.016	325	0.027	5176	0.056	5162	0.009	3442	0.014	5162	0.008	3442
0.2243	0.5671	0.057	2561	0.040	2554	0.022	7615	0.028	2554	0.043	2554	0.008	3448
0.2239	0.5890	0.046	2649	0.033	2649	0.052	5135	0.029	2615	0.039	2649	0.008	3448
0.2243	0.6326	0.015	318	0.037	5515	0.053	5515	0.011	3448	0.009	1931	0.042	5515
0.2243	0.6762	0.016	318	0.009	3448	0.021	5847	0.010	3448	0.015	10650	0.016	10643
0.2239	0.7635	0.020	318	0.034	5996	0.150	5996	0.010	3448	0.015	5996	0.031	5996
0.2244	0.8289	0.021	9248	0.009	3448	0.047	9248	0.012	9194	0.020	9092	0.013	9221
0.2243	0.8943	0.044	2581	0.031	2581	0.028	5914	0.017	2581	0.038	2581	0.009	3442
0.2247	0.9598	0.021	318	0.021	5989	0.116	5982	0.010	3442	0.013	1579	0.025	5989
0.2239	1.0470	0.032	4444	0.014	1694	0.027	11775	0.009	3442	0.025	1694	0.008	3442
0.2238	1.1997	0.040	3408	0.033	3401	0.021	5948	0.030	3408	0.032	3408	0.010	3442

Table F.12: Data: Tests 4.0-4.5 for $\frac{r}{r_c}$=75%

$\dot{m}_f$ [g/s]	$\dot{m}_{ox}$ [g/s]	A_{P1} [psig]	f_{P1} [Hz]	A_{P2} [psig]	f_{P2} [Hz]	A_{P4} [psig]	f_{P4} [Hz]	A_{P6} [psig]	f_{P6} [Hz]	A_{P7} [psig]	f_{P7} [Hz]	A_{P8} [psig]	f_{P8} [Hz]
0.2593	0.5235	0.019	318	0.009	3428	0.010	3428	0.015	1843	0.016	1843	0.009	3428
0.2593	0.5671	0.019	318	0.012	1545	0.011	3428	0.011	3428	0.007	3428	0.010	3428
0.2591	0.5890	0.059	5095	0.126	5095	0.097	5095	0.008	5095	0.026	5095	0.031	5074
0.2588	0.6326	0.019	318	0.032	5501	0.028	5501	0.010	3421	0.009	1843	0.029	5501
0.2585	0.6762	0.024	318	0.010	3415	0.017	5806	0.011	3415	0.011	11436	0.009	3415
0.2594	0.7417	0.020	318	0.013	3692	0.011	3415	0.011	3415	0.007	3415	0.009	3415
0.2590	0.7853	0.023	318	0.017	3625	0.040	5955	0.011	3625	0.014	3625	0.007	3415
0.2597	0.8943	0.049	2574	0.030	8631	0.049	6057	0.023	2574	0.030	2574	0.021	6057
0.2593	0.9598	0.109	2615	0.086	2615	0.044	6138	0.041	2615	0.064	2615	0.015	6131
0.2590	1.0470	0.024	318	0.031	6158	0.059	6158	0.012	3367	0.013	1646	0.022	6152
0.2590	1.1125	0.024	318	0.045	6043	0.139	6043	0.010	3354	0.026	6030	0.048	6030
0.2588	1.2434	0.020	318	0.011	1660	0.042	9925	0.009	3354	0.015	1660	0.019	9797
0.2591	1.3742	0.066	3408	0.062	3408	0.048	6816	0.033	3408	0.057	3421	0.015	3408
0.2914	0.5671	0.021	318	0.011	1524	0.011	1524	0.009	3340	0.007	1524	0.008	3340
0.2903	0.6326	0.017	318	0.015	1640	0.017	1640	0.011	3340	0.018	1640	0.010	3340
0.2916	0.6544	0.020	318	0.015	1572	0.013	1599	0.011	3340	0.012	1572	0.010	3340
0.2909	0.7198	0.028	2513	0.023	2513	0.033	5860	0.016	2513	0.029	3415	0.118	5860
0.2914	0.7635	0.026	3530	0.059	3530	0.036	3523	0.024	3530	0.068	3530	0.016	6402
0.2905	0.8289	0.019	318	0.006	3381	0.011	11741	0.008	3381	0.007	2710	0.010	11633
0.2907	0.8943	0.242	2466	0.169	2466	0.090	2466	0.114	2466	0.180	2466	0.021	5989
0.2909	0.9816	0.042	2574	0.023	2574	0.025	2574	0.023	2574	0.027	2574	0.034	6036
0.2909	1.0689	0.022	2649	0.027	6158	0.015	1721	0.010	3401	0.023	1721	0.012	6158
0.2908	1.1779	0.020	318	0.025	6152	0.019	6145	0.011	6152	0.020	1660	0.078	6145
0.2916	1.2652	0.017	318	0.009	3421	0.044	9783	0.011	9573	0.023	1768	0.047	9736
0.2911	1.3742	0.027	3503	0.022	5196	0.024	5196	0.019	3503	0.021	1619	0.034	5196
0.2909	1.5487	0.091	3421	0.065	3421	0.066	3421	0.088	3421	0.078	3421	0.010	11985

REFERENCES

[1] Coultas, T. A., "Combustion Instability," *Liquid Propellant Rocket Combustion Instability*, edited by D. T. Harrje and F. H. Reardon, NASA SP-194, National Aeronautics and Space Administration, 1972, pp. 14–23.

[2] Dranovsky, M. L., Yang, V., Culick, F. E. C., and Talley, D. G., *Combustion Instabilities in Liquid Rocket Engines: Testing and Development Practices in Russia*, Progress in Astronautics and Aeronautics, American Institute of Astronautics and Aeronautics, 2007.

[3] Culick, F. E. C. and Yang, V., "Overview of Combustion Instabilities in Liquid-Propellant Rocket Engines," *Liquid Rocket Engine Combustion Instability*, edited by V. Yang and W. Anderson, Progress in Astronautics and Aeronautics, American Institute of Astronautics and Aeronautics, 1995, pp. 3–37.

[4] Borenstein, S., "NASA's Rocket May Shake Too Much," Associated Press, 2008.

[5] Sutton, G. P., "History of Liquid Propellant Rocket Engines in the United States," *Journal of Propulsion and Power*, Vol. 19, No. 6, 2003, pp. 978–1007.

[6] Melcher, J. C. and Allred, J. K., "Liquid Oxygen/Liquid Methane Testing of the RS-18 at NASA White Sands Test Facility," *44th AIAA/ASME/SAE/IEEE Joint Propulsion Conference*, No. AIAA-2008-4843, American Institute for Aeronautics and Astronautics, Hartford, CT, 2008.

[7] Melcher, J. C. and Allred, J. K., "Liquid Oxygen/Liquid Methane Test Results of the RS-18 Lunar Ascent Engine at Simulated Altitude Conditions at NASA White Sands Test Facility," *45th AIAA/ASME/SAE/IEEE Joint Propulsion Conference*, No. AIAA-2009-4949, American Institute for Aeronautics and Astronautics, Denver, CO, 2009.

[8] McBride, J. M., "Blade Arrangement," *Liquid Propellant Rocket Combustion Instability*, edited by D. T. Harrje and F. H. Reardon, NASA SP-194, National Aeronautics and Space Administration, 1972, pp. 389–394.

[9] Sutton, G. P. and Biblarz, O., *Rocket Propulsion Elements*, John Wiley & Sons, New York, 7th ed., 2001.

[10] Gaydon, A. G. and Wolfhard, H. G., *Flames: Their Structure, Radiation, and Temperature*, Chapman and Hall, London, 3rd ed., 1970.

[11] Rayleigh, J. W. S., *The Theory of Sound*, Vol. 2, Dover Publications, Inc., New York, 1945.

[12] Gaydon, A. G., *The Spectroscopy of Flames*, Chapman and Hall, London, 2nd ed., 1974.

[13] Nori, V. N. and Seitzman, J. M., "CH* Chemiluminescence Modeling for Combustion Diagnostics," *Proceedings of the Combustion Institute*, Vol. 32, 2009, pp. 895–903.

[14] Luque, J. and Crosley, D. R., "LIFBASE, Database and Spectral Simulation for Diatomic Molecules (v. 1.6)," http://www.sri.com/psd/lifbase, 1999.

[15] Dexter, C. E., Fisher, M. E., Hulka, J. R., Denisov, K. P., Shibanov, A. A., and Agarkov, A. F., "Scaling Techniques for Design, Development, and Test," *Liquid Rocket Thrust Chambers: Aspects of Modeling, Analysis, and Design*, edited by V. Yang, M. Habiballah, J. Hulka, and M. Poppe, Progress in Astronautics and Aeronautics, American Institute of Astronautics and Aeronautics, 2004, pp. 553–600.

[16] Cavitt, R., *Experimental Methodology for Measuring Combustion and Injection Coupled Responses*, UAHuntsville Master's Thesis, Huntsville, AL, 2007.

[17] Cavitt, R. C., Frederick, R. A., and Bazarov, V. G., "Laboratory Scale Survey of Pentad Injector Stability Characteristics," *Journal of Propulsion and Power*, Vol. 24, No. 3, 2008, pp. 534–540.

[18] Byrd, R. E., *Laboratory Scale Injector Instability Mode Assessment*, UAHuntsville Master's Thesis, Huntsville, AL, 2008.

[19] Byrd, R. E., Huynh, H. H., and Frederick, R. A., "Instability Characteristics of a GOX/Methane Injector," *Journal of Propulsion and Power*, accepted for publication.

[20] Huynh, H. H., *Mode Assessment of a Single-Element Shear Coaxial Injector*, UAHuntsville Master's Thesis, Huntsville, AL, 2009.

[21] Huynh, H. H., Sweeney, B., and Frederick, R. A., "Mode Assessment of a Single-Element Shear Coaxial Injector," *45th AIAA/ASME/SAE/IEEE Joint Propulsion Conference*, No. AIAA-2009-5493, American Institute for Aeronautics and Astronautics, Denver, CO, 2009.

[22] Jensen, R., Dodson, H., and Claflin, S., "LOX/Hydrocarbon Combustion Instability Investigation," Tech. Rep. NASA 182249 and RI/RD 89-179, Rockwell International: Rocketdyne Division, Canoga Park, CA, July 1989.

[23] Sohn, C. H., Seol, W.-S., Shibanov, A. A., and Pikalov, V. P., "On the Method for Hot-Fire Modeling of High-Frequency Combustion Instability in Liquid Rocket Engines," *KSME International Journal*, Vol. 18, No. 6, 2004, pp. 1010–1018.

[24] Sohn, C. H., Seol, W.-S., Shibanov, A. A., and Pikalov, V. P., "Hot-Fire Injector Test for Determination of Combustion Stability Boundaries Using Model Chamber," *Journal of Mechanical Science and Technology*, Vol. 19, No. 9, 2005, pp. 1821–1832.

[25] Sohn, C. H., Seol, W.-S., and Shibanov, A. A., "Combustion Stability Characteristics of the Model Chamber with Various Configurations of Triplet Impinging Injectors," *Journal of Mechanical Science and Technology*, Vol. 20, No. 6, 2006, pp. 874–881.

[26] Lee, K.-J., Seo, S., Song, J.-Y., Han, Y.-M., Choi, H.-S., and Seol, W.-S., "Combustion Stability Assessment of Double Swirl Coaxial Injectors Using Simulant Propellants," *41st AIAA/ASME/SAE/IEEE Joint Propulsion Conference*, No. AIAA-2005-4443, American Institute for Aeronautics and Astronautics, Tuscon, AZ, 2005.

[27] Morrell, M. R., Seitzman, J. M., Wilensky, M., Lubarsky, E., Lee, J., and Zinn, B., "Interpretation of Optical Emissions for Sensors in Liquid Fueled Combustors," *39th Aerospace Sciences Meeting and Exhibit*, No. AIAA-2001-0787, American Institute for Aeronautics and Astronautics, Reno, NV, 2001.

[28] Zinn, B. T., Lubarsky, E., and Neumeier, Y., "Real-Time Control for Optimal Liquid Rocket Combustor Performance," Tech. Rep. AFRL-SR-AR-TR-06-0020, Georgia Institute of Technology, Atlanta, GA, 2006.

[29] Bibik, O., Lubarsky, E., Shcherbik, D., Hadjipanayis, M., and Zinn, B. T., "Rotational Traveling of Tangential Wave in Multi-Injectors LRE Combustor Simulator," *46th AIAA Aerospace Sciences Meeting and Exhibit*, No. 2008-1001, American Institute of Aeronautics and Astronautics, Reno, NV, 2008.

[30] Hardalupas, Y. and Orain, M., "Local Measurements of the Time-Dependent Heat Release Rate and Equivalence Ratio Using Chemiluminescent Emission from a Flame," *Combustion and Flame*, Vol. 139, 2004, pp. 188–207.

[31] Lee, J. G., Kim, K., and Santavicca, D., "A Study of the Role of Equivalence Ratio Fluctuations During Unstable Combustion in a Lean Premixed Combustor," *38th AIAA/ASME/SAE/IEEE Joint Propulsion Conference*, No. AIAA-2002-4015, American Institute for Aeronautics and Astronautics, Indianapolis, IN, 2002.

[32] Lee, J. G. and Santavicca, D. A., "Experimental Diagnostics for the Study of Combustion Instabilities in Lean Premixed Combustors," *Journal of Propulsion and Power*, Vol. 19, No. 5, 2003, pp. 735–750.

[33] Eberhart, C. J., Lineberry, D. M., and Moser, M. D., "Experimental Cold Flow Characterization of a Swirl Coaxial Injector Element," *45th AIAA/ASME/SAE/IEEE Joint Propulsion Conference*, No. AIAA-2009-5140, American Institute for Aeronautics and Astronautics, Denver, CO, 2009.

[34] Mulkey, H. W., Moser, M. D., and Hitt, M. A., "GOX/Methane Combustion Efficiency of a Swirl Coaxial Injector Element," *45th AIAA/ASME/SAE/IEEE Joint Propulsion Conference*, No. AIAA-2009-5141, American Institute for Aeronautics and Astronautics, Denver, CO, 2009.

[35] Ikard, R. L., Brooks, J. W., and Frederick, R. A., "Unsteady Chemiluminescence Imaging of a Swirl-Coaxial Injector," *45th AIAA/ASME/SAE/IEEE Joint Propulsion Conference*, No. AIAA-2009-5051, American Institute for Aeronautics and Astronautics, Denver, CO, 2009.

[36] NASA Glenn, "Specification for 5,500±100 lbf (vac) Engine, Revised," Dec 2007.

[37] Bazarov, V., Yang, V., and Puri, V., "Design and Dynamics of Jet and Swirl Injectors," *Liquid Rocket Thrust Chambers: Aspects of Modeling, Analysis, and Design*, edited by V. Yang, M. Habiballah, J. Hulka, and M. Poppe, Progress in Astronautics and Aeronautics, American Institute of Astronautics and Aeronautics, 2004, pp. 19–103.

[38] Anonymous, "Liquid Rocket Engine Injectors," Tech. Rep. NASA SP-8089, National Aeronautics and Space Administration, Washington, DC, 1976.

[39] Saffell, R. J. and Moser, M. D., "GOX/Methane Injector Effects on Combustion Efficiency," *44th AIAA/ASME/SAE/IEEE Joint Propulsion Conference*, No. AIAA-2008-4952, American Institute for Aeronautics and Astronautics, Hartford, CT, 2008.

[40] Salgues, D., Mouis, A.-G., Lee, S.-Y., Kalitan, D., Pal, S., and Santoro, R., "Shear and Swirl Coaxial Injector Studies of LOX/GCH4 Rocket Combustion Using Non-Intrusive Laser Diagnostics," *44th AIAA Aerospace Sciences Meeting and Exhibit*, No. AIAA-2006-0757, American Institute for Aeronautics and Astronautics, Reno, NV, 2006.

[41] Rogero, S., Wesley, R. D., and Hefner, R. J., "Location and Mounting," *Liquid Propellant Rocket Combustion Instability*, edited by D. T. Harrje and F. H. Reardon, NASA SP-194, National Aeronautics and Space Administration, 1972, pp. 467–475.

[42] Barrere, M. and et al., *Rocket Propulsion*, Elsevier Publishing Co., New York, NY, 1960.

[43] Rasband, W. S., "ImageJ 1.41o," http://rsbweb.nih.gov/ij/.

[44] Dasch, C. J., "One-Dimensional Tomography: A Comparison of Abel, Onion-Peeling, and Filtered Backprojection Methods," *Applied Optics*, Vol. 31, No. 8, 1992, pp. 1146–1152.